Surface Modification of Etched Ion-Track Polymer Membranes by Atomic Layer Deposition

Oberflächenmodifizierung geätzter Ionenspurmembranen mittels Atomlagenabscheidung

Zur Erlangung des Grades eines Doktors der Naturwissenschaften (Dr. rer. nat.)
genehmigte Dissertation von M.Sc. Anne Spende aus Göttingen
Tag der Einreichung: 17. Mai 2016, Tag der Prüfung: 06. Juli 2016
Darmstadt 2016 — D 17

1. Gutachten: Prof. Dr. Christina Trautmann
2. Gutachten: Prof. Dr. Wolfgang Ensinger

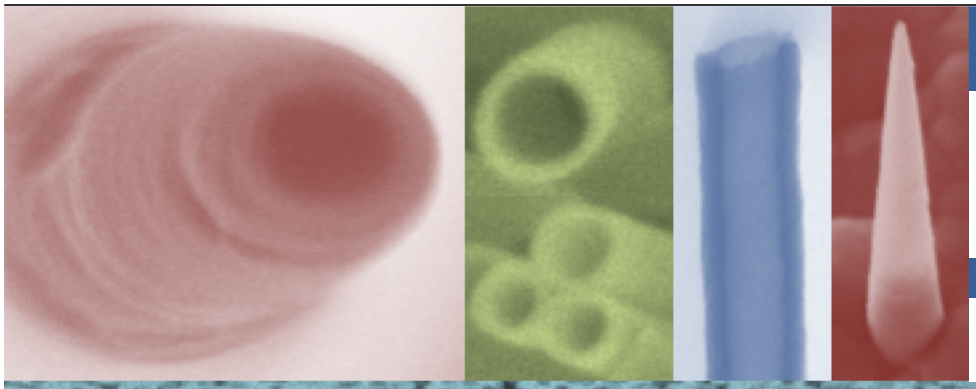

TECHNISCHE UNIVERSITÄT DARMSTADT

Fachbereich Material- und Geowissenschaften
Ionenstrahlmodifizierte Materialien

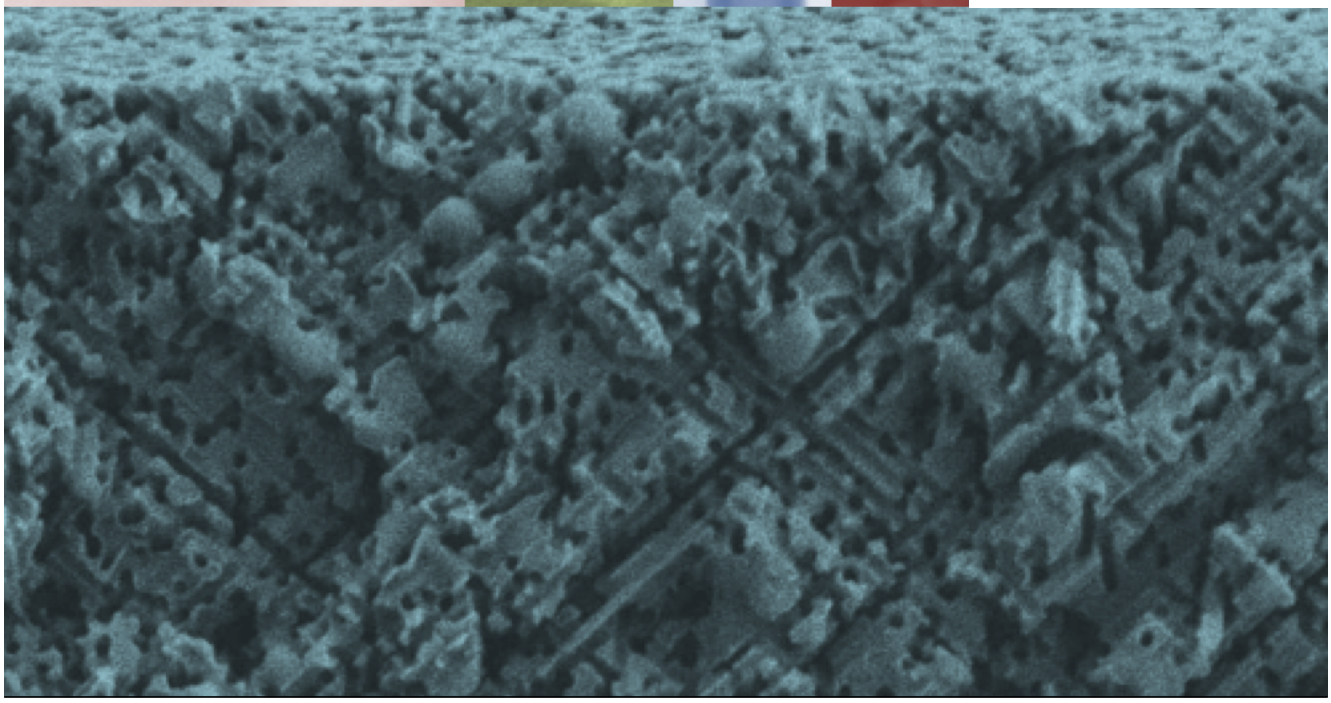

Surface Modification of Etched Ion-Track Polymer Membranes by Atomic Layer Deposition
Oberflächenmodifizierung geätzter Ionenspurmembranen mittels Atomlagenabscheidung

Genehmigte Dissertation von M.Sc. Anne Spende aus Göttingen

1. Gutachten: Prof. Dr. Christina Trautmann
2. Gutachten: Prof. Dr. Wolfgang Ensinger

Tag der Einreichung: 17. Mai 2016
Tag der Prüfung: 06. Juli 2016

Darmstadt 2016 — D 17

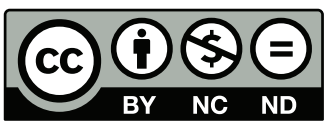

Erklärung zur Dissertation

Hiermit versichere ich, die vorliegende Dissertation ohne Hilfe Dritter nur mit den angegebenen Quellen und Hilfsmitteln angefertigt zu haben. Alle Stellen, die aus Quellen entnommen wurden, sind als solche kenntlich gemacht. Diese Arbeit hat in gleicher oder ähnlicher Form noch keiner Prüfungsbehörde vorgelegen.

Darmstadt, den 16. Mai 2016

_____

(A. Spende)

Abstract

Inorganic nanochannels integrated in solid state membranes as well as nanotubes are of high relevance for fundamental research and industrial applications in catalysis, filtration, sensorics, solar energy harvesting, biomedicine, and nanofluidics. Currently, lots of effects are being devoted to develop reproducible and efficient fabrication techniques that enable the precise tailoring of geometry, dimensions, and properties of the nanochannels.

This thesis presents the combination of ion-track technology with low-temperature atomic layer deposition (ALD). Cylindrical and conical nanotubes as well as highly-ordered nanotube networks exhibiting aspect ratios above 3000 were synthesized. 30-µm thick polycarbonate membranes were irradiated with ∼GeV swift heavy ions at the UNILAC accelerator of GSI under normal or tilted beam incidence. By subsequent wet-chemical etching, each individual ion track was dissolved and thus converted into an open nanochannel. The length of the nanochannel was determined by the thickness of the polymer, whereas geometry and diameter ($\geq$ 18 nm) were controlled by the etching parameters. To reduce the channel diameter further and modify the surface of the channel walls without affecting the channel shape, titania (TiO_2), silicon dioxide (SiO_2), and alumina (Al_2O_3) were deposited onto the templates by ALD. This sequential and self-limiting surface modification technique provided the precise control of the deposited thickness due to layer-by-layer growth.

From small angle X-ray scattering (SAXS) analysis average channel diameter, diameter distribution before and after ALD as well as coating thickness were deduced. The results demonstrated homogeneous and conformal deposition along the entire cylindrical nanochannels down to inner diameters below 10 nm. For these samples, X-ray photoelectron spectroscopy (XPS) evidenced almost stoichiometric composition of the ALD layers deposited onto the membrane surface. For all investigated nanostructures, the dissolution of the supporting polymer template by wet-chemical methods and the following visualization of the resulting structures by electron microscope (SEM) in scanning and transmission mode revealed exactly defined geometries, diameters, and wall thicknesses. The preparation of arrays of free-standing conical nanotubes from multichannel membranes and the novel alike preparation of free-standing single tubular nanocones from single channel membranes enabled the comparison between the asymmetric etching process in single and multichannel membranes that resulted in the agreement of the radial base etching rates whereas the tip etching was by a factor of $\sim$ 2 faster for single channels. In addition, the base diameter was determined at the replica of the single channel itself, which enabled precise computation of the tip diameter. The homogeneity of the ALD processes inside the nanochannels was confirmed by energy dispersive X-ray spectroscopy (EDX) of the released nanotubes.

In addition, ionic conductance (*I-V*) studies of cylindrical and conical single nanochannels before and after ALD demonstrated conformal deposition processes inside the single channels in polycarbonate. Surface charges induced by variation of the pH value of the electrolyte influenced the recorded ionic currents in agreement with the theory of nanofludics for channel diameters up to 100 nm. Furthermore,

the gating of single conical nanochannels in polycarbonate membranes surface modified with a 5 nm thick TiO_2 film was enabled by a straight-forward set-up comparable to n-type JFETs.

Zusammenfassung

Anorganische Nanokanäle integriert in Festkörpermembranen und Nanoröhren sind von großer Bedeutung für Grundlagenforschung und industrielle Anwendungen in den Bereichen Katalyse, Filtration, Sensorik, Solarenergiegewinnung, Biomedizin und Nanofluidik. Zur Zeit werden viele Prozesse untersucht, um eine reproduzierbare und effiziente Herstellung zu gewährleisten, die zudem die genaue Einstellung der Geometrie, der Dimensionen und der Eigenschaften der Nanokanäle ermöglicht.

Diese Dissertation präsentiert die Kombination der Ionenspurtechnologie mit der Tieftemperatur-Atomlagenabscheidung (engl. atomic layer deposition, ALD). Zylindrische und konische Nanoröhren sowie geordnete Nanoröhren-Netzwerke mit Aspektverhältnissen über 3000 wurden hergestellt. 30-µm dicke Polycarbonatfolien wurden mit schweren Ionen, die kinetische Energien im Bereich ∼GeV aufwiesen, am UNILAC Beschleuniger der GSI unter senkrechtem und gekipptem Einfallswinkel bestrahlt. Durch nachfolgendes nasschemisches Ätzen wurde jede einzelne Ionenspur aufgelöst und in einen offenen Nanokanal transformiert. Die Länge des Nanokanals war durch die Dicke des Polymers bestimmt, wohingegen die Geometrie und der Durchmesser ($\geq$ 18 nm) durch die Ätzparameter kontrolliert wurden. Um den Kanaldurchmesser weiter zu reduzieren und die Oberfläche der Kanalwände zu modifizieren ohne die Form des Kanals zu verändern, wurden Titandioxid (TiO_2), Siliziumdioxid (SiO_2) und Aluminiumoxid (Al_2O_3) mittels ALD auf die Template abgeschieden. Diese sequentielle und selbst-limitierende Oberflächenmodifikationstechnik ermöglichte die präzise Kontrolle der abgeschiedenen Schichtdicke durch Schicht-für-Schicht Wachstum.

Aus Kleinwinkelröntgenstreuungsanalysen (engl. small angle X-ray scattering, SAXS) wurden der durchschnittliche Kanaldurchmesser, die Durchmesserverteilung vor und nach der ALD-Beschichtung sowie die Dicke der Beschichtung abgeleitet. Die Ergebnisse zeigten homogene und konformale Beschichtung entlang der gesamten Kanallänge für innere Durchmesser unter 10 nm. Für diese Proben wurde mittels Röntgenphotoelektronenspektroskopie (engl. X-ray photoelectron spectroscopy, XPS) eine fast stöchiometrische Zusammensetzung der ALD-Beschichtung an der Membranoberfläche nachgewiesen. In allen Fällen führte die Auflösung des Polymertemplats mittels nasschemischer Methoden zu selbsttragenden Nanostrukturen. Visualisierung dieser mittels Rasterelektronenmikroskopie (engl. scanning electron microscopy, SEM) zeigte exakt definierte Geometrien, Durchmesser und Wandstärken der Nanoröhren. Die Präparierung von Arrays freistehender konischer Nanoröhren aus Vielkanalmembranen und dieselbe neuartige Präparation freistehender einzelner röhrenförmiger Nanokegel aus Einzelkanalmembranen erlaubte den Vergleich des asymmetrischen Ätzprozesses in Einzel- und Vielkanalmembranen. Die radialen Ätzraten für die Basis der Kegel stimmten überein, während das radiale Ätzen der Kegelspitzen für Einzelkanäle doppelt so schnell war. Zudem wurde der Basisdurchmesser an der Replik des Einzelkanals gemessen, was die genaue Berechnung des Spitzendurchmessers ermöglichte. Die Homogenität der ALD-Prozesse in den Kanälen wurde durch energiedispersive Röntgenspektroskopie (engl. energy dispersive X-ray spectroscopy, EDX) nachgewiesen.

Ionische Leitfähigkeitsuntersuchungen (*I-V*) zylindrischer und konischer Einzelkanäle vor und nach

ALD-Beschichtungen bewiesen die konformale Beschichtung von Einzelkanälen in Polycarbonatmembranen. Durch Variation des pH Wertes des Elektrolyten induzierte Oberflächenladungen beeinflussten die gemessenen ionischen Ströme für Kanaldurchmesser bis zu 100 nm in Übereinstimmung mit der Nanofluidiktheorie. Desweiteren wurden mit einem unkomplizierten Aufbau vergleichbar mit einem n-Kanal JFET konische Einzelkanäle in Polycarbonatmembranen gesperrt, welche mit 5 nm TiO_2 oberflächenmodifiziert waren.

Publications

This thesis is based on the following publications and results were presented at the international conferences listed below. Furthermore, some results are already described in Bachelor theses and an internship report.

Peer-Reviewed Publications

A. Spende, N. Sobel, M. Lukas, R. Zierold, Jesse C. Riedl, L. Gura, I. Schubert, , J. M. Montero Moreno, K. Nielsch, B. Stühn, C. Hess, C. Trautmann, and M. E. Toimil-Molares

TiO_2, SiO_2, and Al_2O_3 coated nanopores and nanotubes produced by ALD in etched ion-track membranes for transport measurements

Nanotechnology 26, 2015, 335301

N. Sobel, C. Hess, M. Lukas, A. Spende, B. Stühn, M. E. Toimil-Molares, and C. Trautmann

Conformal SiO_2 coating of sub-100 nm diameter channels of polycarbonate etched ion-track channels by atomic layer deposition

Beilstein Journal of Nanotechnology 6, 2015, 472-479

Further Publications

A. Spende, I. Alber, N. Sobel, C. Hess, M. Lukas, B. Stühn, R. Zierold, J. M. Montero Moreno, K. Nielsch, C. Trautmann, and M. E. Toimil-Molares

High Aspect Ratio Nanotubes fabricated by Ion-Track Technology and Atomic Layer Deposition

GSI Scientific Report 2013

Talks at Workshops and Conferences

A. Spende, L. Movsesyan, N. Sobel, C. Hess, M. Lukas, B. Stühn, J. M. Montero Moreno, R. Zierold, K. Nielsch, C. Trautmann, and M. E. Toimil-Molares

Nanotubes, Nanocones, and Nanotube Networks Fabricated by Ion-Track Technology and ALD of TiO_2, SiO_2, and Al_2O_3

International Conference on Atomic Layer Deposition, ALD 2015, Portland, Oregon, USA

A. Spende, N. Sobel, C. Hess, M. Lukas, B. Stühn, J. M. Montero Moreno, R. Zierold, K. Nielsch, C. Trautmann and M.E. Toimil-Molares
SiO_2-, Al_2O_3-, and TiO_2-nanotubes synthesized by low-temperature ALD in etched ion-track membranes
Spring Meeting 2015, German Physical Society, Berlin, Germany

A. Spende, I. Alber, N. Sobel, C. Hess, M. Lukas, B. Stühn, J. M. Montero Moreno, R. Zierold, K. Nielsch, C. Trautmann and M.E. Toimil-Molares
Alumina-, titania-, and silicon dioxide-nanotubes synthesized by atomic layer deposition in ion-track etched membranes
Ion Beams and Nanostructures, Paderborn, Germany

A. Spende , I. Alber, N. Sobel, C. Hess, M. Lukas, B. Stühn, J. M Montero Moreno, R. Zierold, K. Nielsch, C. Trautmann and M.E. Toimil-Molares
Titania-, Alumina- and Silicon dioxide-Nanotubes with High Aspect Ratios (> 500) Fabricated by Ion-Track Technology and Atomic Layer Deposition
MRS Spring Meeting 2014, Materials Research Society, San Francisco, California, USA

Posters at Workshops and Conferences
A. Spende, , N. Sobel, C. Hess, M. Lukas, B. Stühn, J. M. Montero Moreno, R. Zierold, K. Nielsch, C. Trautmann and M.E. Toimil-Molares
Atomic layer deposition of Al_2O_3, TiO_2, and SiO_2 in etched ion-track polycarbonate membranes
International Symposium on Swift Heavy Ions in Matter, SHIM2015, Darmstadt, Germany

A. Spende, I. Alber, N. Sobel, C. Hess, M. Lukas, B. Stühn, J. M. Montero Moreno, R. Zierold, K. Nielsch, C. Trautmann1 and M.E. Toimil-Molares
Alumina-, titania- and silicon dioxide-nanotubes with high aspect ratios (1500) synthesised by ion-track technology and ALD
Baltic International Conference on Atomic Layer Deposition, ALD 2014, Helsinki, Finland

A. Spende, I. Alber, N. Sobel, C. Hess, M. Lukas, B. Stühn, J. M. Montero Moreno, R. Zierold, K. Nielsch, C. Trautmann and M.E. Toimil-Molares
Surface modification of etched ion-track templates by atomic layer deposition of SiO_2, Al_2O_3, and TiO_2
International Workshop on Electrodeposited Nanostructures, EdNano, Oberwesel, Germany

Bachelor Theses (co-supervised)
Nils Ulrich
Synthesis and Characterisation of ALD-Coated Conical Nanopores for Ion-Transport Studies
Technische Universität Darmstadt, September 2015

Leonard Gordian Gura
Ionic Transport Studies of ALD-Coated Single Etched Ion-Track Nanopores

Technische Universität Darmstadt, September 2015

Internship Report (co-supervised)
Nils Ulrich
Conical Nanotubes Synthesized by Ion-Track Technology and Atomic Layer Deposition
Technische Universität Darmstadt, February 2015

Wenn die Wissenschaft ihren Kreis durchlaufen hat, so gelanget sie natürlicher Weise zu dem Puncte eines bescheidenen Misstrauens, und sagt, unwillig über sich selbst, wie viele Dinge giebt es doch, die ich nicht einsehe.

Immanuel Kant

Contents

1 Introduction

Nanostructures are gaining increasing importance in science and technology due to the novel technologies in fabrication of nanosized devices as well as tailoring specific properties. The ability to synthesize and assemble nanoscale building blocks has opened numerous applications in many different fields including solar energy harvesting [1], biomedicine [2], magnetics [3, 4], and thermoelectrics [5–7].
In the fields of nanofluidics, filtration, catalysis, and sensorics, synthetic nanochannels embedded in solid state membranes provide promising perspectives as e.g. transistor [8], chemical, biochemical and drug separator [9–11], biocatalyst [11] as well as humidity sensor [12]. In biology, membranes containing one individual nanochannel are of special interest to mimic the transport through the membrane of biological cells [13, 14] as well as to sense and recognize single molecules [15, 16]. The translocation of a macromolecule through a nanochannel can be monitored by resistive-pulse sensing for channel diameters similar to the size of the macromolecule [17–19]. Nanochannels characterized by a diameter of a few nm are essential to investigate transport of molecules such as DNA [20], drugs [21], and water [22] through nanoconfinements. The electrophoretic mobility of a protein controls its movement through a nanochannel and thus the transport depends on the protein mass and charge [23]. Charge selectivity is also observed for ionic transport, e.g. potassium selective channels transport potassium in, but not out of a biological cell [24, 25]. For a better understanding of biological transport processes, synthetic nanochannels are advantageous due to higher robustness.
In literature, several techniques are reported aiming at the fabrication of single solid-state nanochannels in a precise and reproducible manner using lithography as well as ion beam and electron beam sculpturing [20]. Many of these approaches are limited to specific materials and can not easily adjust the geometry, length, and diameter of the nanochannel. Nowadays, the fabrication of solid-state nanochannels exhibiting diameters below 10 nm remains challenging. To overcome this limit, the fabrication process is complemented by a second step, were the channel diameter is further reduced by material deposition [26, 27] or by extended electron beam exposure [28].
In this work, ion-track nanotechnology was applied to synthesize high aspect ratio nanochannels in polycarbonate membranes. By means of atomic layer deposition (ALD), the cylindrical and conical nanochannels were conformally coated with TiO_2, SiO_2, and Al_2O_3 reducing the channel diameter down to 7 nm. Furthermore, the surface modification by ALD was applied to single-channel membranes to test their suitability for nanofluidic experiments.

Nanochannels as Model System for Nanofluidics

The transport of fluid through a single channel with a diameter below 100 nm is governed by the high surface-to-volume ratio of the channel [29, 30]. Surface charges at the liquid-solid interface strongly influence the transport due to the formation of an electrical double layer (EDL) at the nanochannel wall [31, 32]. In the case of conical nanochannels, the EDL can induce a diode-like, also called rectifying, behavior of the channel [27, 33–36]. To investigate the ionic transport through such nanochannels, a

method is required that allows to control all relevant parameters of the channel independently, namely, channel length, diameter, and geometry. Etched ion-tracks in polymer membranes provide this adjustability and are thus utilized since more than a decade for this kind of studies [13, 14, 33, 37–40]. However, the effect of dangling bonds and swelling of the polymer in solution is not completely understood. Additionally, the etching of polycarbonate (PC) results in carboxylate groups ($-COO^-$) at the inner channel walls [41]. No surface charges are formed, if the liquid exhibits the pH value of the point of zero charge (PZC) of the wall material. Thus, in nanochannels of alike dimensions surfaces exhibiting various points of zero charge are of special interest for systematic transport studies. The surface modification with different inorganic materials in etched ion-track polymer membranes is promising. To avoid effects on the channel shape and control the diameter reduction precisely, a conformal deposition process such as ALD is required. Nanochannels in PC have very smooth channel walls [42]. Conformal deposition thus provides smooth inorganic surfaces. These smooth walls are of great benefit for the systematic investigation of ionic transport through such nanochannels as well as applications, since rough channel walls as they are known for polyethylene terephthalate (PET) do not provide well-defined nanoconfinements [43].

Promising applications of nanochannels are novel nanofluidic electronic devices such as nanosized transistors that regulate ionic currents in liquid electrolytes instead of electron currents in solids [8, 44–46]. Fan et al. and Karnik et al. describe a single silica nanotube with a source and drain contact at the two opening sides and the gate attached to the central section of the tube [44, 45]. They demonstrated that the electric field applied via the gate electrode influences ionic transport through the nanotube and that the surface quality of the tube plays an important role. Yanagi et al. applied a nanopore in a thin silicon nitride membrane for DNA sequencing [8]. The nanopore was positioned between the gate contact and the channel, that is contacted to source and drain. In air and water as well as KCl solution, stable operation as p-type and n-type field effect transistor was demonstrated. During DNA translocation through the nanopore, the potential changes around the nanopore caused changes in the source-drain current. A single nanochannel in PET that exhibits conical geometry was gated by Kalman et al. [46]. Electron beam evaporation was applied to coat the tip side of the membrane with a 50 nm thick gold layer acting as gate electrode and a SiO_2 layer on top, which isolated the gate electrode from the electrolyte (KCl). To enhance adhesion of both thin films, titanium layers were deposited in between polymer and gold as well as between gold and SiO_2. This set-up regulated the cation selectivity of the conical nanochannel in PET and thus the transported ionic current. The deposition process led to a diameter reduction of several nm but details to which extend the tips of 5 to 15 nm diameter were modified could not be clarified. Gated nanochannels reported so far require several process steps with difficult control in particular of the small tip size. In contrast to evaporation techniques, ALD provides a much simpler approach due to conformal coating of the entire inner and outer surface of a sample. Thus, the inner channel walls as well as tip and base sides can be coated with a non-insulating material, such as TiO_2, that can serve as gate electrode on the tip side. Furthermore, the defined cycle number of an ALD process results in a well-controllable reduction of the tip diameter.

Nanoporous Templates

All template methods utilize a cast to shape the material during the fabrication process. For the synthesis

of nanostructures with defined dimensions, porous alumina membranes (anodic aluminum oxide, AAO) and etched ion-track membranes are widely used.

AAO templates are synthesized by anodic oxidation of aluminum in acidic solution [47, 48]. This fabrication allows to control the channels, whereas the channel density is given by the arrangement of the channels [49]. By double anodization, self-organization is obtained resulting in hexagonally packed parallel aligned channels and thus channel densities up to $\sim 10^{12} \frac{\text{channels}}{\text{cm}^2}$ [50]. However, the adjustment of the channel shape and the variability of interconnectivity are limited [51].

In contrast, ion-track technology provides templates with tailored number, length, geometry, and diameter of nanochannels [52–54]. The method is based on the irradiation of insulating targets such as polymer foils with swift heavy ions, which are available at large accelerator facilities. At beam energies in the range of MeV to GeV, the kinetic energy of the heavy ions is sufficiently high for the penetration of the ions through foils with thicknesses of several tens of μm. During deceleration, each ion creates a track with a diameter of 5-10 nm that consists of broken polymer chains and other defects [52, 55–57]. Wet-chemical etching selectively dissolves the damaged material and thus converts each ion track into a nanochannel. By varying the parameters of the etching process (duration, concentration of etchant, temperature, etc.) the size of the nanochannels can be adjusted in the range of 10-20 nm up to several μm [52–54, 58–60]. Due to the dimensions of the unetched ion-track, the synthesis of nanochannels of diameter below 10 nm is difficult. Commonly, ion-track technology is applied to polymers such as polycarbonate (PC) and polyethylene terephthalate (PET), but also works for few other inorganic materials (e.g., quartz and mica). Commercially available polymeric etched ion-track membranes are used as specific filters exhibiting a small size distribution of the channels. For the synthesis of nanowires and nanotubes by electrochemical [42, 60–64] and electroless deposition [65, 66], ion-track membranes are of great interest due to the flexibility to adjust geometry, length, and diameter of the nanowires.

The fact that each ion creates a track, which is transformed into an individual nanochannel, enables the precise control over the number of channels with irradiation fluences between one single ion per sample and $\sim 10^{10} \frac{\text{ions}}{\text{cm}^2}$. Besides producing parallel oriented nanochannels, the angle of irradiation can be varied and the irradiation can be performed from different directions resulting in intersecting ion-tracks, which lead to templates consisting of interconnected nanochannels. Networks with different orientation and integration levels can be synthesized [54, 67].

By varying the etching parameters, cylindrically, conically, biconically, and cigar-shaped nanochannels are achieved [54, 58, 60]. Compared to other nanoporous templates such as AAO the great flexibility of the ion-track technology is unique for the synthesis of nanochannels in polymers.

Surface Modification of Nanochannels

To tailor the surface properties of a nanochannel without affecting its shape, the deposition of a thin film is required. For the synthesis of thin films, several physical and chemical methods exist. They can be characterized by the aspect (length-to-diameter) ratio that they coat homogeneously. Physical techniques sublimate solid materials to enable resublimation of the gas on the substrate. Physical vapor deposition (PVD) as well as sputtering are performed in vacuum to avoid collisions of the sublimated material. Depending on the adhesion coefficient the resublimation takes place on the substrate. Due to the straight trajectories a homogeneous coating is achieved for aspect ratios below 10 [68–70]. In

contrast, chemical deposition methods are based on the reaction of substances in the medium or on the substrate. These techniques require binding partners and exhibit limited reaction kinetics. Thus, both binding partners can move into a channel before they react. Most chemical based deposition techniques such as chemical vapor deposition (CVD) are characterized by a continuous growth of the coating layer. This growth can result in a faster growth on the surface of the sample compared to the inner surface of the channel and thus lead to an inhomogeneous layer thickness or even a closing of the channel. This limits the maximum aspect ratio that is coated homogeneously by CVD to about ten [71–74]. Sol-gel coating processes and other solution-based chemical deposition methods enable a homogeneous thin film deposition inside structures with an aspect ratio up to 1000 [75, 76]. The same value is possible by electrochemical depositions [77, 78]. Electroless plating [65, 66] as well as chemical modification [79, 80] are established methods for the surface modification of nanochannels with aspect ratios above 1000. However, the homogeneity of these coatings is not sufficient for conformal deposition inside the nanochannels and thus affects the shape of the channel.

In contrast, atomic layer deposition (ALD) is based on successive, separated, and self-terminating gas-solid surface reactions that enable coating processes with a monolayer thickness precision [81]. Thermal ALD induces chemical reactions at suitable temperatures and separates the self-limiting half-reactions in time. The resulting time independence of the process provides the monolayer thickness control. Since the entering of gas into nanochannels is governed by diffusion, sufficient time provides the deposition of uniform films on the inner surface of nanochannels characterized by aspect ratios up to 10 000 [81–85]. Plasma-enhanced ALD utilizes ionized gas precursor molecules (by e.g. N_2 plasma) that chemically bind to the surface of the sample. For this process, a broader range of precursors is available. However, homogeneous coating is only achieved for structures with aspect ratios below 50 due to the high reactivity of radicals [86]. To avoid too long process times caused by low growth rates, spatial ALD was developed. The separation of the self-limiting half-reactions in time is replaced by spatial separation of the precursor gases by inert gas and the substrat moving between the precursor gases. Costs are reduced because the process is performed under ambient pressure instead of low pressure [87]. Nowadays, spatial ALD is applied for planar substrates and in industry for roll-to-roll coating of foils [88, 89].

In total, the layer-by-layer growth characteristic of ALD in combination with the time independence of a thermal ALD-process seem to be most suitable to provide conformal coatings of high aspect ratio nanostructures. Specific surface properties such as catalytic activity, hydrophobicity, and corrosion resistivity can be tuned by depositing a specific material. Successful coatings with the three oxides TiO_2, SiO_2, and Al_2O_3 by ALD are reported for various porous systems including AAO [90–94]. Nanochannels with a diameter of 40 nm in AAO were coated with less than 3 nm thick TiO_2 layers by Sander et al. resulting in an aspect ratio of 38 [90]. Elam et al. deposited Al_2O_3 in AAO nanochannels exhibiting an aspect ratio of 770 [91]. SiO_2 coatings of AAO nanochannels up to an aspect ratio of 3000 were described by Romero et al., who also investigated the ionic transport of NaCl solution through such a multichannel membrane [92]. In addition, these three oxides were applied to modify the surface of cylindrical etched ion-tracks in PC multichannel membranes [21, 95–99]. For instance, Bae et al. deposited TiO_2 and Al_2O_3 up to an aspect ratio of 300 in PC [97].

In this work, etched ion-tracks in PC were synthesized with various channel diameters and geometries as well as interconnected. To reduce the channel diameters in a controlled manner, the templates were

coated with TiO_2, SiO_2, and Al_2O_3 by ALD. These materials can be deposited by thermal ALD processes, which enable the surface modification of complex three dimensional structures. Due to the thermal instability of the PC above 140 °C [100], the processes had to be performed at low temperatures compared to the standard processes usually operated between 250 and 300 °C. This required the optimization of the process parameters considering the slower reaction kinetics as well as the high aspect ratios of the channels. Dissolution of the polymer template resulted in self-supporting nanotubes. Besides the coating of multichannel membranes, the optimized process parameters were utilized to modify the surface of single nanochannels. These channels were investigated by ionic conductance measurements.

Objectives of this Thesis

To investigate if ALD is suitable for tailored coating of high aspect ratio nanostructures exhibiting various geometries, the high flexibility of etched ion-track templates regarding arrangement, number, geometry, and dimensions of nanochannels was utilized. For all studies, 30-µm thick polycarbonate foils served as template. In systematic series, parallel aligned nanochannels of cylindrical and conical geometry as well as highly-ordered networks of cylindrical nanochannels were fabricated and subsequently coated with various thicknesses of TiO_2, SiO_2, and Al_2O_3.

Besides characterization of the as-synthesized samples, the nanostructures were released from the template by dissolution of the polymer before analysis. Different preparation ways of the self-supporting nanostructures provided access to all information about morphology and composition, which were studied by various complementary methods. Small angle X-ray scattering (SAXS) was applied to analyze the conformity of the ALD processes within cylindrical nanochannels (initial diameters 18-55 nm, ALD layer thicknesses 5-22 nm). At the flat surface of these membranes, the composition of the deposited layers was analyzed by X-ray photoelectron spectroscopy (XPS). Energy dispersive X-ray spectroscopy (EDX) of all kinds of released nanotubes showed the composition of the coating on the inner channel walls. Imaging these nanotubes with scanning electron microscopy (SEM) in transmission mode enabled further investigation of the homogeneity of the coating along the entire channel length. SEM of arrays of free-standing conical nanotubes was applied to study qualitatively their mechanical stability depending on material and thickness of the walls (10-20 nm). The ALD coating of highly-ordered nanochannel networks was investigated by the visualization of cross-sections of coated membranes as well as free-standing networks with SEM.

To develop single-channel devices, the deposition of TiO_2, SiO_2, and Al_2O_3 in cylindrical and conical nanochannels was transferred from multichannel membranes to single-channel membranes. It was tested by ionic conductance measurements ($I-V$), if ALD is a suitable tool to precisely adjust the (tip) diameter of cylindrical and conical single nanochannels. In addition, the three oxides exhibit different points of zero charge. To show the influence of the induced surface charges depending on the wall material and thus the tailoring of single channels provided by ALD, the pH value of the electrolyte was varied. As first application, single conical nanochannels coated with 5 nm TiO_2 were gated by small modifications of the *I-V* set up resulting in nanofluidic transistors comparable to n-type JFETs.

Part I.

Materials and Methods

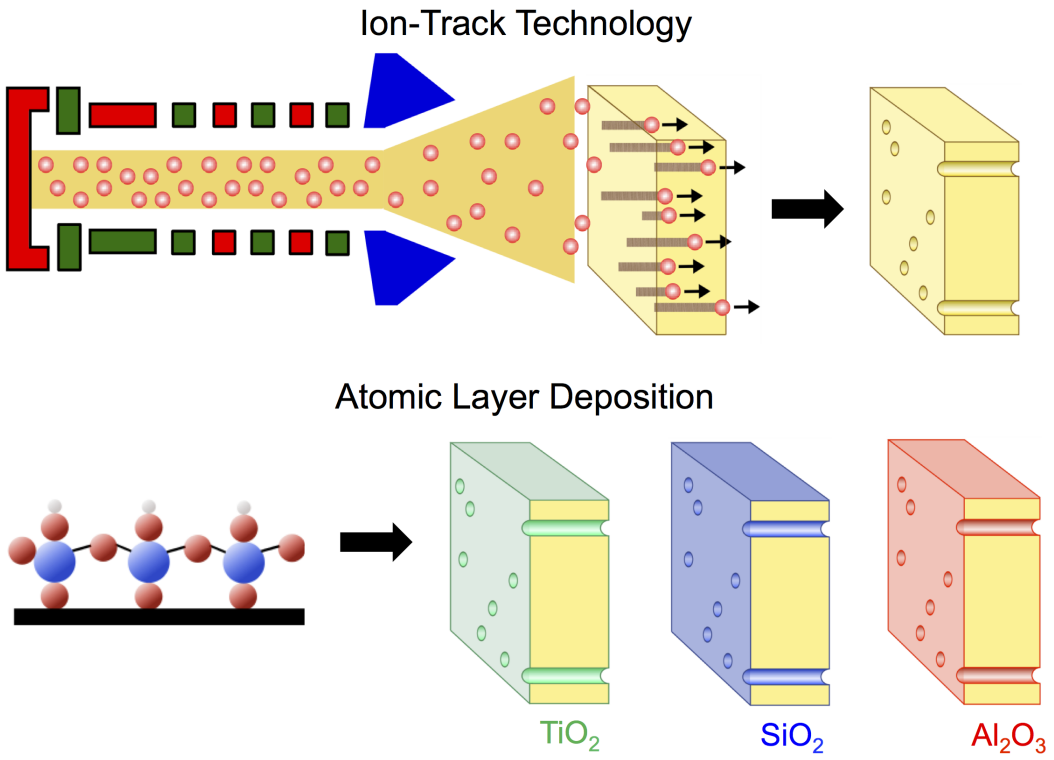

This part presents the different methods applied for the synthesis of layer-by-layer coated nanochannels together with the various employed characterization techniques.

Ion-track technology was applied to fabricate polymer membranes containing single or multiple or interconnected nanochannels of cylindrical or conical geometry (Chapter 2). By low-temperature atomic layer deposition (ALD) the templates were coated with TiO_2, SiO_2, and Al_2O_3 (Chapter 3). Ionic conductometry was applied to characterize the surface-modified single nanochannels. Thus, the basics of nanofluidics and ionic conductometry are explained in Chapter 4. For the investigation of morphology and composition of the coatings, the samples were prepared in various ways (Chapter 5). The characterization methods, experimental set-ups, and parameters are given in Chapter 6.

2 Ion-Track Technology

Ion-track technology provides polymeric templates with precisely controllable geometry, length, size, and density of nanochannels [52–54]. By applying suitable parameters, the nanochannels can be adjusted to exhibit aspect ratios (length to diameter) up to 1000 [64, 101]. The approach consists of two steps: (1) ∼30-µm thick polycarbonate foils are irradiated with a well-defined number of swift heavy ions resulting in cylindrical ion tracks. (2) Subsequent wet-chemical etching converts each track into an open nanochannel. The following Sections 2.1 and 2.2 describe both steps in detail, especially regarding the aim of various geometries as well as number of nanochannels.

2.1 Heavy Ion Irradiation

The interaction of swift heavy ions with matter depends strongly on the energy of the ions. For specific energies below 0.1 MeV per nucleon (MeV/n), a projectile ion collides elastically with the target nuclei. The ion loses energy by many collisions denoted as nuclear stopping [53, 102]. In contrast, ions with energies above 0.1 MeV/n mainly transfer their energy to the target electrons by excitation and ionization of the target atoms. This process is called electronic stopping [102]. The energy transfer within one collision is small because the collision partners are the light electrons. The many collisions with the target electrons do not result in significant momentum transfer of the projectile and thus the trajectory of the ion is straight. The straight trajectory of the ions is a great benefit for the ion-track technology because it allows the synthesis of nanoporous templates with parallel aligned channels. Thus, processes ascribed to electronic stopping are described in more detail below.
For electronic stopping, the energy loss per unit length is described quantitatively by the Bethe-Bloch equation [103].

$$\left(\frac{dE}{dx}\right)_{\mathrm{e}} = \frac{4\pi e^4 \cdot (Z_{\mathrm{eff}})^2 \cdot Z_{\mathrm{t}} \cdot N_{\mathrm{t}}}{m_{\mathrm{e}} v_{\mathrm{p}}^2} \left(\ln\left(\frac{2 m_{\mathrm{e}} v_{\mathrm{p}}^2}{I}\right) - \beta^2 - \delta - U \right), \tag{2.1}$$

where e is the elementary charge, m_{e} the electron mass, v_{p} the velocity of the ion, Z_{eff} the equilibrium effective charge of the projectile ion, Z_{t} the atomic number of the target, N_{t} the density of target atoms, I the ionization energy of the target atoms, and β the velocity of the ion in units of speed of light. Relativistic effects and contributions of electrons from inner atomic shells are taken into account by the correction factors δ and U, respectively. According to the Bethe-Bloch equation, the energy loss in a specific target material depends on the velocity of the projectile ion and its effective charge. Due to electron captures and losses on the way through the target the charge state of the ion varies. Additionally, the semi-empirical Barka equation describes the dependency of the effective charge on the projectile velocity [52]:

$$Z_{\mathrm{eff}} = Z_{\mathrm{p}} \left[1 - \exp\left(-125 \frac{v_{\mathrm{p}}}{c} Z_{\mathrm{p}}^{-2/3} \right) \right], \tag{2.2}$$

with the atomic number of the projectile Z_p. At a given projectile velocity, heavier ions have a higher effective charge state resulting in a higher electronic energy loss than light ions. Since the damage is proportional to $\frac{dE}{dx}$, heavier ions create larger tracks. Therefore, swift heavy ions are better suited to create homogeneous ion tracks in polymers.

The processes ascribed to electronic stopping can form ion tracks and occur at ultra short timescales. $10^{-17} - 10^{-16}$ s after the collision of projectile ion and target electrons, the initial ionization processes generate electrons, so-called delta electrons. At $10^{-15} - 10^{-14}$ s, these electrons propagate and further ionize atoms resulting in an electron collision cascade that can range over a large radial distance (up to 0.5 µm) from the initial ion trajectory. By electron-phonon coupling, the energy is transferred to the lattice at $10^{-13} - 10^{-10}$ s. According to the thermal-spike model, this leads to a strong temperature increase and melting of the target material along the ion trajectory [57, 104]. Due to fast cooling, the disorder/damage in the molten zone is conserved. This zone exhibits a radius of several nm and is called core of the ion track [52, 55–57, 60, 105]. Radiation-sensitive materials such as polymers can also be damaged by the electron collision cascade. Since this has larger dimensions, the outer region of the ion track is called halo. For the used amorphous polycarbonate [100], the energy loss around the ion trajectory is radially isotropic resulting in cylindrical ion tracks.

To guarantee a homogeneous ion track through the complete thickness of the polymer foil, the ion has to pass completely through the polymer in the regime of electronic stopping. For Au ions accelerated at the linear accelerator UNILAC at GSI Helmholtzzentrum für Schwerionenforschung, the maximum available specific energy is 11.4 MeV/n. The corresponding projectile range in polymers is about 175 µm allowing the irradiation of stacks of thin foils of total thickness below the maximum range [106]. In contrast to porous sponge-like membranes commonly used for filtration processes, the irradiation with swift heavy ions provides parallel aligned ion tracks with an angular spread of typically $< 1°$ [63].

The number of ion tracks per area is adjusted by the applied ion fluence. Fluences of $\sim 10^9 \frac{\text{ions}}{\text{cm}^2}$ and $\sim 10^6 \frac{\text{ions}}{\text{cm}^2}$ were used to fabricate templates exhibiting arrays of randomly distributed, parallel aligned cylindrical or conical nanochannels. In order to fabricate membranes with one single nanochannel, a metal mask with a centered aperture of ∼200 µm diameter is placed in front of the polymer foil stack. By magnetic defocusing, the flux of the beam is reduced such that about one ion passes the aperture per second. At such a low flux, the beam can be deflected electrostatically as soon as a detector behind the polymer foil registers one ion [37, 38, 58–60, 107]. Standard irradiations were performed under beam incidence normal to the sample surface. To produce templates with interconnected nanochannels, the irradiation was performed under a beam incident angle of 45° from 4 different directions with a fluence of $\sim 10^9 \frac{\text{ions}}{\text{cm}^2}$ each [54, 67].

In this work, ∼30-µm thick amorphous polycarbonate foils (Makrofol N, Bayer [100]) with a diameter of ∼3 cm were used. They exhibit a smooth and a rough surface. Figure 2.1.1 shows the monomer structure of polycarbonate. Swift heavy ion irradiation under vacuum conditions leads to scissoring of the polymer chains resulting in new chemical end groups [55, 108, 109]. Some carbonate groups are transformed into carbonyl groups [110], hydroxil groups bond to phenyl groups [55, 108, 110] and other end groups like alkyne groups, alcohols, and vinyl derivates can be formed [55, 110]. These end groups increase the chemical reactivity with hydroxil groups of an etchant like NaOH, yielding increased preferential chemical etching of the track material compared to the surrounding unirradiated matrix. Additionally,

small molecule fragments such as CO_2 or hydrocarbons (C_nH_m) outgas during ion irradiation forming free volumes around the end groups. This makes the tracks more accessible for the etchant and thus increases the etchability [108, 111, 112]. Since the end groups are better soluble in the etchant, the transport of the reagent is enhanced [110].

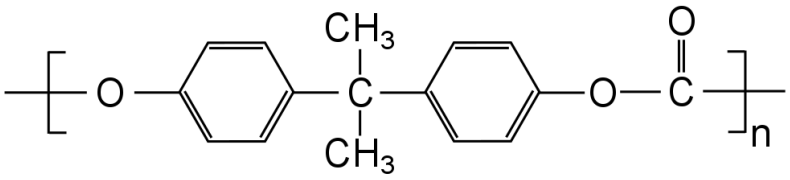

Figure 2.1.1.: Monomer structure of polycarbonate.

2.2 Selective Track Etching

Selective chemical etching allows the transformation of ion tracks into open nanochannels. Since the damages caused by the ions increase the chemical reactivity along the tracks, the track etching velocity (v_T) is increased compared to the etch rate of the undamaged bulk material (v_B). The ratio of the bulk etching velocity v_B and the track etching velocity v_T characterizes the opening angle $\theta = \arcsin\left(\frac{v_\mathrm{B}}{v_\mathrm{T}}\right)$ of the resulting nanochannel (Figure 2.2.1). The etching ratio depends on polymer properties (e.g. material, thickness, and aging) as well as on post treatments, characteristics of the etchant (e.g. content, temperature, concentration, and pH), and irradiation parameters (e.g. energy loss, temperature, and atmosphere) [113]. If these parameters are controlled, geometry and size of the nanochannels can be tailored. Here, cylindrical and conical nanochannels with various diameters were synthesized. Before selective etching, the irradiated polymer foils were exposed to Ultraviolet (UV) light of wavelength between 280 and 400 nm in air at room temperature for 60 min each side to achieve a small distribution of the channel size [56, 110, 114–116].

In this work, polycarbonate foils were used to fabricate templates, since nanochannels in this material are known to exhibit a rather smooth wall in contrast to polyethylene terephthalate (PET) probably due to the semicrystalline structure of the latter [42, 117].

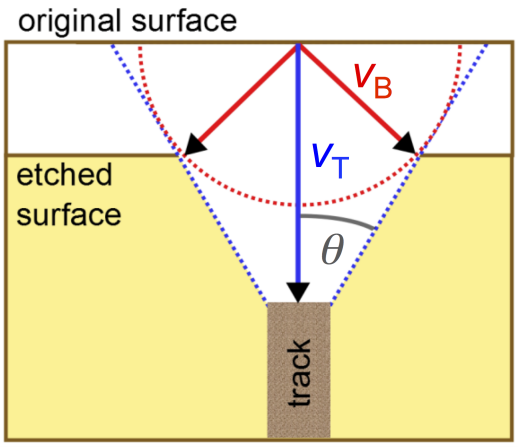

Figure 2.2.1.: Selective etching of ion tracks. The opening angle $\theta = \arcsin\left(\frac{v_\mathrm{B}}{v_\mathrm{T}}\right)$ depends on the ratio of the bulk etching velocity (v_B) and the track etching velocity (v_T).

2.2.1 Cylindrical Nanochannels

To etch cylindrical nanochannels, the track etching velocity has to be much higher than the bulk etching velocity $v_T \gg v_B$. In addition, the etching is performed under symmetric conditions from both sides of the membrane. The diameter of the resulting nanochannels is adjusted by the etching time [52, 54, 58–60, 118]. The shortest etching times, which guarantee a breakthrough and a cylindrical shape of the nanochannels, result in aspect ratios (length-to-diameter) up to 1000. Here, the ion tracks in polycarbonate were etched using 6 M aqueous sodium hydroxide (NaOH) solution at ∼50 °C in a thermostated beaker with magnetic stirring as shown in Figure 2.2.2a. To synthesize the network templates exhibiting interconnected cylindrical nanochannels, the etching was performed in the same way using foils with interconnected ion-tracks (Figure 2.2.2b).

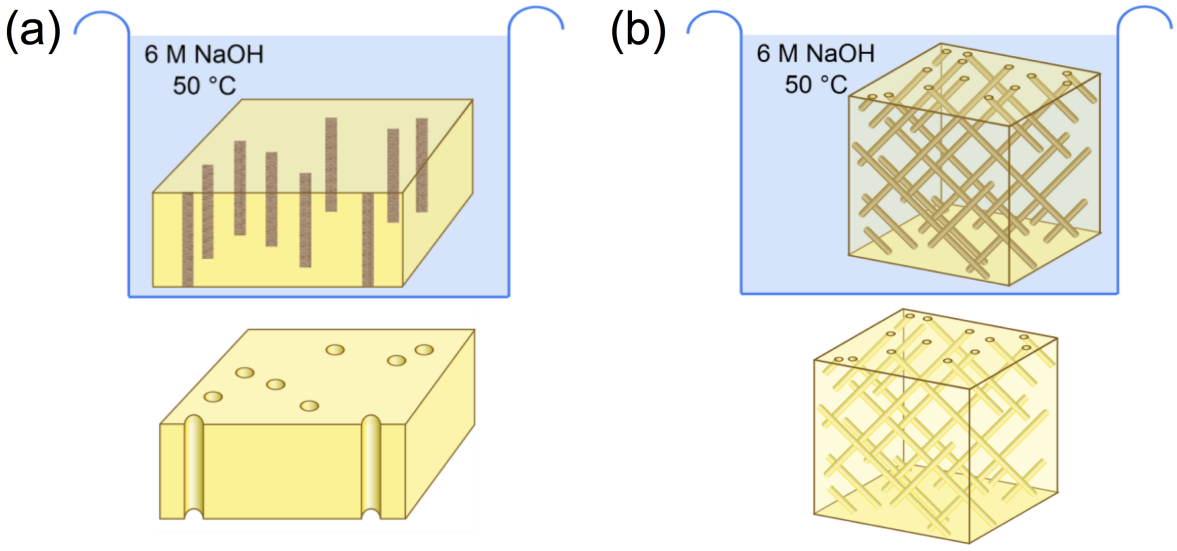

Figure 2.2.2.: Schematics of the symmetric etching: A much higher track etching velocity than bulk etching velocity ($v_T \gg v_B$) results in cylindrical nanochannels either parallelly aligned (a) or interconnected (b).

2.2.2 Conical Nanochannels

To synthesize conical nanochannels, the etching is performed under asymmetric conditions. The track etching velocity has to be slightly higher than the bulk etching velocity $v_T > v_B$ [37, 38, 119–121]. The opening angle can be varied by modifying the etchant with additves [60, 107]. In this work, the irradiated polycarbonate foils were placed in an electrochemical cell between two Teflon compartments as shown in Figure 2.2.3. To achieve asymmetric etching conditions, the compartment at the rough side of the membrane was filled with an etching solution of a 40:60 mixture of 9 M aqueous NaOH solution and methanol (CH_3OH) from where the etching would start forming the base of the cones, whereas the second compartment (at the smooth side of the membrane) contained deionized H_2O (Millipore Direct-Q^{TMS}) at the future tip of the channel [122]. The water acts as stopping solution by neutralizing the etchant after the breakthrough. The methanol increases the bulk etching velocity and slightly the track etching velocity [107]. The conical etching was performed at ∼30 °C. To monitor the etching process, an electrical potential of 1 V was applied between two Au electrodes by a DAQ card (National Instruments, PCI-MIO-16XE-50). The negative electrode was placed in the stopping solution to repel the negatively charged ions from the channel tip resulting in a slower etching process at the tip after the breakthrough of the channel [116]. The current flow between the two electrodes was recorded applying a Keithley picoammeter 6485 in order to define the time of breakthrough [37]. To stop the etching process, electrodes and solutions were removed from the electrochemical cell and the membrane was rinsed several times with deionized H_2O.

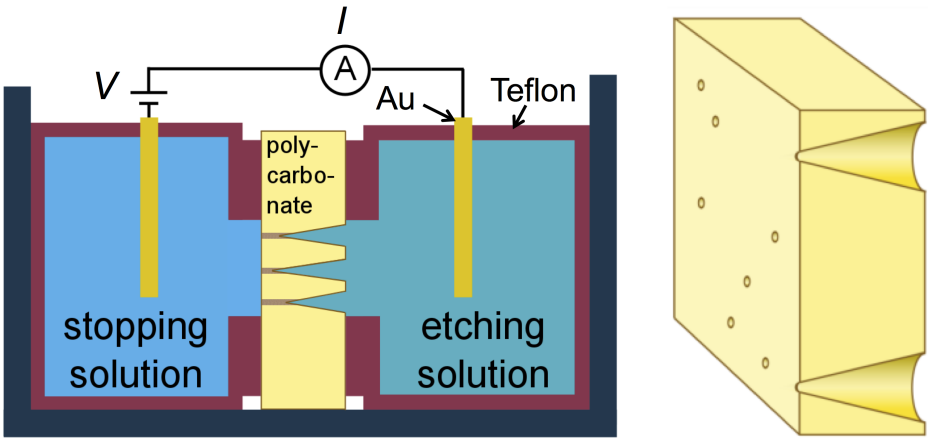

Figure 2.2.3.: Conical nanochannels are created by asymmetric etching conditions and a bulk etching velocity slightly lower than the track etching velocity ($v_T > v_B$).

3 Atomic Layer Deposition (ALD)

Atomic layer deposition (ALD) was applied to modify the inner surface of the high aspect ratio nanochannels in the polycarbonate membranes with layers of TiO_2, SiO_2, and Al_2O_3. This deposition method enables the control of the deposited layer thickness with monolayer precision. Here, thermal ALD was applied, which means that the reaction is temperature activated and takes place in the gas-phase. The high precision in thickness is achieved by splitting the reaction into two self-limited half-reactions on the sample surface [95, 123]. In order to have two independent half-reactions, they are separated in time. This is realized in four steps denoted as ALD cycle. They are shown schematically in Figure 3.0.1: (a) The first gaseous precursor chemisorbs to suitable free binding sites on the sample surface until saturation is reached. Thus, this is the first self-limited half-reaction. (b) Purging with an inert gas removes remaining precursor molecules and reaction byproducts. (c) The second gaseous precursor reacts with the first one forming the desired material until all first precursor molecules reacted. Thus, the second self-limited half-reaction results in a monolayer of deposited material. (d) Purging with inert gas is performed again, in order to achieve a clean reaction environment for the growth of further layers. Repeating the ALD-cycle results in thin films synthesized layer-by-layer. This reaction scheme requires precursors, which do not react with themselves, reaction byproducts or the deposited monolayer. Moreover, the precursor needs to be volatile enough to be distributed homogeneously on the whole sample surface. After the second half-reaction, the second precursor must offer the same free binding sites as the pristine sample surface to enable the growth of further layers.

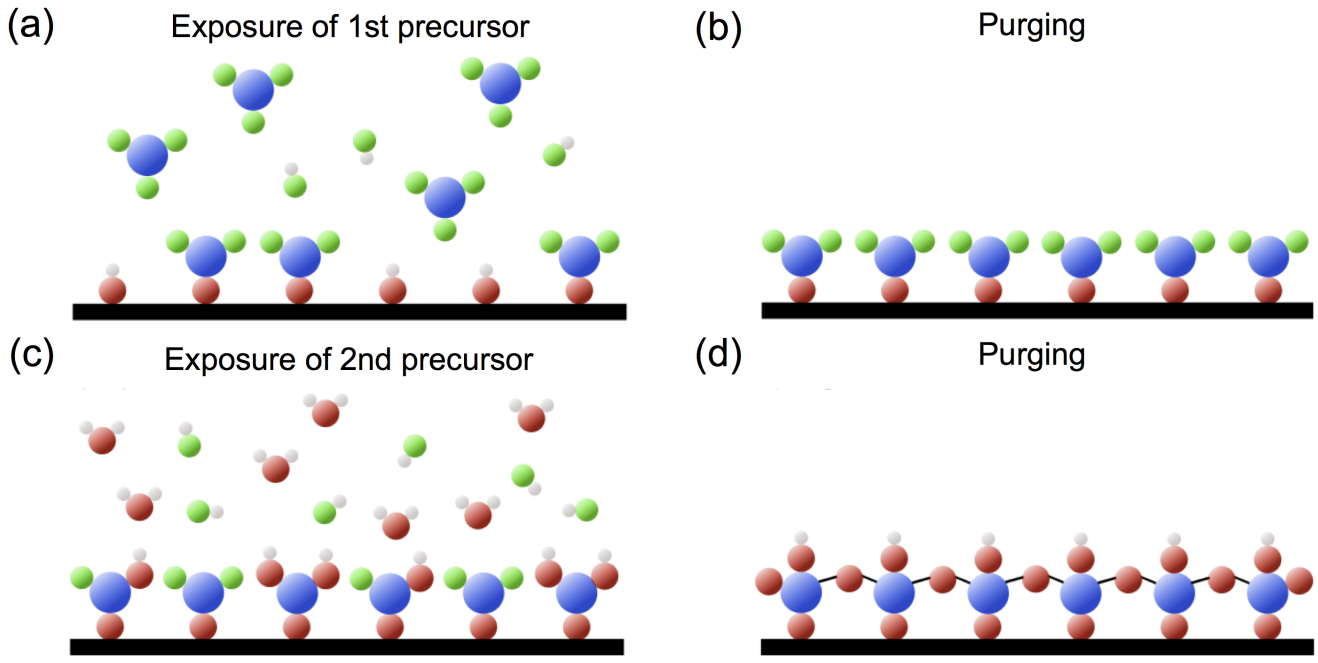

Figure 3.0.1.: (a)-(d) Scheme of an ALD cycle containing 4 steps to deposit a monolayer.

In principle, an ALD reactor consists of a vacuum chamber, which is equipped with various lines for the supply of inert gas and precursors. Each precursor line transports only one type of precursor from a stainless steel container directly into the vacuum chamber. The supply of all gases is controlled by high precision and fast switching pneumatic valves. To minimize the probability of impurities in the deposited layers, ALD is operated in medium vacuum. Perfect layers and layer-by-layer growth is achieved in the so-called ALD-window [81, 123], where the growth rate is constant for the optimum deposition temperatures (Figure 3.0.2 (1)). If the temperature on the sample surface is too low, the precursors condensate (2) or have an insufficient reactivity (3). The precursors decompose (4) or desorb (5) at too high temperatures. Additionally, the growth rate is limited, if there is a lack of reactive sites at the sample surface (6). In order to enable saturation of the half-reactions, the amount of precursor material has to be sufficient and the exposure time long enough. Depending on the topography of the sample, the diffusivity of the precursors, and the reaction speed, one ALD cycle may be in the range of minutes, making the deposition of films thicker than 100 nm very inefficient.

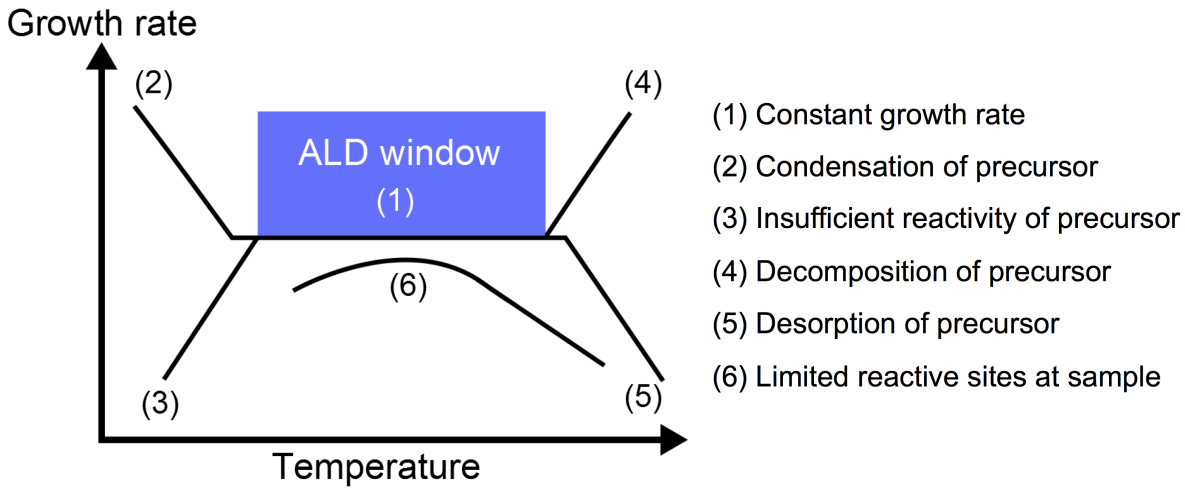

Figure 3.0.2.: Within the ALD-window optimum deposition conditions are provided resulting in a constant growth rate [81, 123].

The amount of exposed precursor is controlled by the pulse time. It has to be long enough to provide a sufficient amount of precursor (Figure 3.0.3). For self-limiting growth, the deposition rate is independent on the pulse time and thus on the amount of precursor [81]. The growth rate increases and decreases in the case of precursor decomposition and etching reactions at the grown layers, respectively. These effects become more probable for longer pulse times.

The layer-by-layer growth due to self-limited surface reactions results in a conformal surface coating, which makes ALD perfectly suitable to coat complex topographies such as porous systems exhibiting large specific surface areas. The homogeneous coating in pores is controlled by the diffusion of the precursors and the remaining precursors as well as reaction byproducts in and out of the pores. In structures with high length-to-diameter ratios, the diffusion processes take longer. Thus, they require extended exposure and purge times in the ALD processes. This work focuses on the surface modification of nanochannels in polycarbonate, which exhibits long-term thermal stability below 140 °C [100]. Therefore, during all applied ALD processes the sample temperature had to be lower. This causes lower reactivity of the precursors [81] and slower diffusion processes compared to established processes. For

example, the coating of flat SiO_2 wafers is usually performed around 300 °C. Lower reactivity and slower diffusion require longer exposure and purge times, respectively.
It is noted that nanoporous polymeric templates differ from substrates commonly coated by ALD by the following means: thermal instability at lower temperatures, larger specific surface area, and higher aspect ratio. Thus, a homogeneous coating could only be achieved by adjusting the deposition parameters, namely lower temperature, extended pulse, exposure, and purge times. For the three deposited oxides TiO_2, SiO_2, and Al_2O_3, the applied parameters are presented in the following sections.

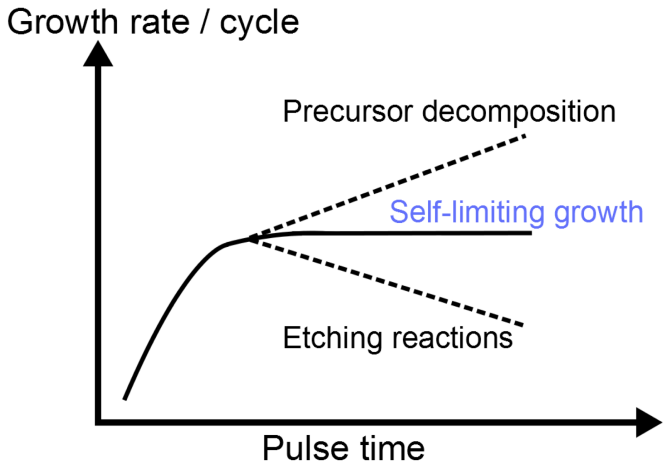

Figure 3.0.3.: Sufficient amounts of precursors, i.e. long enough pulse times, enable self-limiting growth [81]. Precursor decomposition and etching reactions at the already deposited layers increase and decrease the growth rate, respectively.

The ALD coatings were performed using three different equipments:

- SiO_2 was deposited by the group of Prof. Dr. C. Hess (Chemie, Technische Universität Darmstadt) in a custom-built reactor. It was operated in stop-mode with an additional exposure time after the precursor pulses, in which the precursor molecules diffuse into the nanochannels.

- TiO_2 and Al_2O_3 coatings were performed by the group of Prof. Dr. K. Nielsch (Institut für Nanostruktur- und Festkörperphysik, Universität Hamburg). The custom-built reactors were operated in stop-mode, which enables the precursor molecules to diffuse into the nanochannels during an additional exposure time after the precursor pulses.

- After installation of a flow-type reactor (R-200 Basic, Picosun) at GSI Helmholtzzentrum für Schwerionenforschung in Darmstadt, TiO_2 and Al_2O_3 were deposited with a continuous flow of inert gas during the entire ALD cycle.

For all three oxides, the ALD processes were operated with purified N_2 as inert purge gas and H_2O as oxygen delivering precursor. As reference a flat Si-wafer piece was placed in the reaction chamber during all ALD processes and the deposited film thickness was determined by ellipsometry.

3.1 Titania (TiO_2)

Titania (TiO_2) is used for various technical applications. Due to its high refraction index, which causes high covering power and tint reducing power, it is applied as white pigment in paints [124]. Since it is non-toxic, these properties are also utilized in food and cosmetics. TiO_2 is a semiconductor that absorbs ultraviolet light enabling its application in solar-cells such as the Grätzel cell [1]. In addition, it is used as chemically active species in various (photo-) catalytic systems [124].
Here, titanium isopropoxide $Ti(OCH(CH_3)_2)_4$ (TTIP, electronic grade, SAFC Hitech) was used as metal delivering precursor to perform TiO_2 coatings. TTIP is a colorless to light-yellow liquid at room temperature, which is flammable. It is acute toxic after inhalation and causes serious eye irritation. Its vapor pressure at room temperature does not enable the evaporation of sufficient amounts from the precursor container. Thus, heating of the precursor bottle is required. Equations 3.1, 3.2, and 3.3 display the mechanisms of the two half reactions and the complete reaction for the TiO_2 coatings. Asteriks indicate surface species [125].

$$\text{1st half reaction} : TiOH^* + Ti(OCH(CH_3)_2)_4 \rightarrow TiOTi(OCH(CH_3)_2)_3^* + C_3H_8O \quad (3.1)$$

$$\text{2nd half reaction} : Ti(OCH(CH_3)_2)^* + H_2O \rightarrow TiOH^* + C_3H_8O \quad (3.2)$$

$$\text{entire reaction} : Ti(OCH(CH_3)_2)_4 + 2\,H_2O \rightarrow TiO_2 + 4\,C_3H_8O \quad (3.3)$$

The first TiO_2 depositions were performed at Universität Hamburg in the group of Prof. Dr. K. Nielsch applying parameters established for the coating of opals [126, 127]. The deposition temperature was ∼95 °C, the N_2 purging flow rate was 50 sccm, and TTIP was heated to ∼80 °C to increase its vapour pressure. One ALD cycle consisted of:

- a 2 s long TTIP pulse (exposure time 45 s)
- N_2 purging (90 s)
- a 0.2 s long H_2O pulse (exposure time 45 s)
- N_2 purging (90 s)

The measured growth rate of this ALD process is ∼0.04 nm/cycle on Si-wafers. Applying these parameters lead to successful TiO_2 depositions in the polymeric nanochannels (Section 7).
At GSI, the deposition temperature was set to ∼110 °C to decrease the condensation of remaining H_2O precursor molecules and increase diffusivity. In the reaction chamber, the N_2 flow rate was 120 sccm. An ALD cycle involved:

- a TTIP pulse operated in boost mode (see explanation below)
- N_2 purging (50 s)
- a H_2O pulse at a precursor line carrier gas flow rate (N_2) of 200 sccm for 0.4 s
- N_2 purging (50 s)

For increasing the vapor pressure of TTIP to ∼164 Pa, it was heated to ∼70 °C [128]. To further increase the amount of TTIP being transported into the reaction chamber, the TTIP pulse was boosted by starting the pulse 0.5 s before the N_2 carrier gas flow rate is set to 600 sccm for 4.8 s. Due to the high flow rate, N_2 fills the precursor container. During the TTIP pulse the flow in the H_2O precursor line was set to 600 sccm, too, resulting in a balanced N_2 flow to the reaction chamber. Applying these parameters resulted in a growth rate of ∼0.01 nm/cycle on Si-wafers due to the chosen deposition temperature [129]. TiO_2 coatings deposited at these temperatures are amorphous [129].

3.2 Silicon dioxide (SiO_2)

Silicon dioxide (SiO_2) is widely used in industry, e.g., for the production of glass and cement as well as in food and pharmaceutical applications [130]. Its usage in semiconductor and microsystem technology as insulating and passivation layer and as substrate for the masks in photo lithography is based on its stability at high temperatures, chemical inertness, and electrically insulating properties [130].
For the ALD deposition, silicon tetrachloride ($SiCl_4$, 99 %, Sigma-Aldrich) was utilized as precursor, which delivers silicon. $SiCl_4$ is a colorless liquid at room temperature. It reacts violently with water and is harmful by inhalation and if swallowed, causing severe burns and irritations at the respiratory system. The reaction mechanism shown in the equations below (surface species are labeled by asteriks) requires a catalyst [131].

$$\text{1st half reaction} \quad : \quad SiOH^* + SiCl_4 \rightarrow SiOSiCl_3{}^* + HCl \tag{3.4}$$

$$\text{2nd half reaction} \quad : \quad SiCl^* + H_2O \rightarrow SiOH^* + HCl \tag{3.5}$$

$$\text{entire reaction} \quad : \quad SiCl_4 + 2\,H_2O \rightarrow SiO_2 + 4\,HCl \tag{3.6}$$

This ALD process was established in the group of Prof. Dr. C. Hess at TU Darmstadt in order to coat polymeric nanochannels as well as mesoporous silica (SBA-15) [99] utilizing pyridine (C_5H_5N, 99,8 %, anhydrous, Sigma-Aldrich) as catalyst for the low-temperature process, which restricted the reaction temperature to ∼60 °C [132]. The N_2 purging flow rate was 200 sccm. An ALD cycle comprised:

- a 0.1 s long pyridine pulse (exposure time 5 s), a 0.1 s long $SiCl_4$ pulse (exposure time 60 s)
- N_2 purging (70 s)
- a 0.1 s long pyridine pulse (exposure time 5 s), a 0.1 s long H_2O pulse (exposure time 60 s)
- N_2 purging (70 s)

The growth rate obtained on Si-wafers is ∼0.18 nm/cycle. The deposition temperature of ∼60 °C leads to amorphous SiO_2 layers.

3.3 Alumina (Al_2O_3)

Due to its electrical insulating, heat conducting, and corrosion protecting properties alumina (Al_2O_3) is applied as dielectric in electrical engineering for e.g. capacitors in high-frequency technology, as substrate for electric devices, where they act simultaneously as cooling element, and as protective layer in e.g. mechanical engineering [133]. In semiconductor technology, ALD of Al_2O_3 and other metal oxides is the only method to fabricate thin insulating layers for trench capacities or gate oxides of scaled metal-oxide-semiconductor field-effect transistors [134].
In this work, Al_2O_3 layers were deposited applying trimethylaluminium ($Al(CH_3)_3$, TMA, electronic grade, SAFC Hitech) as metal delivering precursor. TMA is a colorless liquid at room temperature, which is pyrophoric, violently reactive with water, spontaneously flammable in air, and causes skin corrosion. It exhibits a vapor pressure of ∼1200 Pa at room temperature [135], which is high enough to evaporate sufficient amounts of TMA out of the precursor container without heating. The following equations show the reaction mechanism to deposit Al_2O_3 with asteriks marking surface species [91].

$$\text{1st half reaction} \quad : \quad AlOH^* + Al(CH_3)_3 \rightarrow AlOAl(CH_3)_2^* + CH_4 \tag{3.7}$$

$$\text{2nd half reaction} \quad : \quad AlCH_3{}^* + H_2O \rightarrow AlOH^* + CH_4 \tag{3.8}$$

$$\text{entire reaction} \quad : \quad 2\,Al(CH_3)_3 + 3\,H_2O \rightarrow Al_2O_3 + 6\,CH_4 \tag{3.9}$$

For the first series of Al_2O_3 coatings, parameters already known for the coating of other high aspect ratio structures that require deposition temperatures below 100 °C were applied by the group of Prof. Dr. K. Nielsch. Al_2O_3 was deposited at ∼95 °C with a N_2 purging flow rate of 10 sccm. An ALD cycle comprised:

- a 0.12 s long TMA pulse (exposure time 45 s)
- N_2 purging (90 s)
- a 0.2 s long H_2O pulse (exposure time 45 s)
- N_2 purging (90 s)

On Si-wafers a growth rate of ∼0.1 nm/cycle is measured for this ALD process.
For subsequent Al_2O_3 depositions at GSI, the process parameters were adjusted to a deposition temperature of ∼110 °C in order to avoid condensation of remaining H_2O molecules as well as to increase reactivity and diffusivity. The N_2 flow rate was 120 sccm in the reaction chamber. An ALD cycle consisted of:

- a TMA pulse for 0.35 s at a precursor line carrier gas flow rate (N_2) of 150 sccm
- N_2 purging (30 s)
- a 0.35 s long H_2O pulse at a N_2 carrier gas flow rate of 200 sccm
- N_2 purging (30 s)

This deposition process exhibits a growth rate of ∼0.1 nm/cycle on Si-wafers. For these deposition temperatures, the Al_2O_3 layers exhibit an amorphous structure.

4 Nanofluidics in Polymeric Nanochannels

In nanofluidics, the transport properties of fluids through miniaturized structures exhibiting at least one characteristic dimension below 100 nm are investigated [29, 30]. The high surface-to-volume ratio of these nanostructures results in phenomena, which do not occur in structures at the micro- and macrofluidic scale [136]. For instance, surface charges at the liquid-solid interface have a strong influence on fluidics in nanochannels. The formation of surface charges leading to an electrical double layer at the solid-liquid interface is presented in Section 4.1. The flow of electrically charged particles solved in the liquid can be controlled by an applied electrical field and is described in Section 4.2. Based on electrostatic and electrokinetic effects the nanochannel diameter was determined by conductometry as presented in Section 4.3. Section 4.4 describes the gating of ionic conductance through a single nanochannel.

4.1 Electrostatics in Liquid

Surface charges originate from the dissociation of surface groups and the nonelectric, specific adsorption of ions from the liquid [29, 30, 137, 138]. The resulting electrostatic effects depend on the solid material and the liquid. For a given material, its surface charge is defined by number and type of acidic and basic groups of the solution due to protonation or deprotonation [31, 32]. Since the pH value specifies the acidity of an aqueous solution, no net charge is formed at the surface for a specific pH value, which is named point of zero charge (PZC). For pristine oxide surfaces in water, mostly H^+ and OH^- are adsorbed at the surface and it can be assumed that the point of zero charge coincides with the isoelectric point (IEP), which is defined as the pH value where a molecule carries no net charge [139]. Table 4.1.1 lists the isoelectric points of the surface materials studied in this work.

Table 4.1.1.: Isolectric point of the surface materials investigated in this work. [a] [140], [b] [141], [c] [142].

Material	Polycarbonate	TiO_2	SiO_2	Al_2O_3
Isolectric Point (pH value)	5[a]	$(4-6)$[b,c]	$(2-3)$[b,c]	9[b,c]

Surface charges cause electrostatic forces that are essential for interactions between ions and surfaces in nanoconfinements filled with liquid. Thus, the surface charges strongly influence transport through nanochannels. Additionally, ions are bound at the surface due to van der Waals forces acting at short distances. In 1948, the interaction of electrostatic and van der Waals forces was described by Derjaguin, Landau, Verwey, and Overbeek in the DLVO theory [143]. They assume an infinite flat surface exhibiting an uniform surface charge density as well as a constant electric potential. In addition, the concentration profiles are taken as static and the dielectric constant is only influenced by the solvent [144, 145]. In contrast to electrostatic forces, van der Waals forces are very insensitive to electrolyte concentration and

pH value [146].
If the pH value of the liquid differs from the IEP of the surface material, the surface charges at the liquid-solid interface result in the formation of an oppositely charged region of counterions to secure charge equalization [147]. This screening layer consisting of fixed and mobile opposite charges is called electrical double layer (EDL) [29, 30] and is described as homogeneous layer in the DLVO theory. In contrast, the newer Gouy-Chapman-Stern model divides the EDL in three regions as shown in Figure 4.1.1a [148]. The surface charges of the solid cause the surface potential Ψ_s. In the solution, the first layer is called inner Helmholtz plane layer (Inner HP) with the potential Ψ_i and consists of co- and counterions, which are non-hydrated and specifically adsorbed on the surface. The second layer is the outer Helmholtz plane layer (Outer HP) with the potential Ψ_d formed by hydrated and partially hydrated counterions. Between inner and outer Helmholtz plane the Stern layer is placed, in which charge and potential gradient are assumed to be linear. In the third layer, mobile co- and counterions are present and thus it is called diffuse layer. Within the latter the slip plane with the potential ζ is located, which can often be approximated by Ψ_d [149]. The slip plane is also called shear surface and separates ions bound to the surface from mobile ions in solution. ζ depends on the pH and ionic strength of the liquid [150–152].
The variation of the electrostatic potential at a charged surface due to a distribution of charged atoms, i.e. within the EDL, is described mathematically by the Poisson-Boltzmann equation [146]. The approximated solution of Debye-Hückel leads to the thickness of the EDL, the so-called Debye screening length (Debye length):

$$\lambda_D \propto \frac{1}{\sqrt{I_s}} = \frac{1}{\sqrt{\sum_i \frac{1}{2} c_i z_i^2}} \tag{4.1}$$

where I_s is the ionic strength depending on the electrolyte concentration c_i and the valency of the ion z_i. The Debye length decreases with increasing electrolyte concentration. For 1 M KCl solution, the Debye length is ∼0.3 nm at room temperature [146]. Decreasing the concentration of the KCl solution to 0.1 M, increases the Debye length to ∼1 nm [146]. Generally, a high ionic strength leads to a thin EDL, which enables co- and counterions to move through the nanochannel (Figure 4.1.1b). In contrast, a low ionic strength results in a thick EDL narrowing the channel for the coions or in the extreme case prohibiting the coions from passing (Figure 4.1.1c). This counterion selectivity is applied for example in ionic separators [154] and proton-gated ion channels [155].
The approach of this work to modify the surface of single nanochannels by ALD of three different oxides enabled the investigation of well-defined and smooth surfaces with various IEPs.

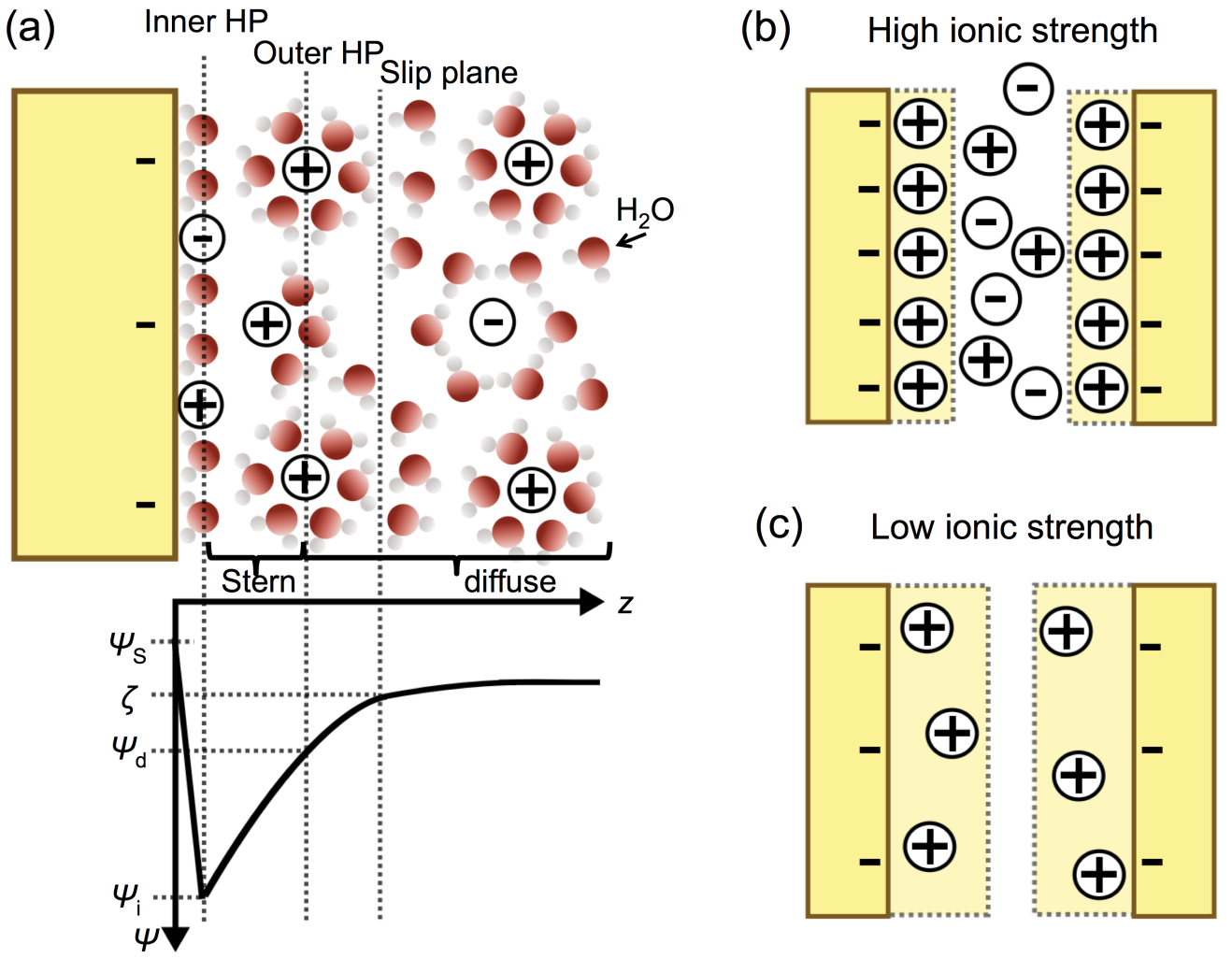

Figure 4.1.1.: Electrical double layer (EDL). (a) Different planes of the EDL according to the Gouy-Chapman-Stern model [148]. For details, see text. (b) The thin EDL (shaded in light yellow) allows transport of co- and counterions through the nanochannel at high ionic strength [153]. (c) A thick EDL results in a counterion selective nanochannel at low ionic strength [153].

4.2 Electrokinetics in Liquid

The flow of an ionic fluid through a nanochannel requires a kinetic motion force like electrokinetic or capillary forces. The latter enables the filling of a nanochannel placed in an ionic electrolyte [156], whereas in this work electrokinetic forces were utilized to transport ions through a nanochannel by applying an electrical potential across the membrane containing the channel. The higher ion concentration in the EDL compared to the rest of the liquid leads to a surface conductance of the ions in the EDL moving in an electric field. Thus, the surface conductance increases with reduced electrolyte concentration [157–159].

If an ion is moved in an aqueous solution by an electrical field, electro-osmosis and electrophoresis can occur. Electro-osmosis is the movement of liquid next to a charged surface due to an electrical field applied parallel to the liquid-solid interface. At a positively charged surface, the high concentration of anions within the EDL transport the fluid towards the anode due to viscous interaction [160]. For low ionic strength, the EDLs overlap in the center of the nanochannel resulting in electro-osmosis governed by the electrical potential $\Psi(z)$ shown in Figure 4.2.1.

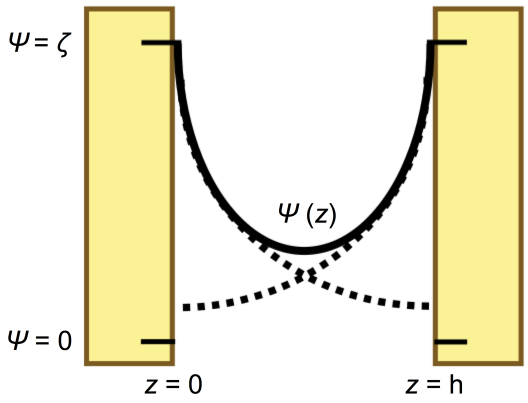

Figure 4.2.1.: Nanochannel with electric potential of each single wall (dashed line) and of overlapping EDL ($\Psi(z)$, solid line). The channel width is h. Adapted from [153].

Electrophoresis is the movement of charged particles or molecules in a medium due to an electrical field. An ion is located in an aqueous solution and its charge is screened by the EDL resulting in a zero net charge of the ion. The application of an electrical field leads the mobile counterions in the EDL to move in the opposite direction as the unscreened ion itself would have moved, i.e. if a cation is screened by the EDL, the anions within the EDL move towards the anode. Due to electro-osmosis this counterion movement results in transport of the liquid. On a global scale, the liquid is in a steady state since the aqueous medium is viscous. Thus, the movement of the ions induced by electrophoresis depends on the thickness of the EDL.

4.2.1 Rectification of Ionic Current in Nanochannels

For cylindrical nanochannels under isotropic electrolyte conditions, the ionic current recorded at a given positive and negative voltage has a similar absolute value resulting in symmetric *I-V* characteristics. However, asymmetric *I-V* curves of nanochannels are observed in biology indicating that more ions are transported in one direction than in the other [161]. Potassium selective channels are such rectifying nanochannels since they transport potassium in, but not out of the cell [24, 25].
Synthetic nanochannels can also show the rectifying, diode-like behavior [27, 33–36]. The rectification of an ionic current was first observed in single-channel polymer membranes by Siwy et al. [13]. Furthermore, they observed voltage gating known from biological ion channels for single conical nanochannels in PET. The rectification of the ionic current requires conical nanochannels exhibiting a tip diameter in the nm range as well as surface charges [33, 36, 162]. There are several explanations in literature. For example, Siwy and Fuliński calculated the electrical potential $\Psi(x)$ inside such a nanochannel, which is shaped like a sawtooth as presented in Figure 4.2.2a [39]. A voltage applied across the membrane is an external electrical potential that superimposes with the potential inside the channel. For the polarity shown in Figure 4.2.2b, the counterions pass the channel, whereas they are blocked for the polarity shown in (c) resulting in a lower ionic current. Thus, the force required to move the ions in one direction is larger than in the other direction.

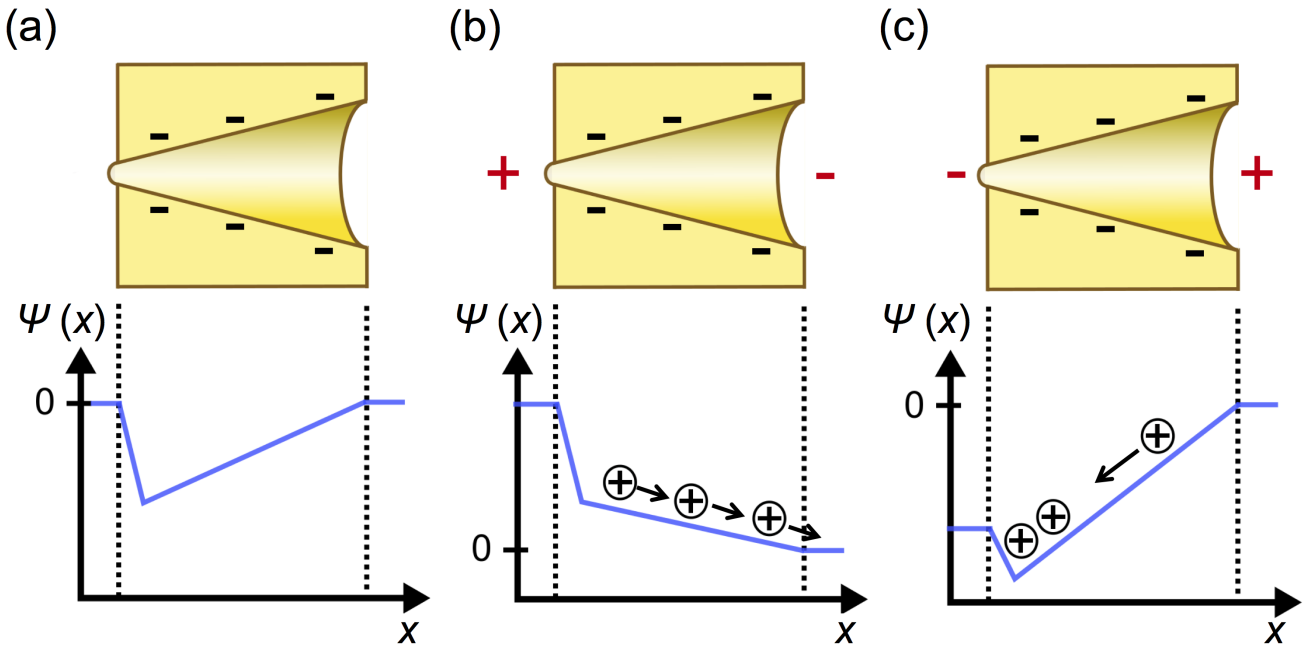

Figure 4.2.2.: Scheme of the principle causing rectification of the ionic current in a conical nanochannel with negatively charged surfaces [39]. (a) Channel potential $\Psi(x)$ without external voltage. (b) Cations pass the channel, if external electric potential is positive at tip. (c) If negative potential is at tip, the cations are blocked leading to a low ionic current.

In addition, the diode-like *I-V* curves are described by concentration changes inside the nanochannel [163–166]. Based on the Possion-Nernst-Planck (PNP) equations, Cervera et al. applied a simple contin-

uum model to calculate the electrical potential inside an asymmetric nanochannel [163]. The resulting potential is asymmetrically shaped and depends on the surface charges. Both, the ratchet and the PNP model, provide the dependency of the *I-V* curves on the EDL, since the EDL screens the surface charges. Schiedt et al. demonstrated this dependency experimentally showing a more pronounced rectification for low electrolyte concentrations due to a thick EDL [17].
Furthermore, rectification is obtained in symmetric nanochannels exhibiting both positively and negatively charged surface regions due to the resulting asymmetric surface charge distribution inside the nanochannel [167]. By combining positively and negatively patterned surface charges with conical nanochannels the rectification is increased [168].
To conclude, the surface charges play an important role for rectification. Experimentally this can be studied by using different wall materials and by varying the pH value of the electrolyte. This motivated us to record *I-V* curves of TiO_2-, SiO_2-, and Al_2O_3-coated nanochannels at various pH values of the electrolyte. The obtained rectifications were quantified applying the ratio:

$$r = \frac{|I(+V_x)|}{|I(-V_x)|} \tag{4.2}$$

where $I(+V_x)$ and $I(-V_x)$ are the ionic currents measured at a certain positive and negative value x of the applied voltage, respectively. In this work, rectifications (r) were calculated at the highest absolute value of the voltage applied during the *I-V* measurements, i.e. ±1 V or ±3 V.

4.3 Ionic Conductance in Nanochannels

If a single-channel membrane is placed into a liquid electrolyte, the nanochannel is filled with the electrolyte due to capillary forces [156]. Applying a voltage across the membrane leads to the flow of an ionic current depending on the applied voltage. By recording a current-voltage (*I-V*) curve, the ionic conductance G of the nanochannel can be calculated from the slope of the curve ($G = \frac{I}{V}$). If the ionic conductance is obtained at the IEP of the surface material, the conductance can be applied to determine the diameter of the nanochannel for a known specific conductivity of the applied electrolyte and a certain geometry.
Being the inverse of the electrical resistance R, the electrical conductance G of a cylinder of length L is given by [169]:

$$G = \frac{1}{R} = \frac{I}{V} = \frac{d_{cyl}^2 \cdot \pi \cdot \kappa}{4 \cdot L} \tag{4.3}$$

where κ is the specific conductivity of the electrolyte and d_{cyl} is the diameter of the cylinder. From this equation the diameter of the cylinder can be deduced if L and κ are known:

$$d_{cyl} = 2 \cdot \sqrt{\frac{I}{V}\frac{L}{\pi \cdot \kappa}} \tag{4.4}$$

For conductometric measurements, the cylinder is regarded as cylindrical nanochannel filled with the electrolyte of specific conductivity κ. The length L corresponds to the thickness of the membrane.
The electrical conductance G of a cone with length L, specific conductivity κ, base diameter D, and tip diameter d_{tip} is given by the following equation [114, 169, 170]:

$$G = \frac{1}{R} = \frac{I}{V} = \frac{d_{\text{tip}} \cdot D \cdot \pi \cdot \kappa}{4 \cdot L} \tag{4.5}$$

resulting in the tip diameter of the cone:

$$d_{\text{tip}} = 4 \cdot \frac{I}{V} \frac{L}{\pi \cdot \kappa \cdot D} \tag{4.6}$$

The base diameter has to be known to determine the tip diameter of a conical nanochannel. In literature, multichannel reference membranes are commonly etched simultaneously without a stabilization voltage. The base diameter is estimated from SEM images of the nanochannels at the membrane surface after Au sputter-coating the multichannel samples [14, 16, 80, 116, 171, 172]. In addition, the so-called replica method determines the base diameter of nanowires electrodeposited in a multichannel reference membrane [107, 172–174]. In this work, the corresponding multichannel reference membrane was etched under identical conditions, i.e. applying the same stabilization voltage, directly after the the single-channel membrane. Then tubular replica were synthesized by ALD in both membranes to compare the dimensions of single and multichannels prepared under identical conditions (Section 8.6). In addition, ALD-coated single-conical nanochannels were prepared as free-standing replica after *I-V* measurements. This provides the base diameter of the single channels used for conductometric measurements.

4.4 Gated Conductance

Transistors are electric semiconducting devices that adjust their electrical resistance as function of an external current or voltage. They are applied to switch electrical currents or amplify electrical signals. In integrated circuits, transistors are ubiquitous due to their small size and integration capability.
The field effect transistor (FET) is a specific type of transistor, which regulates the conductance or the size of the conductive channel by a transversal electrical potential. The conductive channel is contacted to three electrodes. One is the source S, where the charge carriers start to flow towards the drain D, the second electrode. Applying a voltage between source and drain (V_{DS}) results in the source-drain current I_{D}. The regulation of the latter is performed by applying a voltage between the third contact, the so-called gate G, and the source [175].
As specific type of a FET, the junction field effect transistor (JFET) exhibits a source-drain current if no voltage is applied to the gate (Figure 4.4.1a). JFETs commonly consist of a semiconductive crystal with positive and negative doped regions. They are called n-type and p-type JFET if the conductive channel is n-doped and p-doped, respectively. The current flow is almost exclusively performed by one type of charge carrier, the majority carriers, and thus a JFET is called unipolar transistor. A gate voltage of

suitable polarity reduces the source-drain current by forming a depletion layer within the conductive channel. By increasing the gate voltage, the depletion layer grows and narrows the conductive channel until it is blocked. Figure 4.4.1b displays the current-voltage characteristic for a given gate voltage (V_{GS}) and an increasing drain-source voltage (V_{DS}). The source-drain current (I_D) increases according to Ohms law until the saturation current I_{DSS} in the channel is reached. Applying increased gate voltages V_{GS} results in lower I_{DSS} (Figure 4.4.1c right). For every V_{DS}, a control curve can be deduced from the current-voltage characteristics for various V_{GS} as shown representatively for $V_{DS} = 6$ V in Figure 4.4.1c (left). The gate voltage that completely blocks the conductive channel is called pinch-off voltage (V_p) [175].

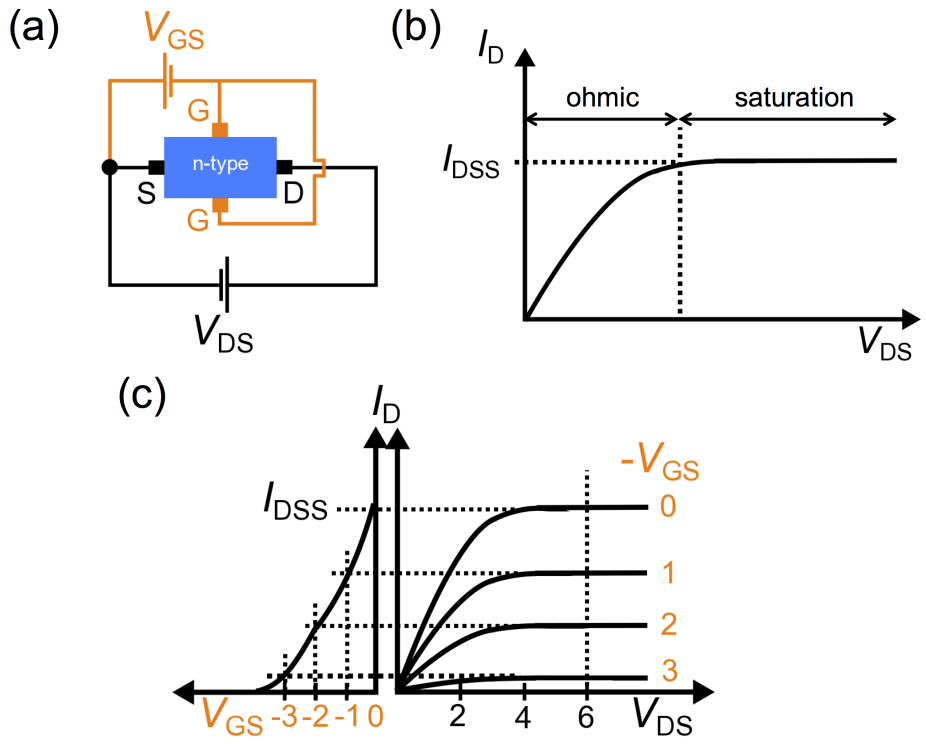

Figure 4.4.1.: n-type junction field effect transistor (JFET). (a) Circuit diagram showing the conductive channel connected to source S and drain D. Applying a voltage between them (V_{DS}) results in the source-drain current I_D. A voltage applied to the gate G (V_{GS}) reduces I_D. (b) Exemplary current-voltage curve for a given gate voltage V_{GS}. (c) Increasing the gate voltage reduces the saturation current I_{DSS} (right). For V_{DS} = 6 V, the deduced control curve is presented on the left. (b,c) adapted from [175].

5 Sample Preparation for Analyses

To characterize morphology and composition of the ALD-coated etched ion-track polycarbonate membranes, various methods were applied. The samples were analyzed before and after ALD-coating as well as after subsequent dissolution of the polymer membrane. Suitable sample preparation protocols were developed for each case, which are described in the following sections.

5.1 Conductive Coating for SEM Imaging

Gold (Au) was sputtered onto as-fabricated samples as well as on nanostructures released from the polymer matrix. The Au sputtering was performed with an EDWARDS Sputter Coater S150B at a Argon pressure of ∼0.1 Torr and a plasma was initiated at a potential of ∼1.6 kV resulting in a current of ∼18 mA. These parameters led to the deposition rate of ∼40 nm Au per minute.
For Scanning Electron Microscopy (SEM) studies, samples were sputtercoated for 30 s onto the smooth side of the membrane. This avoided charging effects of the uncoated and ALD-coated membranes when analyzing the nanochannels at the membrane surface.

5.2 Release of Nanotubes from Polycarbonate Templates for SEM Investigation in Transmission

To study thickness, homogeneity, and conformity of the ALD coating inside the nanochannels of multichannel membranes, the polycarbonate template was dissolved in dichloromethane (DCM, > 99.5%, Carl Roth GmbH). For this, the sample was placed on the inner wall of a Teflon funnel and ∼50 ml DCM were dropped onto it. A standard copper-lacey transmission electron microscopy grid (Cu-lacey TEM-grid, Plano GmbH) was positioned at the bottom of the funnel collecting the released nanostructures.

5.3 Fabrication of Free-Standing Nanostructures

To verify that all nanochannels had been ALD-coated, to investigate the homogeneity of the nanotubes within one sample and test the mechanical stability of the resulting nanostructures, the coated templates of conical nanotubes and nanotube networks were mechanically stabilized by fixing them onto a metallic layer on the rough side of the membrane as shown schematically in Figure 5.3.1 [122]. First, Au was sputtered for 5 min to achieve a ∼200 nm thick layer (a), which acted as working electrode for the

subsequent electrodeposition of copper (Cu). For reinforcement, a ~20 µm thick Cu layer was electrodeposited in an electrochemical cell using a copper-sulfate based electrolyte (238 g/L $CuSO_4$ and 21 g/L H_2SO_4) in a two electrode configuration applying -0.5 V between a Cu ring pressed on the sputtered Au layer (cathode) and a Cu rod (anode) for 10 min (b). After rinsing with deionised water, a ring clamped the sample (c) onto a aluminum pin sample plate (Plano GmbH). The nanocones were released from the polymer matrix by immersing the sample in ~25 ml dichloromethane (DCM, > 99.5%, Carl Roth GmbH) for two days. Within this time, the solution was exchanged two times with fresh DCM. After dissolution of the polymer matrix, a free-standing array of conical nanotubes was achieved (d). For the networks, the template was dissolved by flushing the sample three times from the top with ~10 ml DCM each time, before the sample was immersed in ~25 ml DCM for a day. Over this period, the DCM was exchanged two times. Finally, Au was sputtercoated for 10 s onto the free-standing nanocones and nanotube networks to reduce charging effects during SEM analysis.

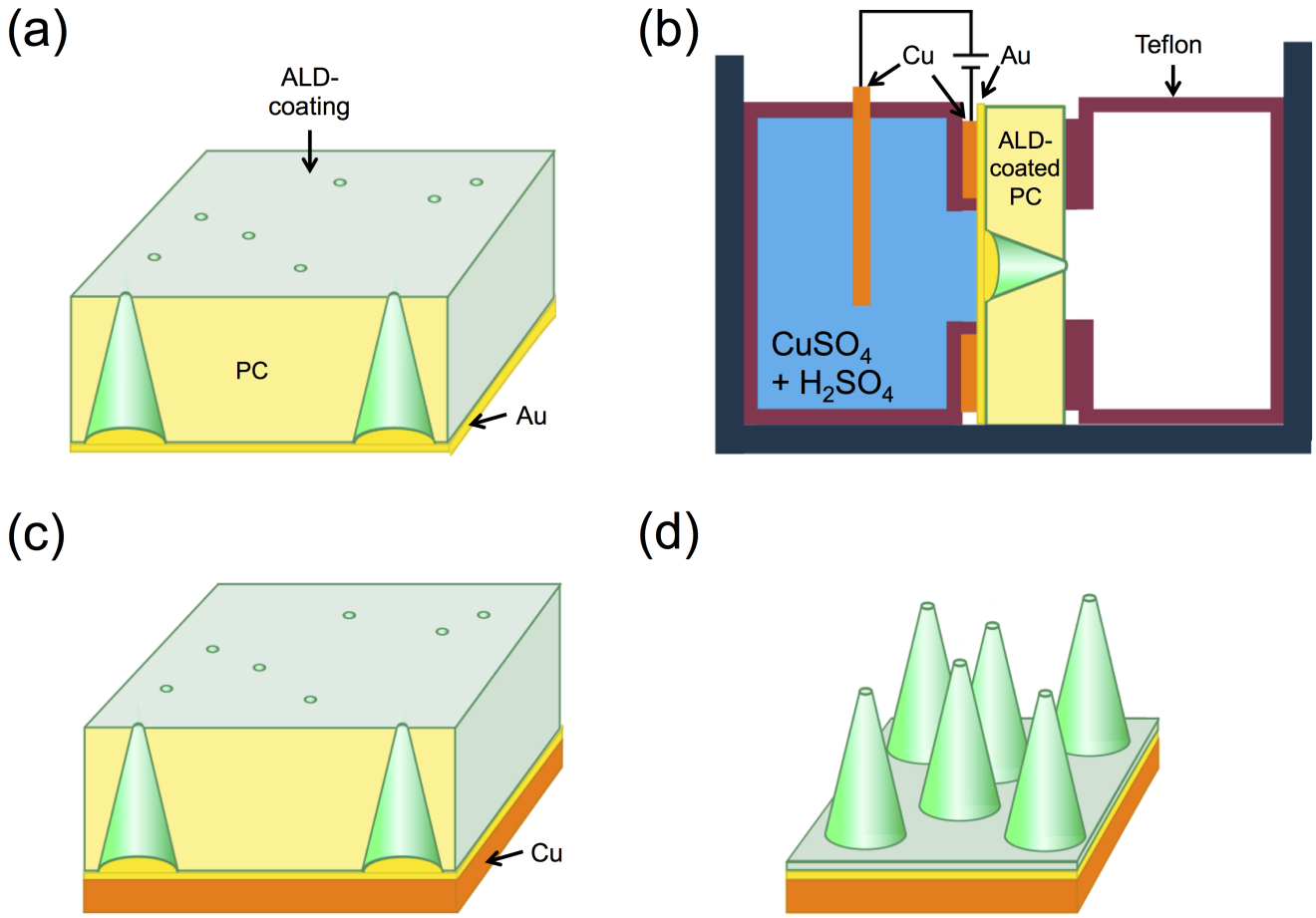

Figure 5.3.1.: Preparation of free-standing nanocones. (a) Sputtering of Au onto the base (large opening) side. (b) Eletrodeposition of Cu to reinforce the Au layer. (c) Sample after sputtering and electrodeposition. (d) Dissolution of the template leads to free-standing nanocones.

5.4 Cross-Sections of the Templates

To properly visualize the cross-section of etched ion-track membranes, a flat breaking edge is required. Due to the softness of the polycarbonate membranes, they have to be treated to become brittle. Etched ion-track membranes irradiated with a fluence of $4 \times 1 \times 10^9 \frac{\text{ions}}{\text{cm}^2}$ and coated with ∼20 nm SiO_2 were sufficiently brittle and broke by touching them with tweezers. Au was sputtered onto all cross-section samples for 10 s to reduce charging effects in the SEM.

6 Characterization Methods

For the investigation of morphology and composition of the nanotubes synthesized by ALD in etched ion-track polycarbonate membranes various characterization methods were utilized. The following sections briefly describe the applied techniques including the settings used for differently prepared samples.

6.1 Scanning Electron Microscopy (SEM)

All scanning electron microscope (SEM) images were obtained using a high resolution field-emission SEM (JEOL JSM-7401F) equipped with various detectors. Three secondary electrons detectors are located at different positions: Two (SEI and LEI) mounted above the sample to image the topography of the sample from different angles and one positioned below the sample to obtain images in transmission mode (STEM-in-SEM). A backscattered electron detector (BSE) allows us to show the contrast between materials within the analyzed area, and a Bruker XFlash 5030 energy dispersive X-ray spectrometer (EDX) provides elemental analysis. To focus and thus image the differently prepared nanotubes properly, various modes of the SEM were applied.
To visualize the openings of the nanochannels at the Au sputtercoated surface of the membrane, the lower secondary electron detector was employed at an accelaration voltage of 4 kV. The working distance was kept at ∼6 mm.
Free-standing nanocone arrays and single nanocones were characterized in the low magnification mode of the lower secondary electron detector employing an acceleration voltage of 20 kV and keeping the working distance at ∼8 mm. The sample was tilted by 20°.
Free-standing nanotube networks were visualized in gentle beam mode of the lower secondary electron detector applying an acceleration voltage of 2 kV and keeping the working distance at ∼8 mm.
To study the walls of cylindrical and conical nanotubes, the nanostructures lying on TEM-grids were investigated in transmission using the transmission electron detector (STEM-in-SEM) at an acceleration voltage of 20 kV and a working distance of ∼4 mm. Top-views of these samples were taken with the lower secondary electron detector at an acceleration voltage of 5 kV.
To record EDX multipoint spectra and integrated EDX spectra of linescans positioned across a tubular nanostructure, the nanotubes were investigated lying on TEM-grids with an acceleration voltage of 20 kV and a working distance of ∼8 mm.

6.2 Small Angle X-ray Scattering (SAXS)

Polycarbonate membranes exhibiting parallel aligned, cylindrical nanochannels were investigated by small angle X-ray scattering (SAXS) in the group of Prof. Dr. B. Stühn (Physik, Technische Universität Darmstadt) before and after ALD-coating. The nanochannels act as scattering objects and the scattering

pattern provides information about the mean size as well as size distribution of a large channel ensemble (here $\sim 10^6$). SAXS was performed on a laboratory instrument with a sealed X-ray tube (Panalytical) applying CuK_α radiation with a wavelength of 1.54 Å and a multilayer X-ray mirror. The goniometer-like sample holder enabled the rotation of the sample around two axis perpendicular to the incoming X-ray beam (accuracy better than 0.01°). A two-dimensional detector (Molecular Metrology) recorded the scattering pattern at a distance of 150 cm from the sample. This set-up yields access to the scattering vector $\mathbf{q}$ ($q = \frac{4\pi}{\lambda} \sin\theta$, with the scattering angle 2θ) between 0.008 $Å^{-1}$ and 0.25 $Å^{-1}$. First, the surface normal of the sample was oriented parallel to the incoming beam ($\gamma = 0°$) to align the beam collinear to the longitudinal axis of the nanochannels. For this alignment, the diffraction resulted in an isotropic scattering pattern consisting of concentric rings. Due to the large aspect ratio of the studied nanochannels, small tilt of the sample with respect to the X-ray beam (e.g. $\gamma = 20°$) caused a highly anisotropic scattering pattern consisting of a narrow streak parallel to the axis of rotation [176]. To obtain information on the electron density within the nanochannel, the scattered intensity, $I(\mathbf{q})$, was analyzed as a function of the scattering vector $\mathbf{q}$. The diameter of the nanochannels as well as the layer thickness on its wall was deduced by fitting the $I(\mathbf{q})$ data with a model function for the form factor. It computes the two-dimensional scattering pattern by describing the nanochannels as hollow cylinders with a specific wall thickness embedded in a polycarbonate matrix. The form factor is based on a cylinder model as described by Engel et al. [176], which was extended by an additional cylindrical shell to integrate the ALD coating on the inner channel wall. Electron density of the wall, polydispersity of the channel diameter as well as instrumental background and resolution were parameters considered during the analysis of the SAXS data [176, 177].

For some samples, SAXS experiments were performed by the group of Dr. P. Kluth (ANU, Canberra, Australia) at the synchrotron facility in Melbourne, Australia. The higher beam intensities as well as the larger distance between sample and detector provide access to a broader range of scattering vectors ($\mathbf{q}$ between 0.0015 $Å^{-1}$ and 1.1 $Å^{-1}$ [178]) and thus enables the investigation of a broader channel diameter range. The samples were mounted on a 4-axis goniometer enabling the x-y positioning of the sample normal to the incoming X-ray beam as well as two different tilt angles. As for the laboratory instrument, the samples were aligned with the X-ray beam before data acquisition was performed under a defined tilting angle with respect to the X-ray beam. The scattering patterns were recorded with a photon energy of 11 keV using a two-dimensional Pilatus 1M hybrid pixel detector placed 96.2 cm distant from the sample. The scattered intensity $I(\mathbf{q})$ as a function of the scattering vector $\mathbf{q}$ was fitted according to the core-shell cylinder model described by Kluth et al. [179] to obtain initial channel diameter, ALD layer thickness as well as polydispersity and roughness of the channels.

6.3 Ellipsometry

To determine the thickness of ALD-layers on Silicon reference wafers (Si-wafers), the nanofilm-ep4 ellipsometer (Accurion GmbH) of the group of Prof. Dr. M. Biesalski (Chemie, Technische Universität Darmstadt) was used. This null ellipsometer varies incident and emergent angle between 10° and 85° relative to the surface normal at a constant wave length of 658 nm. The recorded data were analyzed

by applying the software Nanofilm P4 (version 1.2.0, Accurion GmbH) with integrated data base for real (n_1) and imaginary refraction indexes n_2 (see table 6.3.1).

Table 6.3.1.: Real (n_1) and imaginary refraction indexes (n_2) at a wavelength of 658 nm applied for the analysis of the data obtained by null ellipsometry.

Refraction Indexes	Air	Si<100>	TiO_2	SiO_2	Al_2O_3
n_1	1	3.829991	2.85	1.4565	1.6579
n_2	0	0.013726	0	0	0

For the estimation of the layer thickness of depositions performed at Universität Hamburg, a SENpro spectral ellipsometer (SENTECH) equipped with a halogen lamp (wavelength 370 to 1050 nm) was applied under an incident angle of 70°. The software SENpro was utilized to fit the spectra according to the Levenberg-Marquardt algorithm in the range between 400 and 850 nm. The modeling for the oxides was based on Cauchy and performed by applying the integrated data base.

6.4 X-ray Photoelectron Spectroscopy (XPS)

The composition of the ALD-coated membrane surfaces was studied by X-ray photoelectron spectroscopy in the group of Prof. Dr. C. Hess (Chemie, Technische Universität Darmstadt). A SSX 100 ESCA Spectrometer (Surface Science Laboratories Inc.) equipped with a monochromatic Mg-K_α and later a Al-K_α source was applied to analyze SiO_2 and TiO_2 as well as Al_2O_3 layers, respectively. SiO_2 was investigated under normal beam incidence, whereas TiO_2 and Al_2O_3 were measured under an angle of 45° with respect to the surface normal. The spot size of the beam ($\sim 0.25 \times 1\,mm^2$ for Mg-K_α source, $\sim 5 \times 5\,mm^2$ for Al-K_α source) was smaller than the sample area. An electron flood gun with 0.5 eV was used to avoid charging of the sample. Detail and survey spectra were measured with a step size of the binding energy of 0.1 and 0.5 eV (0.4 eV for SiO_2), respectively. All spectra were referenced to the main C1s component at 284.5 eV. A Voigt function (30 % Gauss fraction) and a Shirley type background were applied to perform the least-square fitting analysis with the software CasaXPS (version 2.3.16 PR 1.6, Casa Software Ltd.). Table 6.4.1 displays the utilized relative sensitivity factors (RSF) to analyze the atomic composition.

Table 6.4.1.: Relative sensitivity factors (RSF) used for XPS analysis.
[a]Including ubiquitous carbon and carbonate species.
[b]Including Ti^{4+} and Ti^{3+} species.
[c]Values taken from Sobel et al. [99].

	C 1s[a]	O 1s	Ti $2p_{3/2}$[b]	Ti-OH	Si 2p	Al 2p
RSF	1 (0.25)[c]	2.93 (0.66)[c]	5.22	2.93	(0.27)[c]	0.537

6.5 Current-Voltage (*I-V*) Curves

The ionic transport properties of a single nanochannel in a polycarbonate membrane were investigated by ionic conductance measurements. The sample was placed between two Teflon compartments of an electrochemical cell, which is shown in Figure 6.5.1a,b (same cell applied for conical etching). Both compartments, which were separated by a single-channel membrane, were filled with 1 M KCl solution exhibiting a specific conductivity $\kappa = 10.68\,\mathrm{Sm}^{-1}$ at 25 °C [180]. Current-Voltage (*I-V*) curves were recorded by applying a triangular voltage between ±1 V (first series) and ±3 V (Figure 6.5.1c) across the membrane via two Au electrodes utilizing a picoammeter/voltage source (Keithley 6487). For voltages between ±3 V, the voltage was increased in steps of 0.15 V and at each voltage the ionic current was measured for different times depending on the surface material: 1 s (uncoated), 3 s (TiO_2), and 10 s (SiO_2 and Al_2O_3). An explanation for the different durations is given in Section 11.4. For the determination of the diameter of a single cylindrical nanochannel and the tip diameter of a single conical nanochannel, surface charge effects were minimized by measuring at the isoelectric point (IEP) of the surface material. Thus, when estimating the (tip) diameter, uncoated and TiO_2-coated nanochannels were studied at pH 5, whereas channels coated with SiO_2 were analyzed at pH 2 and Al_2O_3-coated channels were investigated at pH 9. The pH of the 1 M KCl solution was adjusted to pH 2 and pH 9 by adding HCl and disodium phosphate (Na_2HPO_4), respectively. The pH adjustment did not influence significantly the electrolyte concentration of 1 M.

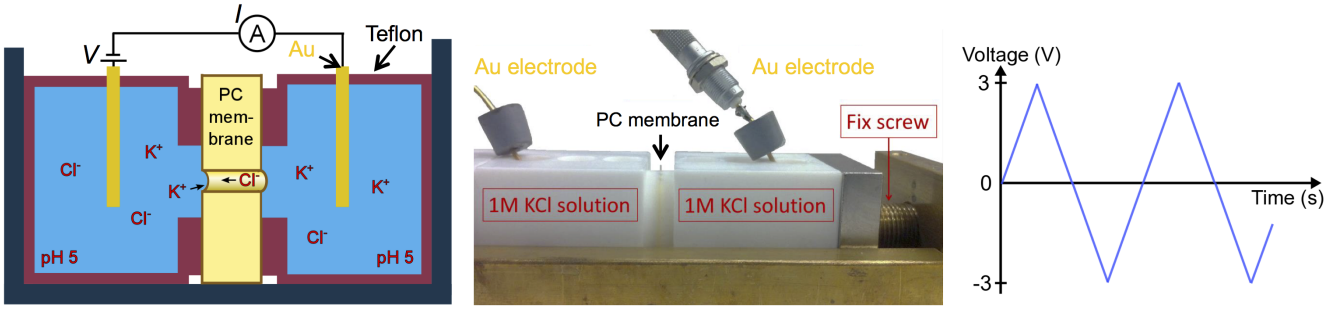

Figure 6.5.1.: Set-up for ionic conductance measurements. (a) Scheme and (b) photo of the electrochemical cell consisting of two Teflon compartments separated by the single-channel membrane, and filled with 1 M KCl. Via the two Au electrodes a triangular voltage (c) is applied across the membrane.

The investigation of the ionic conductance in ALD-coated, **cylindrically** etched ion-track polycarbonate membranes was divided into the following steps:

- Simultaneous etching of single and multichannel membranes in the same large beaker.
- *I-V* measurement of single-channel membranes to deduce the diameter of the uncoated nanochannels.
- Simultaneous ALD coating of single and multichannel membranes.
- *I-V* measurement of single-channel membranes at the IEP to determine the diameter after coating.
- *I-V* curves recorded at various pH values of the electrolyte.

- Dissolution of the multichannel membrane to release the reference nanostructures onto Cu-lacey TEM-grids and investigate them with STEM-in-SEM.

The steps listed below were performed to study the ionic conductance in ALD-coated, **conically** etched ion-track polycarbonate membranes:

- Etching of single and multichannel membranes right after each other by applying exactly the same asymmetric etching conditions.
- *I-V* measurement of single-channel membranes to deduce the tip diameter of the uncoated nanochannels.
- Simultaneous ALD coating of single and multichannel membranes.
- *I-V* measurement of single-channel membranes at the IEP to determine the tip diameter after coating.
- *I-V* curves recorded at various pH values of the electrolyte.
- Preparation of the coated single nanochannels as free-standing nanocones to determine the base diameter by SEM.
- Preparation of one half of the multichannel membrane as free-standing nanocones to estimate the base diameter by SEM, if the single cone is not found.
- Dissolution of the second half of the multichannel membrane to release the reference nanotubes onto a Cu-lacey TEM-grid and investigate them by using STEM-in-SEM regarding length and wall thickness of the nanocones.

6.6 Current-Voltage (*I-V*) Curves of Gated Nanochannels

To control the current flow through single conical nanochannels, a n-type junction field effect transistor (J-FET, Figure 6.6.1a) was set up. As displayed in Figure 6.6.1b, the studied single-channel membrane separated the two Teflon compartments of an electrolytical cell. The drain-source voltage V_{DS} was applied across the single-channel membrane by two Au electrodes and varied triangular between ±3 V using a DAQ card (National Instruments, PCI-MIO-16XE-50, Figure 6.6.1c). To record the drain current I_D, a picoammeter (Keithley 6485) was utilized. A voltage source (ELV, Switch Power Supply SPS 9001 M) was used to apply the gate-source voltage V_{GS} (Figure 6.6.1d) to the copper ring, which was pressed onto the tip side of the TiO_2-coated membrane, and thus acted as gate electrode.

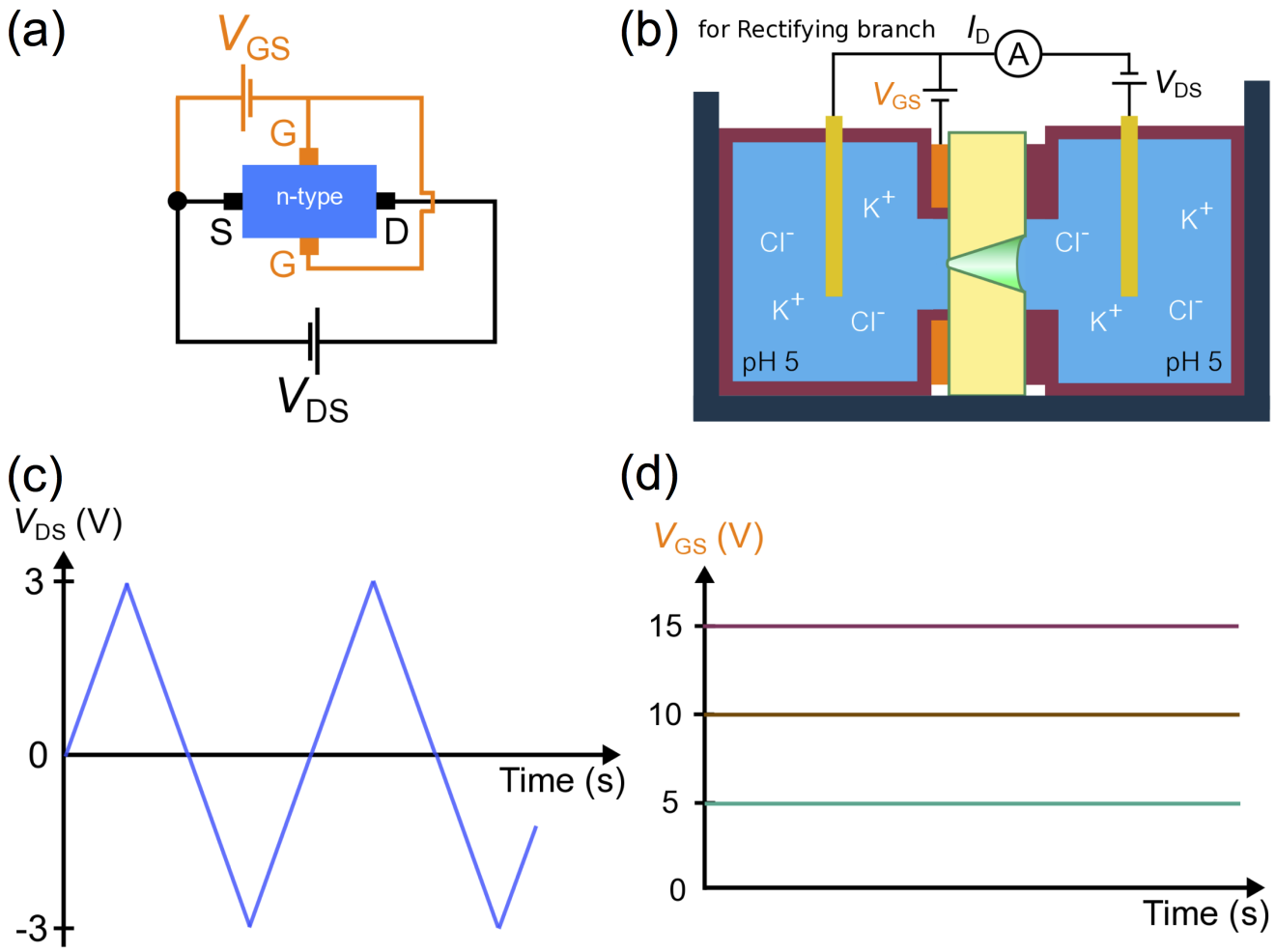

Figure 6.6.1.: Set-up for gated ionic conductance measurements. (a) Circuit diagram of an n-type junction field effect transistor. Scheme (b) of the set-up consisting of two Teflon compartments, which are placed in an electrolytical cell, separated by the single-channel membrane, and filled with 1 M KCl. Via the two Au electrodes the triangular drain-source voltage V_{DS} (c) is applied across the membrane, whereas the gate-source voltage V_{GS} (d) is applied to the tip side of the membrane via a copper ring, which is pressed onto the TiO_2-coated membrane surface and thus acts as gate electrode.

Part II.

Morphology and Composition of Atomic Layer Deposition Coatings

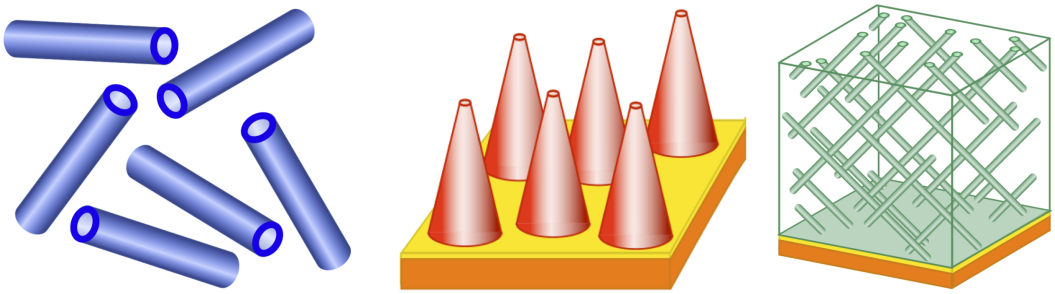

In this part, the TiO_2, SiO_2, and Al_2O_3 nanostructures synthesized by ALD in etched ion-track polycarbonate templates exhibiting various channel geometries are presented. The morphology and composition of the nanotubes prepared in systematic series were studied by different complementary methods.

Chapter 7 focuses on the investigation of cylindrical nanotubes with different outer diameters and wall thicknesses. For conical nanotubes, the influence of the number of ALD cycles on the growth process was studied (Chapter 8). Furthermore, nanocones fabricated in single-channel membranes are discussed. The synthesis and characterization of cylindrical interconnected nanotubes are presented in Chapter 9.

7 Cylindrical Nanotubes

The morphology and composition of oxide nanostructures fabricated by low-temperature ALD in cylindrically etched ion-track membranes was investigated. First, basic results are presented before the influence of the specific parameters initial channel diameter (Section 7.1) and number of ALD cycles (Section 7.2) on the synthesis is discussed. In Section 7.3, the composition of the TiO_2, SiO_2, and Al_2O_3 layers inside the nanochannels as well as on the membrane surface is analyzed. A qualitative study of the mechanical stability is given in Section 7.4. The imaging process of the SEM operated in transmission mode and the resulting method to determine the thickness of the deposited layers inside the nanochannels is discussed in Section 7.5.

The main desired characteristic of a controlled deposition process in a porous system is the homogeneous coating of all channels. This criterion is especially important for this work, since it guarantees the successful tailoring of single-channel membranes in further experiments.

Figure 7.0.1 displays representative SEM images of the smooth surface of a 170 s etched PC sample. One quarter of the etched membrane served as uncoated reference (a), whereas the other three sections were ALD-coated with different thicknesses of TiO_2 (b), SiO_2 (c), and Al_2O_3 (d). Calculating the fluence at various positions of the sample sections resulted in alike fluences of $5.8 \pm 0.3 \times 10^8 \frac{\text{ions}}{\text{cm}^2}$ (uncoated), $5.8 \pm 0.4 \times 10^8 \frac{\text{ions}}{\text{cm}^2}$ (TiO_2), $6.0 \pm 0.6 \times 10^8 \frac{\text{ions}}{\text{cm}^2}$ (SiO_2), and $6.1 \pm 0.5 \times 10^8 \frac{\text{ions}}{\text{cm}^2}$ (Al_2O_3). Thus, the amount of nanochannels is constant within the typical variation given by the inhomogeneity of the ion irradiation ($10 - 20\,\%$), indicating no channel closures. For each sample, the inset shows a representative channel opening. The mean diameter of ~ 200 channel openings was determined from the SEM images ($Ø_{SEM}$) and is given above each low magnification image. As expected, ALD reduces the diameter of all nanochannels at the membrane surface indicating the homogeneous coating of all channels of a sample. In the case of TiO_2 and SiO_2, these diameters are not in agreement with the nominal coating thicknesses and the values deduced from SAXS measurements ($Ø_{SAXS}$). The discrepancy is probably linked to the fact that SEM provides only information about the channel size at the sample surface and not along the full channel length. In addition, the quantitative estimation of the channel diameter includes a systematic error due to the Au sputtering, which influences shape, size, and apperance of the channel openings (e.g. inset b2).

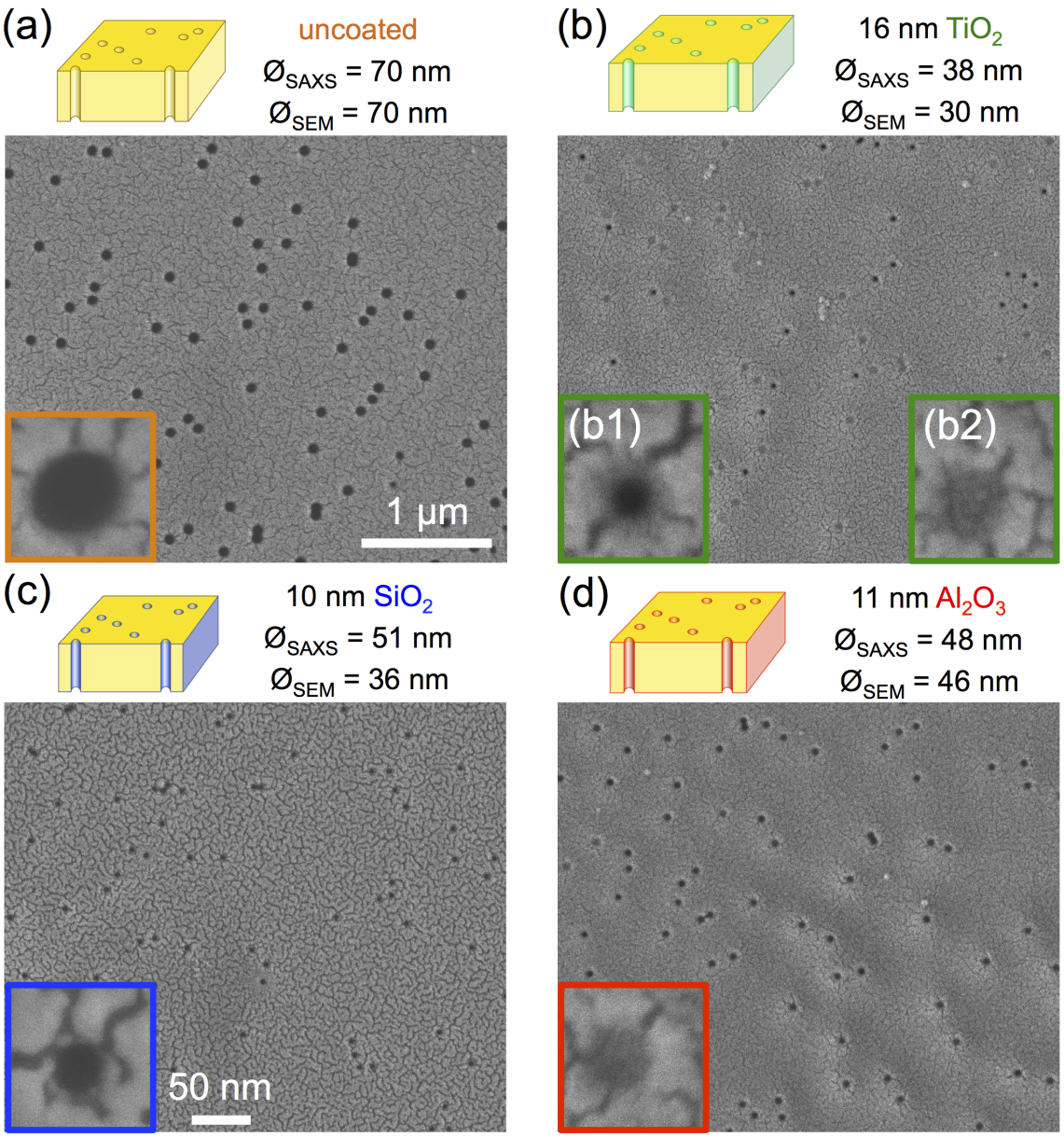

Figure 7.0.1.: Smooth surface of four sections of an 170 s etched ion-track polycarbonate membrane visualized by SEM after Au sputtering. The fluence of all etched sample sections are in excellent agreement. (a) uncoated section, (b) TiO_2-coated section, (c) SiO_2-coated section, and (d) Al_2O_3-coated section. The scale bar shown in (a) is valid for all low magnification images. The insets show representative channel openings of each sample at high magnification (scale bar displayed in c). For the TiO_2 and SiO_2 sample, the determined diameters are smaller than diameters deduced from SAXS.

For further analysis, the polycarbonate templates were dissolved providing access to the released nanostructures along their entire length and to obtain information about the deposition process at all positions of the nanochannels (Section 5.2). Figure 7.0.2 shows representative SEM images of nanostructures released from cylindrical nanochannels onto TEM-grids. Due to alignment of the nanotubes relatively to the detector the tube-like shape is directly verified by looking into the end of a nanotube (a, TiO_2 and b, SiO_2) and along the long axis of a nanotube (c, TiO_2).

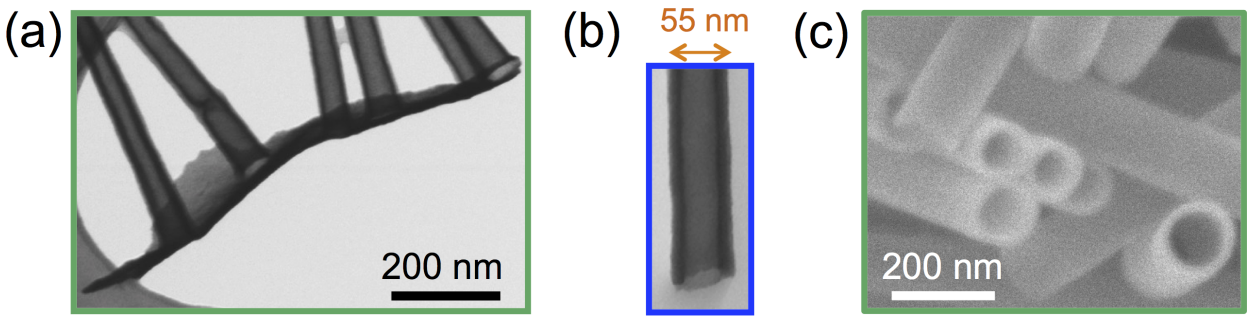

Figure 7.0.2.: SEM images of nanotubes released onto TEM-grids. (a,b) TiO_2 and SiO_2 tube ends recorded in transmission mode (STEM-in-SEM). (c) View along the long axis of a TiO_2 nanotube.

In most cases, the top-view SEM images present nanostructures as shown in Figure 7.0.3a. The ∼30-µm long TiO_2 nanostructures located across a bar of the copper TEM-grid evidence that the ALD deposition process covers the entire nanochannels. In the transmission mode (STEM-in-SEM, b), the morphology of the identical nanostructures is revealed with dark edges and bright centers corresponding to respectively more and less material the electron beam has to pass. This feature, visible in the high magnification images of (b), provides clear proof of a conformal ALD process all along the entire high aspect-ratio nanochannels. Some nanotubes are still attached to residual parts of the ALD-layer deposited at the surface of the template (orange circle).

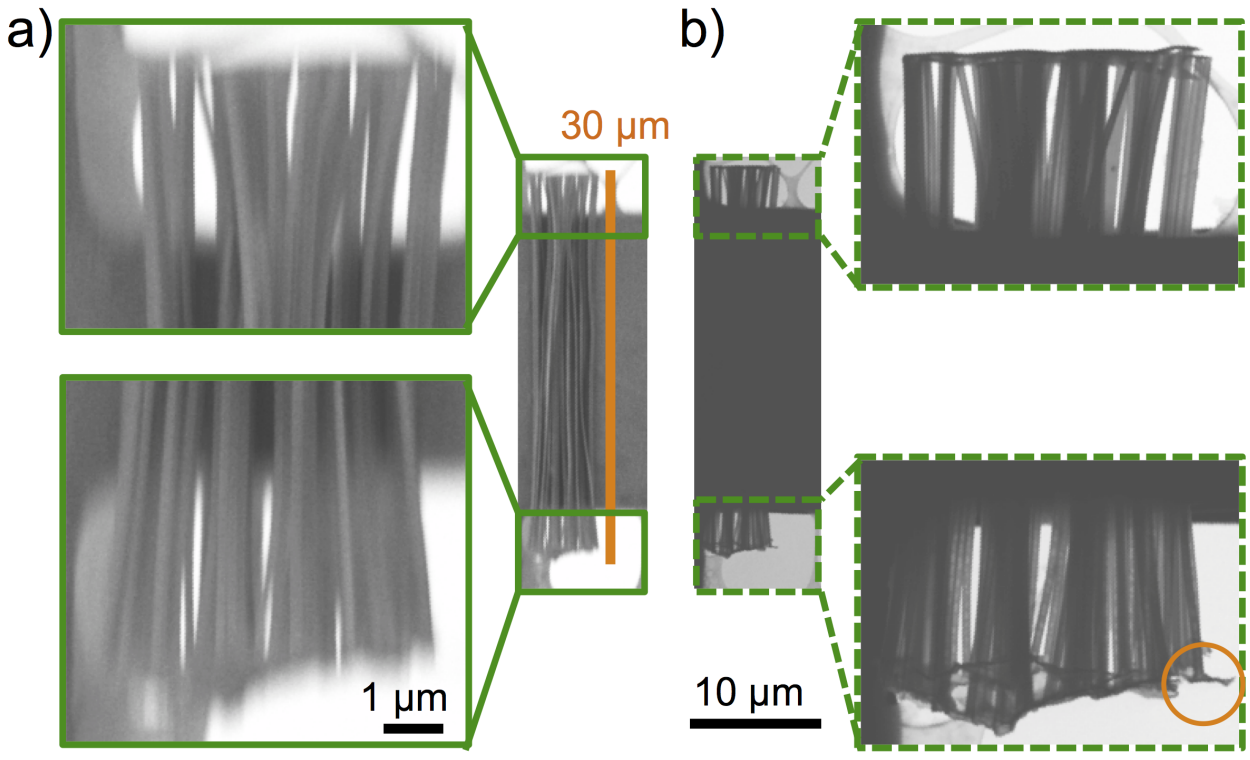

Figure 7.0.3.: SEM images of bundle of TiO_2 nanotubes on a TEM-grid. (a) The ∼30-µm long nanotubes are positioned across the bar of the copper TEM-grid. (b) Same nanotubes imaged in transmission mode (STEM-in-SEM). The orange circle marks nanotubes, which are still connected to residual parts of the ALD layer deposited at the membrane surface. The scale bar of the high and low magnification images is given in a and b, respectively.

The SiO_2 nanotubes diplayed in Figure 7.0.4a nicely show the tubular shape of all nanostructures as well as the homogeneity of the wall thickness. Figure 7.0.4b demonstrates the suitability of STEM-in-SEM for the analysis of nanotubes due to the visualization of different material thicknesses at centers and walls of the tubes as well as crossings of super-imposed SiO_2 nanotubes. Flat Al_2O_3 pieces (c), which are still connected to broken Al_2O_3 nanotubes, indicate the coating of the membrane surface.

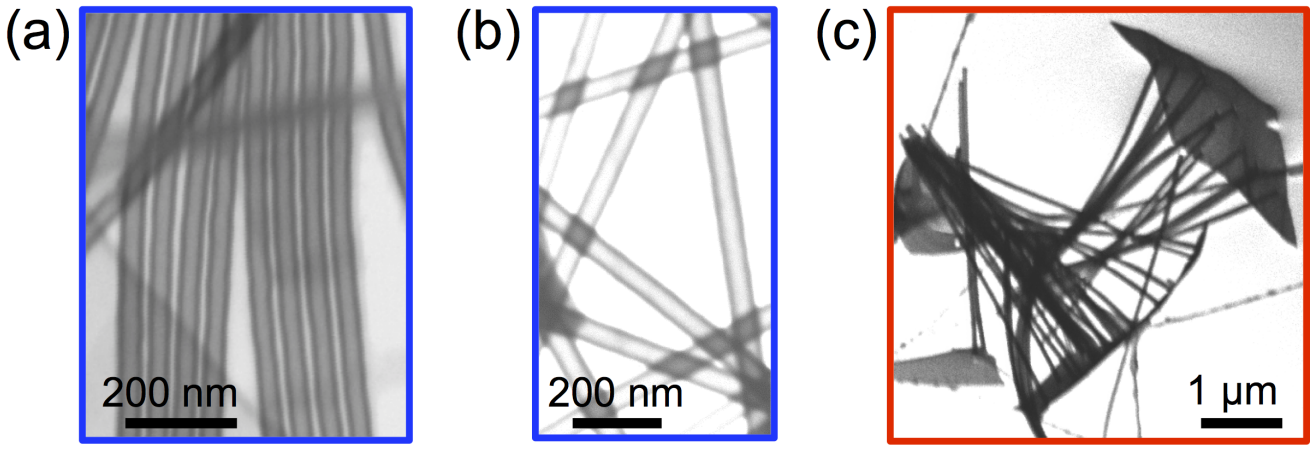

Figure 7.0.4.: STEM-in-SEM images of nanotubes lying on TEM-grids. (a) SiO_2 nanotubes exhibiting homogeneous walls. (b) SiO_2 nanotubes revealing various material thicknesses at centers, walls, and crossings. (c) Flat Al_2O_3 pieces are still attached to broken nanotubes indicating a coating process at the entire template surface.

Different impressions of nanotubes (Figures 7.0.2, 7.0.3, 7.0.4) indicate a homogeneous and conformal ALD deposition of the three oxides in the polycarbonate template. To evidence a controlled surface tailoring, systematic studies were performed, which are presented in the following sections.

7.1 Dependence of ALD Coating on Initial Channel Diameter

To test the independence of the ALD process from the size of the nanochannels, 10 templates with channel diameters between ∼18 and ∼55 nm were prepared by applying different etching times between 40 and 130 s, respectively. One quarter of each sample was used as reference for the initial diameter and thus stayed uncoated. All other sample sections were coated by applying 125, 28, or 30 ALD cycles for a nominal ∼5 nm thick TiO_2, SiO_2, or Al_2O_3 layer, respectively. TiO_2 and Al_2O_3 coatings of this series were performed at Universität Hamburg (group of Prof. Dr. K. Nielsch). SiO_2 layers were deposited in the group of Prof. Dr. C. Hess at TU Darmstadt. For all oxides, Figure 7.1.1 depicts representative STEM-in-SEM images of sections of the released nanotubes for 4 different initial diameters. All transmission images show the same wall thickness, which was measured at different positions along the tube for 10-15 tubes per sample. This wall thickness is in excellent agreement with the film thickness deposited on the reference Si-wafer. The corresponding mean values of the layer thickness are given in Table 7.1.1. The rather large uncertainties of the STEM-in-SEM data are caused by the error (standard deviation) propagation for the subtraction of the inner diameter from the outer diameter to obtain the double wall

thickness. However, this method was more precise than measuring the wall thickness directly, especially for the ∼5 nm thin walls.

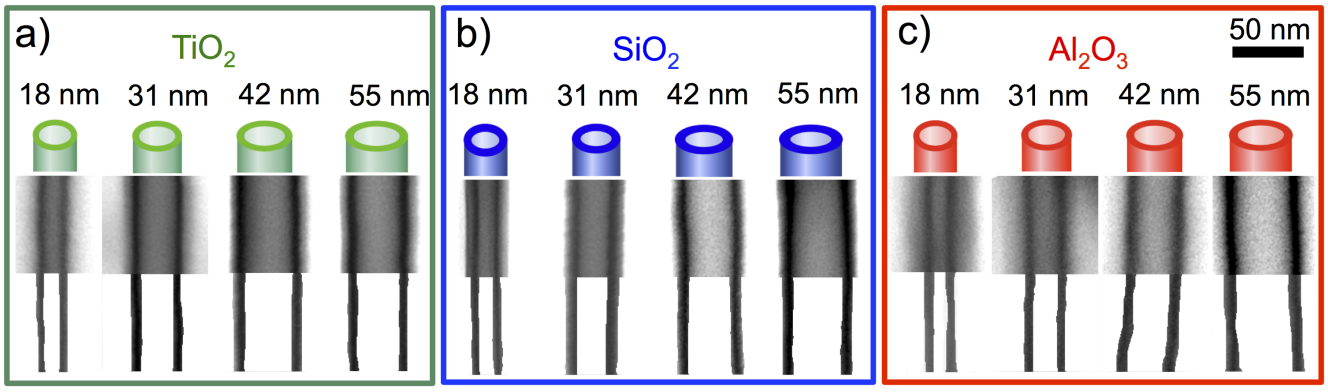

Figure 7.1.1.: STEM-in-SEM images of representative single cylindrical nanotubes exhibiting a nominal 5 nm thick wall of TiO_2 (a), SiO_2 (b), and Al_2O_3 (c) for initial channel diameters of ∼18 nm, ∼31 nm, ∼42 nm, and ∼55 nm. The scale bar shown in (c) is valid for all presented STEM-in-SEM images.

Table 7.1.1.: Thickness of ALD layers in nanochannels with various inital diameters deduced from STEM-in-SEM and SAXS after a deposition resulting in a nominal 5 nm thick coating.

Initial diameter (nm)	**Layer thickness** (nm)					
	TiO_2		SiO_2		Al_2O_3	
	STEM	SAXS	STEM	SAXS	STEM	SAXS
18	4 ± 1	2.9 ± 0.2	4 ± 1	4.1 ± 0.1	5 ± 1	4.1 ± 0.3
31	6 ± 3	3.9 ± 0.2	5 ± 1	5.8 ± 0.1	6 ± 2	3.4 ± 0.2
42	4 ± 7	3.6 ± 0.2	5 ± 2	5.2 ± 0.1	6 ± 2	4.0 ± 0.5
55	6 ± 4	5.3 ± 0.1	5 ± 2	5.9 ± 0.2	6 ± 4	4.9 ± 0.2

The same samples were analyzed by SAXS. This method provides a mean of about 10^6 nanochannels. The outer and inner diameter have to be deduced from modeling the scattering pattern. The narrow streak of the scattered intensity is displayed in Figure 7.1.2 for the sample section etched 90 s and coated with 125 ALD cycles of TiO_2.

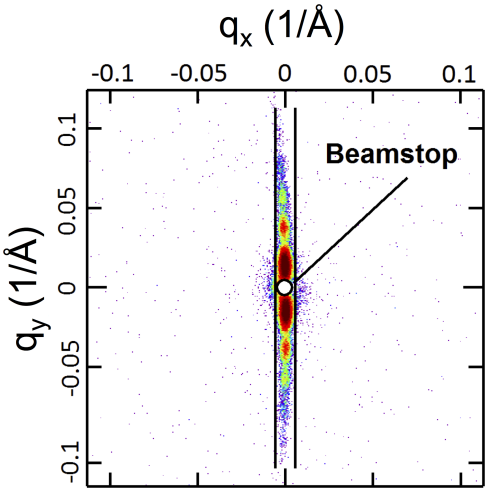

Figure 7.1.2.: Scattering pattern obtained by SAXS under a tilting angle of 20° for the sample etched 90 s and coated with nominal 5 nm TiO_2.

Figure 7.1.3a shows the resulting scattered intensity, $I(\mathbf{q})$, as function of the scattering vector $\mathbf{q}$ and the corresponding fit. Additionally, the scattered intensity before ALD is shown in the same graph and alike measurements for SiO_2 and Al_2O_3 are displayed in Figure 7.1.3b and c, respectively. For all uncoated samples, the oscillations of the scattered intensity as well as the excellent fit to it evidence cylindrical shaped and well aligned etched ion-tracks with a size distribution $< 3\,\%$ as described earlier by Cornelius et al. and Engel et al. [176, 181]. After ALD coating, the typical intensity oscillations are preserved but shifted to larger values of $\mathbf{q}$ as expected for smaller channel diameters (indicated by the arrows). The model of a cylindrical channel in polycarbonate with an additional wall of constant electron density describes these scattered intensities well demonstrating highly conformal ALD processes along the entire channel length. The polydispersity of the cylinder diameter is constant around 10 % and is not affected by the coating.

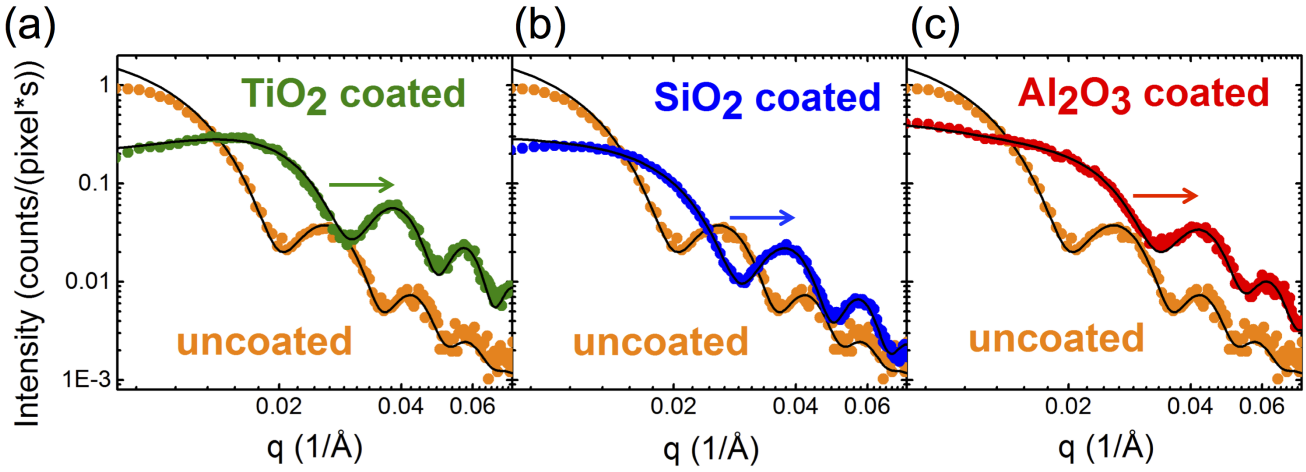

Figure 7.1.3.: SAXS intensity oscillations deduced from the scattering patterns before and after ∼ 5 nm ALD of 90 s etched membranes. Black solid lines are fits according to the core-shell model of Engel et al. [176].

Figure 7.1.4 summarizes the diameter before and after ALD obtained by STEM and SAXS, whereas the corresponding layer thicknesses are displayed in Table 7.1.1. The uncertainty of the SAXS analysis is smaller than the data symbols. The initial channel diameter deduced from SAXS increases linearly with increasing etching time as already reported by Kuttich et al. [177]. The corresponding radial etching rate of $\sim 23.9 \pm 0.5 \frac{\text{nm}}{\text{min}}$ was deduced from the slope of the data for the uncoated sample sections shown in Figure 7.1.4. In the case of TiO_2-coated samples, the diameters deduced from SAXS are in excellent agreement with the reduced diameters expected from the nominal ALD layer thickness. STEM-in-SEM analysis is in good agreement except of the sample etched for 130 s. For SiO_2 depositions, SAXS investigations lead to diameters that coincide with the expected ones, only in a few cases slightly smaller diameters are obtained. STEM-in-SEM yields the same diameter as SAXS for 40 s etching but for longer etching times the diameters are smaller. The SAXS analysis of Al_2O_3-coated samples reveals inner diameters that coincide with the expected ones for the samples etched 40 s as well as 70 s and longer. However after 50 and 60 s etching time, the SAXS data deviate after coating possibly indicating that the ALD process is not homogeneous for the small initial diameters. However, the diameters of the 40 s etched sample deduced from both characterization methods after coating are in agreement with the nominal coating thickness. Furthermore, the diameters obtained by STEM-in-SEM for the 50 and 60 s etched samples coincide with the expected diameter reduction. For longer etched samples, STEM-in-SEM analysis reveals diameters smaller than induced by the nominal coating thickness. For 50 and 60 s etching time, the origin of the deviations of the SAXS data is not known, but may be related to an inhomogeneous coating of the nanochannels over a large sample area. The fact that STEM-in-SEM obtains slightly smaller diameters after ALD than SAXS for samples with larger initial diameters may be caused by the uncertainty in the determination of inner diameters of these tubes due to less contrast in the STEM-in-SEM images (Section 7.5).

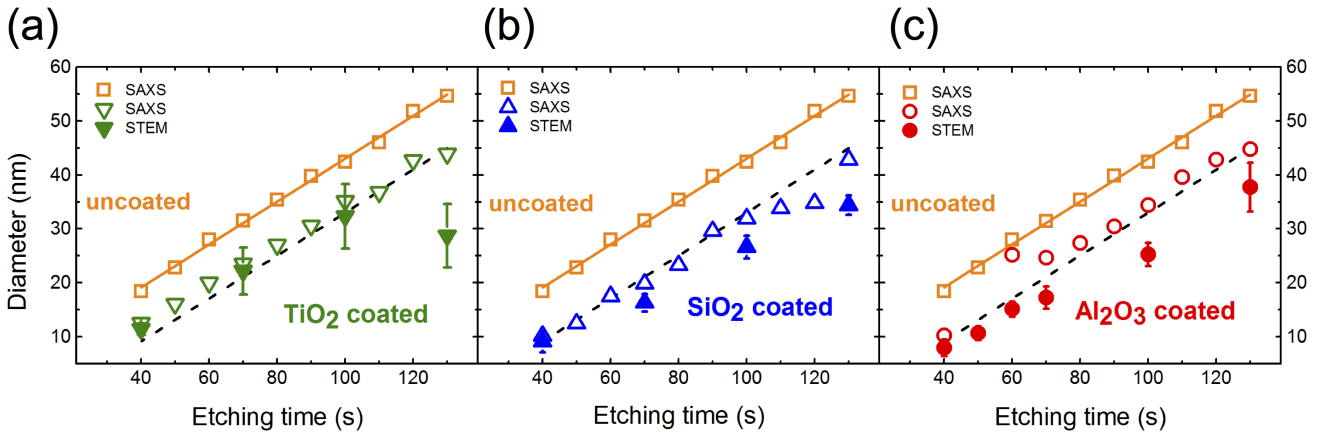

Figure 7.1.4.: Channel diameter before and after ALD coating as a function of etching time analyzed by SAXS and STEM-in-SEM. (a) TiO_2 coated, (b) SiO_2 coated, (c) Al_2O_3 coated. The uncertainties of the SAXS analysis are smaller than the data symbols (~0.2 nm). Linear fits to the diameters deduced from SAXS are shown as solid lines, dashed lines are guides to the eye to diameters of coated channels for a nominal ALD layer thickness of 5 nm.

Overall, the analyses by SAXS and STEM-in-SEM coincide well. Furthermore, the resulting channel diameters are in agreement with the nominal ALD-deposited thickness indicating the suitability of the chosen pulse-, exposure-, and purge times of the low-temperature ALD processes for the reaction of the gaseous precursors at the whole surface area of various high aspect-ratio nanochannels. These results clearly demonstrate the independence of the layer thickness from the initial channel diameter down to an outer diameter of ∼18 nm. This leads to an inner diameter smaller than 10 nm over the entire 30-µm tube length resulting in an aspect ratio inside the tubes of more than 3000 for all three deposited oxides.

7.2 ALD Coating as Function of Number of ALD Cycles

The ideal ALD process is characterized by a layer-by-layer growth and results in a constant growth rate, which means the coating thickness increases linearly with the number of ALD cycles. To determine the growth mode inside the cylindrical nanochannels, series of samples with same initial channel diameter (∼50 nm) were prepared. Then we deposited nominal 5, 10, 15, 20, and 22 nm thick layers, which required different numbers of ALD cycles for each of the three materials. The TiO_2- and Al_2O_3-coatings for this series were performed at Universität Hamburg (group of Prof. Dr. K. Nielsch). An additional series of Al_2O_3 samples was synthesized at GSI. SiO_2 layers were deposited at TU Darmstadt (group of Prof. Dr. C. Hess). Figure 7.2.1a,b,c show representative STEM-in-SEM images of sections of the released TiO_2, SiO_2, and Al_2O_3 nanotubes, respectively. The inner diameter decreases with increasing number of ALD cycles. For quantitative analysis, the outer and inner diameters were measured at various positions along 10-15 nanotubes of each sample. Both are constant along the entire tube length evidencing a conformal growth process inside the high aspect-ratio nanochannels even for the largest film thickness. Mean layer thicknesses determined from the STEM-in-SEM images as well as SAXS analysis are displayed in Figure 7.2.1d,e,f and Table 7.2.1 as a function of ALD cycles. The error of the wall thickness analysis by STEM-in-SEM was calculated by error propagation and is represented by the error bars. The thickest TiO_2 layer obtained after 610 ALD cycles (22 nm) could not be analyzed by SAXS due to experimental limitations. For Al_2O_3, SAXS data of the samples coated in Hamburg and at GSI are not given, since fits to the scattered intensity did not converge. This indicates possibly an inhomogeneous coating over a larger sample area, although the amount of tubes transferred to the TEM-grids and their morphology was alike for all three oxides, demonstrating conformal coating of a significant amount of channels for Al_2O_3, too. The maximum coating thickness resulted in channels exhibiting an inner diameter smaller than 10 nm corresponding to an aspect ratio larger than 3000 for all three materials. In addition, their layer thicknesses depend linearly on the number of ALD cycles evidencing layer-by-layer growth. The growth rate (slope of curve) strongly depends on the deposited material being ~ 0.03 nm/cycle for TiO_2, ~ 0.15 nm/cycle for SiO_2, and ~ 0.05 nm/cycle for Al_2O_3 (Hamburg). In the polymeric nanochannels, the growth rates of TiO_2 and SiO_2 are slightly smaller compared to the flat Si-wafer, whereas in the case of Al_2O_3 it is smaller by almost a factor of three (Sections 3.1, 3.2, 3.3). This may be caused by diffusion limitations during the ALD process and was avoided by further optimizing exposure and purge times for the Al_2O_3 depositions performed at GSI. This resulted in a growth rate of ~ 0.1 nm/cycle in perfect

agreement with depositions on flat Si-wafers.

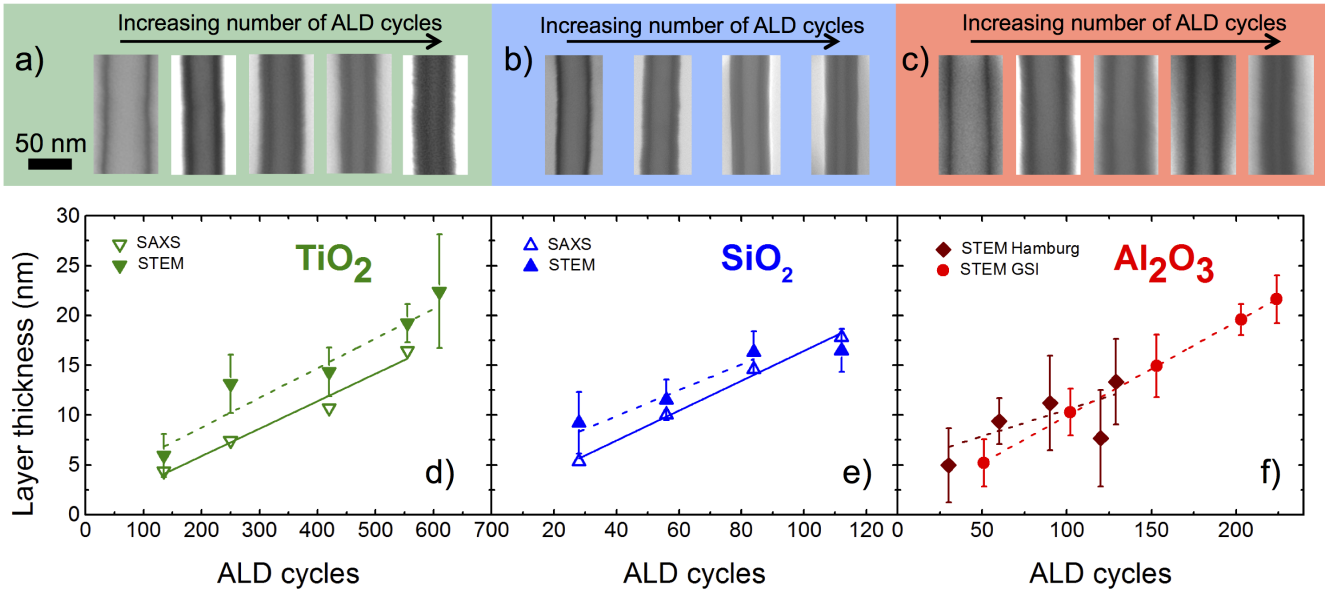

Figure 7.2.1.: STEM-in-SEM images of series of TiO_2- (a), SiO_2- (b), and Al_2O_3- (c) nanotubes and the corresponding wall thicknesses as a function of number of ALD cycles deduced from STEM-in-SEM images and SAXS (d), (e), (f). For all STEM-in-SEM images, the scale bar shown in (a) is valid. The layer thicknesses increase linearly with the number of ALD cycles. Dashed and solid lines are linear fits to STEM-in-SEM and SAXS data, respectively. The error bars show the standard deviation for the thickness analysis of STEM-in-SEM images. The uncertainties of the SAXS analysis are with ∼0.2 nm smaller than the data symbols.

Table 7.2.1.: ALD layer thickness in nanochannels with ∼50 nm initial diameter for various number of ALD cycles corresponding to different nominal coating thicknesses. For 610 cylces of TiO_2 (22 nm), experimental limitations prohibit SAXS analysis. Fits to the scattered intensities of the Al_2O_3 layers did not converge and thus the SAXS data are not given. For TiO_2 and SiO_2, the uncertainties of the SAXS analysis are ∼0.2nm.

Nominal coating (nm)	**Layer thickness** (nm)					
	TiO_2		SiO_2		Al_2O_3	
	STEM	SAXS	STEM	SAXS	STEM	STEM (GSI)
5	6 ± 2	4.3	9 ± 3	5.3	5 ± 4	5 ± 2
10	13 ± 3	7.4	12 ± 2	10.0	9 ± 2	10 ± 2
15	14 ± 2	10.7	16 ± 2	14.6	11 ± 5	15 ± 3
20	19 ± 2	16.5	17 ± 2	17.8	8 ± 5	20 ± 2
22	22 ± 6	n.a.	n.a.	n.a.	13 ± 4	22 ± 2

To overcome the limitations of the laboratory SAXS instrument at TU Darmstadt and study nanochannels with diameters of a few nm, some samples were analyzed at the synchrotron facility in Melbourne, Australia. For a test sample (∼ 50 nm initial diameter and nominal 10 nm ALD coating with SiO_2),

Figure 7.2.2 shows the scattered intensities $I(\mathbf{q})$ as function of the scattering vector $\mathbf{q}$ recorded at the laboratory and synchrotron SAXS facilities. In both cases, the pronounced SAXS intensity oscillations are in excellent agreement in the range $0.03 \leq \mathbf{q} \geq 0.06$. At lower $\mathbf{q}$ slight differences are observed, whereas at higher $\mathbf{q}$ the scattered intensities differ strongly. The core-shell model described by Kluth et al. [179] reproduces perfectly the data obtained in the laboratory. For the synchrotron data, the fit differs at low scattering vectors. However, both fits result in very similar values for the initial diameter, the diameter after coating, and the ALD layer thickness, which are given in Table 7.2.2. In addition, the obtained values are in agreement with the fit of the laboratory data according to the model function reported by Engel et al. [176] and the STEM-in-SEM data of this sample.

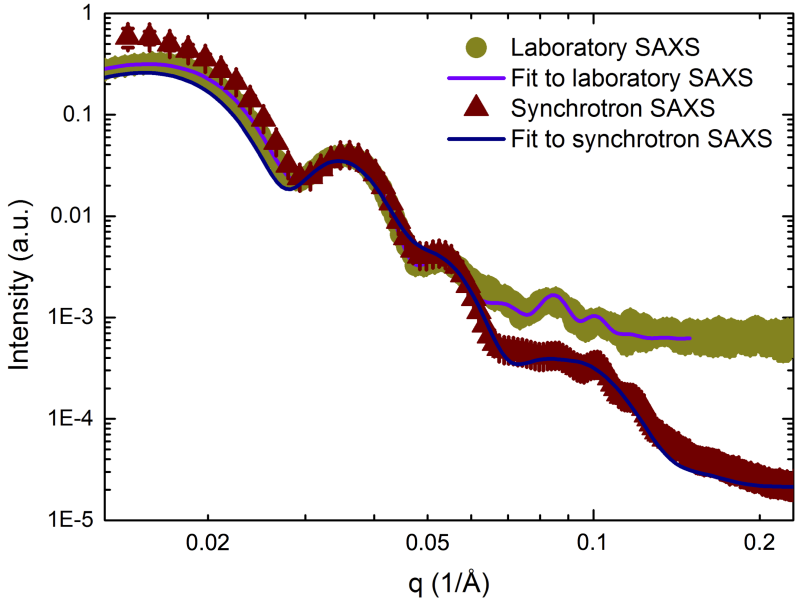

Figure 7.2.2.: For one 2 min etched sample coated with a nominal 10 nm thick SiO_2 layer, the scattered intensities deduced from scattering patterns obtained by laboratory and synchrotron SAXS are compared. Both data sets were fitted by applying the core-shell model described by Kluth et al. [179].

Table 7.2.2.: Comparison of laboratory and synchrotron SAXS analyis. After 2 min etching and nominal 10 nm SiO_2 coating, the sample was analyzed by STEM-in-SEM and SAXS applying a laboratory instrument as well as synchrotron radiation. From the SAXS data, the dimensions of the cylindrical nanochannels were deduced by applying the core-shell models of Engel et al. [176] and Kluth et al. [179].

	STEM	SAXS		
		laboratory		synchrotron
		Engel	Kluth	Kluth
Initial diameter (nm)	46 ± 3	48.4 ± 0.2	46.8 ± 0.2	46.0 ± 0.2
Inner diameter (nm)	23 ± 2	28.4 ± 0.1	27.4 ± 0.1	28.6 ± 0.1
Layer thickness (nm)	12 ± 2	10.0 ± 0.1	9.7 ± 0.1	8.7 ± 0.1

The fact that the intensity oscillations occur and the deduced values agree with the ones obtained 18 months earlier before transporting the sample by plane to Australia, demonstrates the robustness and stability of SiO_2-coated nanochannels in ∼30-µm thick polycarbonate membranes. Series of nanochannels with an initial diameter of ∼25 nm (60 s etching) and 7, 8.5, 9.5, and 10.5 nm coating thicknesses of SiO_2, TiO_2, and Al_2O_3 layers were analyzed. Figure 7.2.3 displays the scattered intensity for the uncoated reference membrane as well as for the SiO_2-coated membranes. The pronounced oscillations and the excellent fits to it demonstrate cylindrically shaped, parallel aligned nanochannels with a narrow size distribution before and after ALD coating of various thicknesses. The intensity oscillations are shifted to larger values of **q** for thicker coatings up to a nominal thickness of 9.5 nm as expected for smaller channel diameters. These observations reveal a highly conformal ALD process along the entire nanochannel length for deposited thicknesses up to 9.5 nm. For all deposited thicknesses, the layer thickness deduced from the scattered intensities is smaller than the nominal one especially for the thickest nominal coating as presented in Table 7.2.3. Limited diffusion of the precursor molecules inside the high aspect ratio nanochannels might cause this effect and could probably be avoided by further increasing the exposure and purge times of the ALD process for the coating of very small nanochannels. However, this SAXS-analysis confirms the sucessful surface modification of etched ion-track polycarbonate membranes by SiO_2-ALD to synthesize nanochannels with diameters below 10 nm.

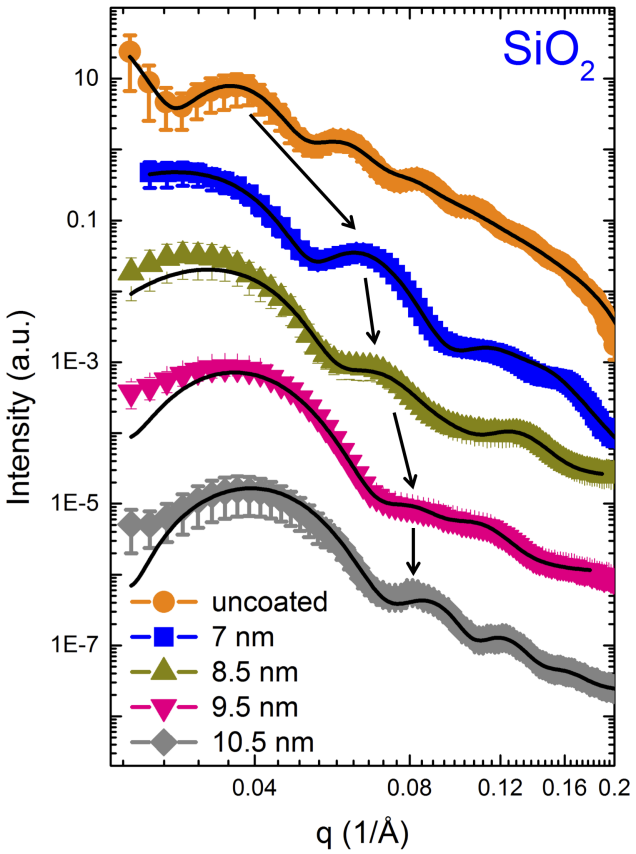

Figure 7.2.3.: Scattered intensities of membranes with a diameter of ∼25 nm after etching without coating and with different thicknesses of the deposited SiO_2 layers recorded by SAXS applying synchrotron radiation. The arrows indicate the shift of the intensity oscillations to larger values of **q** for smaller channel diameters. For each sample, the solid black line is the corresponding fit according to the the core-shell model by Kluth et al. [179].

Table 7.2.3.: Dimensions of nanochannels with initial diameter ∼25 nm and various nominal thicknesses of the deposited SiO_2 layers deduced from SAXS analysis with synchrotron radiation utilizing the core-shell model reported by Kluth et al. [179]. The corresponding intensity oscillations are depicted in Figure 7.2.3.

Nominal coating (nm)	Layer thickness (nm)	Outer diameter (nm)	Inner diameter (nm)
7	5.7 ± 0.1	26 ± 0.1	14.6 ± 0.1
8.5	6.8 ± 0.1	25.8 ± 0.1	12.2 ± 0.1
9.5	8.7 ± 0.2	25.4 ± 0.2	8.0 ± 0.1
10.5	8.5 ± 0.1	24.2 ± 0.1	7.2 ± 0.04

For alike prepared nanochannels coated with various layer thicknesses of TiO_2 and Al_2O_3, the scattered intensities recorded by applying synchrotron SAXS are shown in Figure 7.2.4a and b, respectively. Intensity oscillations occur for both oxides. However, no reasonable fit could be obtained by the core-shell model described by Kluth et al. [179]. These fits resulted in positive electron density contrast, which is not expected for the electron densities deduced from the laboratory SAXS analysis of TiO_2 ($\sim 800-1000 \frac{e}{nm^3}$) and Al_2O_3 ($\sim 1166 \frac{e}{nm^3}$), which are higher than the one of polycarbonate ($\sim 381 \frac{e}{nm^3}$). Replacing the Gaussian distribution of the outer diameter with a Schulz-Zimm distribution as performed by Engel et al. [176] lead to a negative electron density contrast and improved the fits, which are displayed in Figure 7.2.4. However, the fit quality is still not satisfactory and thus no size values are given. For the TiO_2 depositions, the reason for these difficulties in fitting of the samples with similar expected inner diameters as the ones presented in Figure 7.2.1d is not understood so far. The results for the Al_2O_3-coated samples are promising, since membranes exhibiting various coating thicknesses (Figure 7.2.1f) or small diameters (Figure 7.1.4c) did not enable converging fits of the data obtained by laboratory SAXS.

Furthermore, the synthesis of nanochannels with diameters of a few nm over a length of ∼30 µm is challenging, since the dimensions of the precursor molecules are only one order of magnitude smaller than the channel diameters hindering an efficient diffusion process. The obtained result that SiO_2 depositions reduce the channels more reliable than TiO_2 and Al_2O_3 coatings might be caused by the small dimensions of the applied precursor ($SiCl_4$) and catalyst (C_5H_5N) compared to the Al_2O_3 precursor ($Al(CH_3)_3$) and the TiO_2 precursor ($Ti(OCH(CH_3)_2)_4$). N. Sobel reported the reduction of nanochannels in mesoporous silica (SBA-15) down to a diameter of 4.8 nm by repeating several times the first half-cycle of the SiO_2 deposition before performing the other half-cycle in the same way [182]. This approach or the utilization of other precursor molecules, e.g. $TiCl_4$ for TiO_2 deposition, may enable homogeneous and conformal coating of very small nanochannels by avoiding diffusion limits.

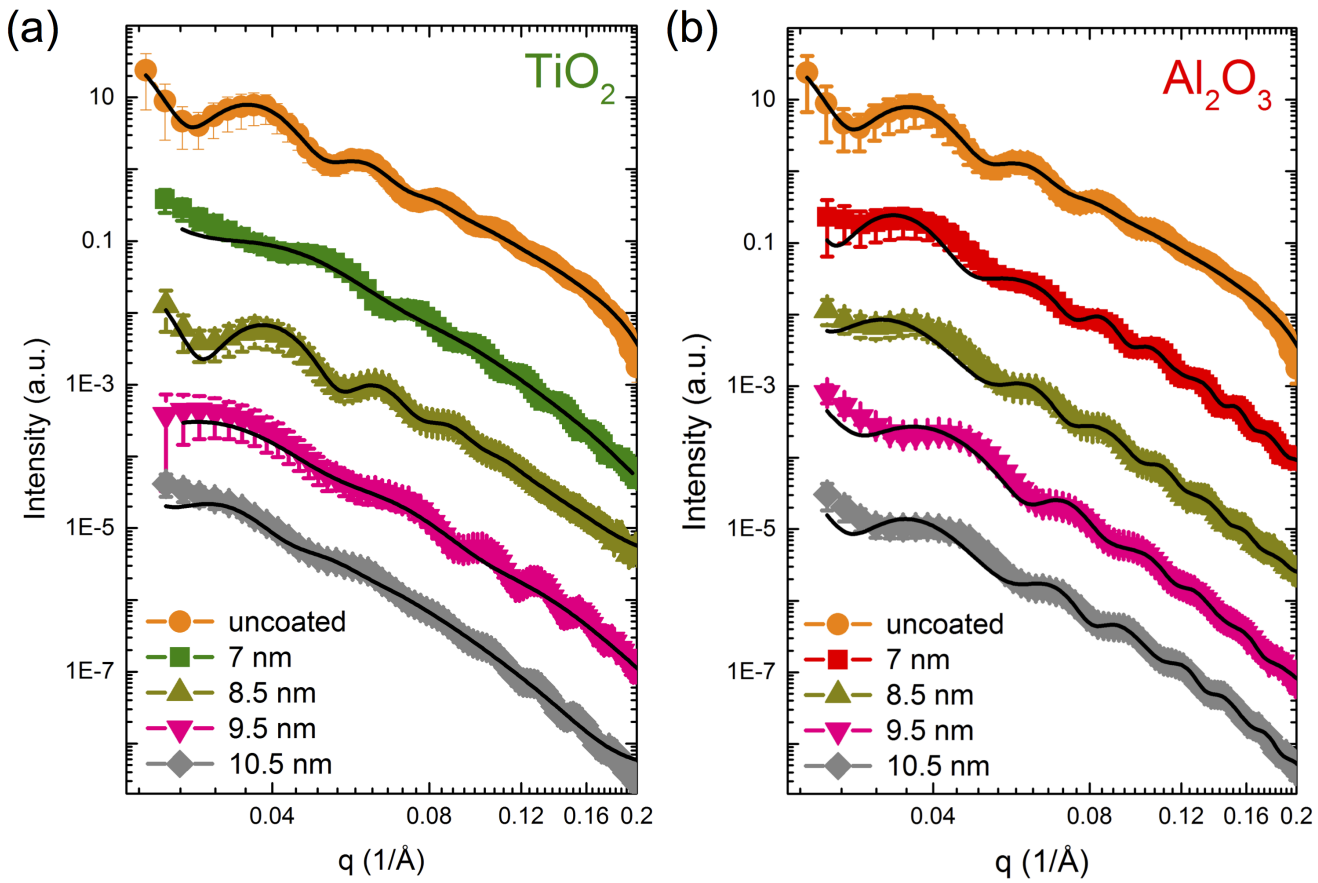

Figure 7.2.4.: Scattered intensities of membranes with an initial diameter of ~25 nm that are coated with various layer thicknesses of TiO_2 (a) and Al_2O_3 (b) by ALD. All data were recorded by SAXS utilizing synchrotron radiation. Solid black lines are the corresponding fits according to the core-shell model by Kluth et al. [179]. For the ALD-coated samples, a Schulz-Zimm distribution was applied for fitting the total diameter [176].

7.3 Composition of ALD Coatings Analyzed by EDX and XPS

Additionally to the morphology, well controlled tailoring of nanochannels by surface modification includes a pure composition of the coating. Thus, the ALD layers were studied by EDX of the released nanotubes. To obtain significant signal, EDX analysis was performed on nanotubes exhibiting walls of ~ 20 nm (outer diameter ~50 nm). Figure 7.3.1 displays integrated EDX spectra of linescans recorded across a single TiO_2 (green), SiO_2 (blue), and Al_2O_3 (red) nanotube lying on a TEM-grid. The spectra contain the respective peaks of titanium, silicon, and aluminum as well as oxygen. Copper and carbon signals are ascribed to contributions of the sample holder, since their height varies depending on the position of the studied nanotube relative to the supporting structures of the TEM-grid. For none of the three materials, nitrogen and chlorine peaks were measured demonstrating pure deposition and preparation processes.

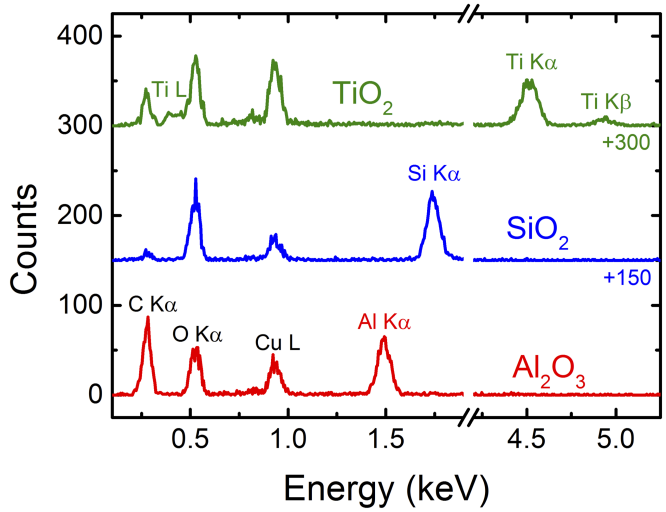

Figure 7.3.1.: Integrated EDX spectra of linescans measured across a single TiO_2 (green), SiO_2 (blue), and Al_2O_3 (red) nanotube exhibiting ~ 20 nm wall thickness and ~50 nm outer diameter. Copper and carbon peaks are attributed to contributions of the Cu-lacey TEM-grid. The spectra are shifted vertically for better visibility.

Since thermal drift of the nanotubes in the SEM precluded acquisition times longer than seven minutes, the count rates are only suitable for a qualitative analysis, even for the analyzed nanotubes with walls of ~ 20 nm. To quantify the composition of the ALD layers at the membrane surface, XPS was applied.
Figure 7.3.2 shows detailed spectra of the Ti 2p, Si 2p, and Al 2p peak as well as the corresponding O 1s signal for nominal 10 nm thick ALD layers. The spectra in Figure 7.3.2a demonstrate the growth of TiO_2, since the Ti^{4+} species dominate the contributions of Ti^{3+} (0.3 at%). This result was found for the 5 nm thick layer, too (0.1 at% of the Ti^{3+} peak). For fitting Ti $2p_{3/2}$ and Ti $2p_{1/2}$ duplets, spin-orbit coupling was considered by a 2:1 ratio of the peak areas and $\Delta x_c = 5.65$ eV binding energy difference resulting in a constant peak width (full width at half maximum - FWHM) for both coating thicknesses. In both cases, the binding energy of the Ti^{3+} peaks is shifted by -1.3 eV with respect to the Ti^{4+} peaks in agreement with literature [183]. O 1s features are assigned to Ti-O-Ti species at $\Delta x_c = 530 - 529.9$ eV and Ti-OH species at $\Delta x_c = 531.6 - 531.5$ eV [184]. Carbon at a binding energy of 284.5 eV was detected as main impurity, which is ascribed to ubiquitous carbon (~ 20 at%) and a small amount of carbonate (~ 0.1 at%). Additionally, a small amount of nitrogen was identified as impurity which may be caused by nitrogen purging during the deposition process.
The spectra of the SiO_2 layer are displayed in Figure 7.3.2b. The Si 2p peak from Si^{4+} species is located at a binding energy of 103.3 eV, which coincides with the binding energy difference (O 1s - Si 2p) of $\Delta x_c = 429.4$ eV of a native SiO_2-film on a Si-wafer [185]. Furthermore, the corresponding FWHM ratio is in agreement with the results of Himpsel et al. [185]. XPS of SiO_2 was performed under normal beam incidence leading to X-rays penetrating deeper into the sample and yielding a signal from the polycarbonate membrane beneath the SiO_2 layer. For the 5 nm thick coating, O 1s and C 1s peaks are therefore ascribed to contributions from the polymer template. Since there are no indications for chemical bonds between the polycarbonate substrate and the SiO_2 layer, Sobel et al. [99] assume a sub-surface cluster growth, which is described by Wilson et al. [186].
In Figure 7.3.2c the spectra of Al_2O_3 consist of an Al 2p peak at 74.1 eV, which results in a binding

energy difference of $\Delta x_c \sim 457\,eV$ and thus is in agreement with literature [187]. The FWHM ratio of the fitted peaks was set constant for the analysis of Al_2O_3. Carbon was detected as only impurity. Its amount decreased for the thicker layer ($\sim 10\,at\%$ ubiquitous at 284.5 eV binding energy and $\sim 1\,at\%$ carbonate at $\sim 288.5\,eV$).

In total, XPS confirmed very pure coatings of TiO_2, SiO_2, and Al_2O_3 on the polymer templates. The absence of a polycarbonate signal within the ALD layers evidences a homogeneous high-quality coating. Quantitative information about the surface composition is displayed in Table 7.3.1 for a pristine polycarbonate membrane as well as nominal 5 and 10 nm thick TiO_2, SiO_2, and Al_2O_3 layers. Since XPS enabled the calculation of the ratio between the respective O 1s to Ti $2p_{3/2}$, Si 2p, and Al 2p peaks, we can conclude that almost stoichiometric bulk compositions are obtained for thicker ALD-films.

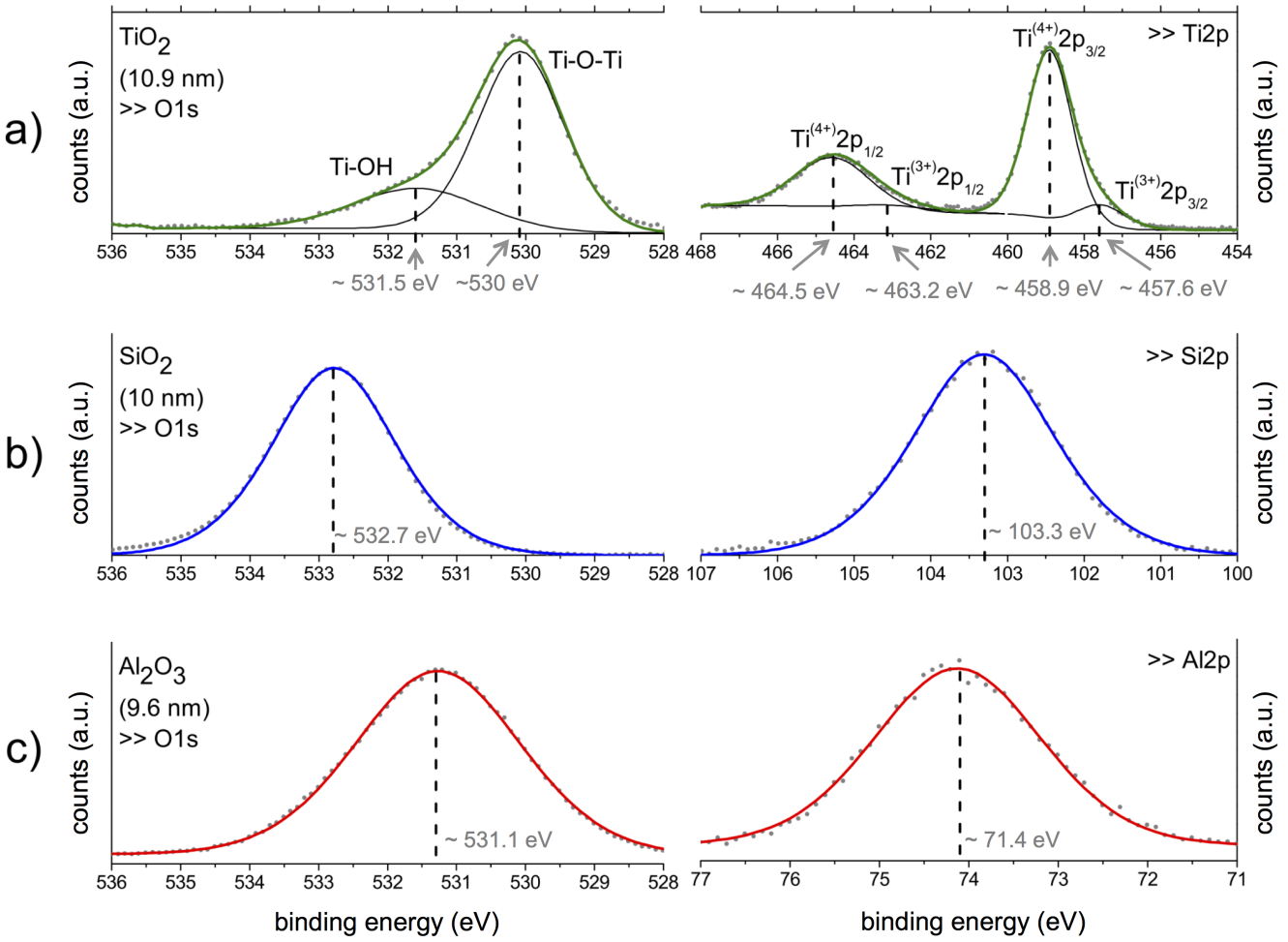

Figure 7.3.2.: Detailed XPS spectra of TiO_2 (a), SiO_2 (b), and Al_2O_3 (c) layers with a nominal thickness of 10 nm recorded at the ALD-coated membrane surfaces. Vertical dashed lines indicate the corresponding binding energies.

Table 7.3.1.: Surface composition (in at%) of pristine polycarbonate as well as nominal 5 and 10 nm thick TiO_2, SiO_2, and Al_2O_3 ALD layers obtained by XPS. [M] denotes the respective element Ti, Si, or Al.
[a]Including ubiquitous carbon and carbonate species.
[b]Including Ti^{4+} and Ti^{3+} species.
[c]Values taken from Sobel et al [99].

Material	Thickness [nm]	C 1s[a]	O 1s	Ti $2p_{3/2}$[b]	Ti-OH	Si 2p	Al 2p	Ratio O/[M]
Polycarbonate	-	83[c]	17[c]	-	-	-	-	-
TiO_2	5.4	19	49	20	12	-	-	2.45
TiO_2	10.9	21	45	20	14	-	-	2.25
SiO_2	5.3	22[c]	56[c]	-	-	22[c]	-	2.45
SiO_2	10.0	12[c]	60[c]	-	-	28[c]	-	2.14
Al_2O_3	4.8	13	58	-	-	-	30	1.93
Al_2O_3	9.6	10	59	-	-	-	32	1.84

7.4 Mechanical Stability

During SEM analysis of nanotubes released from the polymer template, many SiO_2 tubes were bent independent from the inner and outer diameter as representatively shown in Figure 7.4.1a and b (marked by orange arrows) for an outer diameter of ∼50 nm, and ∼10 and ∼15 nm thick walls, respectively. Many of the nanotubes have a length of ∼30 µm, which coincides with the thickness of the template used (a). Even on the lacey carbon film of the TEM-grid long undamaged sections of the SiO_2 nanotubes are found (inset of b). In contrast, TiO_2- and Al_2O_3- nanotubes of the same diameter and wall thickness are noticeably shorter and always straight (c, TiO_2 and d, Al_2O_3). Obviously, TiO_2 and Al_2O_3 nanotubes are more brittle and break readily, whereas SiO_2 tubes remain complete due to their high flexibility. This is an interesting result, since the fracture toughness of bulk [188] and thin film SiO_2 [189] is about four times less compared to the one of TiO_2 [190] and Al_2O_3 [191].

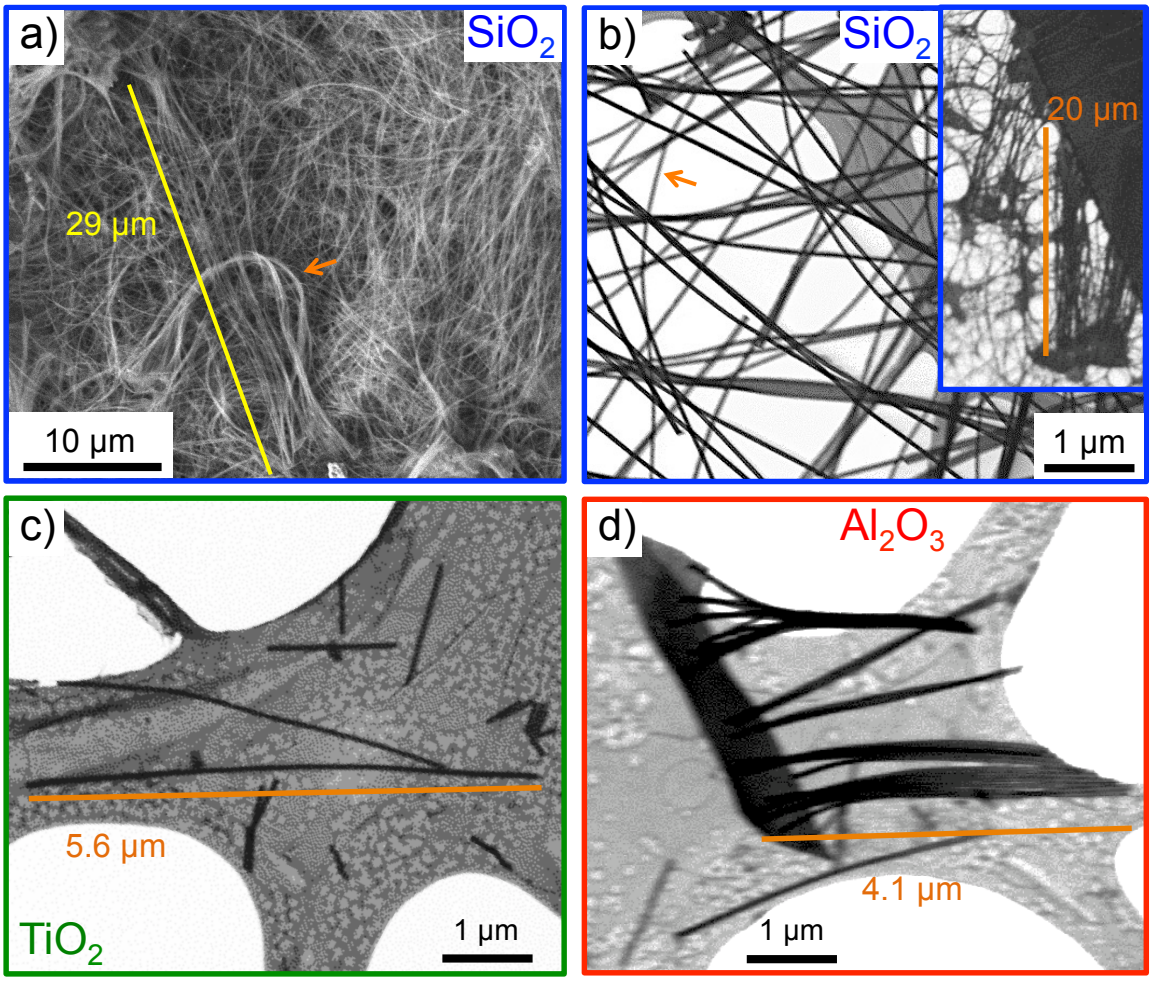

Figure 7.4.1.: Mechanical stability of cylindrical nanotubes. SiO_2 tubes with a wall thickness of ∼10 nm (a) and ∼15 nm (b) are highly flexible (examples are marked by orange arrows). SiO_2 nanotubes of full length (∼ 30 µ) are found regularly (a and inset of b). In contrast, TiO_2 (c) and Al_2O_3 (d) tubes with a wall thickness of ∼15 nm are much more brittle and easily break evidenced by the many short tube sections.

7.5 Geometry of Tube Walls in STEM-in-SEM Images

To determine the wall thickness of the nanotubes in STEM-in-SEM images, two different methods were tested. One was the measurement of the outer (D_o) and inner diameter (D_i) applying a measuring tool integrated in the SEM software directly at the as recorded image and subsequent calculation of the wall thickness (T) according to:

$$T = \frac{D_o - D_i}{2} \tag{7.1}$$

D_o and D_i were determined for 10 to 15 nanotubes of each sample at various positions of each tube in order to determine a mean value and the corresponding standard deviation for each sample.
The second method was based on the fundamental question, which geometrical information can be obtained during the imaging process with the SEM operated in transmission mode. A three dimensional structure is visualized in a two dimensional image according to the amount of material, that the elec-

tron beam passes, which is shown schematically in Figure 7.5.1a. Thus, parts with more material (i.e. thicker) appear darker. To quantify the material thickness $t(x)$ at each point of the nanotube, a coordinate system was introduced with the point of origin located in the center of the tube as displayed in Figure 7.5.1b. Since the cylindrical nanotubes are rotationally symmetric, only the first quadrant was taken into account for the first step of the geometric description of the passed material thickness. To calculate the value of the outer diameter with respect to the coordinate system (d_o) at each position x of the first quadrant, a cosine with a period of 4 times the outer radius R_o and an amplitude of R_o was applied via:

$$d_o(x) = R_o \cos\left(\frac{2\pi}{4R_o}x\right) \tag{7.2}$$

where $0 \leq x \leq R_o$. The inner diameter in the first quadrant (d_i) was described alike by:

$$d_i(x) = R_i \cos\left(\frac{2\pi}{4R_i}x\right) \tag{7.3}$$

with the inner radius R_i and $0 \leq x \leq R_i$. To calculate the material thickness in the first quadrant, d_i has to be subtracted from d_o on condition that $d_i = 0$ for $R_i < x \leq R_o$.
For the calculation of the material thickness passed in total, the first and fourth quadrant have to be taken into account. Due to the rotational symmetry of the tubes, the material thickness determined for the first quadrant was doubled. Thus, the material thickness was calculated in total via:

$$t(x) = 2 \times \left(R_o \cos\left(\frac{2\pi}{4R_o}x\right) - R_i \cos\left(\frac{2\pi}{4R_i}x\right)\right) \tag{7.4}$$

on the condition that $0 \leq x \leq R_o$ as well as $d_i = 0$ for $R_i < x \leq R_o$. In addition, the resulting graphs were mirrored at the y-axis to present the material thickness of an entire nanotube in the graphs.

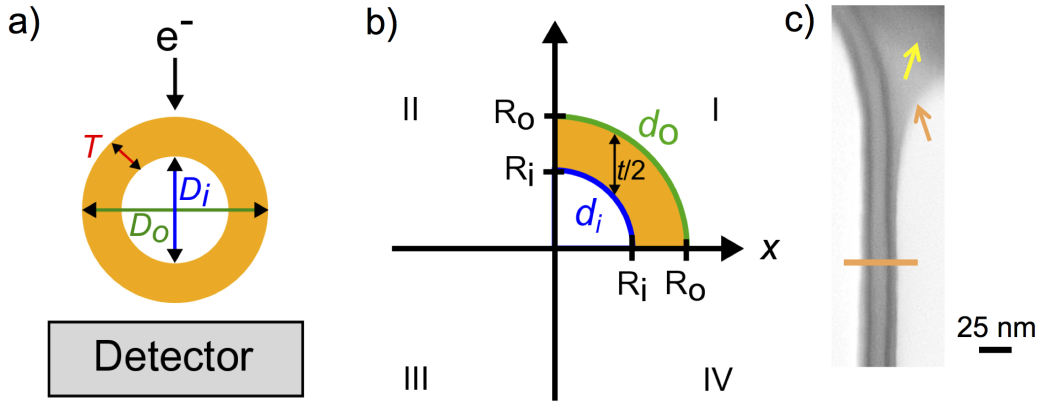

Figure 7.5.1.: Material thickness passed by the electron beam in STEM-in-SEM. (a) Scheme of the experimental setup in STEM-in-SEM. (b) Introduction of a coordinate system to calculate the passed material thickness. (c) Representative STEM-in-SEM image including marks for a linescan (orange line), polymer residues (orange arrow), and the carbon film of the TEM-grid (yellow arrow).

The material thickness distribution of a nanotube, which is passed by the electron beam, was calculated for the sample series exhibiting various initial diameters (Figure 7.5.2a, Section 7.1) and different coating thicknesses (Figure 7.5.2b, Section 7.2) taking the initial diameter deduced from the SAXS data as starting point. In both cases, the material thickness exhibits a maximum at the position $x = R_i$ and a minimum (being twice the coating thickness) at the center of the tube ($x = 0$). Furthermore, there are no contributions from d_i at $R_i < x \leq R_o$ resulting in graphs exhibiting the same slope for various initial diameter and graphs laying on top of each other for different layer thicknesses in that regime. In the regime, where d_i contributes, the graphs show different behavior for all samples. Comparing the behavior of these graphs in the regime, where d_i contributes, reveals a steeper slope for smaller initial diameters indicating a better contrast in the STEM-in-SEM images of such tubes and thus a more accurate determination of the inner tube diameter. For various initial diameters and an ALD layer thickness of 5 nm, i.e. an inner diameter constantly 5 nm smaller than the initial one, the difference between the maximum and the minimum material thickness is varying by ~2 nm. This value differs more (~5 nm) for various coating thicknesses. In this case, as expected the maximum material thickness is located nearer to the center of the tube the thicker the coating layer is.

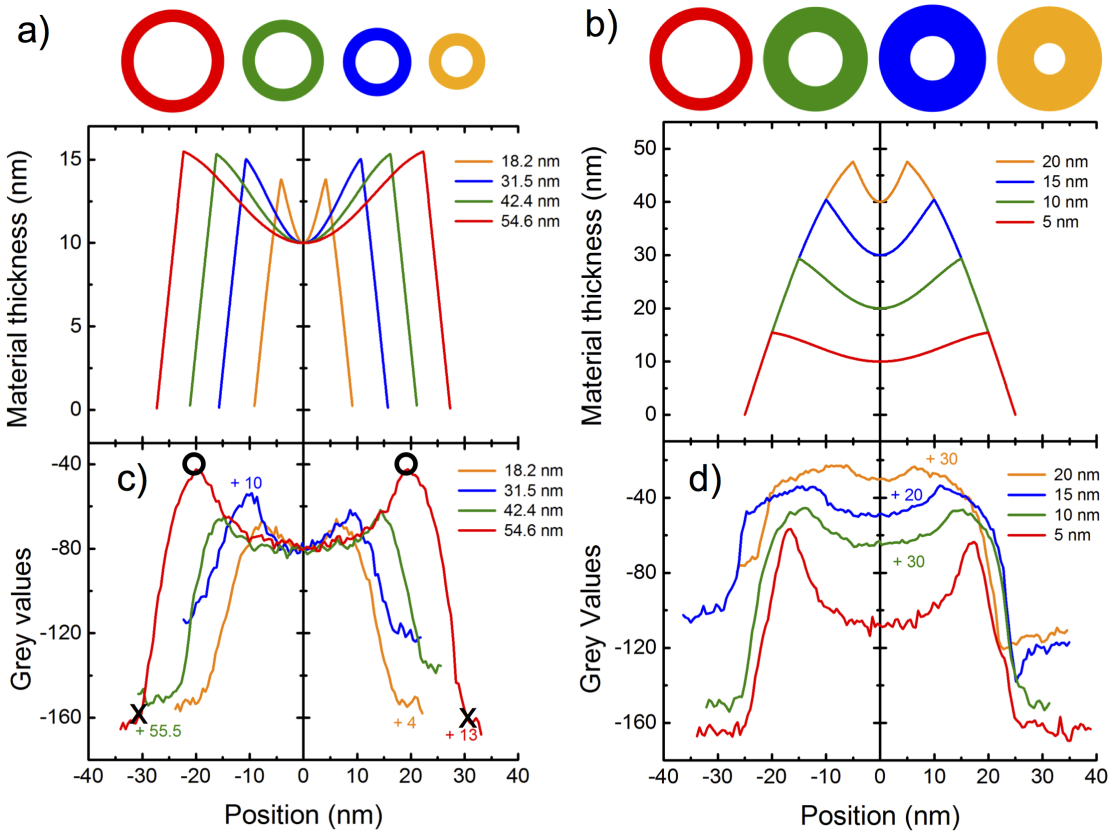

Figure 7.5.2.: Comparison of calculated and experimental data concerning the material thickness passed by the electron beam in STEM-in-SEM. Calculated material thickness for various initial diameter and a nominal coating of 5 nm (a) as well as an initial diameter of 50 nm and different layer thicknesses (b). (c) and (d) show the respective grey values deduced from linescans taken across single nanotubes in STEM-in-SEM images. The centers of the linescans were shifted to a grey value of -80 for the different initial diameters and to various grey values for the various coating thicknesses.

To compare these calculated results with STEM-in-SEM images, linescans across single nanotubes were taken from as recorded images of the SiO_2 samples (e.g. orange line in 7.5.1c). The intensities of the absorption observed in STEM-in-SEM images is shown as grey values in Figure 7.5.2c and d for different initial diameters and various coating thicknesses, respectively. Since the linescans of a given tube at different positions and of different tubes of a given sample were alike, one representative linescan is displayed for each sample. To facilitate the comparison between calculated data and recorded linescans, the center of the linescans were shifted to a grey value of -80 for the different initial diameters and to various grey values for the various coating thicknesses. The general features such as position of the maximum and minimum material thickness as well as the shape of the experimental graphs is similar to the calculated ones in both cases. Differences in grey values could not be transformed to differences in material thickness due to different contrast and brightness settings of the SEM to image each sample best. Nevertheless, initial and inner diameter were deduced from the linescans as exemplary marked in Figure 7.5.2c to calculate the wall thickness. The initial diameter was measured at the positions were the material thickness starts to increase (black crosses). The distance between the positions of maximum material thickness was taken as inner diameter (black circles), since the calculations showed that the maxima are found where $x = \mathrm{R_i}$. The values for initial (D_o) and inner diameter (D_i) as well as wall thickness (T) calculated, measured directly at the STEM-in-SEM images (according to equation 7.1), and deduced from the linescans are given in Table 7.5.1. For both series, the values obtained from the as recorded STEM-in-SEM images are in agreement with the ones calculated by considering the imaging process of the geometric dimensions of a tube. Since the SAXS-data shown in Section 7.1 and 7.2 coincide with the STEM-in-SEM data, they are in agreement with the calculated values, too. However, the analysis of the linescans lead only for the different layer thicknesses to coincident wall thicknesses. In the case of various initial diameter, the wall thicknesses deduced from the linescans are too big due to the determination of too large initial diameters. The STEM-in-SEM images reveal more polycarbonate residues attached to the outer surface of the tubes the smaller the tubes initial diameter is as marked by an orange arrow representatively in Figure 7.5.1c. This polymer layer can be identified by eye when measuring the initial diameter at the as recorded STEM-in-SEM image, whereas it does not appear in the linescans. Since further cleaning steps, i.e. rinsing with DCM, did not lead to less polymer residues attached to the outer surface, a precise determination of the initial diameter and thus the layer thickness applying linescans is not possible for samples exhibiting outer diameters less than ~50 nm. Therefore, the morphology of all samples was characterized directly at the as recorded STEM-in-SEM images according to the method described first at the beginning of this section. Furthermore, the analysis of the imaging process confirms the suitability of this method to determine the deposited layer thickness, which is additionally in agreement with the results obtained by SAXS. Moreover, the tubular shape of the synthesized nanostructures is impressively confirmed by the alike shapes of experimental and calculated graphs.

Table 7.5.1.: Comparison of three different methods to obtain the deposited wall thickness: (1) Calculation according to equation 7.4 with the initial diameter deduced from the SAXS data as starting point. (2) By a measuring tool included in the SEM software directly at the STEM-in-SEM (STEM) images applying equation 7.1. (3) Taking a linescan of the grey values in an STEM-in-SEM image followed by measuring the distances between the starts of the increase of the graph (black crosses in Figure 7.5.2c) and maxima (black circles in Figure 7.5.2c) to obtain initial and inner diameter, respectively.

Various initial diameter

Initial diameter D_o (nm)			Inner diameter D_i (nm)			Wall thickness T (nm)		
SAXS (calc.)	STEM	Linescan	calc.	STEM	Linescan	calc.	STEM	Linescan
18.2	18 ± 2	36 ± 3	8.2	9 ± 2	11 ± 2	5	4 ± 1	13 ± 2
31.4	25 ± 2	39 ± 4	21.4	17 ± 2	15 ± 3	5	5 ± 1	12 ± 3
42.2	36 ± 3	45 ± 2	32.2	27 ± 2	29 ± 4	5	5 ± 2	8 ± 2
54.6	56 ± 3	58 ± 2	44.6	45 ± 3	40 ± 3	5	5 ± 2	9 ± 2

Various wall thicknesses

Initial diameter D_o (nm)			Inner diameter D_i (nm)			Wall thickness T (nm)		
SAXS (calc.)	STEM	Linescan	calc.	STEM	Linescan	calc.	STEM	Linescan
50.0	50 ± 5	50 ± 2	40.0	31 ± 4	35 ± 3	5	9 ± 3	8 ± 2
48.4	46 ± 4	53 ± 3	28.4	23 ± 2	28 ± 4	10	12 ± 2	13 ± 3
49.2	48 ± 3	55 ± 5	19.2	16 ± 3	23 ± 4	15	16 ± 2	16 ± 3
48.1	44 ± 4	46 ± 3	8.1	11 ± 1	12 ± 4	20	17 ± 2	17 ± 3

8 Conical Nanotubes

The optimized parameters for the TiO_2, SiO_2, and Al_2O_3 ALD processes obtained during the synthesis of cylindrical nanotubes were subsequently applied for the fabrication of nanostructures with other geometries. This chapter presents the synthesis and characterization of ALD-coated conical nanochannels. Similar to the cylindrical nanostructures, we studied the deposited layer thickness as function of number of ALD cycles (Section 8.1) and the composition of the walls (Section 8.2). The fabrication of free-standing tubular nanocones forming arrays and their mechanical stability are discussed in Section 8.3 and Section 8.4, respectively. Furthermore, the coating of single-channel membranes was investigated by the synthesis of single free-standing conical nanotubes (Section 8.5). This enabled us to compare the morphology of single tubular nanocones and nanocone arrays (Section 8.6).
To avoid overlapping of nanochannels caused by large base diameters in the μm range, membranes with a fluence of $\sim 10^6 \frac{\text{ions}}{\text{cm}^2}$ were applied for conical etched ion-tracks. TiO_2 and Al_2O_3 coatings were performed using the ALD equipment of GSI. SiO_2 layers were deposited in the group of Prof. Dr. C. Hess at TU Darmstadt.

8.1 ALD Coating as Function of Number of ALD Cycles

To investigate the ALD processes in the case of conical nanochannels, series of etched ion-track membranes with conical channels were coated with nominal ∼10 nm, ∼15 nm, and ∼20 nm thick ALD-layers. Figure 8.1.1 presents STEM-in-SEM images of released TiO_2, SiO_2, and Al_2O_3 conical nanotubes after nominal ∼15 nm coating. For all three oxides, the representative nanocones demonstrate a shape conform ALD process along the entire ∼30 μm length of the etched ion-tracks. In particular, the nanotubes reveal a precise conical shape with smooth outer and inner surface. The smooth outer surface replicates the smooth inner surface of etched ion-track nanochannels in polycarbonate in contrast to the rougher surface of Al_2O_3-coated nanochannels in PET described in [43]. As for cylindrical channels, the smooth inner surfaces of the nanotubes evidence conformal and homogeneous ALD processes. These deposition characteristics are confirmed by the high magnification images in (Figure 8.1.1b), which reveal a constant wall thickness of ∼16 nm along the complete SiO_2 nanocone in agreement with the nominal deposited thickness.

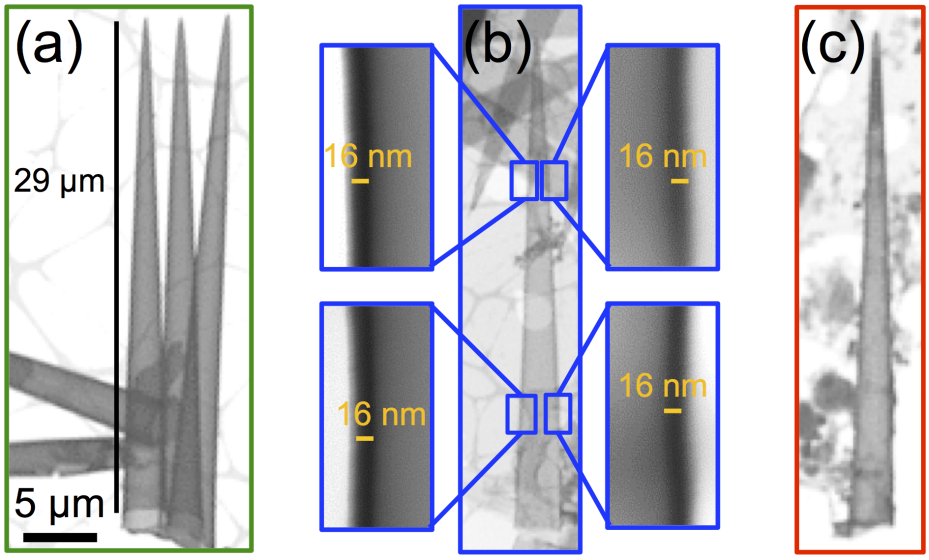

Figure 8.1.1.: STEM-in-SEM images of ∼ 30-µm long conical TiO_2 (a), SiO_2 (b), and Al_2O_3 (c) nanotubes exhibiting ∼15 nm thick walls. The scalebar shown in (a) is valid for (a-c). High magnification images marked in (b) evidence a homogeneous wall thickness along the entire length of the nanotube.

To analyze the layer growth quantitatively, the wall thickness was measured directly in the SEM images at various positions along ∼10 nanotubes per sample and the obtained mean values are given in Table 8.1.1. Additionally, the graphs presented in Figure 8.1.2 contain the resulting data demonstrating linear dependencies of the deposited thickness on the number of ALD cycles for the three oxides. Linear fits to the data lead to growth rates of ∼0.008 nm/cycle for TiO_2, ∼0.22 nm/cycle for SiO_2, and ∼0.09 nm/cycle for Al_2O_3. Thus, the growth rate of TiO_2 in the conical nanochannels coincides well with coatings of reference Si-wafers (Section 3.1) and reference membranes for single channel investigations (Section 11.2.1). Compared to layers deposited at Universität Hamburg including the ones in cylindrical channels discussed in Section 7.2, the growth rate is a factor of 3 lower possibly due to the applied process temperature at GSI between 100 and 150 °C, where an insufficient reactivity of the water vapor with the adsorbed titanium precursor hinders the film growth [129]. For SiO_2, the growth rate in the conical nanochannels is in good agreement with depositions performed on Si-wafers (Section 3.2) and coincides with coatings of cylindrical nanochannels (Section 7.2) evidencing conformal layer-by-layer growth independent from the template geometry. The Al_2O_3 coating in conical nanochannels exhibits a growth rate, which is in agreement with depositions performed on Si-wafers at GSI and Universität Hamburg (Section 3.3) and coatings of cylindrical nanochannels at GSI (Section 7.2).
In total, the conformal coating of high aspect ratio nanochannels independent from the channel geometry by layer-by-layer growth emphasizes the advantages of ALD compared to other surface modification techniques in nanochannels (electroless, chemical), which result in irregular or rough inner walls.

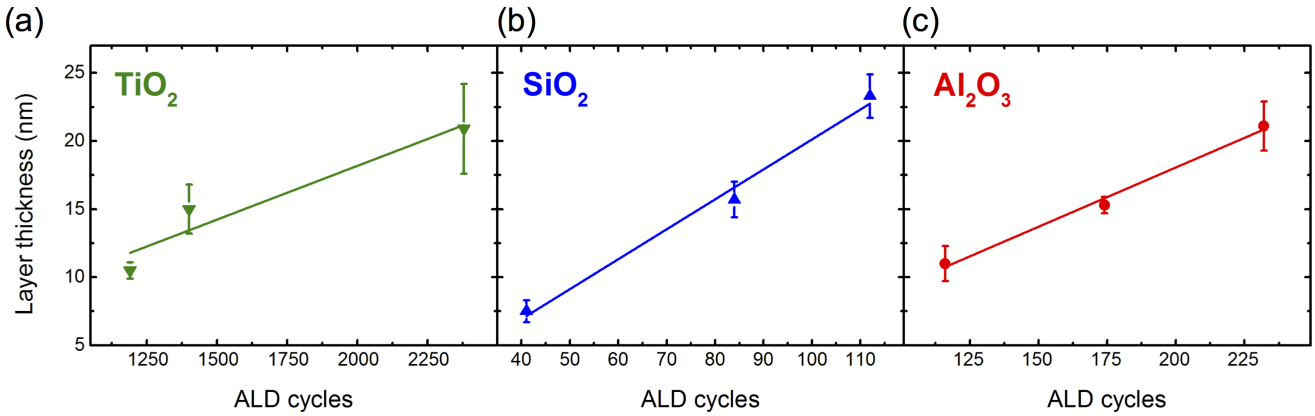

Figure 8.1.2.: Wall thickness of conical nanotubes as a function of number of ALD cycles. For all three ALD processes, the mean value of the deposited layer thickness depends linearly on the number of ALD cycles inside the conical nanochannels. Error bars represent the standard deviation obtained for three different positions of ∼10 nanotubes.

Table 8.1.1.: ALD layer thickness of conical nanotubes for various number of ALD cycles corresponding to different nominal coating thicknesses.
[a] During the deposition of 10 nm SiO_2, the pyridine reservoir was empty at a nominal coating thickness of 7 nm and thus the ALD process had to be stopped.

Nominal coating (nm)	**Layer thickness** (nm)		
	TiO_2	SiO_2	Al_2O_3
10	11 ± 1	$(7 \pm 1)^a$	11 ± 2
15	15 ± 2	16 ± 2	15 ± 1
20	21 ± 3	23 ± 2	21 ± 2

8.2 Composition of the Wall of Conical Nanotubes

To ensure a well defined surface tailoring of the conical nanochannels, the chemical composition of the tubular nanocones was investigated by using EDX. To obtain significant count rates, conical nanotubes with ∼20 nm thick walls were transferred onto TEM-grids. For TiO_2 (green), SiO_2 (blue), and Al_2O_3 (red) nanocones the recorded multipoint spectra displayed in Figure 8.2.1a contain the respective peaks of titanium, silicon, and aluminum as well as oxygen. Copper and carbon peaks were ascribed to contributions from the Cu-lacey TEM-grid leading to various heights of these signals depending on the position of the nanocones relative to the supporting structures of the sample holder. The absence of contamination in the nanocones evidences the deposition of pure TiO_2, SiO_2, and Al_2O_3 layers inside the conical polycarbonate nanochannels by ALD. Figure 8.2.1b shows the aluminum and oxygen signal of an EDX linescan recorded across a representative Al_2O_3 nanocone marked as orange line in the STEM-in-SEM image presented in the inset. Higher amounts of counts at the position of the tube walls and nearly constant numbers of counts between the walls are a further proof of the tubular shape of the nanocones.

To quantify the precise thickness of the walls, the resolution of the applied EDX was not sufficient.

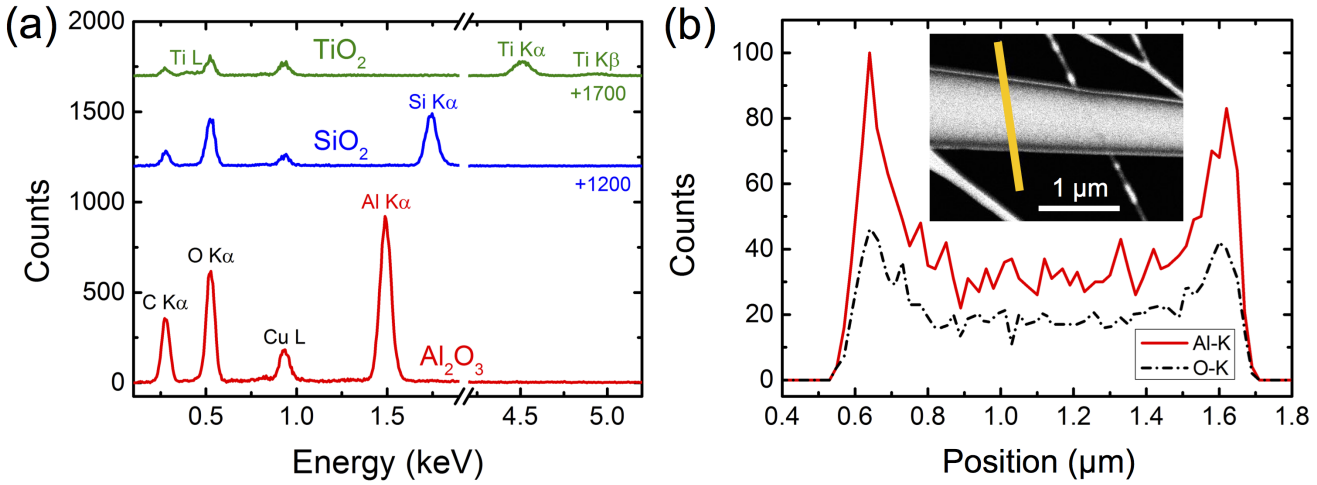

Figure 8.2.1.: (a) Multipoint EDX spectra of TiO_2 (green), SiO_2 (blue), and Al_2O_3 (red) tubular nanocones exhibiting ~20 nm thick walls. Copper and carbon peaks are attributed to contributions of the applied Cu-lacey TEM-grid. (b) EDX linescan recorded across an Al_2O_3 nanocone. The inset shows the corresponding STEM-in-SEM image (dark field) with the position of the linescan marked in orange. Aluminum and oxygen signal represent the tubular shape of the cone.

8.3 Free-Standing Conical Nanotubes

To investigate the homogeneity of the ALD process over the whole sample area, the ALD-coated multichannel membranes were mechanically stabilized by fixing them onto a metallic layer on one side of the membrane and subsequent dissolution of the polymeric templates (Section 5.3). Figure 8.3.1 depicts representative SEM images recorded under an angle of 20° for samples ALD-coated with ~20 nm TiO_2 (a), Al_2O_3 (b), and SiO_2 (c). The wall thickness was determined at tubes released from reference samples, which were coated simultaneously and analyzed by STEM-in-SEM. For all three materials, an array of free-standing nanocones is observed over the whole sample area. The higher magnification images shown in Figure 8.3.1d,e,f further prove the shape conform ALD process inside the conical nanochannels and enable the determination of the base diameter at the very end of the nanocone as representatively marked in d. For all analyzed nanocones, the Au and Cu ring formed at the base by the Au sputtercoating and Cu electrodeposition during sample preparation is visible (indicated with an orange circle in Figure 8.3.1e) validating the tubular shape of the nanocones. In addition, nearly no Au and Cu rings without surrounding tubular nanocone were observed demonstrating the ALD-coating of all nanochannels and the high mechanical stability of the nanotubes.
For all three oxides, arrays of ~30-μm high free-standing conical nanotubes were successfully synthesized homogeneously in areas of a few cm^2.

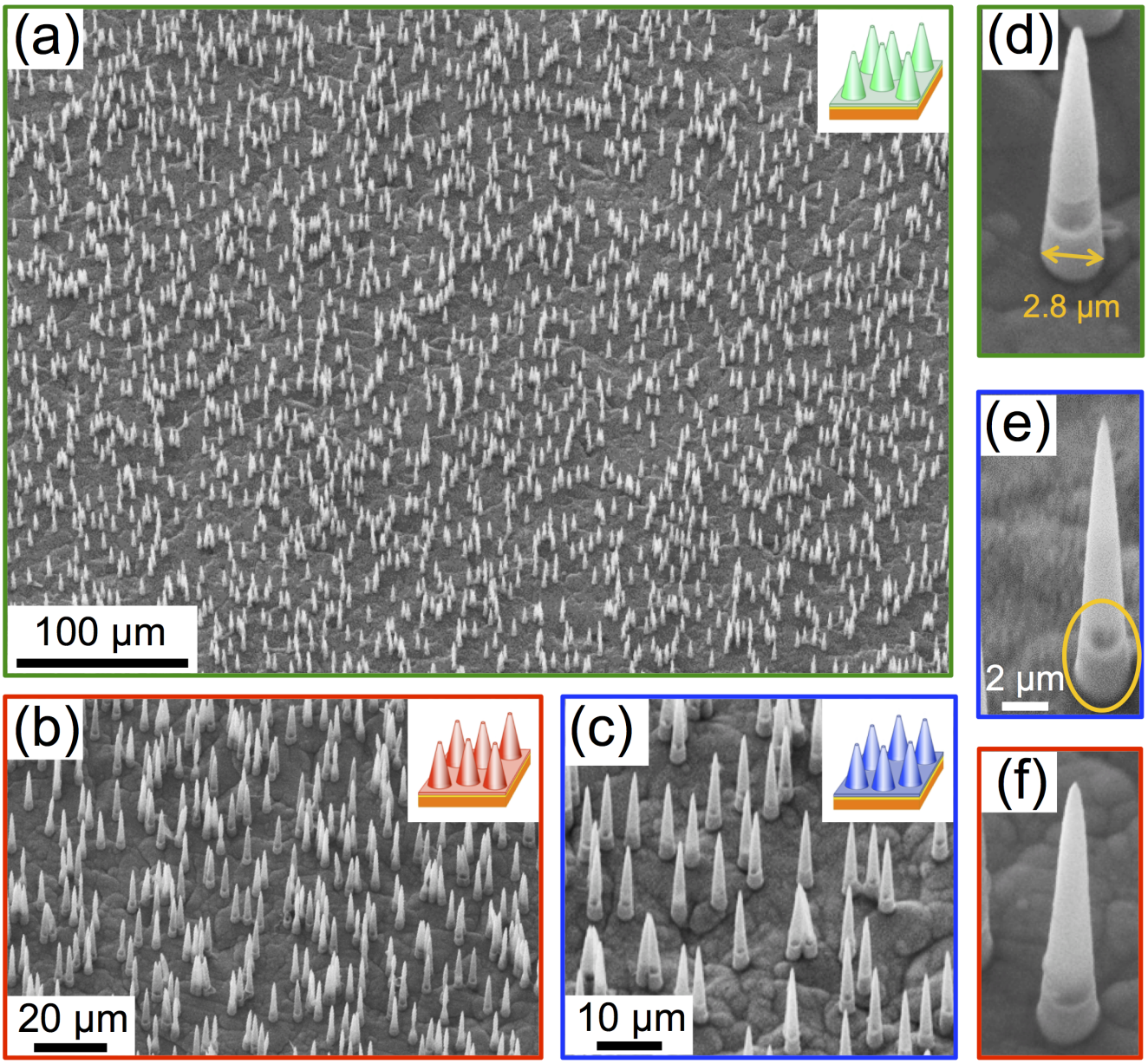

Figure 8.3.1.: SEM images of arrays of free-standing TiO_2 (a,d), Al_2O_3 (b,f), and SiO_2 (c,e) nanocones with ∼20 nm thick walls recorded under an angle of 20°. (d,e,f) At high magnification, sputtered Au and electrodeposited Cu are visible inside the tubular nanocones (marked with an orange circle in e). The corresponding scale bar is shown in e.

8.4 Mechanical Stability of Free-Standing Conical Nanotubes

The successful preparation and visualization of free-standing conical nanotube arrays enabled the investigation of the mechanical stability of the cones depending on wall material and thickness. Figure 8.4.1 shows representative SEM images of TiO_2 (a-c), SiO_2 (d-f), and Al_2O_3 (g-i) free-standing nanocones exhibiting wall thicknesses of ∼20 nm (1st column), ∼15 nm (2nd column), and ∼10 nm (3rd column) thickness. SEM imaging was performed under an angle of 20°, whereas STEM-in-SEM was applied to determine the wall thicknesses by analyzing tubes released from reference samples, which were coated simultaneously. After the whole preparation process all free-standing nanocones with ∼20 nm thick walls are stable (a,d,g). Figure 8.4.1b,e,h reveal that many SiO_2 and some Al_2O_3 nanocones consisting of thinner walls, namely ∼15 nm, are damaged. In the case of ∼10 nm thick walls, the low mechanical instability is even more pronounced for Al_2O_3 (c,f,i). Due to emptying the pyridine reservoir during the deposition of 10 nm SiO_2, the ALD process had to be stopped after deposition of ∼7 nm. The resulting tubular nanocones are all damaged (f). These observations indicate that thicker walls increase the mechanical stability of the conical nanotubes. The fact that nearly no TiO_2 cones are damaged for all studied wall thicknesses (a-c) is remarkable. Even in the case of ∼10 nm wall thickness (c) and a smaller opening angle of the cones (narrower shape), almost all cones are free-standing. Thus, the TiO_2 tubular nanocones exhibit clearly the highest mechanical stability, whereas the Al_2O_3 nanocones are more fragile, and the SiO_2 ones are the least stable. During sample preparation the damage of the nanocones can be caused by mechanical forces during the dissolution of the polycarbonate template in solution, sample transport, or sputtering. Considering the fracture toughness values for bulk TiO_2 (∼3.2 MPa·$m^{1/2}$ [190]) and Al_2O_3 (∼5 MPa·$m^{1/2}$ [191]) as well as thin film (∼0.77 MPa·$m^{1/2}$ [189]) and bulk SiO_2 (∼0.79 MPa·$m^{1/2}$ [188]), the highest instability is expected for SiO_2 tubes, which is in agreement with the obtained results. The low stability of the Al_2O_3 nanocones compared to TiO_2 ones can be attributed to the electrical insulating properties of Al_2O_3. Low conductivity led to electrical charging under the electron beam of the SEM, which was observed in-situ as bending and finally collapsing Al_2O_3 and SiO_2 nanocones during imaging.

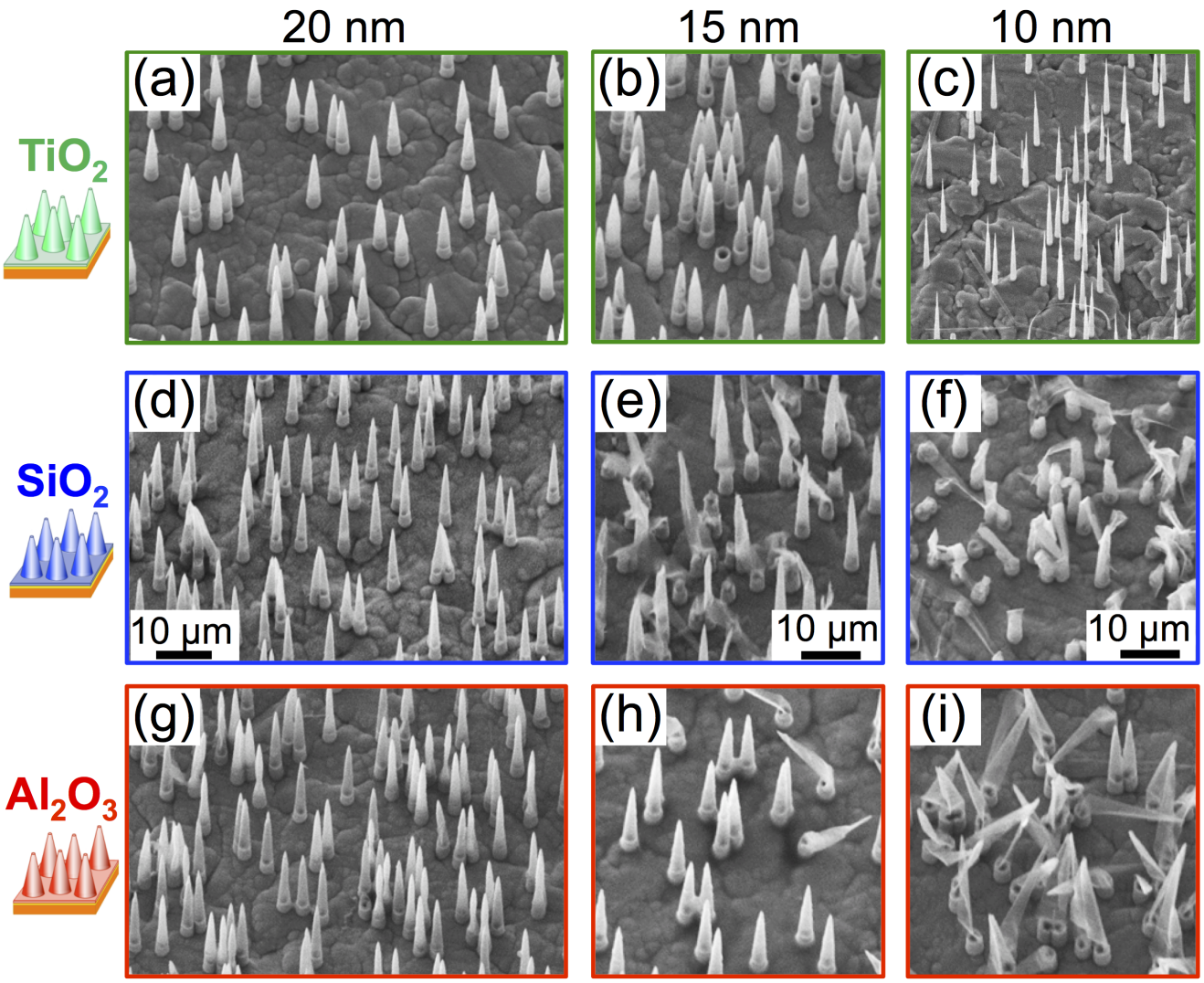

Figure 8.4.1.: SEM images of free-standing TiO_2 (a-c), SiO_2 (d-f), and Al_2O_3 (g-i) nanocones with ∼20 nm (1st column), ∼15 nm (2nd column), and ∼10 nm (3rd column) thick walls. (c) The TiO_2 cones with ∼10 nm thick walls exhibit a smaller opening angle. (f) During the deposition of 10 nm SiO_2, the pyridine reservoir was empty at a nominal coating thickness of 7 nm and thus the ALD process had to be stopped. For all images, the scale bars are identical.

8.5 Single Free-Standing Conical Nanotubes

The high mechanical stability of free-standing TiO_2 and Al_2O_3 (thick walls) conical nanotubes fabricated as array enabled the advanced synthesis of single free-standing conical nanotubes. For the fabrication of single conical nanochannels, polycarbonate foils irradiated with one single heavy ion per foil were etched applying exactly the same process as for the multichannel membranes (Sections 2.2.2 and 6.5). In addition, a multichannel membrane was etched directly afterwards under identical conditions to be used later as reference for the wall thickness and the tube length. The surface modification by ALD was performed simultaneously for single and multichannel reference membranes. Figure 8.5.1a presents a SEM image of a single free-standing tubular nanocone with ∼10 nm thick TiO_2 wall recorded under an angle of 20°, which remained intact during the whole preparation process including mechanical stabi-

lization of the coated template, dissolution of the polymer in solution, Au sputtering to reduce charging effects during SEM analysis, the imaging process itself as well as all sample transportation processes. In addition, the high magnification image displayed in (b) reveals the same features of the single tubular nanocone as obtained for the arrays: a conical shape exhibiting a smooth outer surface as well as a tubular structure, which is indicated by sputtered Au and electrodeposited Cu being visible inside the cone at a certain distance from the base. Figure 8.5.1c presents the same characteristics for a single Al_2O_3 cone with a wall thickness of ∼15 nm.
Although ∼30 % of alike prepared single nanocones were observed broken or have not been found on the metallic stabilization layer, the robustness of the single tubular nanocones is impressive.

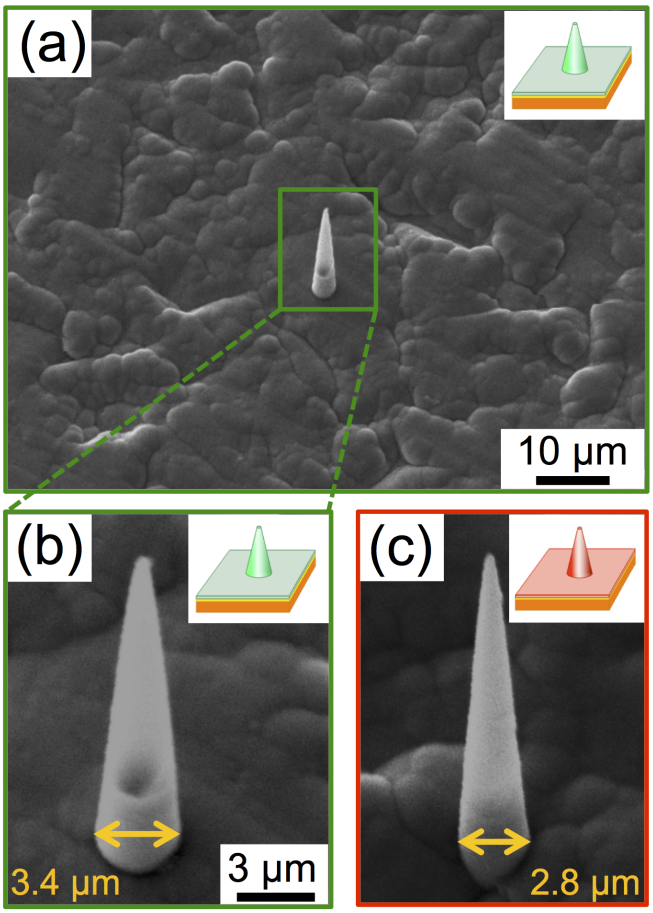

Figure 8.5.1.: SEM images of single free-standing TiO_2 (a,b) and Al_2O_3 (c) nanocones with a wall thickness of ∼10 nm and ∼15 nm, respectively.

8.6 Dimensions of Single (Free-Standing) Conical Nanotubes Compared to Arrays

Since each tubular nanocone is a replica of an etched ion-track nanochannel, the comparison of nanotubes grown in single and multichannel membranes under exactly the same conditions allows the investigation of the similarity of the respective etching processes. Thus, nanochannels were fabricated under identical etching conditions right after each other in two foils irradiated with only one ion per foil and $10^6 \frac{\text{ions}}{\text{cm}^2}$ (Section 6.5). The subsequent ALD process is performed simultaneously for both membranes. One half of the multichannel membrane was used to release the synthesized nanotubes onto a TEM-grid in order to determine the deposited wall thickness as well as the tube length by STEM-in-SEM as presented in Section 8.1. For a given channel length, the geometric dimensions of a conical nanochannel are defined by the diameter of tip and base. Therefore, these two diameters were estimated for single and multichannel membranes, i.e. single and arrays of tubular nanocones.

The base diameters were determined from SEM images of free-standing conical nanotubes recorded under an angle of 20° as presented in Section 8.3 and Section 8.5 for arrays and single cones, respectively. Measurements obtained under an angle of 0° resulted in exactly the same values. From STEM-in-SEM images, the base diameter could not be determined reliably, since most of the observed tubes broke displaced from the layer deposited on the membrane surface (Figure 8.1.1c) prohibiting the calculation of a mean value from a reasonable amount of tube measurements. This emphasized the need to prepare arrays of free-standing tubular nanocones in order to estimate the etched base diameter from a replica.

To determine the tip diameter before and after ALD, STEM-in-SEM images of nanocones released onto TEM-grids were applied in the case of multichannel membranes, whereas *I-V* measurements were performed in the case of single-channel membranes. The different procedures were required due to the following reasons.

(1) A high-magnification top-view of a free-standing nanocone was only imaged once in high-quality (Figure 8.6.1a). Additionally, inner and outer tip diameters can not be determined distinctively from this image due to perspective and contrast problems. These prohibit the analysis of the tip for free-standing nanocones in arrays or as single nanostructure.

(2) In contrast, STEM-in-SEM images of nanotubes released from multichannel membranes enabled the visualization of the tips and were thus utilized to determine the outer D_o and inner diameter D_i at the tip as exemplarily depicted in Figure 8.6.1b-e. The outer diameter corresponds to the diameter adjusted by the etching process, whereas the inner diameter is tailored by the number of ALD cycles. For the analyzed tips, $\frac{D_o - D_i}{2}$ resulted in the nominal coating thickness proving a layer-by-layer growth even at the tip of the nanochannels and thus confirming a conformal deposition by ALD along the entire ∼30 µm length of the etched ion-tracks in polycarbonate.

(3) In the case of single cones, the release onto TEM-grids would most probably cause the loss of the nanotube. Furthermore, the base diameter would be inappropriate to estimate in most cases due to askew breaking as discussed above.

(4) The tip diameter of a single conical nanochannel can be deduced from ionic conductance measurements performed before and ALD coating, if the base diameter is known (Section 6.5). Characterization before ALD provides the initial channel diameter, whereas analysis after coating reveals information

about the inner diameter of the surface-modified single-channel. After finishing all *I-V* measurements, the single cones were prepared as free-standing nanotubes to determine the base diameter required for the calculation of the tip diameter.

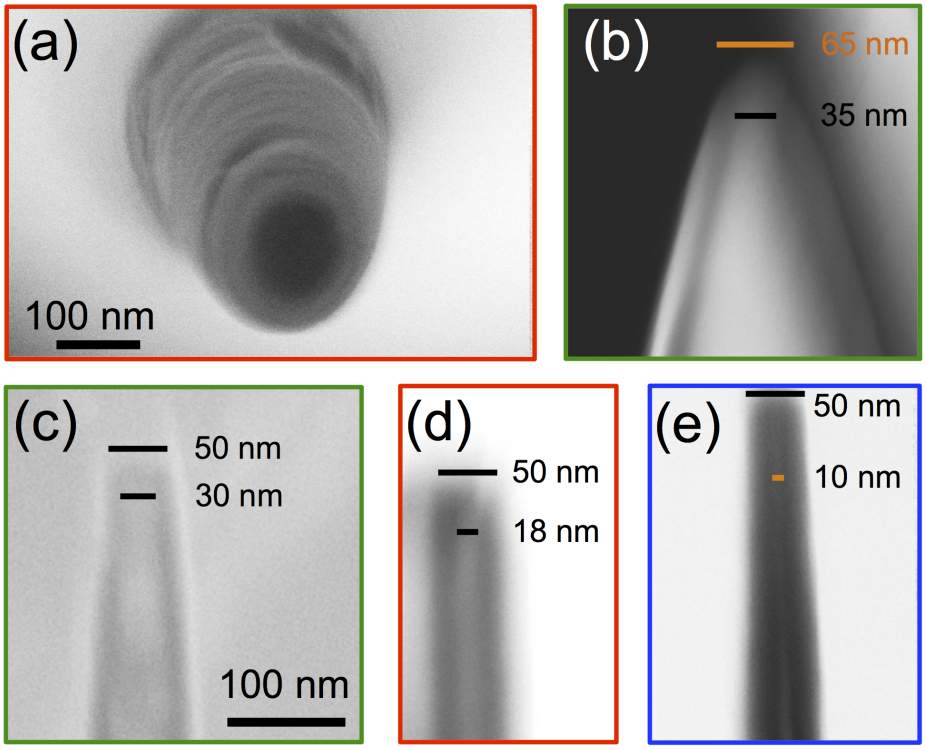

Figure 8.6.1.: Tips of conical nanotubes synthesized in multichannel membranes. (a) Top-view of a free-standing Al_2O_3 nanotube with a nominal wall thickness of ∼20 nm recorded by SEM under a tilting angle of 0°. (b-e) STEM-in-SEM images of tips of conical nanotubes. (b) TiO_2 nanocone with outer tip diameter of ∼65 nm and inner tip diameter of ∼35 nm due to ∼15 nm coating imaged in dark-field mode. (c-e) The ∼50 nm outer diameter of the TiO_2 (c), Al_2O_3 (d), and SiO_2 (e) nanocone tips are reduced by ALD coatings of nominal ∼10 nm, ∼15 nm, and ∼20 nm, respectively. The scalebar shown in (c) is valid for (b-e).

To compare the etching processes in single and multichannel membranes quantitatively, the radial etching rates (diameter/etching time) of base and tip were calculated for both cases and are given in Table 8.6.1. Since the breakthrough time measured for single channel membranes varies strongly (up to 30 s, as also reported by L. Burr [122]) and for the most applications of single conical nanochannels (e.g. sensors) the tip is the relevant geometric part, the etching time was defined as the time between the breakthrough and the end of the etching process. The obtained radial base etching rates of single channel and multichannel membranes coincide well, whereas the mean value of the radial etching rate for six single channels is by a factor of ∼2 higher than for multichannel membranes and fluctuates more. The latter might be caused by the inhomogeneity of material and thickness of the foil as well as less tubes taking into account for the calculation.

Since an accurate value for the tip diameter of the single channel can not be adopted from the STEM-in-SEM images of the conical nanotubes released from the multichannel membranes, it has to be deduced from the *I-V* measurements. According to equation 4.6, this requires the base diameter. In literature,

usually the base diameter is determined for a multichannel reference membrane that is etched simultaneously without applying a stabilization voltage. This differs from the procedure described in this thesis [14, 16, 80, 116, 171, 172]. However, the common procedure to apply the base diameter obtained from a multichannel reference membrane to calculate the tip diameter is confirmed by the comparison of free-standing tubular nanocones presented here. Additionally, the preparation of the single free-standing conical nanotube after the *I-V* measurements enabled the precise calculation of the tip diameter for the studied channel, since the base diameter was estimated at the analyzed channel itself. This is a big advantage for the analysis of single conical nanochannels, since small deviations of the base diameter result in significantly different tip diameters.

Table 8.6.1.: Radial etching rates of base and tip obtained from the corresponding diameters of conical single and multichannels in etched ion-track polycarbonate membranes.

Radial etching rate	Base (μm/min)	Tip (nm/min)
$10^6 \frac{\text{ions}}{\text{cm}^2}$	0.20 ± 0.07	5.6 ± 1.8
Single channel	0.22 ± 0.03	9.9 ± 4.4

9 Nanotube Networks

The conformal ALD-coating of nanochannels in polycarbonate membranes independent of the channel geometry opened up further variations of the template. Interconnected nanochannels synthesized in etched ion-track membranes provide the tailoring of all characteristics of such a structure: thickness of the structure, amount and diameter of the channels as well as angle of crossings. Shape-conform ALD coating of nanochannel networks increase the variability by further tailoring of the porosity and the specific surface area as well as the physical and chemical nature of the inner surfaces. Such structures are mechanically stable and of interest for the investigation of filtration and catalysis in well-defined porous structures as well as applications in e.g. photoelectrochemistry. Additionally, releasing the deposited structures from the polymer would result in nanotube networks that are highly tunable especially in terms of high surface-to-volume ratios compared to nanowire arrays and networks as well as nanotube arrays.

During the ALD process, interconnected nanochannels represent more complex diffusion paths for the precursor molecules compared to parallel nanochannels. Furthermore, the length of the channels is increased compared to parallel channels in a membrane of the same thickness.

As proof-of-concept, series of network templates were prepared by irradiating ∼30-µm thick polycarbonate foils under an incident angle of 45° from 4 directions with a fluence of $\sim 10^9 \frac{\text{ions}}{\text{cm}^2}$ each. After symmetric etching, 10, 15, and 20 nm thick TiO_2-, SiO_2-, and Al_2O_3-layers were ALD-deposited into the channels. Section 9.1 presents cross-sectional SEM-images of nanochannel networks. The free-standing networks of cylindrical nanotubes obtained after dissolution of the template are discussed in Section 9.2.

9.1 Cross-Sections of Nanotube Networks

Samples etched for 8 min and coated with nominal 20 nm SiO_2 became highly brittle and upon touching with twizzers they broke. This enabled easy SEM imaging of cross-sections. Figure 9.1.1 presents representative SEM images of such SiO_2-coated interconnected cylindrical nanochannels in a ∼30-µm thick polycarbonate membrane. The low magnification image displayed in (a) demonstrates the network structure and its extension over the whole template thickness as indicated by the straight orange line. The higher magnification image shown in (b) was recorded under an angle with respect to the top of the membrane as indicated by the red arrow in (d) and visualizes the smoothness of this membrane side. In contrast, the imaging under a tilting angle with respect to the bottom of the membrane as indicated by the orange arrow in (d) shows the roughness of the other side of the membrane (c). As presented exemplarily in (e), further magnification reveals interconnections of the nanochannels as well as the 4 different directions of the ion irradiation, which are indicated with the yellow arrows. Additionally, the island formation of the Au film is visible at this magnification. The Au was sputtercoated to enable better focusing. For the nanochannels, a diameter of ∼120 nm is obtained in agreement with the radial etching rate observed for network templates ($\sim 20 \frac{\text{nm}}{\text{min}}$) and the nominal coating thickness of the SiO_2 layer.

Obviously, the ALD coating does not affect the shape of the nanochannels and thus, the presented images are in good agreement with cross-sections of uncoated networks imaged by L. Movsesyan and L. Burr [122, 192]. Furthermore, the conformal coating results in a highly porous template with inorganic inner surfaces. However, the brittleness of these samples is not advantageous for applications.

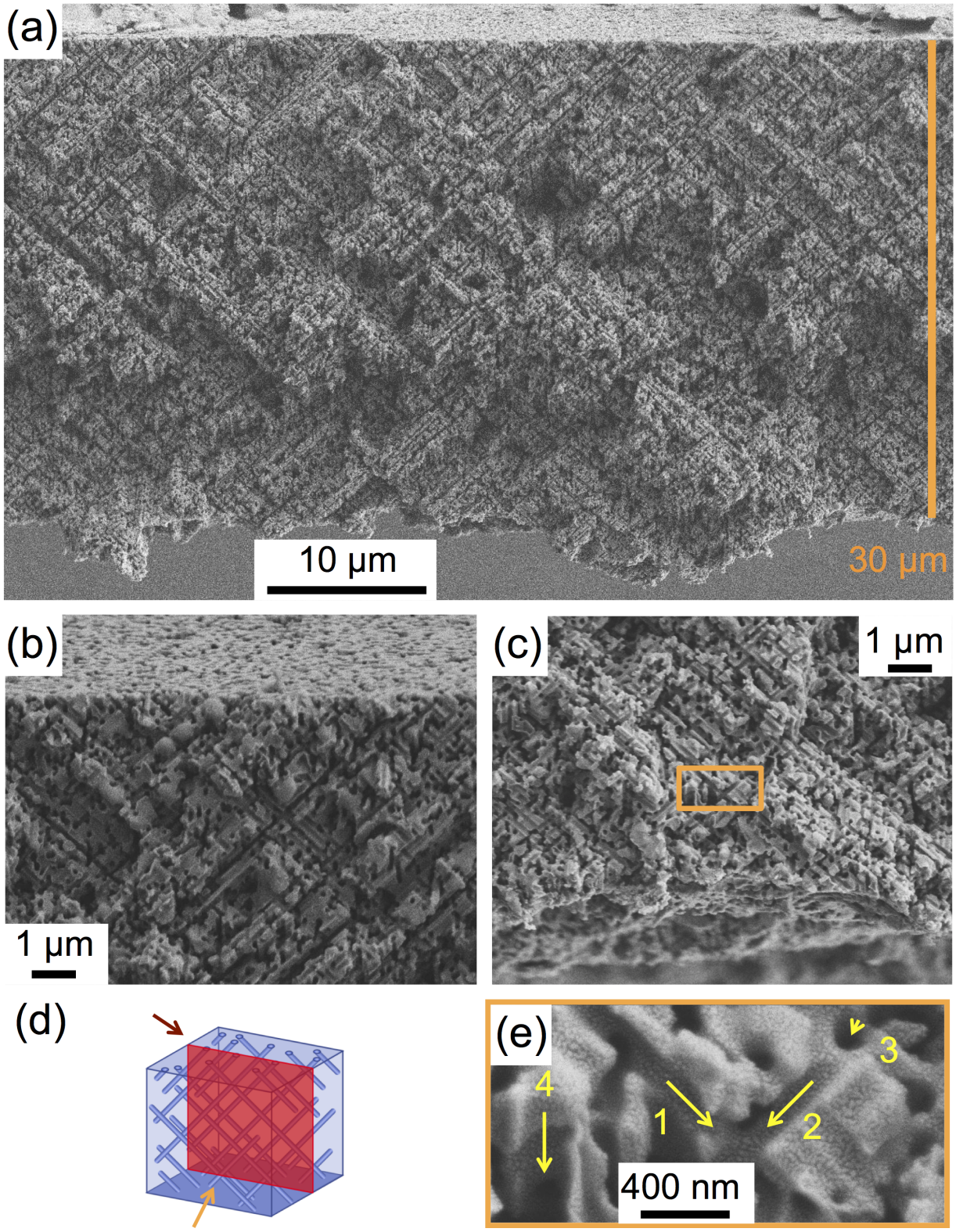

Figure 9.1.1.: Cross-sectional SEM-images of a PC membrane irradiated under 45 °from 4 directions. After etching, the surface was ALD-coated with nominal 20 nm SiO_2. (a) The network structure of the coated cylindrical nanochannels extends over the entire ∼30-µm thick membrane. At higher magnification the smooth (b) and rough surfaces (c) of the membrane are clearly distinguishable by tilting the sample and imaging the cross-section (red in d) from top and bottom as indicated by the red and orange arrow in (d), respectively. (e) The further magnified inset marked orange in (c) shows the 4 directions of ion irradiation that are indicated by the yellow arrows as well as the island formation of the sputtered Au.

9.2 Free-Standing Nanotube Networks

A network template prepared by 10 min etching was coated with a nominal 10 nm thick TiO_2 layer at Universität Hamburg. In collaboration with L. Movsesyan [62, 192], the sample was mechanically stabilized by a metallic layer, the template was dissolved, and the synthesized nanostructure was characterized by SEM (detailed description of sample preparation in Section 5.3). Figure 9.2.1 displays representative SEM images of the nano-network consisting of cylindrical nanotubes. Low magnification demonstrates the homogeneity of the free-standing TiO_2 nanotube network over an area of several hundred μm^2 (a). Higher magnification reveals the characteristic of a network: interconnections (marked with orange circles in b). Further magnification presents the tubular and cylindrical shape of the interconnected nanostructures as well as smooth walls (c). Additionally, the interconnections are clearly visible from outside (some are marked with circles) and seeing into them reveals the interconnection of the confined volume (marked with yellow circles). All these observations prove the conformal deposition inside network templates by ALD. Furthermore, they show the high mechanical stability of a highly-ordered nanotube network. Inside the nanotubes and on their outer surface the Au sputtercoating performed for better focused images is visible.

For all free-standing networks synthesized by Al_2O_3-coating as well as other deposited thicknesses of TiO_2 and SiO_2, the characterization by SEM showed an mostly undamaged ALD layer on top of the membrane despite some cracks. Focusing into these cracks revealed intact network structures. However, repeating the flushing with DCM more often and elongating the insertion into the dissolving solution did not affect the nanostrucures. Additionally, mechanical rubbing with soft and hard tissue or fine-grained abrasive paper did not influence the obtained result or completely removed the nanostructures, respectively. These observations demonstrate the high mechanical stability of the nanotube networks, which is promising for applications but challenging for characterization.

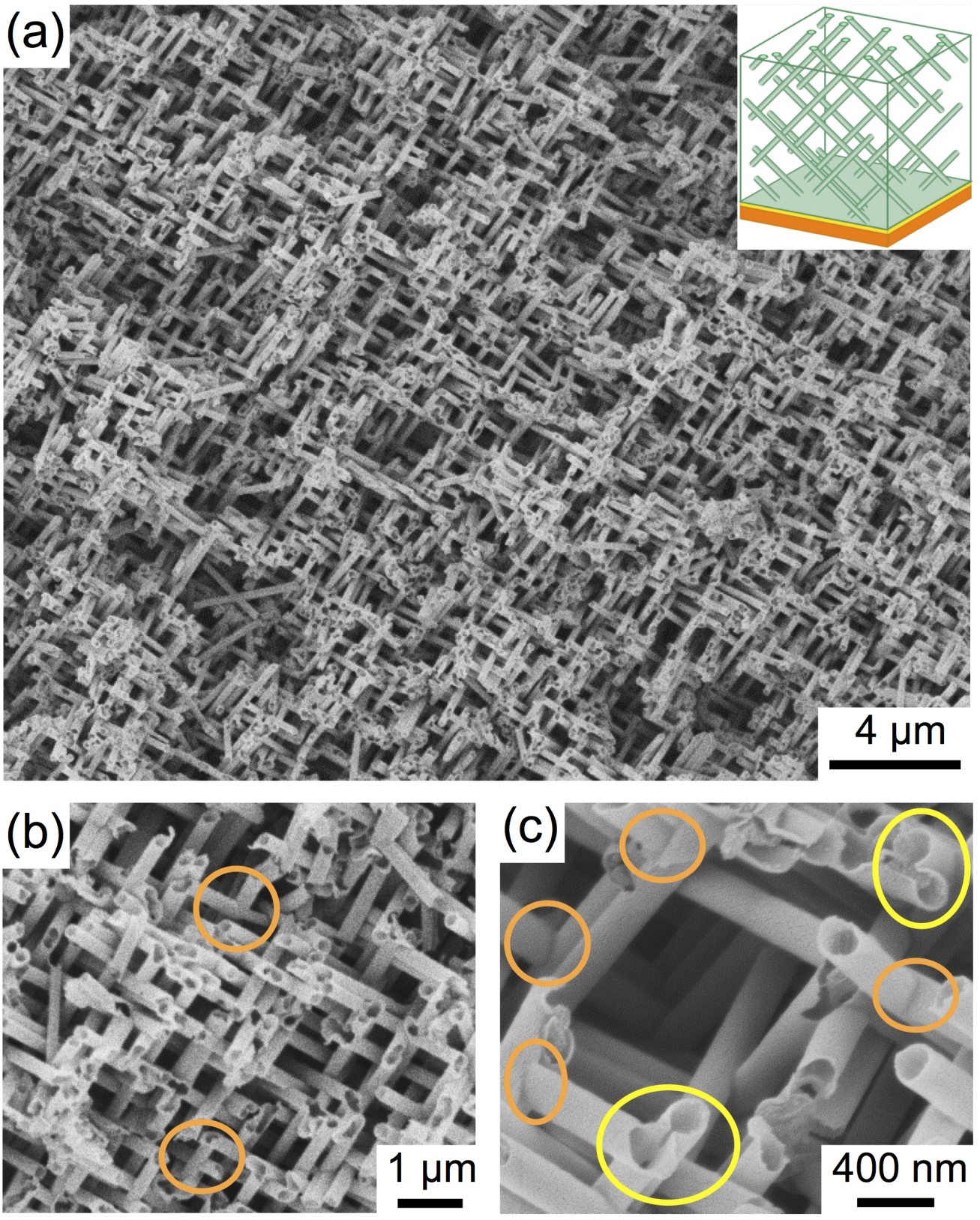

Figure 9.2.1.: SEM images of a highly-ordered and interconnected free-standing network consisting of cylindrical TiO_2 -nanotubes with ∼10 nm thick walls. (a) The network is stable and homogeneous over several hundred μm^2. (b,c) Higher magnification reveals interconnections (some marked with orange circles), the tubular and cylindrical shape as well as the smooth walls of the nanostructures. The yellow circles in (c) mark interconnected nanotubes.

10 Conclusions of Nanotube Synthesis

This part presented the morphology and composition of cylindrical and conical nanotubes as well as nanotube networks of TiO_2, SiO_2, and Al_2O_3 synthesized by ALD in ∼30-µm thick polycarbonate membranes.

For cylindrical nanochannels, systematic studies by a scanning electron microscope operated in transmission mode (STEM-in-SEM) and laboratory small angle X-ray scattering (SAXS) demonstrated the independence of the layer thickness from the initial channel diameter. For all three deposited oxides, the diameter reduction by ALD was homogeneous over the entire channel length down to inner diameters below 10 nm evidencing the synthesis of nanotubes with an aspect ratio inside the tubes of more than 3000. Furthermore, layer-by-layer growth was possible in cylindrical nanochannels as small as 10 nm in diameter. This confirmed the conformal coating of parallel aligned nanochannels exhibiting a higher aspect ratio as reported beforehand [21, 92, 95–99].

SAXS measurements performed in the laboratory and at the synchrotron as well as with different analysis codes [176, 179] were in quantitative agreement. In addition, the SAXS analysis at the synchrotron facility revealed that the diameter reduction down to a few nm is challenging and requires the optimization of the three ALD processes probably due to diffusion limits caused by the precursor size being only one order of magnitude lower than the channel size. Further elongation of exposure and purge times, the use of smaller precursor molecules, e.g. $TiCl_4$ for TiO_2 ALD, or the approach of N. Sobel, who repeated each half-cycle directly after itself for a few times before performing the other half-cycle [182], may overcome this limitation.

The calculation of the geometrical features, which are preserved during imaging of the nanotubes in transmission mode of the SEM, showed that the wall thickness of the nanotubes is determined most accurately directly from the STEM-in-SEM images. In addition, the calculation confirmed the tubular shape of the analyzed nanostructures.

Besides the coating of cylindrical nanochannels, the parameters optimized for the deposition of TiO_2, SiO_2, and Al_2O_3 in polymeric templates were applied for conical channels. Without restriction, layer-by-layer growth was observed demonstrating the independence of the conformal surface modification from the geometry of the template. This conformity is the great advantage of ALD compared to other surface modification techniques such as chemical or electroless methods that lead to rough or undefined channel walls [16, 65, 66, 80]. As for cylindrical channels, the outer and inner surface of the tubes replicate the smooth surface of the etched ion-tracks in polycarbonate providing well-defined channels with various wall materials. Thus, these channels are more suitable for the systematic investigation of ionic conductance in ALD-coated nanochannels than the recently published ALD-coated conical nanochannels in polyethylene terephthalate (PET) [43], which forms rough channel walls [42].

Regarding the composition of the coating in cylindrical and conical nanochannels, energy dispersive X-ray spectroscopy (EDX) analysis of TiO_2, SiO_2, and Al_2O_3 nanotubes released from the polycarbonate template evidenced pure deposition and preparation processes. X-ray photoelectron spectroscopy (XPS)

demonstrated almost stoichiometric bulk composition for 10 nm thick films on the membrane surface. Unique arrays of free-standing, ∼30-µm high conical nanotubes with different wall thicknesses in the order of a few ten nm were successfully prepared homogeneously in areas of few cm^2. Dependent on the material and thickness of the wall, the free-standing nanocones showed qualitatively different mechanical stability: Thicker walls increased the stability. SiO_2 cones were the most fragile in agreement with its fracture toughness value [188, 189]. The high mechanical stability of the cones exhibiting TiO_2 walls coincides with its fracture toughness value [190]. Due to electrical charging under the electron beam, bending and finally collapsing Al_2O_3 and SiO_2 nanocones were observed in-situ during SEM analysis. Instead of standing free, cylindrical nanotubes prepared in the same way exhibiting the same wall thicknesses and diameters equivalent to the tip diameter were very flexible forming bundles of lying nanotubes. This emphasizes the advantage of the conical nanotubes for applications requiring free-standing nanostructures such as drug delivery directly into cells [21]. However, lying symmetric SiO_2 nanotubes exhibit high mechanical stability and flexibility in contrast to TiO_2 and Al_2O_3 tubes, which break easily. This is in contrast to the fracture toughnesses of the three bulk materials [188–191].

The successful preparation of arrays of free-standing tubular nanocones that are mechanical stable was consequently transferred to single channel membranes leading to the advanced synthesis of single free-standing conical nanotubes. This unique method is advantageous for the precise calculation of the tip diameter from ionic conductance measurements since the required base diameter of the studied channel can be determined exactly from the SEM image of the free-standing prepared single tubular nanocone. The comparison between the radial base etching rate of single channels and multichannels etched under identical conditions resulted in coinciding values. The distinct values of outer and inner tip diameter were not accessible at the free-standing nanocones. Accordingly, they were determined by *I-V* measurements before as well as after ALD for single channels and by STEM-in-SEM of released nanotubes lying on TEM-grids for multichannel membranes. The resulting mean values of the tip etching rates differed by a factor of ~ 2. In contrast to the procedure described in this thesis, commonly the base diameter is estimated from a multichannel membrane etched simultaneously without applying a stabilization voltage [14, 16, 80, 116, 171, 172]. However, the here presented comparison of free-standing conical nanotubes arranged as single or arrays confirms the procedure to utilize the base diameter obtained from the multichannel reference membrane for the determination of the tip diameter.

The conformal surface modification by ALD independent on the geometry of the etched ion-tracks in polycarbonate membranes opened up further variation of the template: interconnected channels. For the highly-ordered networks consisting of interconnected cylindrical nannochannels, the cross-sectional SEM-images recorded after ∼20 nm SiO_2 ALD revealed a highly porous template, that was extended over a thickness of ∼30 µm. Additionally, the huge increase in brittleness after deposition of ∼20 nm SiO_2 may be applied for the imaging of cross-sections of other porous samples irradiated with high fluences. The free-standing TiO_2 network with ∼10 nm thick walls was impressively homogeneous and stable over several hundred μm^2. In addition, it consisted of cylindrical tubes with smooth walls and exhibited interconnections of the nanotubes.

All these observations evidenced conformal deposition inside network templates by ALD, which is promising for further investigations aiming applications in e.g. catalysis or solar energy harvesting due to the increased surface area compared to nanowire arrays and networks as well as nanotube

arrays. Furthermore, they enable systematic studies due to the possibility to tailor all characteristics of such a structure: thickness of the porous structure, outer and inner diameter of the nanotubes, angle of crossings as well as amount and physical as well as chemical properties of tubes.

Part III.

Ionic Conductance in ALD-Coated Single Nanochannels

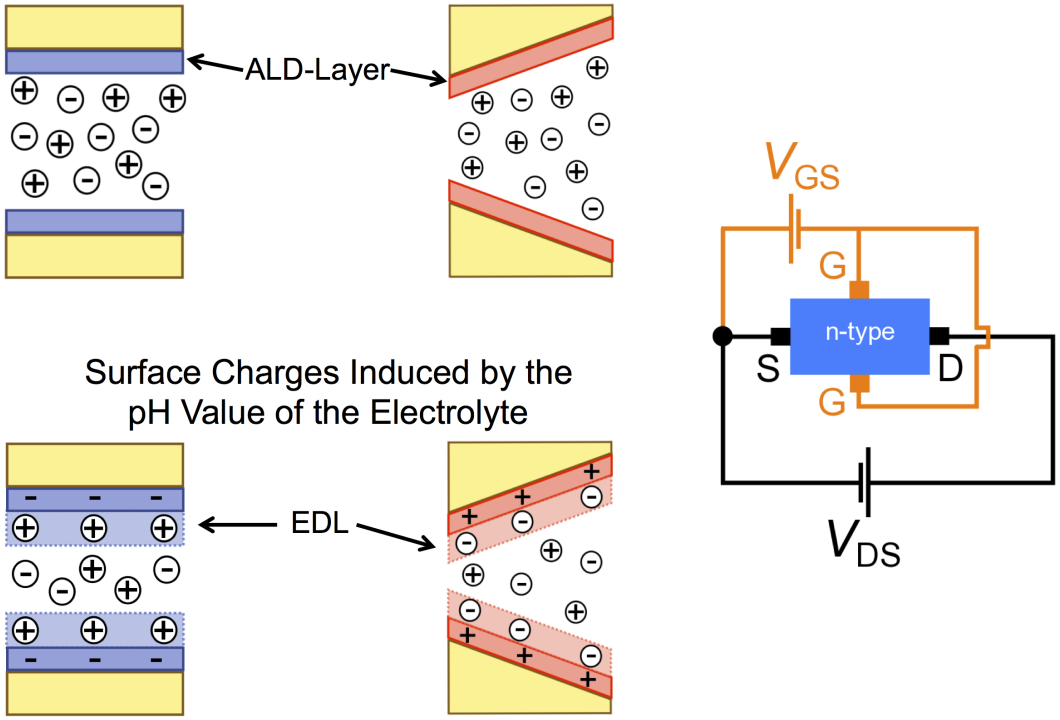

As presented in Part II, the ALD coating of TiO_2, SiO_2, and Al_2O_3 reduces the diameter of polycarbonate nanochannels in a very precise and controllable manner without affecting their initial geometry. This is applied in this third part of the thesis to single-channel membranes employed world-wide for the investigation of ionic and particle transport along a channel of confined dimensions. In first tests, the influence of the ALD surface modification on the ionic conductance of single cylindrical (Chapter 11) and conical (Chapter 12) channels is investigated for all three oxides. *I-V* characteristics are recorded and analyzed as function of the pH value of the electrolyte. Additionally, Section 12.2 presents the ionic conductance of a gated TiO_2-coated conical channel embedded in the polycarbonate template.

11 Single Cylindrical Nanochannels

In this chapter, single cylindrical channels ALD-coated with TiO_2, Al_2O_3, and SiO_2 are studied by conductometry. *I-V* conductance measurements were performed to determine the diameter of a given nanochannel before and after ALD and thus the influence of the deposited layer thickness. As reference, nanotubes released from multichannel reference membranes, which were synthesized simultaneously, were applied. To ensure the suitability of the multichannel membrane as reference, the etching rate of single and multichannels was compared (Section 11.1). Detailed studies of single symmetric channels coated with TiO_2, Al_2O_3, and SiO_2 are presented in Section 11.2. Ionic conductance dependent on the pH value of the electrolyte and the surface material of a single nanochannel was investigated (Section 11.3). Additionally, the effect of the oxide layer deposited onto both membrane surfaces on ionic conductance measurements (Section 11.4) and the reproducibility of synthesis and ionic transport in single cylindrical nanochannels (Section 11.5) are discussed.

11.1 Uncoated Single Cylindrical Nanochannels

Figure 11.1.1a shows representative *I-V* characteristics of single cylindrical nanochannels prepared by symmetric etching of ∼30-µm thick single-ion irradiated polycarbonate membranes applying various etching times between 70 and 250 s. For all etching times, the current depends linearly on the voltage demonstrating ohmic behavior. Thus, there is no rectification as expected for a symmetric geometry of the channels [56]. In each case, the channel diameter was calculated according to equation 4.4 by deducing the electrical conductance from the slope of the corresponding *I-V* curve. The diameters estimated for all analyzed nanochannels are plotted in Figure 11.1.1b as a function of etching time. The radial etching rate for the single cylindrical nanochannels is $26.1 \pm 3 \frac{\text{nm}}{\text{min}}$. This value coincides with the radial etching rate of the simultaneously etched multichannel reference membranes and all other multichannel membranes etched symmetrically ($23.9 \pm 0.5 \frac{\text{nm}}{\text{min}}$, Section 7.1), for which the ALD-deposited nanotubes were released and analyzed by STEM-in-SEM. For single tracks, the radial etching rate shows higher fluctuation probably caused by thickness fluctuations and inhomogeneities of the polycarbonate. The agreement of the etching rates allowed the utilization of simultaneously etched and ALD-coated multichannel membranes as reference for initial and inner diameter as well as deposited layer thickness (see Section 6.5 for preparation steps).

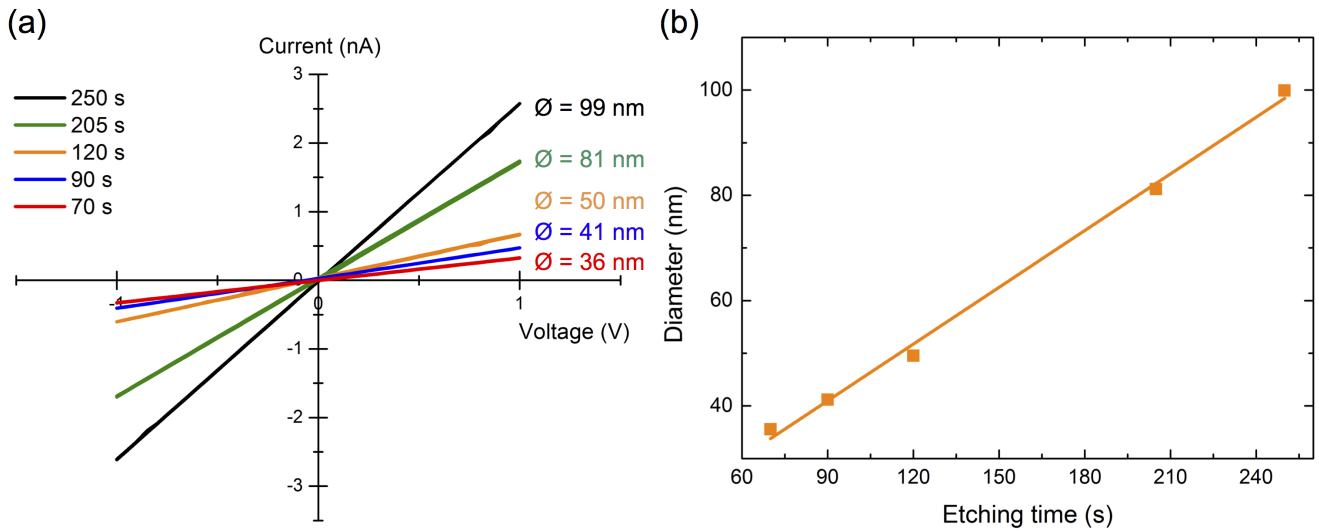

Figure 11.1.1.: (a) *I-V* curves of single cylindrical nanochannels in polycarbonate etched for various times. The diameters ∅ were deduced from the ionic conductance by applying equation 4.4. (b) Channel diameter as a function of etching time.

11.2 ALD-Coated Single Cylindrical Nanochannels

The surface modification of single cylindrical nanochannels in polycarbonate membranes was performed by ALD of TiO_2, Al_2O_3, and SiO_2. To characterize the depositions inside the single channels, *I-V* curves were measured at the IEP of the surface material. This section presents representative *I-V* characteristics for each oxide.

11.2.1 TiO_2 Coating

To investigate the ionic conductance in TiO_2-coated etched ion-track polycarbonate membranes, single tracks were etched for 120 s and a nominal 10 nm thick TiO_2 layer was deposited by ALD. Directly after etching, the *I-V* characteristic was recorded (Figure 11.2.1a, orange) to deduce the diameter of the uncoated single channel using equation 4.4. The resulting value of ∼42 nm is in good agreement with the outer diameter of the nanotubes released from the simultaneously etched (big beaker) and coated multichannel reference membrane obtained by STEM-in-SEM (Figure 11.2.1b, orange arrow). The lower etching rate compared to data presented in Section 7.1 and 11.1 is attributed to a decrease of the UV lamp intensity by aging. After TiO_2 ALD, the ionic conductance of the single nanochannel was measured at the IEP of the surface material (pH ∼5). This *I-V* curve (Figure 11.2.1a, green) shows an ohmic behavior demonstrating that the symmetric geometry of the channel is maintained and thus evidencing a conformal ALD process inside the single nanochannel. The deduced diameter of ∼24 nm is in good coincidence with the reduction expected from the nominal coating thickness and the inner diameter measured by STEM-in-SEM on the reference nanotubes (Figure 11.2.1b, green arrow).

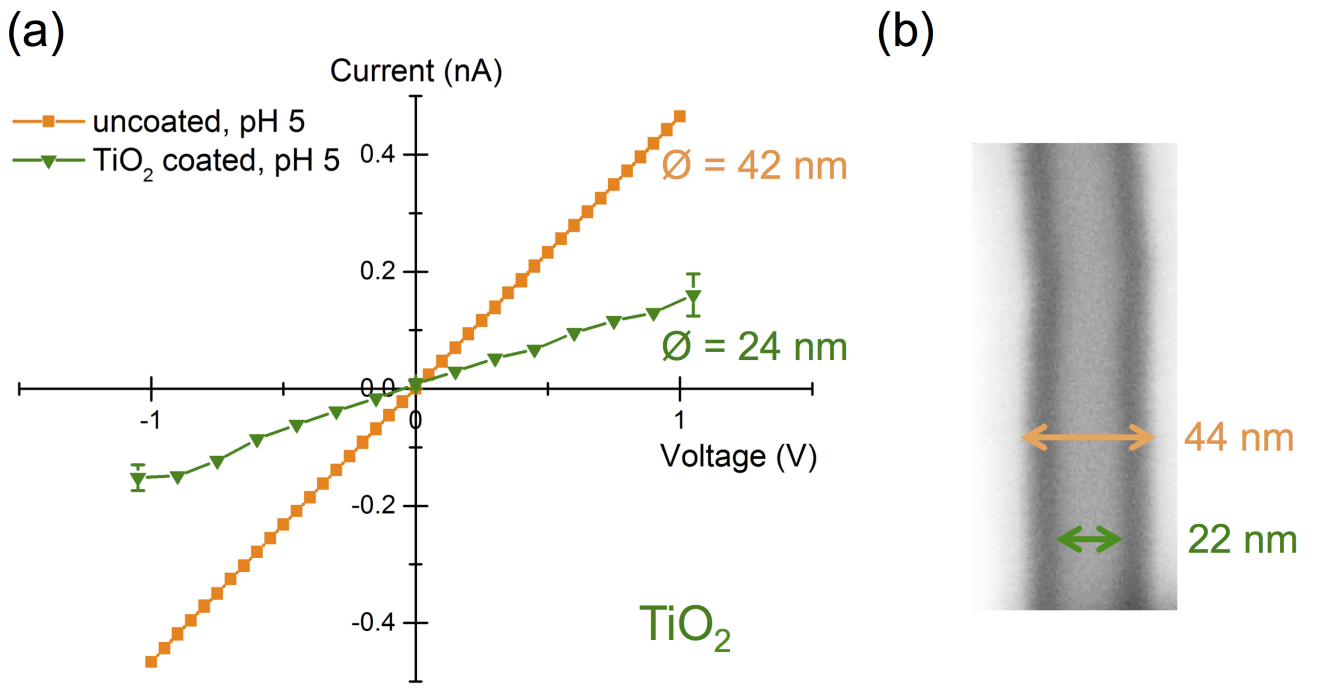

Figure 11.2.1.: (a) *I-V* curves of a 120 s etched single cylindrical nanochannel before and after ∼10 nm TiO_2 deposition by ALD. (b) Representative STEM-in-SEM image of a nanotube released from the corresponding multichannel reference membrane. The orange and green arrow mark outer and inner diameter of the tube, respectively.

11.2.2 Al_2O_3 Coating

Figure 11.2.2a displays the *I-V* measurement of a single cylindrical nanochannel in a polycarbonate membrane synthesized by 90 s symmetric etching (orange). The corresponding ionic conductance leads to a diameter of ∼25 nm (equation 4.4), which coincidences well with the outer diameter of the reference nanotubes released from the equally treated multichannel membrane (Figure 11.2.2b, orange arrow). Due to aging of the UV lamp, both membranes were UV irradiated with less intensity resulting in a smaller etching rate as usually observed. Nominal 5 nm Al_2O_3 were deposited onto both membranes by ALD. At pH ∼9 (IEP of Al_2O_3), the Al_2O_3-coated single nanochannel leads to an *I-V* curve characterized by a linear dependency of the ionic current on the applied voltage (Figure 11.2.2a, red). This evidences a conformal deposition process along the entire ∼30-µm long nanochannel. The reduced diameter of ∼14 nm was estimated according to equation 4.4 and is in agreement with the value expected from the nominal coating thickness as well as the inner diameter of the reference nanotubes (Figure 11.2.2b, red arrow).

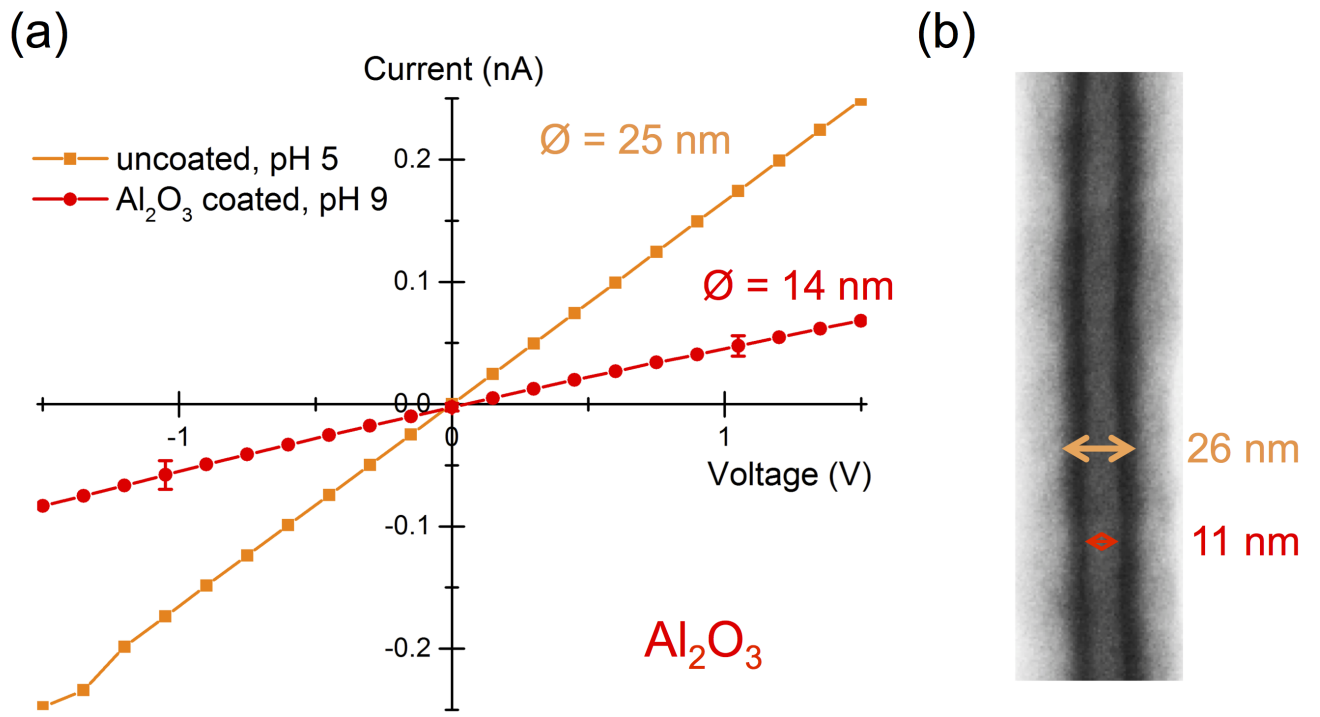

Figure 11.2.2.: (a) *I-V* curves of a single cylindrical nanochannel recorded directly after 90 s etching and after the deposition of ~5 nm Al_2O_3. (b) STEM-in-SEM image of a representative reference nanotube. The diameter before and after ALD is marked by an orange and red arrow, respectively.

11.2.3 SiO_2 Coating

Figure 11.2.3a shows the *I-V* curve of a single cylindrical nanochannel after 120 s etching (orange). The diameter deduced from the *I-V* measurement is ~54 nm (equation 4.4) in good agreement with the etching rates obtained for single and multichannel membranes. However, the outer diameter of the nanotubes released from the corresponding multichannel reference membrane is smaller (Figure 11.2.3b, orange arrow). After ALD coating with nominal 10 nm SiO_2, the *I-V* characteristic of the single nanochannel was recorded at the IEP of SiO_2 (pH ~2). As for the two other oxides, this *I-V* curve (Figure 11.2.3a, blue) shows ohmic behavior evidencing a conformal layer formation inside the nanochannel. Considering this *I-V* data, the SiO_2 layer reduces the channel diameter down to ~38 nm coinciding with the reduction expected from the nominal deposited thickness and the wall thickness of the reference nanotubes (Figure 11.2.3b).

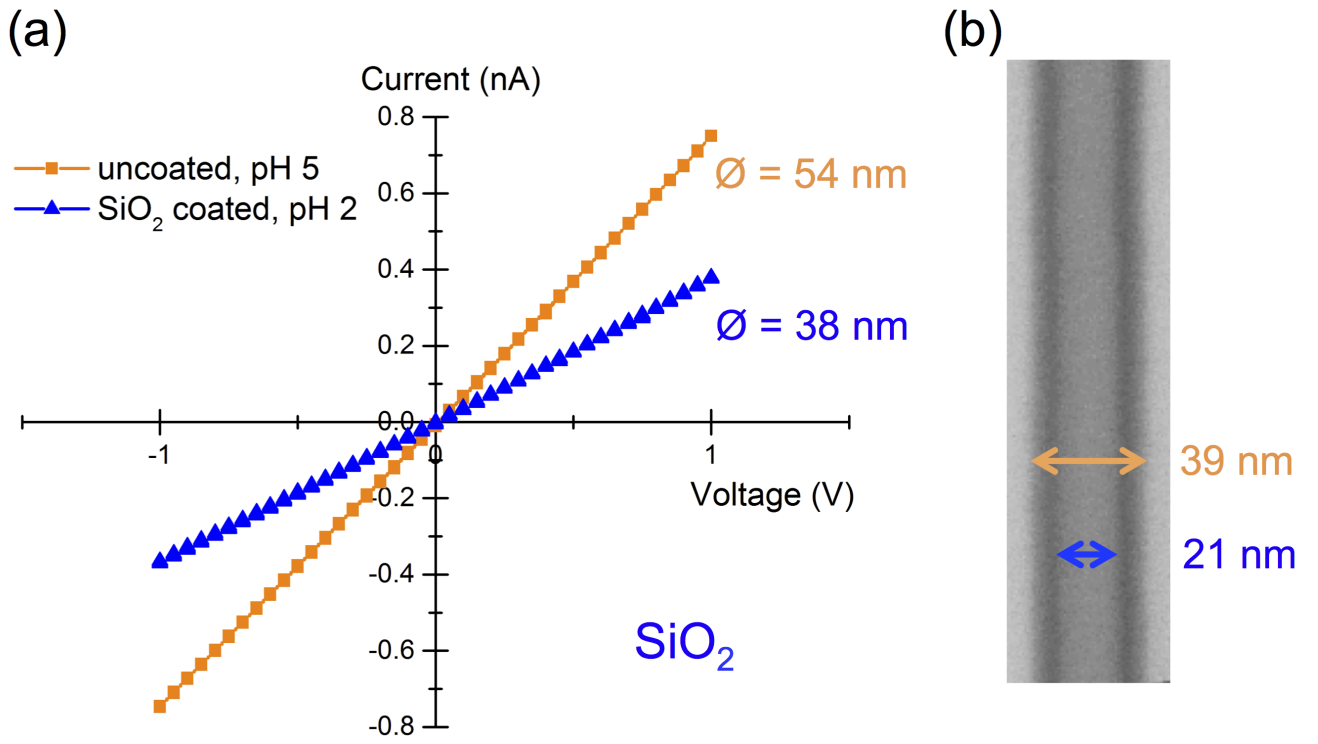

Figure 11.2.3.: (a) *I-V* curves of a single cylindrical nanochannel after 120 s etching and ALD-coated with a ∼10 nm SiO_2 layer. (b) Section of a representative nanotube released from the multichannel reference membrane obtained by STEM-in-SEM. The orange arrow marks the outer diameter of the tube, while the inner diameter is indicated by the blue arrow.

11.3 Ionic Conductance as a Function of the pH Value of the Electrolyte

The successful conformal and controllable diameter reduction of single cylindrical nanochannels by ALD coating led to a decreased ionic conductance. In this section, the *I-V* characteristics of TiO_2-, Al_2O_3-, and SiO_2-coated single cylindrical channels are studied as a function of the pH value of the electrolyte. To make the influence of the pH value easier observable, a triangular voltage was varied between ± 3 V for all following analyses.

11.3.1 TiO_2-Coated Channels

Figure 11.3.1a displays the *I-V* curves measured for the single cylindrical nanochannel with initial diameter ∼42 nm (orange) and coated with nominal 10 nm TiO_2 (Figure 11.2.1) at pH ∼2 (blue), pH ∼5 (green), and pH ∼9 (red). The highest ionic conductance is observed at pH ∼5, which is the isoelectric point (IEP) of TiO_2. Due to the absence of surface charges at the IEP, the deduced diameter of ∼24 nm corresponds to the nanochannel size. The surface groups (−TiOH) of the metal oxide TiO_2 are amphoteric in aqueous solution [193]. Thus, they are protonated at a pH < IEP according to [193]:

$$-\mathrm{TiOH} + \mathrm{H^+} \rightleftharpoons -\mathrm{TiOH_2}^+ \tag{11.1}$$

resulting in a positively charged surface. At a pH > IEP, the surface groups are deprotonated according to [193]:

$$-\mathrm{TiOH} \rightleftharpoons -\mathrm{TiO^-} + \mathrm{H^+} \tag{11.2}$$

leading to a negatively charged surface. For the presented single cylindrical nanochannel with a TiO_2 surface, the surface charges at the studied pH values as well as the formed electrical double layer (EDL) are shown schematically in Figure 11.3.1b. In the *I-V* curves, a decreased ionic conductance is observed for pH ≠ IEP due to hindered ionic transport caused by the EDL. According to the theory of nanofluidics, the counterion selectivity caused by the EDL should decrease the transport of cations at pH < IEP and of anions at pH > IEP. The thickness of the EDL layers (λ_D) can in principle be calculated from the diameters ∅ deduced from the ionic conductance:

$$\lambda_D = \frac{\varnothing_{\mathrm{pH=IEP}} - \varnothing_{\mathrm{pH\neq IEP}}}{2} \tag{11.3}$$

Unfortunately, the amount of analyzed nanochannels was not sufficient for statistical significance. However, from the presented *I-V* curves first estimations result in EDL thicknesses of ∼4 nm for pH ∼2 and ∼ 2.5 nm for pH ∼9. These values are one order of magnitude larger compared to data reported in literature for the applied 1 M KCl solution [146]. N. Sobel investigated the contact angle of water at the flat surfaces of pristine polycarbonate membranes and after deposition of ∼10 nm TiO_2 by ALD onto these surfaces [182]. The strong reduction of the contact angle after ALD coating was ascribed to an increase of hydroxyl groups on the studied surface. The first estimations of the EDL layer thickness indicate the same effect of the TiO_2 surface modification inside the nanochannel. The observed rectification ratios of ∼1 for pH ∼2 and ∼1.3 for pH ∼9 indicate a symmetric surface charge distribution inside the cylindrical nanochannel and thus prove the homogeneous TiO_2 deposition inside the entire channel by ALD.

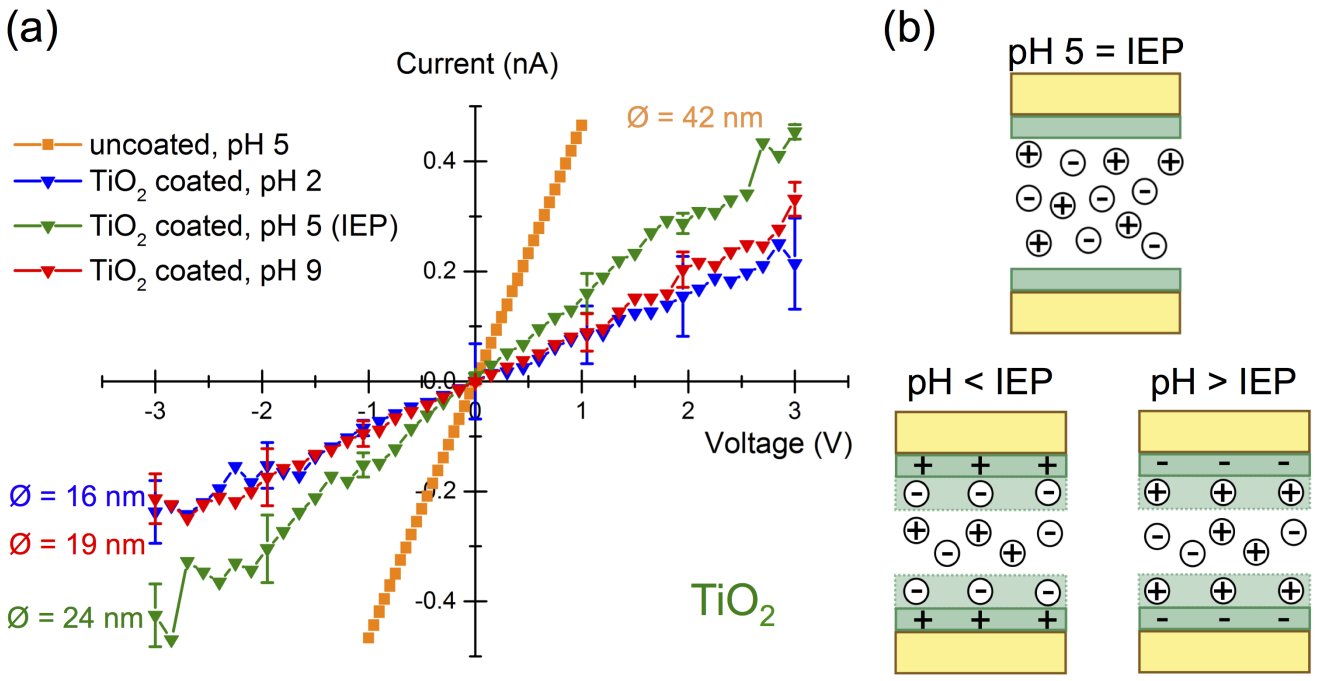

Figure 11.3.1.: (a) *I-V* curves of a single cylindrical nanochannel exhibiting an initial diameter of ~42 nm recorded at different pH values after the deposition of ~10 nm TiO_2. In each case, the diameter ∅ was deduced according to equation 4.4. (b) Schemes of the surface charges and EDL for different pH values of the 1 M KCl solution used as electrolyte. Proportions are not to scale.

11.3.2 Al_2O_3-Coated Channels

For the nanochannel with an initial diameter of ~25 nm (orange) after 90 s etching that was coated with nominal 5 nm Al_2O_3 (Figure 11.2.2), *I-V* curves were obtained at different pH values (Figure 11.3.2a). The highest ionic conductance is observed at the IEP of Al_2O_3 (pH ~9, red). The deduced diameter of ~14 nm presents the nanochannel size after coating, since no surface charges are present at the IEP. In aqueous solution, the surface groups (−AlOH) of Al_2O_3 are zwitterionic leading to protonation at pH < IEP [194, 195]:

$$-\mathrm{AlOH} + \mathrm{H^+} \rightleftharpoons -\mathrm{AlOH_2}^+ \tag{11.4}$$

Thus, the surface inside the nanochannel is charged positively resulting in the formation of an EDL as schematically shown in Figure 11.3.2b. The measured ionic conductance is reduced at pH ~5 (green) and further decreased at pH ~2 (blue) in agreement with less screening in the case of higher surface charge concentration. The estimated Debye lengths (equation 11.3) are ~0.5 nm in the case of pH ~5 and ~ 1.5 nm in the case of pH ~9 being a factor of ~ 2 and ~5 larger as given in literature for 1 M KCl solution [146]. A symmetric surface charge distribution inside the cylindrical channel is indicated by the rectification ratios of ~1 for pH ~5 and ~1.2 for pH ~2 demonstrating a conformal deposition of Al_2O_3 inside the single nanochannel.

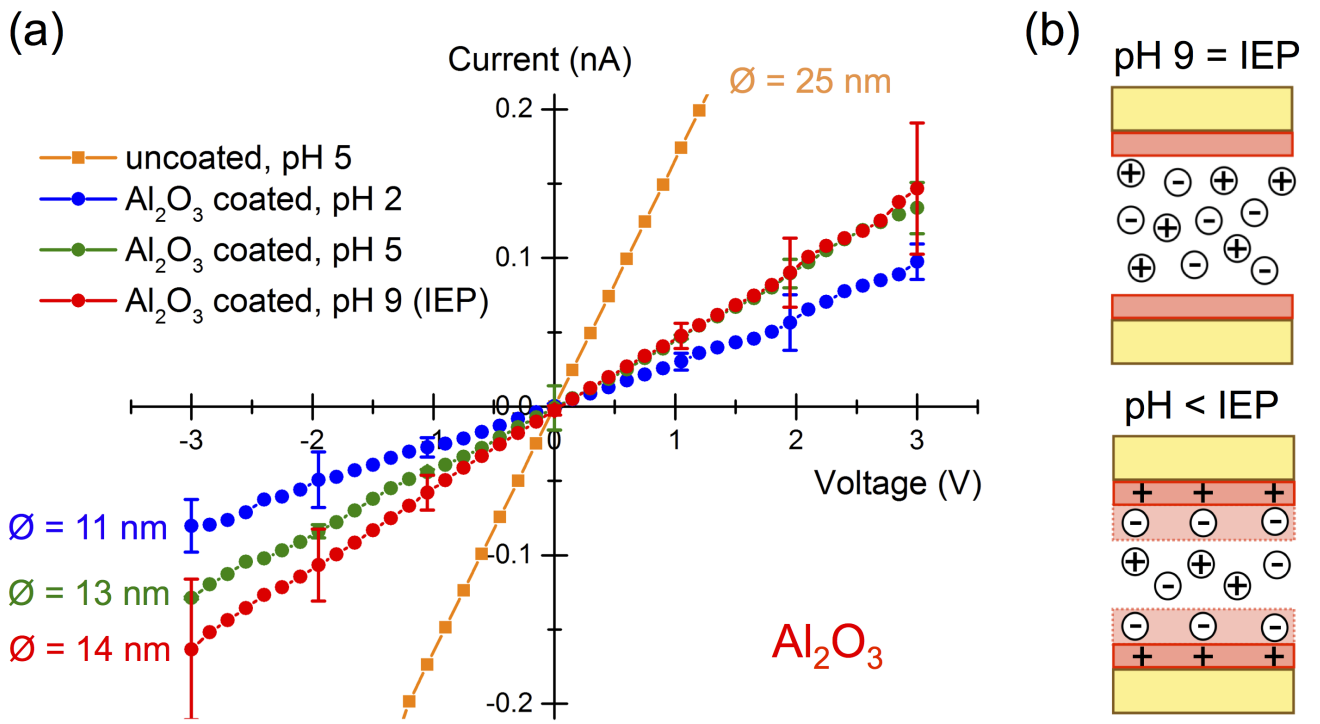

Figure 11.3.2.: (a) After deposition of ~5 nm Al_2O_3, the *I-V* curves of a single cylindrical nanochannel with an initial diameter of ~25 nm were recorded at different pH values. According to equation 4.4 the diameters ∅ were calculated. (b) The schemes show the surface charges as well as the EDL (proportions not to scale).

11.3.3 SiO_2-Coated Channels

Figure 11.3.3a shows the *I-V* characteristics of a single cylindrical nanochannel that was etched for 90 s (orange). The diameter deduced from the ionic conductance is ~36 nm in agreement with the outer diameter of the reference nanotubes released from the multichannel membrane (Figure 11.3.3b, orange arrow). After coating with a nominal 5 nm thick SiO_2 layer, STEM-in-SEM reveals tubes with expected inner diameters (Figure 11.3.3b, blue arrow). However, the ionic conductance measured at the IEP of SiO_2 (pH ~2, blue) results in a diameter of ~8 nm for the simultaneously coated single channel (Figure 11.3.3a, blue). At pH ~5 (green) and pH ~9 (red) of the 1M KCl solution used as electrolyte, the ionic conductance is increased in contrast to the EDL theory, which predicts hindered ionic transport due to negative surface charges formed by dissociation of H^+ from the functional −SiOH surface groups (Figure 11.3.3 c) [196, 197]. For several single cylindrical channels, the lowest ionic conductance was observed at the IEP after SiO_2 deposition. Nevertheless, the rectification ratio is ~0.9 for all pH values indicating a symmetric surface charge distribution and thus a conformal coating inside the single channel.

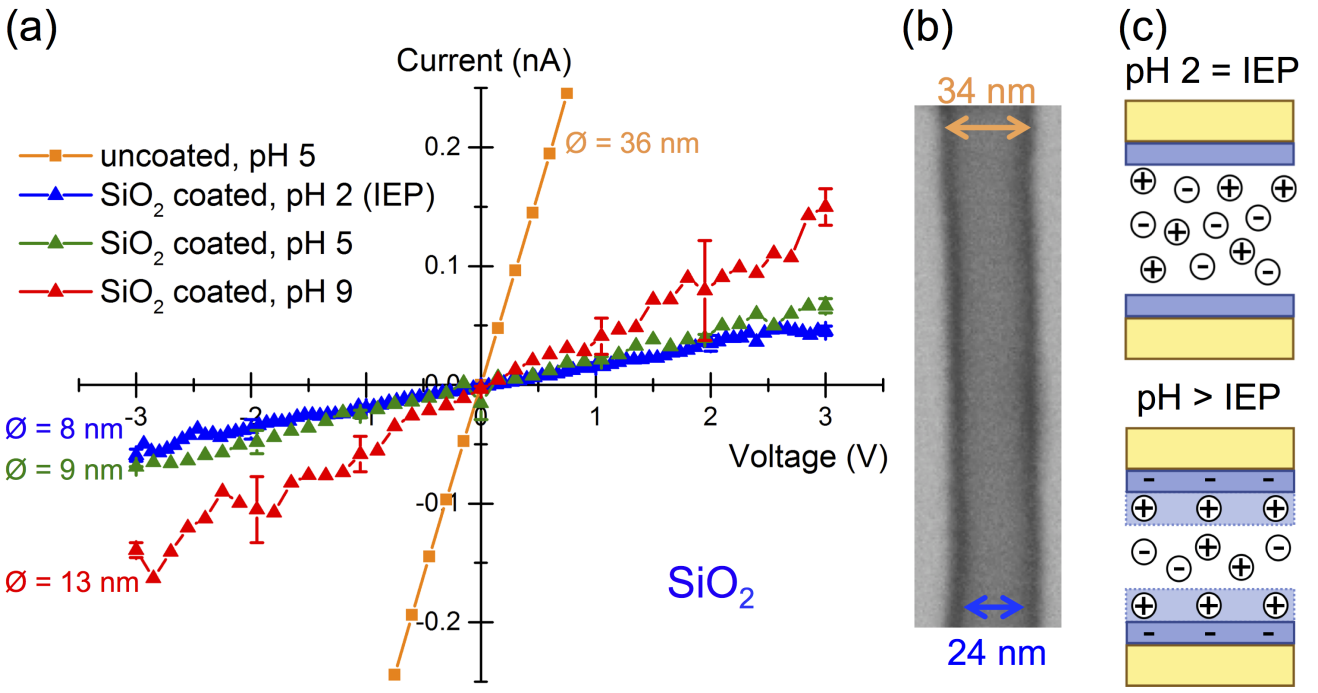

Figure 11.3.3.: (a) *I-V* characteristics of a single cylindrical channel with a diameter of ~36 nm measured after etching and at various pH values of the electrolyte after deposition of ~5 nm SiO_2. 1 M KCl solution was utilized as electrolyte. (b) Representative section of a nanotube released from the multichannel reference membrane visualized by STEM-in-SEM. Outer and inner diameter are marked by an orange and blue arrow, respectively. (c) For the different pH values, the schematics display the surface charge and the EDL. Proportions are not to scale.

At a given pH value of the electrolyte, the surface charges of a single cylindrical nanochannel depend on the ALD-deposited material due to their different IEPs. Thus, the ALD coating enables the adaptation of polymeric nanochannels to a broad range of acidic and basic environments without introducing surface

charges. On the other hand, the surface modifications can be applied to sense changes of the pH value of an electrolyte for various initial pH values.

11.4 Capacitance Effect in Nanochannels with Oxide Walls

The *I-V* curves of single-channel membranes that exhibit initial diameters between 25 and 120 nm and are coated with TiO_2-, SiO_2-, and Al_2O_3-layers, show hysteresis if they are recorded by applying the standard settings, which are used for uncoated membranes (see Section 6.5 for details of the set-up). Figure 11.4.1 displays the representative *I-V* curve of a nanochannel with ∼50 nm diameter coated with a ∼10 nm thick SiO_2 layer recorded at the IEP of the surface material (pH ∼2). Applying the standard parameters for the voltage steps, i.e. steps of 0.15 V and recording the ionic current for 1 s at each voltage, results in hysteresis (Figure 11.4.1 dark yellow). Increasing the delay time, i.e. extending the measuring time at each voltage step, to 10 s reduces the hysteresis (Figure 11.4.1 blue) indicating that a capacitance effect causes the hysteresis.

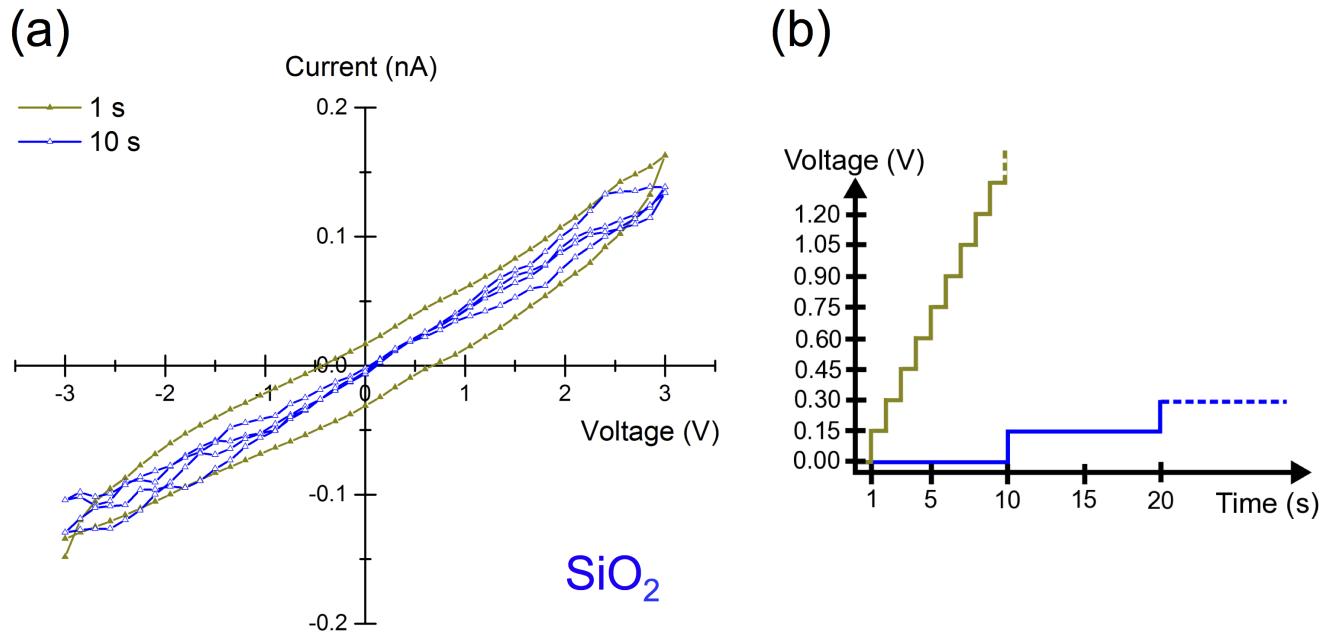

Figure 11.4.1.: *I-V* curves of a single cylindrical nanochannel with an initial diameter of ∼50 nm and a ∼10 nm thick SiO_2 coating. (a) For voltage steps of 0.15 V and measuring time of 1 s at each voltage step (green-yellow), hysteresis is observed. Extending the delay time to 10 s reduces the hysteresis (blue). (b) Scheme of the applied voltage steps and delay times.

The two flat surfaces of the polycarbonate membrane are huge compared to the opening areas of the single nanochannel at the membrane surfaces. For a voltage applied across such a membrane placed in an electrolyte, the flat surfaces can act as capacitor, which is schematically displayed in Figure 11.4.2. Since polymers exhibit relatively low surface-charge densities [198], no capacitor effect superimposing the ionic conductance measurements is expected. However, the surface modification by ALD, which deposits the oxide layers on all surfaces of the membrane, may result in *I-V* curves showing hysteresis due to charging and discharging of the surface depending on the coating material.

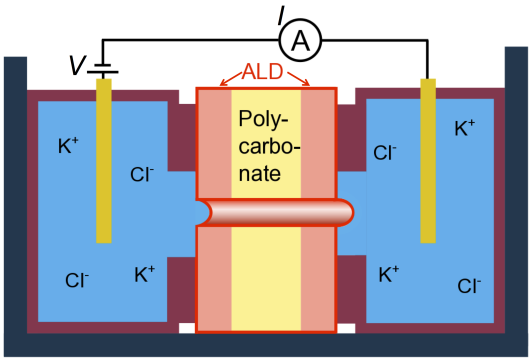

Figure 11.4.2.: Scheme of *I-V* measurements for membranes with ALD coating on all surfaces.

To distinguish, if the hysteresis is caused by charging of the oxide layer inside the nanochannel or/and surface charges on the flat surfaces of the membrane, *I-V* curves were recorded for membranes without nanochannel, which were ALD-coated with 5 (filled symbols) and 10 nm (open symbols) thick TiO_2 and Al_2O_3 layers (Figure 11.4.3). For a delay time of 1 s, the hysteresis is independent of the thickness of the TiO_2-layer at the IEP (Figure 11.4.3a). In the case of Al_2O_3, the *I-V* curves show a more pronounced hysteresis for thicker layers (Figure 11.4.3b). Due to the good dielectric properties of Al_2O_3 compared to the semiconducting TiO_2, we suppose that the hysteresis can be ascribed to capacitance effects.

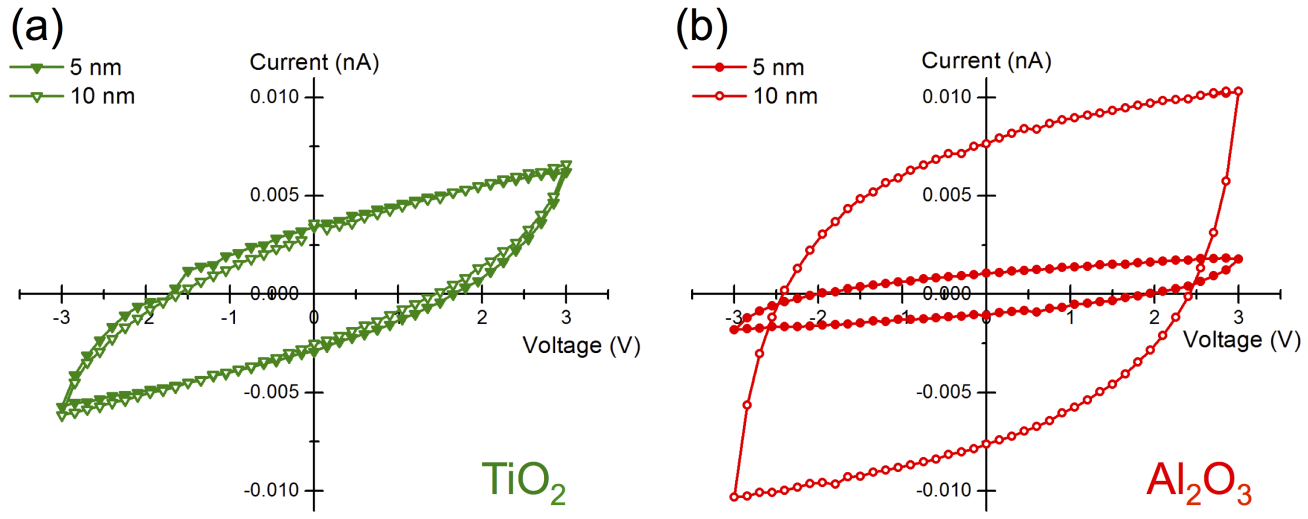

Figure 11.4.3.: *I-V* curves of unetched samples coated with 5 and 10 nm thick TiO_2 (a) and Al_2O_3 (b) layers. The measurements were performed by applying a delay time of 1 s. (a) The hysteresis is independent of the TiO_2 layer thickness. (b) A thicker Al_2O_3 layer results in a more pronounced hysteresis.

If the delay time is increased from 1 s (filled symbols) to 10 s (open symbols), ~10 nm thick TiO_2 and Al_2O_3 layers on unetched polycarbonate membranes show less hysteresis (Figure 11.4.4). Since charging of a capacitor is time dependent, these observations provide further evidence that the hysteresis is related to capacitance. Besides the background noise, no current was recorded in the *I-V* curves of unetched and uncoated as well as non ion-irradiated and uncoated samples. Furthermore, the uncoated single-channel membranes do not cause hysteresis as presented in Figure 11.1.1 (Section 11.1). Thus, we assume that the capacitance is created by surface charges formed at the oxide layer on the flat sur-

faces of the membrane and inside of the nanochannels. The area of both flat surfaces (top and bottom) is about $7 \times 10^{-4}\,m^2$, whereas the surface area inside the single nanochannel is in the order of $10^{-12}\,m^2$ for 30-µm long nanochannels with diameters smaller than 100 nm. Due to the 8 orders of magnitude smaller surface inside the nanochannels, it is assumed that the capacitance effect is dominated by the oxide layer deposited on the surfaces of the membrane. The investigation of samples after removing these layers by e.g. reactive-ion etching could clarify, if the coating inside the nanochannel also contributes to the hysteresis.

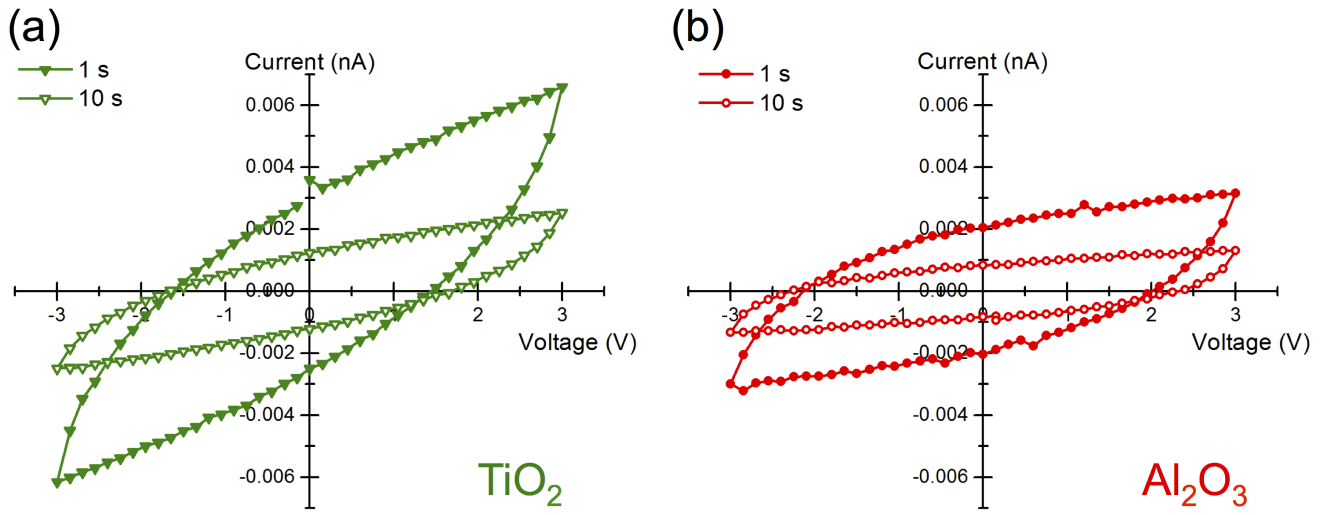

Figure 11.4.4.: Longer delay times during recording the *I-V* curves reduce the hysteresis for ∼10 nm thick TiO_2 (a) and Al_2O_3 (b) layers.

In the case of TiO_2, a delay time of 3 s was suitable to minimize the hysteresis for most of the analyzed samples. To optimize the measuring time for the investigated *I-V* characteristics, a delay time of 3 s (TiO_2) and 10 s (SiO_2, and Al_2O_3) was applied. The minimization of capacitance effects by adjusting the delay time is already reported in literature [14].

11.5 Comments on Channel Closing during Synthesis and Ionic Conductometry of Cylindrical Channels

The synthesis and characterization of ALD-coated single cylindrical nanochannels includes several steps. At each of these steps, the channel can be deformed or even closed leading to measuring artifacts or impracticability of the sample, respectively. Small channels of few tens of nm tend to be instable. For unknown reasons many channels collapse after etching blocking ionic currents. Thus, the efficiency of single nanochannel fabrication is low. Here, a rough estimation of the yield as well as the reproducibility experienced during the performed measurement series is given.

After etching, the single channels were stored in deionised water before their diameter was determined by *I-V* measurements directly afterwards. Etching single ion-tracks with diameters below 50 nm had an output of ∼40 % open channels, whereas channels with diameters smaller than 30 nm tended to close

even more often. For closed channels, no ionic current can be recorded. Some of the channels reopened during the conductometric measurements when applying the voltage. For all open channels, the deduced diameters were in agreement with the multichannel reference membranes.
Since ALD is operated in vacuum, the samples had to be dried before coating. As soon as the membranes were dry, they were inserted into the respective ALD chamber. The subsequent *I-V* characterization revealed the expected diameter reduction in ∼50 % of the cases. It is assumed that the shape of single channels was affected during drying before ALD, e.g. by capillary forces, since the nanotubes released from the multichannel membranes validated conformal ALD depositions. However, the deformation of the channels was not observed for multichannel membranes.
In the case of SiO_2, the deduced diameters at the IEP often deviated significantly from the value expected from the equally prepared multichannel reference membranes. The diameters estimated before ALD were in agreement with the reference samples, the coating in the multichannel membrane coincided with the nominal coating thickness, and this ALD process was highly reproducible in multichannel membranes. Thus, it is rather unlikely, that the coating thickness was thicker in only single channels. Furthermore, the rectification ratios after coating were ∼1 indicating a homogeneous deposition inside the nanochannels. Thus, the channel size might be reduced already during transport of the uncoated samples to the ALD facility at TU Darmstadt, although this was performed in deionised water to avoid closing of the polymeric nanochannels. Etching at TU Darmstadt directly before ALD (as performed at GSI) may solve this problem.
If a nanochannel was open after ALD-coating (in total ∼ 20 %), the obtained *I-V* curves could be reproduced up to eight weeks after the first investigation of the channel, whereas for uncoated channels closing occured after a few days. Performing ionic transport experiments at different pH values, required the exchange of the electrolyte as well as rinsing of the channel in between two measurements. Each exchange contains a risk to result in a closed channel, which is however much higher for uncoated channels. These observations demonstrate an increased stability of the nanochannels after oxide coating.
Due to the ionic currents being mostly below 1 nA, the measurements were extremely sensitive to vibrations and external electric fields. According to equation 4.3, the current depends linearly on the specific conductivity of the electrolyte. Decreasing the concentration of the KCl solution from 1 M to 0.1 M reduces the specific conductivity and thus the current by almost a factor of 10 [180]. Since our measurements were performed without vibration damping and a complete Faraday cage, the results obtained for low electrolyte concentrations are not shown due to lack in reliability.

12 Ionic Conductance and Geometry Analysis on Same Single Conical Nanochannel

The challenge in existing works about transport measurements in single conical nanochannels integrated in polymer membranes is the uncertainty of the dimensions of the individual channel. The base diameter required for the calculation of the tip diameter is commonly determined at multichannel reference membranes. Although the base etching rates of single and multichannel membranes are in agreement as shown in Section 8.6, small deviations of the base diameter result in the calculation of significant different tip diameters. Here, we have the unique chance to first analyze the *I-V* characteristics of a single conical nanochannel and subsequently remove the polymer matrix releasing the tubular replica consisting of the ALD-coating. Characterization of the free-standing single nanocone by SEM provided the base diameter. This enables the accurate calculation of the tip diameter based on base diameter analysis of the same single channel. We applied this approach to single conical nanochannels after ALD coating with TiO_2, Al_2O_3, and SiO_2 and investigation of their *I-V* characteristics at various pH values of the electrolyte (Section 12.1). Furthermore, small modifications of the *I-V* set-up allowed us to gate single TiO_2-coated conical nanochannels (Section 12.2). In Section 12.3, the reproducibility of synthesis and ionic transport in single conical nanochannels is discussed.

12.1 *I-V* Curves of Single Conical Nanochannels Dependent on the pH Value of the Electrolyte

Asymmetrically etched ion-tracks in ∼30-µm thick polycarbonate membranes were coated with TiO_2, Al_2O_3, and SiO_2 by ALD. For each material, *I-V* curves were recorded at the IEP of the surface material to characterize the deposition inside the single channels. The steps performed to determine the geometry of the single channel are given in Section 6.5. Variations of the pH value of the electrolyte enabled the study of the influence of the oxide layers on the ionic transport.
As for the single cylindrical channels, capacitance effects were avoided by applying delay times of 3 s, 10 s, and 10 s for coatings of TiO_2, SiO_2, and Al_2O_3, respectively.

12.1.1 Ionic Conductance in TiO_2-Coated Channels

Figure 12.1.1a shows the *I-V* curves of a single conical nanochannel with a base diameter of ∼1.8 µm. Since the single free-standing cone was not identified, the base diameter was determined from the reference nanocones released from the simultaneously coated multichannel membrane (Figure 12.1.1b). For the uncoated channel (Figure 12.1.1a, orange), the calculation of the tip diameter according to equation

4.6 (applied to the higher ionic currents at positive voltages) results in ∼55 nm. After deposition of a nominal 10 nm thick TiO_2-layer, the ionic conductance measured at the IEP of TiO_2 (pH ∼5, Figure 12.1.1a, green) corresponds to a tip diameter of ∼33 nm in good agreement with the nominal coating thickness and the wall thickness of the reference conical nanotubes. Before ALD, a rectification ratio of ∼1.8 is observed that might be caused by dangling bonds in the polymer that change the size of the nanochannel and form locally charged surface areas [17, 199]. After ALD, the *I-V* curve shows almost ohmic behavior (rectification ratio ∼1.1) and thus indicates the absence of local variations of surface charges. This demonstrates the possibility to stabilize the shape of a conical nanochannel in polymer by conformal ALD coating.

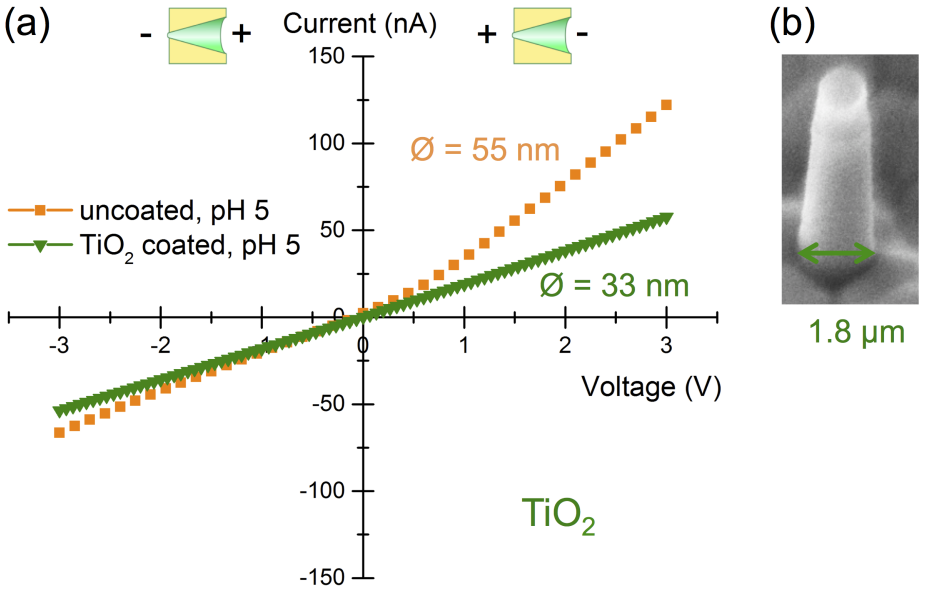

Figure 12.1.1.: (a) *I-V* curves of a single conical nanochannel before and after ALD coating with ∼10 nm TiO_2. (b) Representative nanocone section released from the multichannel reference membrane and employed to determine the base diameter by SEM. All of the nanocones of this sample were broken (during dissolution of the template).

Another example of a single conical nanochannel coated with TiO_2 is shown in Figure 12.1.2. SEM-analysis of the reference conical nanotubes revealed a base diameter of ∼2 µm. From the *I-V* characteristic of the uncoated single channel (Figure 12.1.2a, orange) a tip diameter of ∼103 nm is deduced by applying equation 4.6 to the higher currents at positive voltages. The deposition of nominal 5 nm TiO_2 reduces the ionic current measured at the IEP of TiO_2 (pH ∼5, Figure 12.1.2a, green). The corresponding tip diameter is ∼92 nm (calculated for the higher ionic currents at positive voltages), which coincides well with the nominal coating thickness. As for the channel described above, rectification ($r \approx 3.5$) is observed for the uncoated channel. However, the rectification is not vanished after ALD-coating for the channel presented in Figure 12.1.2 ($r \approx 4.2$). This objection to EDL theory might be caused by a slightly lower IEP of the deposited TiO_2 layer. This was not observed for all TiO_2 coated single channels e.g. the one described above.

At pH ∼2 (Figure 12.1.2a, blue) and pH ∼9 (Figure 12.1.2a, red), the rectification ratios are ∼0.4 and ∼13.7, respectively. Thus, the surface charges induced by a pH value of the electrolyte beyond the IEP lead to the formation of an EDL, which selectively decreases ionic transport through the nanochannel.

Since TiO_2 is zwitterionic in aqueous solution [193], its surface is positively charged for pH ~2 and negatively charged for pH ~9 as schematically shown in Figure 12.1.2b. In agreement with EDL theory, the ionic current is lower at negative voltages due to cation selectivity at pH ~9, whereas anion selectivity results in a lower current at positive voltages at pH ~2. From the presented *I-V* curves the increase of the Debye screening length (λ_D^{tip}) was estimated by applying:

$$\lambda_D^{tip} = \frac{\varnothing_{pH=IEP}^{tip} - \varnothing_{pH\neq IEP}^{tip}}{2} \tag{12.1}$$

A Debye screening length of ~6 nm was obtained for changing the pH from ~5 to ~9. Varying the pH from ~5 to ~2 induces an EDL with a thickness of ~34 nm. The latter is two orders of magnitude higher as described in literature for the applied 1 M KCl solution [146]. Furthermore, at pH values beyond the IEP the TiO_2-layer provides enough surface charges to control the flow of ions through a conical nanochannel with ~92 nm tip diameter, which is huge compared to channels described in literature [33, 36, 162]. N. Sobel observed a strong reduction of the contact angle of water after deposition of ~10 nm TiO_2 onto a flat polycarbonate surface by ALD [182]. This showed the increase of hydroxyl groups at the membrane surface, whereas our results indicate the increase of these groups inside the nanochannel.

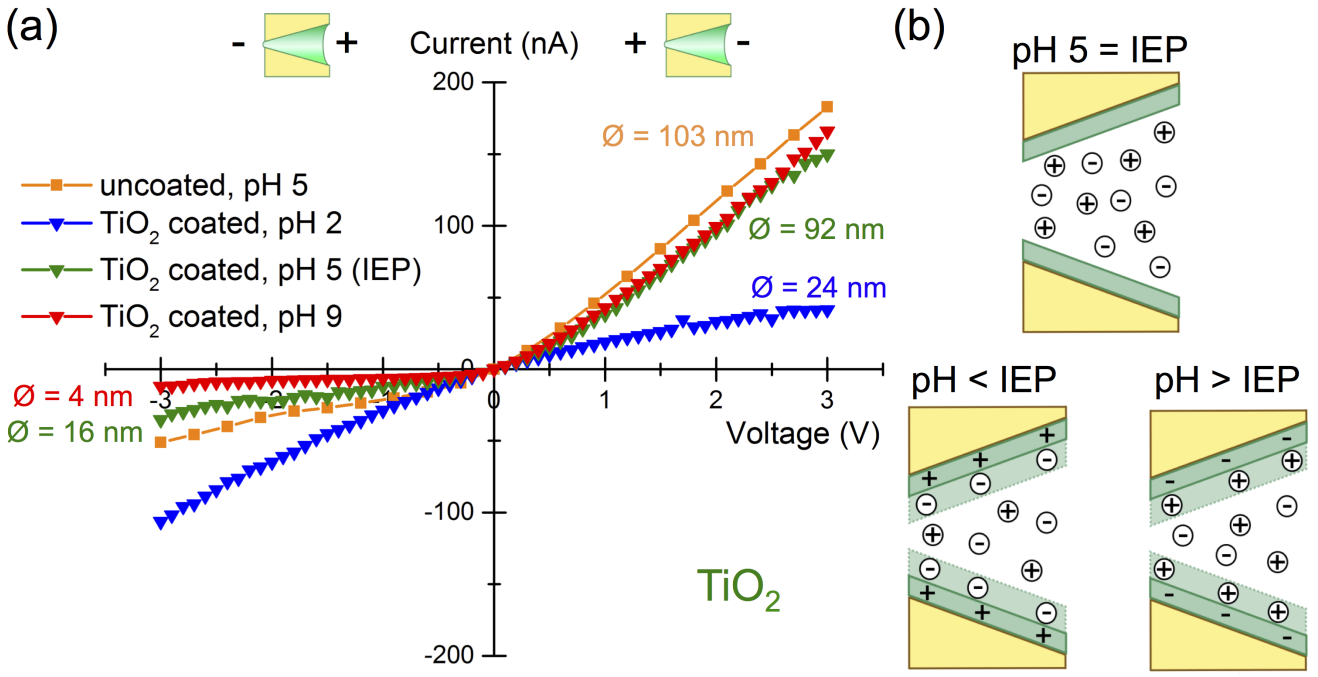

Figure 12.1.2.: (a) *I-V* curves of a TiO_2 coated nanochannel (~5 nm) with tip diameter ~92 nm recorded at pH 2, pH 5, and pH 9. (b) Schemes of the formed surface charges and the resulting EDL for various pH.

12.1.2 Ionic Conductance in Al_2O_3-Coated Channels

Figure 12.1.3a displays the *I-V* characteristics of a single conical nanochannel with a base diameter of ∼2.8 μm as measured at the free-standing replica by SEM (Figure 12.1.3b). After etching (Figure 12.1.3a, orange), an initial tip diameter of ∼117 nm is deduced from the ionic conductance by applying equation 4.6. After ALD-coating of nominal 15 nm Al_2O_3, the *I-V* curve was recorded at the IEP of Al_2O_3 (pH ∼9, Figure 12.1.3a, red). For negative voltages, a tip diameter of ∼103 nm is calculated, which does not coincide with the nominal coating thickness and the wall thickness obtained for the reference tubular nanocones. However, the analysis of cylindrical nanochannels by SAXS showed a variation of the deposited thickness over a larger area of the multichannel membranes coated with Al_2O_3, although STEM-in-SEM revealed uniform wall thicknesses (Section 7.2). This might occur for the conical channels, too, although the analysis by STEM-in-SEM of conical nanotubes released from multichannel membranes resulted in an alike morphology for all three materials (Section 8.1).

The ionic conductance of the untreated polymeric channel shows an almost ohmic behavior ($r \approx 1.1$). After ALD, the *I-V* curve recorded at the IEP of Al_2O_3 (pH ∼9) exhibits a rectification ratio of ∼0.62, which indicates the presence of positive surface charges. These might be induced by a higher IEP of the deposited Al_2O_3 layer.

Due to its amphoteric properties in aqueous solution, Al_2O_3 surfaces are positively charged for a pH value of the electrolyte smaller then the IEP as schematically drawn in Figure 12.1.3c [194, 195]. The formed EDL leads to an increase of the rectification ratio to ∼0.42 at pH ∼5 (Figure 12.1.3a, green). The rectification is with $r \approx 0.15$ even more pronounced at pH ∼2 (Figure 12.1.3a, blue) caused by less screening of the surface charges and thus an increased electric potential inside the channel. Quantification of the Debye length (equation 12.1) results in ∼12.5 nm for pH ∼5 and ∼22 nm for pH ∼2. These values are a factor of ∼42 respective ∼73 larger as reported for 1 M KCl solution [146]. The fact that increasing the acidity of the electrolyte induces enough surface charges at the Al_2O_3 layer to reduce the anion flow from base to tip demonstrates the control of the ionic current despite the huge tip diameter of the channel [33, 36, 162].

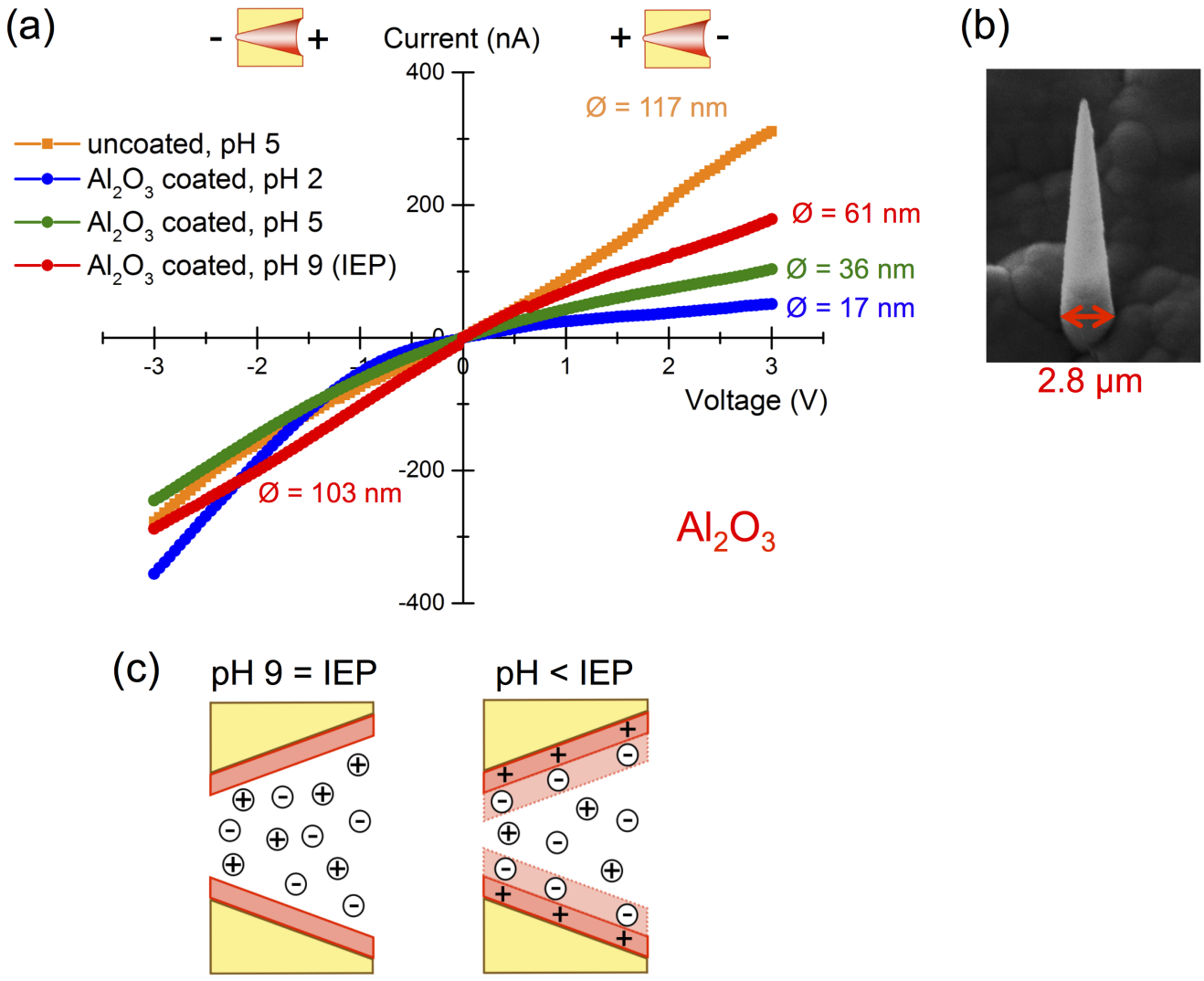

Figure 12.1.3.: (a) *I-V* curves of a single conical nanochannel investigated by ionic conductance measurements before and after ~15 nm Al_2O_3 deposition at various pH values of the electrolyte. (b) SEM image of the free-standing replica prepared after completing the *I-V* studies. (c) Schemes of surface charges and formed EDLs for uncharged and positively charged Al_2O_3 surface.

12.1.3 Ionic Conductance in SiO_2-Coated Channels

Figure 12.1.4a depicts the *I-V* measurements of a single conical nanochannel that exhibits a base diameter of ∼2.9 µm. This value was obtained by SEM-imaging of the free-standing reference nanocones. For the etched nanochannel, a tip diameter of ∼158 nm is calculated by applying equation 4.6 to the ionic currents recorded at positive voltages (Figure 12.1.4a, orange). Onto the sample, nominal 10 nm SiO_2 were deposited by ALD. Recording the *I-V* curve at the IEP of SiO_2 (pH ∼2, Figure 12.1.4a, blue) revealed a decreased ionic current. The corresponding tip diameter is ∼98 nm not in agreement with the nominal coating thickness. However, a much too strong reduction of the diameter after SiO_2 ALD was already observed for the single cylindrical nanochannel presented in Figure 11.2.3a. The uncoated channel leads to almost ohmic behavior ($r \approx 1.2$), which is not affected significantly by the SiO_2-coating ($r \approx 0.9$, pH ∼2). Both observations are in agreement with the absence of surface charges at the IEP according to EDL theory. Thus, conformal surface modification inside the single conical nanochannel is evidenced.

At pH values above the IEP, the zwitterionic properties of SiO_2 cause negative charging of the oxide surface in aqueous solution, which is shown schematically in Figure 12.1.4b [196, 197]. Thus, the formed EDL results in a rectification of $r \approx 1.9$ at pH ∼5. For measurements at pH ∼9, the rectification ratio is increased to ∼2.3, which is caused by less screening of the surface charges and the resulting increase of the electrical potential inside the channel. To compare the rectification ratios at pH ∼5 and pH ∼9, they were obtained at ∼2.5 V, since the ionic current increases steeply for voltages above 2.5 V at pH ∼5. However, this steep increase was not observed at other pHs measured subsequently indicating an unique artifact. Due to channel closing the measurements at pH ∼5 could not be repeated.

In contrast to the single cylindrical nanochannel surface modified with a SiO_2 layer deposited by ALD (Section 11.3.3), the behavior of the conical channel described above is in agreement with EDL theory. Quantitative analysis of the Debye length (equation 12.1) revealed ∼27 nm in the case of pH ∼5 and ∼33.5 nm in the case of pH ∼9. Thus, the thickness of the EDL is for both pH values two orders of magnitude higher than usually observed for 1 M KCl solution [146]. The strong dependence of the cation flow from base to tip through a nanochannel with such a huge tip diameter [33, 36, 162] shows the presence of a high amount of surface charges compared to the untreated polymeric nanochannel. N. Sobel measured the contact angle of water at the flat surfaces of pristine polycarbonate membranes and ∼10 nm thick SiO_2-layers deposited onto these surfaces by ALD [99, 182]. From the strongly reduced contact angle after the surface modification, an increase of hydroxyl groups was concluded. Our results obtained from the dependency of the ionic current on the pH value of the electrolyte indicate the same effect of the SiO_2-coating on the inner walls of the conical nanochannel.

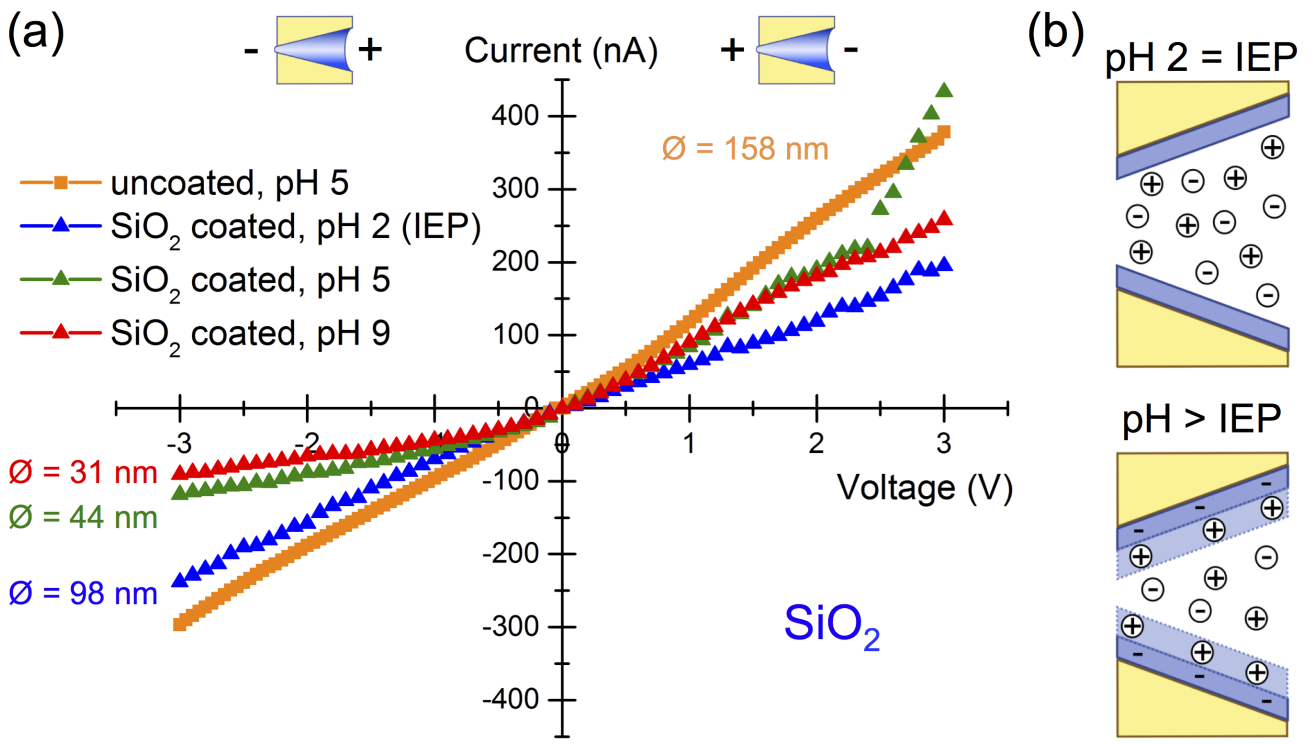

Figure 12.1.4.: (a) *I-V* characteristics measured at various pH for a nanochannel with ∼158 nm initial tip diameter, which is reduced to ∼98 nm after SiO_2 coating of nominal 10 nm. (b) Schematic of surface charges induced by the pH of the electrolyte and the subsequently formed EDL.

Overall, the pH dependency of TiO_2, Al_2O_3, and SiO_2 coated single conical nanochannels in ∼30-µm thick polycarbonate membranes are in good agreement with the EDL theory enabling the precise tailoring of these nanochannels for further studies as well as applications.

12.2 Nanofluidic Transistor

To externally control the flow of ions through a nanoconfinement, i.e. without changing the electrolyte, is of high interest for applications in sensing devices, chemical circuits, and ionic logic systems. Several set-ups of these so-called nanosized transistors are described in literature [8, 44–46]. All of these approaches require several complex fabrication steps. We present a novel set-up, which is achieved by a few, comparable simple steps due to the combination of ion-track technology and ALD.

In these first studies, the effect of an electrical field applied at the tip side of a conical nanochannel integrated in a polycarbonate membrane is discussed. We performed these experiments with TiO_2-coated nanochannels (Section 12.2.1) because of TiO_2 being a non-insulating material and having displayed the highest mechanical stability (see Section 8.4). Furthermore, the amphoteric properties of TiO_2 and the IEP value of pH ∼5 reward initially uncharged as well as oppositely charged surfaces (Section 12.2.2). To demonstrate the need of the TiO_2 layer for the observed effect, control experiments were performed with uncoated channels of equivivalent dimensions (Section 12.2.3).

12.2.1 TiO_2-Coated Conical Nanochannels as Junction Field Effect Transistors

A single conical nanochannel exhibiting a length of ∼30 µm and a base diameter of ∼2 µm was coated with ∼ 5 nm TiO_2 by ALD resulting in a tip diameter of ∼23 nm. This membrane was mounted in the electrochemical cell with a copper ring pressed onto the tip side of the TiO_2-coated membrane (see Section 6.6, Figure 6.6.1). Figure 12.2.1a displays the recorded *I-V* curves measured between the two electrodes source (S) and drain (D) for various gate voltages V_{GS}. Although they were measured at the IEP of TiO_2 (pH 5), a rectification of ∼4.5 occurs for $V_{GS} = 0$ V, which might be caused by a slightly too high pH of the applied electrolyte as observed for some other TiO_2 coated channels, too (Section 12.1.1, Figure 12.1.2). Increasing the gate voltage results in a more pronounced rectification and thus in a reduced negative current until it vanishes at the so-called pinch-off voltage $V_p \approx 21.5$ V. Qualitatively, a negative potential applied to the gate at the tip side of the conical nanochannel leads to an increase of negative surface charges (Figure 12.2.1b) and thus a negative potential inside the channel. Shape as well as value of this potential need to be simulated. Due to the observed rectification behavior it is assumed to be similar to the sawtooth-shaped potential reported by Siwy et al. for conical nanochannels exhibiting surface charges [39]. A higher applied negative gate voltage leads to a more negatively charged surface and thus an increased potential inside the channel, which is at the pinch-off voltage deep enough to trap all cations. Since the described gated nanochannel is conductive without applying a gate voltage, it is comparable to a JFET. Furthermore, an applied gate voltage leads to an electric potential inside the nanochannel, which results in counterion selectivity according to the EDL theory and thus majority carriers, which is one of the characteristics of a JFET. The discussed channel can be blocked by applying a negative potential to the tip side of the channel leading to the circuit diagram of a n-type JFET. However, applying a positive potential up to 30 V at the same position resulted in no reproducible ionic currents. For an applied negative potential being higher than the pinch-off voltage, the recorded ionic current is positive possibly caused by anions, the minority carriers, passing the channel from tip to base.
The error of the measured I_D is ∼2 % for 4 repetitions of the V_{DS} period. This reproducibility is high compared to the ∼10 % given by Schiedt et al. for conical channels in PET [17]. The obtained *I-V* curves were not influenced by applying the gate voltages with different step sizes, in various orders, and repeating the measurements days later evidencing the robustness and stability of this gated nanochannel.
To deduce the control curves presented in Figure 12.2.1c and make the gated ionic current visible at a first glance, the *I-V* curves of the rectified branch were drawn according to the conventions commonly applied for n-type JFETs. Thus, the negative measured V_{DS} and I_D are shown with positive signs for various gate voltages in Figure 12.2.1d. The control curves of the specific $V_{DS} = 1$, 1.5, 2, 2.5, and 3 V are shown with negative gate voltages on the x-axis, since the negative pole of the gate was contacted to the nanochannel. For all control curves, I_D stays constant until it decreases steeply at $V_p \approx 21.5$ V demonstrating the behavior of a lossless switch. The pinch-off voltage V_p needed to block the ionic current is very high compared to earlier studies [46]. However, in the present set-up, the gate voltage is not applied directly to the tip of the nanochannel but via the copper ring with a diameter of ∼16 mm. Due to the poor conductive properties of TiO_2, there is a potential drop between the copper ring and the nanochannel in the ∼5 nm thick TiO_2 layer on the surface of the membrane. As consequence, V_p increased to ∼21.8 V by applying a copper ring with a diameter of ∼19 mm for the same membrane.

The same experiment performed for an alike single conical nanochannel coated with ~5 nm TiO_2 exhibiting a tip diameter of ~27 nm yielded the behavior of a lossless switch, too. The obtained V_p of ~21.7 V is slightly higher showing the tendency that for a larger tip diameter an increased electrical potential is needed to block the channel.

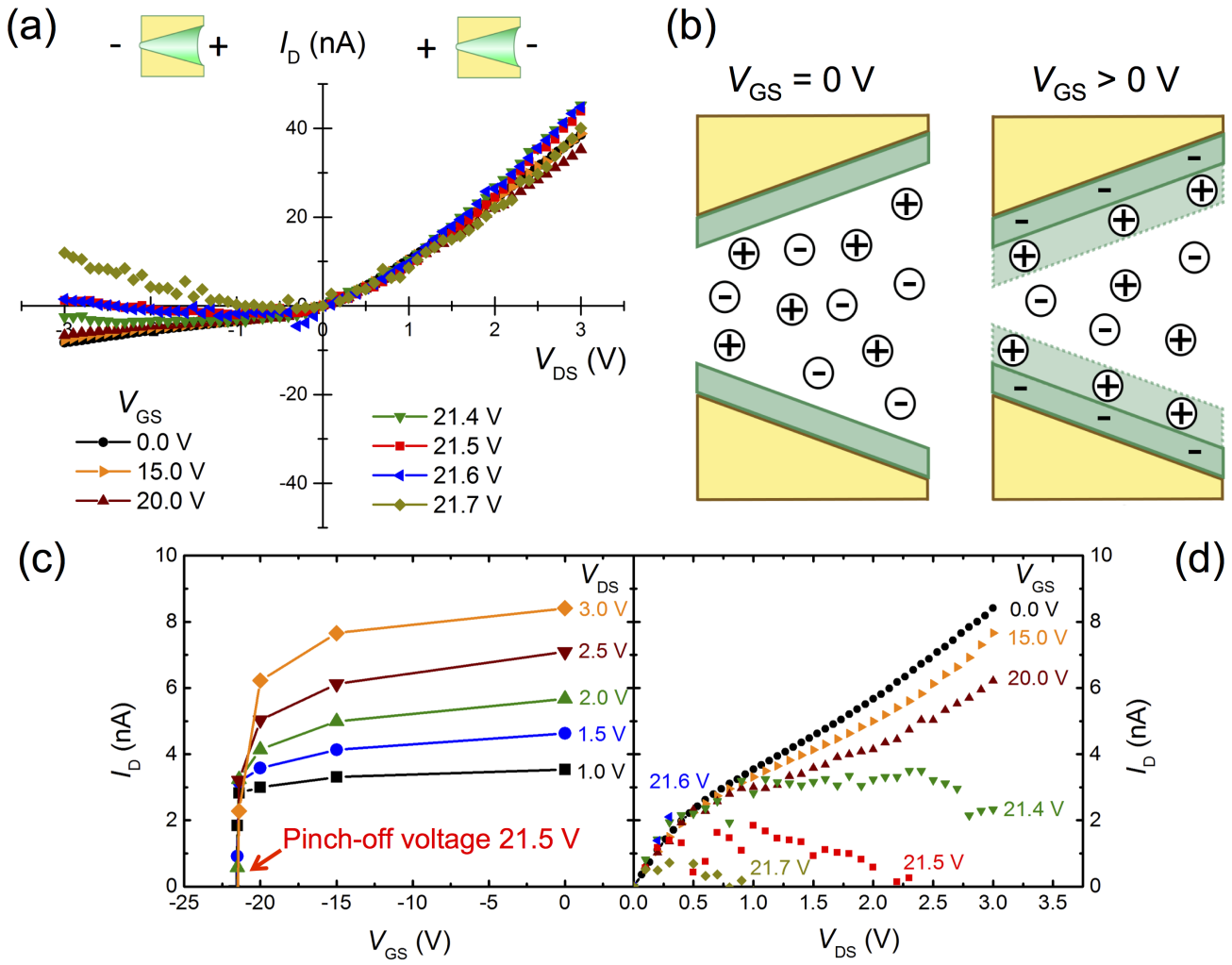

Figure 12.2.1.: (a) *I-V* curves of a single conical nanochannel with a tip diameter of ~23 nm after ~5 nm TiO_2 ALD-coating for various gate voltages V_{GS} measured by using 1 M KCl as electrolyte at pH ~5 (IEP of TiO_2). (b) Schemes explaining the effect of the gate voltage in a qualitative way. (c) Control curves for various drain-source voltages V_{DS} deduced from the corresponding ionic currents of the rectified branch shown in (d). The uncertainty of I_D is ~2 %.

In contrast to the usual behavior of a FET, the studied TiO_2-coated nanochannels show no slow decrease in the control curves of the current until the pinch-off is reached. Thus, the energy loss for switching the channel from being open to being blocked is low and the ionic current adjusts rapidly to the status of the switch induced by the gate voltage. This is interesting for the application of gated TiO_2-coated conical nanochannels in high frequency switching operations. The observed independence of the pinch-off voltage on the drain-source voltage indicates a well-defined working point proving the suitability of the presented nanochannel for switching applications. However, a fine regulation of the transported ionic

current is not possible with this set-up and the above mentioned simulations of the electric potential inside the gated nanochannel that is induced by the gate voltage may help to understand this behavior.

12.2.2 Blocking of Gated TiO_2-Coated Conical Nanochannels Dependent on the pH Value of the Electrolyte

To study the influence of surface charges on the gating of a TiO_2-coated conical nanochannel in polycarbonate, the pH value of the 1 M KCl solution was varied. For no applied gate voltage ($V_{GS} = 0$ V), Figure 12.2.2a displays the *I-V* curves recorded after deposition of ∼5 nm TiO_2 at pH ∼2, pH ∼5, and pH ∼9. At the IEP of TiO_2 (pH ∼5, blue), the calculation of the tip diameter by applying the higher ionic currents at positive voltages results in ∼47 nm. Additionally, a rectification ratio of ∼13.3 is observed maybe caused by a lower IEP of the coating, although this was not observed for all TiO_2-coated nanochannels (see Section 12.1.1, Figure 12.1.1).
Due to its amphoteric properties in aqueous solution [193], TiO_2 is negatively charged at pH ∼9 (Figure 12.2.2b). Thus, the *I-V* curve recorded at this pH value without applying a gate voltage exhibits a rectification ratio of ∼16.5 as shown in Figure 12.2.2a (red).
At pH ∼2 of the aqueous 1 M KCl solution, the TiO_2 layer inside the channel is positively charged [193] (Figure 12.2.2b). Figure 12.2.2a (blue) displays the *I-V* characteristics measured at this pH value. However, the recorded current is lower at negative voltages leading to a slight rectification of $r \approx 1.35$, which is not in agreement with the expected positive surface charges and the results of other TiO_2-coated channels investigated at pH ∼2 (Section 12.1.1, Figure 12.1.2).
The following paragraphs discuss the behavior of the ionic current at these three pH values for various applied gate voltages.
Figure 12.2.3a shows the *I-V* characteristics of the TiO_2-coated conical nanochannel introduced in Figure 12.2.2 at pH ∼5 for different gate voltages. As for the gated ALD-coated channel presented above, the increase of the gate voltage enhances the rectification until the negative current is blocked completely at $V_p^{pH5} \approx 22.7$ V. Assuming the sawtooth-shaped potential calculated by Siwy et al. for conical channels with surface charges [39], the gate voltage is at the pinch-off voltage high enough to form a suitable amount of negative surface charges to enhance the electrical potential inside the channel enough for trapping all cations (Figure 12.2.3b). At $V_{GS} > V_p$, anions moving from tip to base may cause the recorded positive current.

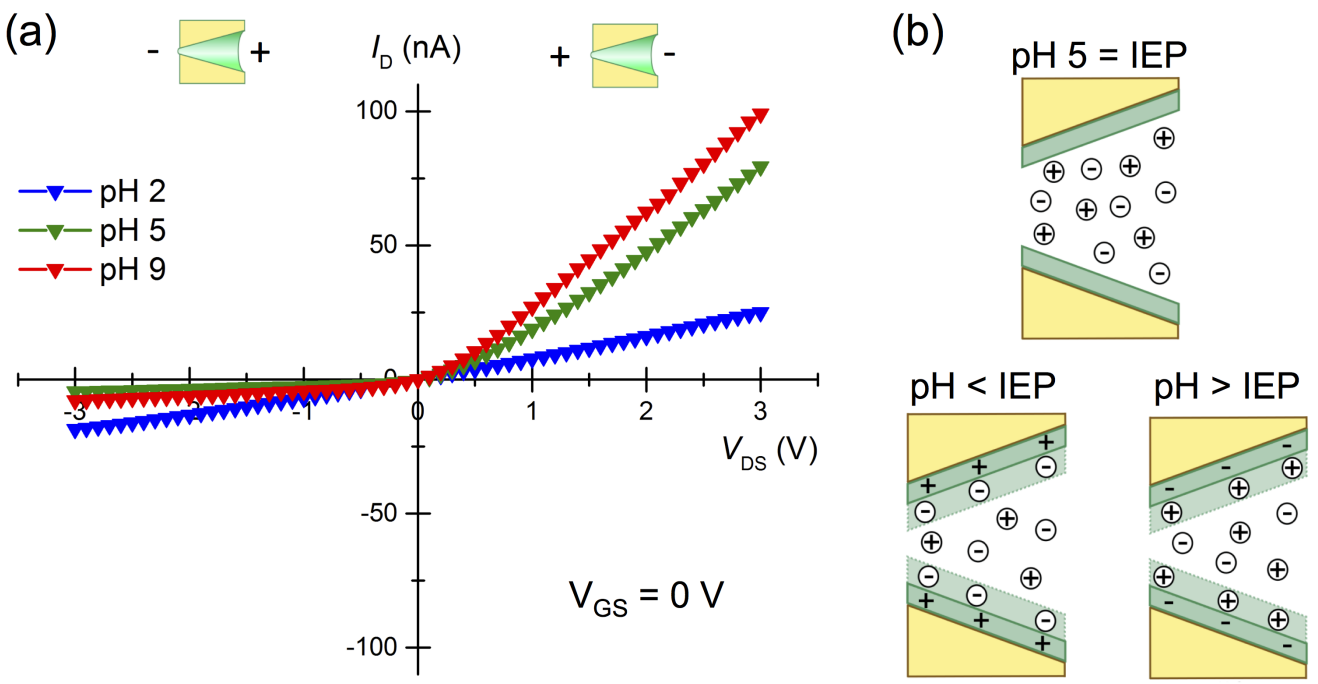

Figure 12.2.2.: (a) For various pH values of the 1 M KCl solution, the *I-V* curves of a single conical nanochannel exhibiting a tip diameter of ∼47 nm after ALD of nominal 5 nm TiO_2 are displayed for $V_{GS} = 0$ V. (b) Schematics show the surfaces charges expected from EDL theory.

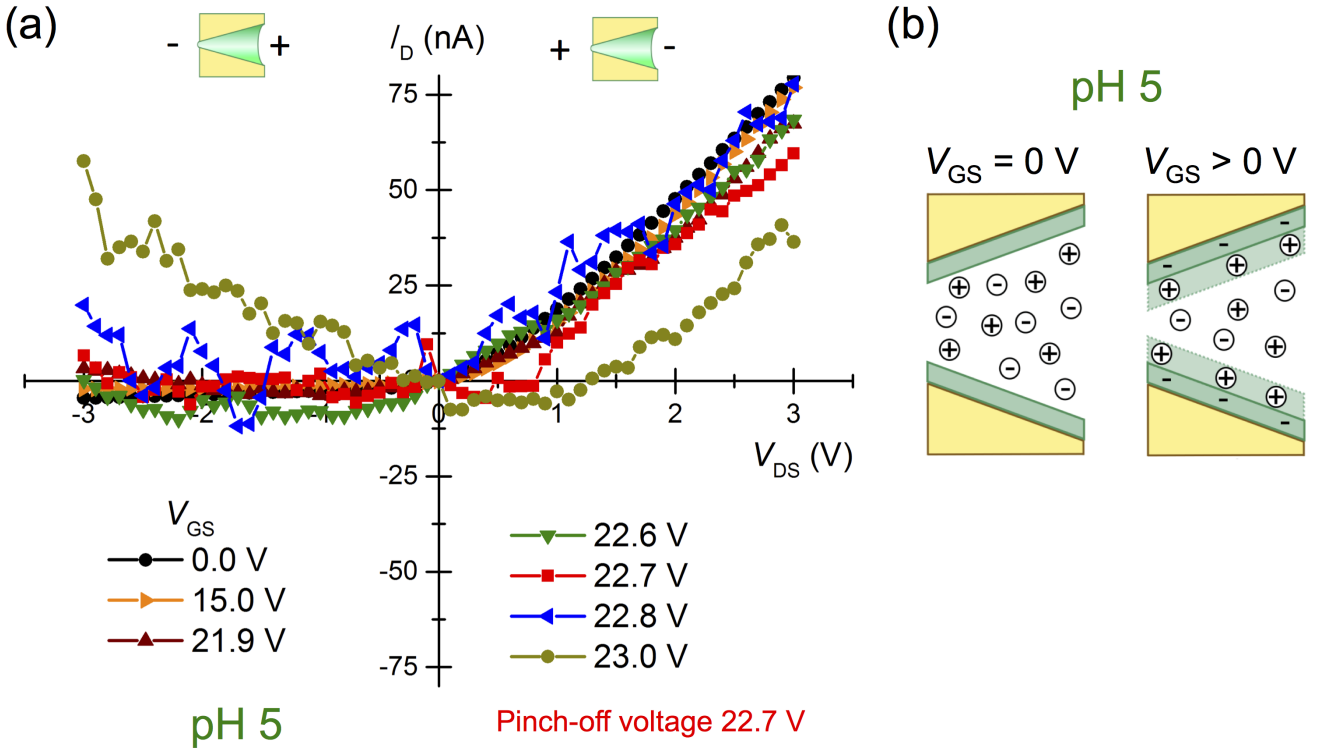

Figure 12.2.3.: (a) *I-V* curves of the single conical nanochannel coated with ∼5 nm TiO_2 and a tip diameter of ∼47 nm that was introduced in Figure 12.2.2 for various gate voltages V_{GS} recorded at pH ∼5 of the electrolyte. (b) Schematics explaining the blocking of the ionic current qualitatively.

For different gate voltages, the *I-V* curves of the channel presented in Figure 12.2.2 were recorded at pH ~9 and are depicted in Figure 12.2.4a. By applying a gate voltage, the rectification ratio is increased until the negative ionic current vanishes at a pinch-off voltage of $V_p^{pH9} \approx 22.6$ V. Thus, the pinch-off voltage of an initially negatively charged surface is slightly lower compared to the one for an approximately uncharged surface at the IEP (Figure 12.2.3a). This indicates a tendency, which is in agreement with the sawtooth-shaped potential, since an already negatively charged surface results in an intrinsic potential inside the channel, which already traps some cations. Thus, a lower gate voltage provides enough additional negative charges to enhance the potential for trapping all cations.

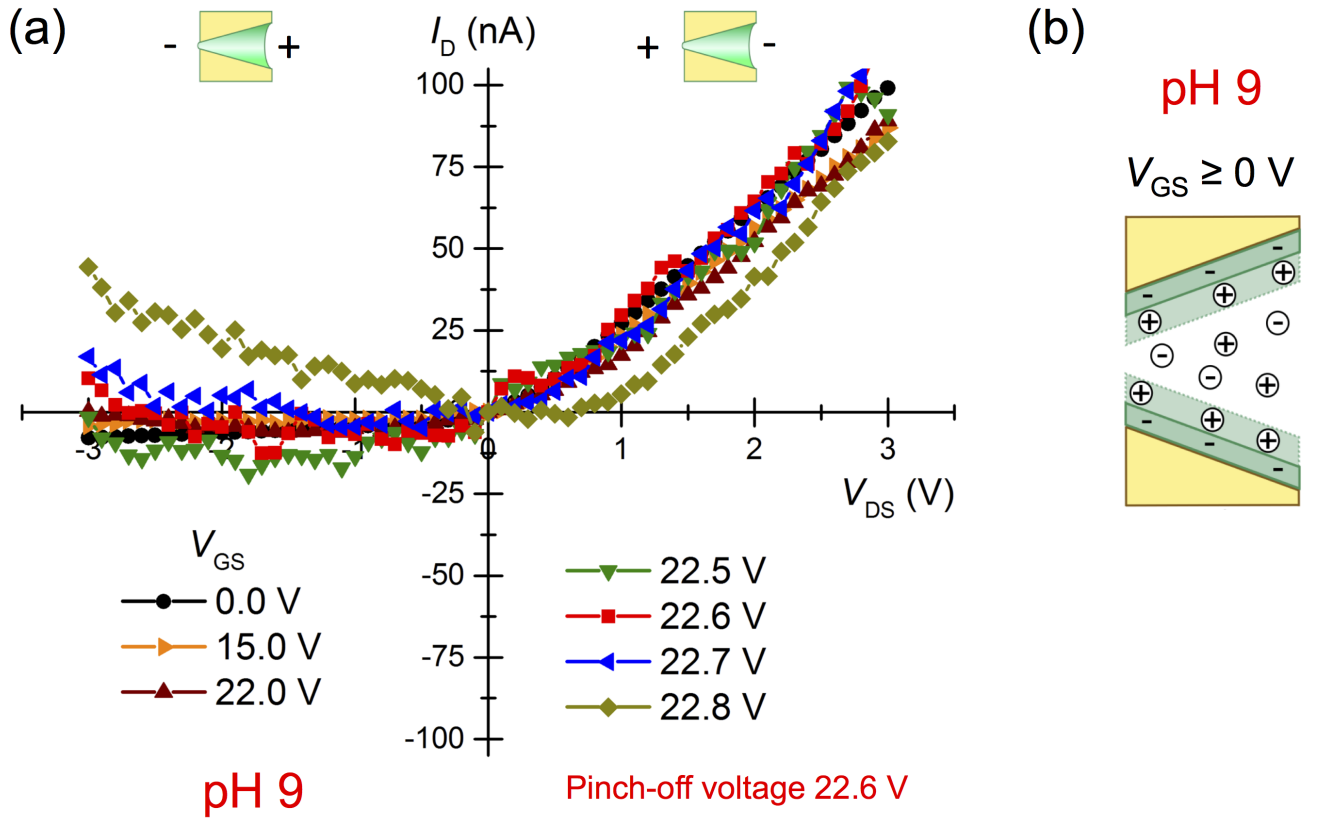

Figure 12.2.4.: (a) *I-V* measurements at pH ~9 of the 1 M KCl solution of the gated and TiO_2-coated single conical nanochannel studied in Figure 12.2.2 for various gate voltages V_{GS}. (b) For an initially negatively charged surface the scheme shows the effect of the gate voltage in a qualitative way.

Figure 12.2.5a displays the *I-V* characteristics of the gated channel introduced in Figure 12.2.2 measured at pH ~2 for different gate voltages. At pH ~2 of the aqueous 1 M KCl solution, the TiO_2 layer inside the channel is positively charged [193] (Figure 12.2.5b). As discussed above, the current at negative voltages is slightly lower without gate voltage, ($r \approx 1.35$), which is not in agreement with the expected positive surface charges. However, the rectification ratio obtained at $V_{GS} = 10$ V is ~0.56 and coincides with the initially positively charged surface and the resulting anion selectivity. The *I-V* curves of this sample were reproducible, although the cation selectivity at $V_{GS} = 0$ V is not understood so far, since it disagrees with the results of other TiO_2-coated channels investigated at pH 2 (Section 12.1.1) and EDL theory. A gate voltage of ~15 V results in a rectification ratio of ~1.1 and thus changes the direction of rectification

again demonstrating the switch of an ALD-coated conical nanochannel from anion- to cation selectivity by gating (Figure 12.2.5b). For all $V_{GS} \geq 15$ V, the surface of the nanochannel is negatively charged and the rectification ratio is increased by applying a higher gate voltage. The ionic current vanishes at $V_p^{pH2} \approx 22.9$ V, which is slightly higher compared to the one for an approximately uncharged channel surface at pH ~5 (Figure 12.2.3a). Therefore, an initially positively charged surface requires by trend a higher gate voltage in the presented set-up to block the negative current completely. Taking the sawtooth-shaped potential into account, the negative charges provided by the gate voltage first have to neutralize the initially positive surface charges (due to the pH value of the electrolyte) before the surface starts to be negatively charged forming a potential inside the channel that traps all cations at the pinch-off voltage.

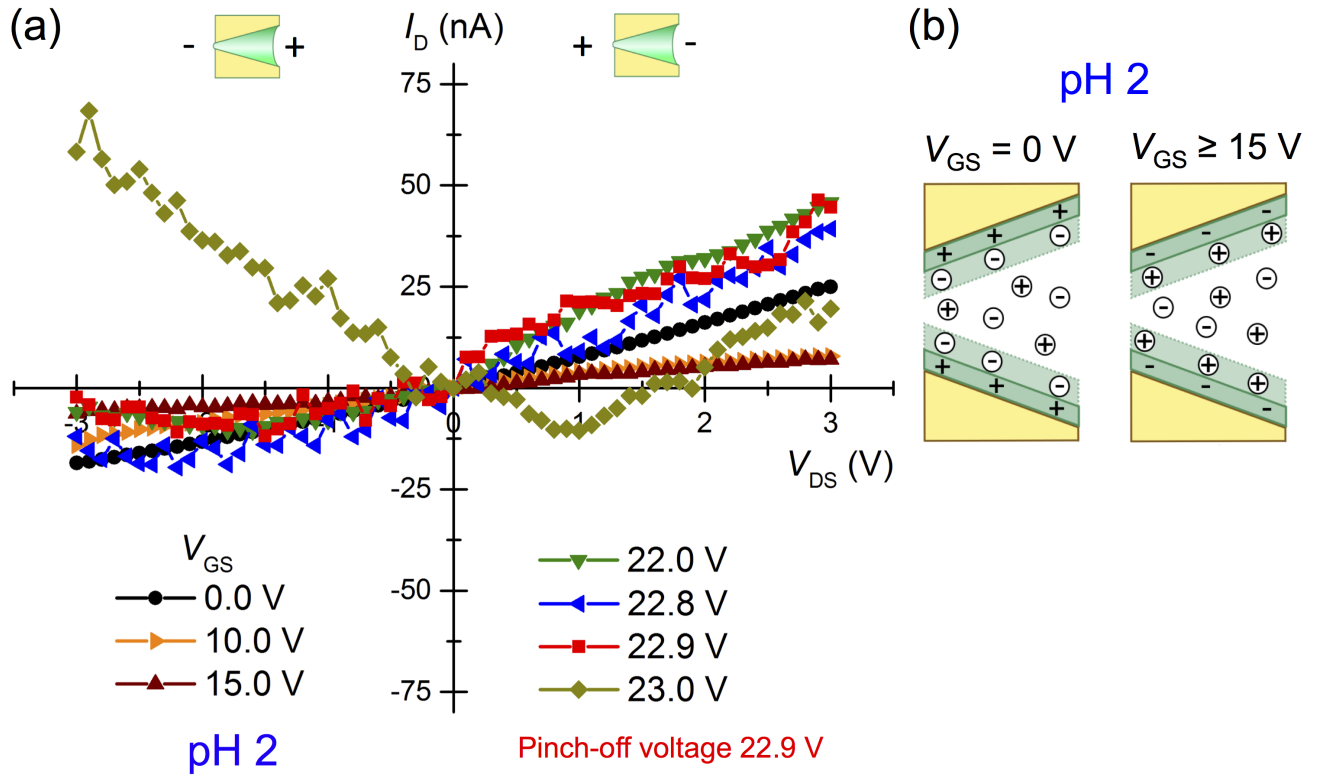

Figure 12.2.5.: (a) Ionic conductance of the TiO_2-coated single conical nanochannel studied in Figure 12.2.2 for various gate voltages V_{GS} recorded at pH ~2. (b) Schemes showing the effect of the gate voltage for an initially positively charged surface.

The experiments presented in this section demonstrate the gating of single conical nanochannels embedded in a polycarbonate template after ALD coating of TiO_2. Furthermore, the sign of the initial surface charges adjusted by variation of the pH value of the electrolyte caused a slight change of the pinch-off voltage, which opens up the application of such channels as pH sensors.

12.2.3 Control Experiment with Uncoated Conical Nanochannel

To prove the contribution of the ALD coating for the blocking of a conical nanochannel, control experiments were performed on uncoated channels at the IEP of polycarbonate (pH ~5). Figure 12.2.6a displays the representative *I-V* curves of an uncoated nanochannel with tip diameter ~17 nm for various gate voltages. In the detailed view of the branch to be rectified, no blocking is observed for gate voltages up to 30 V (Figure 12.2.6c). There is a slight decrease of the ionic current at $V_{GS} = 10$ and 15 V but I_D increases for higher V_{GS} in contrast to the TiO_2-coated channels. The deduced control curves, which are shown in Figure 12.2.6b, confirm the absence of a pinch-off voltage for the uncoated nanochannel, although it exhibits a smaller tip. The increase of I_D for gate voltages above 15 V may be caused by polarization of the polymer. From the performed control experiment, it is concluded that the surface modification by ALD enables the gating of the polymeric conical nanochannel due to the achieved semiconducting layer inside the channel and on the membrane surface.

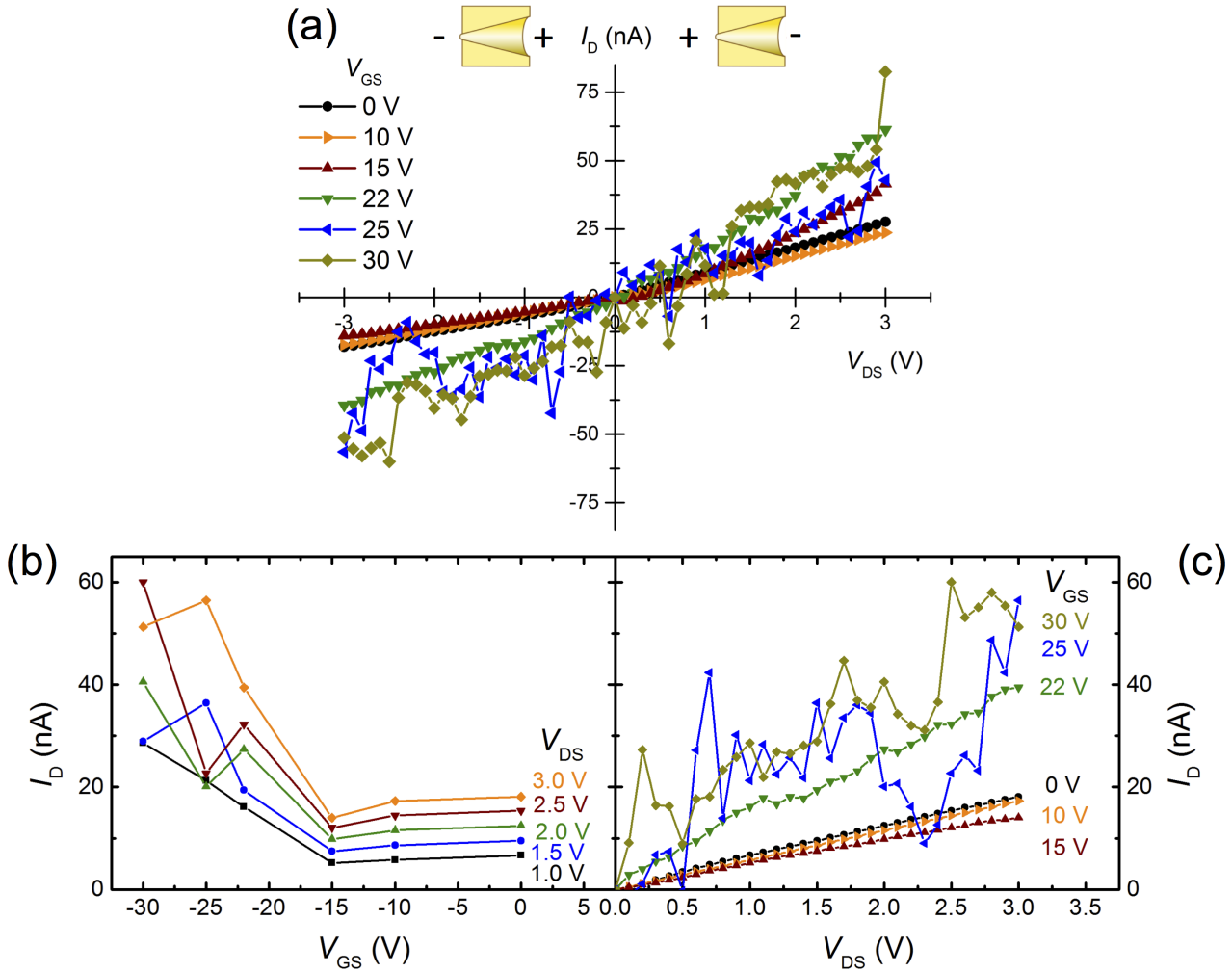

Figure 12.2.6.: (a) Representative *I-V* curves of an uncoated single conical nanochannel with a tip diameter of ~17 nm recorded at pH ~5 (IEP of polycarbonate) for various gate voltages V_{GS}. (b) For various drain-source voltages V_{DS}, the control curves were deduced from the corresponding ionic currents of the rectified branch shown in (c).

12.3 Comments on Channel Closing during Synthesis and Ionic Conductometry in Conical Channels

Many steps are required for the synthesis and characterization of ALD-modified single conical nanochannels. Each treatment can cause deformation or closing of the channel, which results in measuring artifacts or uselessness of the channel, respectively. During the test series presented in this work, rough estimations of the yield as well as the reproducibility were obtained.

Directly after asymmetric etching the single channels were stored in deionised water. The *I-V* curves applied for the determination of the base diameter were measured within a few hours. For ∼70 % of the analyzed single channels, a current was recorded. However, the tip diameters varied strongly due to the variation of the breakthrough time up to 30 s. The latter is also reported by L. Burr [122] and was probably caused by one side of the polycarbonate membranes being rough in the µm range, which resulted in different lengths of the ion-tracks depending on their position. During etching the moment of breakthrough was difficult to identify in the current-time curves, and thus only ∼10 % of the open conical channels exhibited the desired tip diameter. This low yield is in agreement with the observations of L. Burr [122].

The samples were dried shortly before they were inserted into the ALD chamber. The coating was followed by *I-V* measurements to deduce the reduction of the tip diameter. In ∼70 % of the cases, the change of the tip diameter coincided with the nominal coating thickness. Thus, in total ∼50 % of the channels can be coated successfully, whereas tailored initial and inner tip diameter were obtained for only ∼7 % of the samples. As for single cylindrical channels, the deformation or closing of the channels is ascribed to effects during drying, e.g. capillary forces because of the reference nanotubes demonstrating conformal ALD coatings.

However, the SiO_2-coated single channels often exhibited too small tip diameters, which might be avoided by etching directly before ALD as performed for TiO_2 and Al_2O_3 depositions and suggested for the symmetric channels.

ALD-coated nanochannels that were open remained stable for three months compared to several days for uncoated channels. Furthermore, the risk of channel closing during exchanging the KCl solution and the required rinsing in between was reduced for coated channels. In comparison to cylindrical channels, the asymmetric channels were more robust in terms of staying open. Thus, the observations demonstrate the advantage of ALD-coating and conical shape.

In addition, the recorded ionic currents were in the range of several tens or a few hundred nA leading to a slightly lower sensitivity to vibrations and external fields (compared to cylindrical channels). However, this increase in stability of the measurements was not endangered by the reduction of the concentration of the electrolyte from 1 M to 0.1 M, which would have reduced the current by almost a factor of 10 (equation 4.5) [180].

13 Conclusions of Ionic Transport Measurements

ALD is suitable to reduce the diameter of cylindrical and conical single nanochannels in a controllable manner, since the surface modification is alike in single- and multichannel membranes. The tailoring provided by TiO_2, SiO_2, and Al_2O_3 coating allows to investigate the influence of the surface material on the ionic conductance.

All cylindrical ALD-coated channels showed an ohmic behavior in the *I-V* curves independent on the pH value of the electrolyte evidencing cylindrically shaped channels as well as symmetric surface charge distributions inside the channels. For TiO_2- and Al_2O_3-coated nanochannels, the ionic conductance was decreased for electrolytes beyond the ioselectric point (IEP). In agreement with nanofluidics theory, the amphoteric properties of the oxides caused surface charges in these cases, which led to the formation of an electrical double layer (EDL) and thus reduced ionic transport due to counterion selectivity. In contrast to EDL theory, many SiO_2-coated nanochannels showed the lowest ionic conductance at the IEP maybe due to an inhomogeneous and position-dependent surface charge density as calculated for cylindrical silica nanopores [200].

In contrast to the results obtained for cylindrical single channels, the conical ones showed ohmic behavior at the IEP only in the case of SiO_2-coated and some TiO_2-coated channels, for which the absence of surface charges was concluded. For the other nanochannels, the rectification might be caused by slightly different IEPs of the surface material inducing surface charges and thus an asymmetric electrical potential inside the nanochannels. A series of *I-V* curves recorded at pH values from 1 to 12 in steps of 1 could clarify this in the future. In agreement with nanofluidics theory, the rectification ratio, i.e. the counterion selectivity and thus the direction of selective transport, depended on the sign of the surface charges. In addition, the rectification was more pronounced at pH values further apart from the IEP coinciding with less screening of the surface charges and thus an increased electric potential inside the channel.

For both geometries, quantification of the Debye screening lengths led to values that are up to two orders of magnitude larger than reported in literature for the applied 1 M KCl solution [146]. A strong increase of hydroxyl groups at the flat surface of polycarbonate membranes after ALD coating of $\sim$10 nm TiO_2 and SiO_2 was observed in contact angle measurements performed by N. Sobel [99, 182]. The results of the presented ionic transport investigations indicate the increase of these groups inside cylindrical and conical nanochannels. This is validated by preliminary studies of SiO_2-coated network templates with dynamic-nuclear-polarization nuclear-magnetic-resonance spectroscopy (DNP-NMR) performed by T. Gutmann (Prof. Dr. G. Buntkowsky, Chemie, TU Darmstadt).

During the *I-V* measurements of ALD-coated single nanochannels, hysteresis was observed dependent on the deposited oxide, its layer thickness, and the delay time between the voltage steps. Systematic studies including membranes without channel and ALD coating could attribute the hysteresis to capacitance, which was probably mainly caused by the oxide layer deposited on the surfaces of the membrane.

Removing these ALD layers by e.g., reactive-ion etching may clarify, to which degree the coating inside the nanochannel contributes to the hysteresis. As reported in literature [14], hysteresis was avoided by increasing the delay time. For the nanostructures analyzed here, delay times of 3 s (TiO_2) and 10 s (SiO_2 and Al_2O_3) were suitable.

The yield of the synthesis of ALD-coated single cylindrical nanochannels was ∼20 % with a reproducibility of the dimensions for almost all channels. The surface modification increased the robustness of the open channels from several days up to eight weeks. Almost half of the synthesized single conical nanochannels could be used for *I-V* measurements. Due to the strong variations of the breakthrough time, the yield was only ∼7 % if a specific tip diameter was required. Compared to cylindrical channels, the conical ones gained more stability from the ALD coating resulting in nanochannels beeing open for three months. For both geometries, the risk of closing during exchange of the electrolyte and rinsing the channel in between is significantly lower for coated channels. In the case of asymmetric channels, a larger volume is confined making a conical channel more robust against blocking by contaminations.

The surface charges of the single cylindrical and conical nanochannels depended on the surface material deposited by ALD due to the various IEPs of the utilized oxides. Therefore, ALD provides the adaptation of polymeric nanochannels to a broad range of acidic and basic environments without introducing surface charges and affecting the geometry of the channel. On the other hand, the oxide layers can be utilized to sense changes of the pH value of the electrolyte inside the channel for various initial pH values. Due to the observed stabilization of the nanochannels, the ALD coating increases their suitability for applications.

As first test of an application, the combination of ion-track technology and ALD in single conical nanochannels was used to realize a nanofluidic transistor. The fabrication steps as well as the set-up are simple compared to the approaches reported in literature [8, 44–46]. A copper ring pressed onto the tip-side of the membranes that were coated with a ∼5 nm thick TiO_2 layer acted as gate electrode by applying a negative potential to it. Increasing the gate voltage led to rectification of the ionic current through the nanochannel, i.e. reduced the negative current, until it vanished at the pinch-off voltage. Qualitatively, the gate potential led to negative surface charges and thus a negative potential at the tip and inside the conical nanochannel. Simulations of this potential are required to define shape and value of the induced potential. However, the observed rectification indicated a sawtooth-shaped potential as reported by Siwy et al. for conical nanochannels with surface charges [39]. At the pinch-off voltage, the gate voltage was suitable high to increase the potential inside the channel deep enough to trap all cations. The conductance without applying a gate voltage as well as the presence of majority charge carriers due to the counterion selectivity of the channel are characteristics of a junction field effect transistor (JFET). The blocking of the channel was induced by a negative gate voltage and thus the circuit diagram of a n-type JFET was set up. Compared to studies reported in literature, the pinch-off voltage was high [46]. However, the copper ring exhibiting a diameter of ∼16 mm did not apply the gate voltage directly to the tip of the nanochannel resulting in a potential drop between the copper ring and the nanochannel due to the semiconducting TiO_2-layer. Deposition of a metallic layer around the tip and contacting the gate electrode to this metallic film is planned for further experiments in order to decrease the pinch-off voltage. However, the presented gated nanochannels prohibited the fine regulation of the ionic current, which might be explained by simulations of the electrical potential inside the channel induced by the

gate voltage.
The control experiment performed at uncoated nanochannels showed that the TiO_2-layers deposited by ALD inside the channel and on the template surfaces are essential for blocking the ionic current. The pinch-off voltage seemed to be adjustable by adaptation of the tip diameter as well as the usage of a copper ring with larger diameter. Variation of the pH value of the electrolyte, slightly changed the pinch-off voltage without modifying the set-up including the studied nanochannel. The gating of TiO_2-coated single conical nanochannels embedded in polycarbonate membranes resulted in set-ups comparable to n-type JFETs showing lossless switch behavior with a well-defined working point as well as an influence of the pH value of the electrolyte on the pinch-off voltage. Besides investigations regarding the application in high frequency operation, the latter provides the application as pH sensors. The suitability for applications is confirmed by the high reproducibility of the ionic currents (uncertainties of the ionic current through the channel were $\sim$2 %) as well as the independence of the measurements on the step size of the gate voltages, their order, and the time in between (up to days).

14 Conclusions and Outlook

ALD is suitable for tailored coating of high aspect ratio nanostructures exhibiting various geometries and complex porosity. The parameters of the TiO_2, SiO_2, and Al_2O_3 deposition processes needed to be adjusted to temperatures below 140 °C as well as to the high aspect ratio of the nanochannels. Investigations of the morphology demonstrated shape-conform and homogeneous depositions along the entire nanochannel lengths in cylindrical, conical, and network nanochannels for all three oxides. Independent from the channel geometry, pure composition as well as layer-by-layer growth were evidenced with complementary characterization methods. The precisely controllable coating process opens up novel tailoring of porous polymer membranes. For instance, the commercially available polymeric etched ion-track membranes used as specific filters can be adjusted to smaller channel sizes and environments exhibiting different pH values.

For all studied nanostructures, dissolution of the polymer template released self-supporting nanotubes. Their mechanical stability enabled the investigation of individual nanostructures. Cylindrical nanotubes were fabricated with inner diameters below 10 nm corresponding to aspect ratios of more than 3000 demonstrating the conformal coating of parallel aligned nanochannels with aspect ratios being higher than described in literature [21, 92, 95–99]. Small angle X-ray scattering (SAXS) analysis applying synchrotron radiation revealed that the surface modification of equivalent channels with inner diameters below 5 nm is still a challenge probably due to diffusion limits. Further extension of exposure and purge times, smaller precursor molecules, e.g. $TiCl_4$ in the case of TiO_2, or the repetition of each half-cycle directly after each self as performed by N. Sobel [182] might overcome this limit.

Free-standing conical nanotubes with a height of ∼30 µm were synthesized in uniform arrays of few cm^2 size. The transfer of the preparation method to single nanocones allowed the comparison of the etching processes in multi- and single-channel membranes showing a faster etching of the tips in membranes irradiated with one single ion (factor ∼2). The agreement of the base etching rates in the case of multichannel membranes etched under identical conditions validates in general the estimation of the base diameter at a multichannel reference membrane [14, 16, 80, 116, 171, 172]. Furthermore, ALD coating is an interesting alternative to produce replica for geometry analysis. Compared to the usually applied electrodeposited nanowires [107, 172–174], ALD is a simpler synthesis technique. For applications requiring free-standing nanostructures such as drug delivery directly into cells [21], conical nanotubes are advantageous due to their high mechanical stability. In addition, single free-standing tubular nanocones provide the investigation of controlled drug delivery into one specific component of the cell.

The networks of oxide nanotubes were free-standing over several hundred of μm^2. Embedded in the template or released, the networks are promising for systematic investigations of processes like filtration or catalysis. Compared to nanowire arrays and networks as well as nanotube arrays, the nanotube networks provide an increased surface area and the combination of ion-track technology with ALD allows the tailoring of all properties of a well-defined porous structure: thickness of the sample, amount and material of tubes, angle of crossings, as well as outer and inner tube diameter.

The conformal ALD coating preserves the smooth surface of the polycarbonate nanochannels reflected by smooth inner tube walls. These channels provide well-defined walls compared to Al_2O_3 depositions in polyethylene terephthalate (PET) [43] as well as channels modified by chemical [16, 80] or electroless techniques [65, 66]. First ionic transport studies of single cylindrical and conical channels evidenced that the deposition of TiO_2, SiO_2, and Al_2O_3 by ALD is equal for multi- and single-channel polycarbonate membranes. Furthermore, the surface modification stabilized the polymeric nanochannels and thus improved their suitability for applications.

For single cylindrical channels, ohmic behavior at various pH values of the electrolyte revealed symmetric channel geometry and surface charge distributions. In the case of conical geometry, a linear dependence of the ionic current on the voltage was obtained for SiO_2- and some TiO_2-coatings at the isoelectric point (IEP) showing the absence of surface charges, whereas for the other samples rectification was observed. The latter might be caused by slightly different IEPs, which could be validated by varying the pH value of the electrolyte from 1 to 12 in steps of 1 in the future.

Overall, the pH dependence of the presented single nanochannels was in agreement with nanofluidics theory. The calculations of the Debye screening length resulted in values that are up to two orders of magnitude larger than reported in literature for 1 M KCl solution [146]. Although the amount of analyzed nanochannels was not sufficient for statistical significance, this indicates an increase in surface charges compared to uncoated channels. Contact angle studies by N. Sobel revealed a strong increase of hydroxyl groups at the flat surface of polycarbonate membranes after ∼10 nm TiO_2- and SiO_2-coating by ALD [99, 182], whereas the results presented in this work indicate the increase of hydroxyl groups inside cylindrical and conical nanochannels. First dynamic-nuclear-polarization nuclear-magnetic-resonance spectroscopy (DNP-NMR) analyses performed by T. Gutmann (Prof. Dr. G. Buntkowsky, Chemie, TU Darmstadt) confirmed the functionalization of the inner channel walls by SiO_2 ALD. Due to the large Debye length, the surface modification with oxides provided a good tool to control the flow of ions through channels with diameters up to 100 nm, which are huge compared to commonly applied channel dimensions [17, 33, 36, 162]. The estimation of the Debye length from *I-V* measurements with statistical significance requires the analyses of many more samples and is integrated in the second period of the DFG project. The present results are very promising in terms of designing single channels with respect of their chemical and physical nature and thus providing novel options for functionalizing polymeric channels. For instance, SiO_2 coatings allow to utilize silanization. Additionally, the ALD-coated channels can be applied to sense changes of the pH value of a given analyte inside the channel for different initial pH values. Furthermore, ALD can be utilized to adapt polymeric nanochannels to a broad range of acidic and basic environments without inducing surface charges and affecting the channel shape.

Nanofluidic transistors were realized by integrating a gate electrode in a straight-forward set-up utilizing an electrochemical cell, which is a simple approach compared to the ones discussed in literature [8, 44–46]. The resulting circuit diagram as well as the behavior of the conical nanochannels make our approach comparable to a n-type JFET. The channels behave like lossless switches and exhibit a well-defined working point providing all properties required for high-frequency switching operations. However, the described gated channels prohibit fine tuning of the ionic current. To understand these features, simulations of shape and value of the electrical potential induced by the gate voltage are required. Control experiments performed with uncoated channels of similar dimensions evidence that the

oxide layer is essential for the blocking of the ionic current. The pinch-off voltage was influenced by the tip diameter of the TiO_2-coated conical nanochannel and the distance of the tip to the gate electrode. The blocking of the ionic current also seems to depend on the surface charges induced by the pH value of the electrolyte in agreement with nanofluidics theory. The robustness of these nanofluidic transistors is promising for applications as pH sensor. To improve the statistics and verify the dependence of the pinch-off voltage on the pH value of the solution, the nanofluidic transistors need to be investigated in more detail.

This thesis presented the highly conformal coating of etched ion-track polycarbonate membranes. Due to the high flexibility of the template and the properties of the oxides deposited by ALD, diversified applications in the fields of nanofluidics, filtration, catalysis, sensorics as well as biomedicine are obvious. First tests of coated single channels including the set-up of a nanofluidic transistor emphasized the suitability for this kind of applications.

Bibliography

[1] M. Grätzel. Photoelectrochemical Cells. *Nature*, 414:338–344, 2001.

[2] K. E. Gonsalves, editor. *Biomedical Nanostructures*. Wiley-Interscience, Hoboken, N.J, 2008.

[3] I. T. Kim and R. Tannenbaum. Magnetic Carbon Nanotubes: Synthesis, Characterization, and Anisotropic Electrical Properties. In J. M. Marulanda, editor, *Electronic Properties of Carbon Nanotubes*. InTech, 2011.

[4] V. K. Varadan, L. Chen, and J. Xie. Magnetic Nanotubes and their Biomedical Applications. In *Nanomedicine: Design and Application of Magnetic Nanomaterials, Nanosensor and Nanosystems*. John Wiley & Sons, Chichester, UK, 2008.

[5] J. Hone, I. Ellwood, M. Muno, A. Mizel, M. L. Cohen, A. Zettl, A. G. Rinzler, and R. E. Smalley. Thermoelectric Power of Single-Walled Carbon Nanotubes. *Physical Review Letters*, 80(5):1042–1045, 1998.

[6] P. Kim, A. Majumdar, and P. McEuen. Thermal Transport Measurements of Individual Multiwalled Nanotubes. *Physical Review Letters*, 87(21):215502, 1998.

[7] X. B. Zhao, X. H. Ji, Y. H. Zhang, T. J. Zhu, J. P. Tu, and X. B. Zhang. Bismuth Telluride Nanotubes and the Effects on the Thermoelectic Properties of Nanotube-Containing Nanocomposites. *Applied Physics Letters*, 86:062111, 2005.

[8] I. Yanagi, T. Oura, T. Haga, J. Ando, M.and Yamamoto, T. Mine, T. Ishida, T.and Hatano, R. Akahori, T. Yokoi, and T. Anazawa. Side-Gated Ultrathin-Channel Nanopore FET Sensors. *Nanotechnology*, 27(11):115501, 2016.

[9] S. J. Son, J. Reichel, Bo He, M. Schuchman, and S. B. Lee. Magnetic Nanotubes for Magnetic-Field Assisted Bioseparation, Biointeraction, and Drug Delivery. *Journal of the American Chemical Society*, 127(20):7316–7317, 2005.

[10] S. B. Lee, D. T. Mitchell, L. Trofin, T. K. Nevanen, H. Söderlund, and C. R. Martin. Antibody-Based Bio-Nanotube Membranes for Enantiomeric Drug Separations. *Science*, 296:2198–2200, 2002.

[11] D. T. Mitchell, S. B. Lee, L. Trofin, N. Li, T. K. Nevanen, H. Söderlund, and C. R. Martin. Smart Nanotubes for Bioseperations and Biocatalysis. *Journal of the American Chemical Society*, 124:11864–11865, 2002.

[12] J. T. Korhonen, P. Hiekkataipale, J. Malm, M. Karppinen, O. Ikkala, and R. H. A. Ras. Inorganic Hollow Nanotube Aerogels by Atomic Layer Deposition onto Native Nanocellulose Templates. *ACS Nano*, 5(3):1967–1974, 2011.

[13] Z. Siwy, Y. Gu, H. A. Spohr, D. Baur, A. Wolf-Reber, R. Spohr, P. Y. Apel, and Y. E. Korchev. Rectification and Voltage Gating of Ion Currents in a Nanofabricated Pore. *Europhysics Letters*, 60(3):349–355, 2002.

[14] Z. Siwy, P. Apel, D. Baur, D. D. Dobrev, Y. E. Korchev, R. Neumann, R. Spohr, C. Trautmann, and K.-O. Voss. Preparation of Synthetic Nanopores with Transport Properties Analogous to Biological Channels. *Surface Science*, 532-535:1061–1066, 2003.

[15] E. A. Heins, Z. S. Siwy, L. A. Baker, and C. R. Martin. Detecting Single Porphyrin Molecules in a Conically Shaped Synthetic Nanopore. *Nano Letters*, 5(9):1824–1829, 2005.

[16] M. Ali, B. Yameen, R. Neumann, W. Ensinger, W. Knoll, and O. Azzaroni. Biosensing and Supramolecular Bioconjugation in Single Conical Polymer Nanochannels. Facile Incorporation of Biorecognition Elements into Nanoconfined Geometries. *Journal of the American Chemical Society*, 130(48):16351–16357, 2008.

[17] B. Schiedt, K. Healy, A. P. Morrison, R. Neumann, and Z. Siwy. Transport of Ions and Biomolecules through Single Asymmetric Nanopores in Polymer Films. *Nuclear Instruments and Methods in Physics Research Section B: Beam Interactions with Materials and Atoms*, 236(1-4):109–116, 2005.

[18] M. Pevarnik, K. Healy, M. E. Toimil Molares, A. Morrison, S. E. Létant, and Z. S. Siwy. Polystyrene Particles Reveal Pore Substructure As They Translocate. *ACS Nano*, 6(8):7295–7302, 2012.

[19] L. M. Innes, C.-H. Chen, M. Schiel, M. Pevarnik, F. Haurais, M. E. Toimil Molares, I. Vlassiouk, L. Theogarajan, and Z. S. Siwy. Velocity Profiles in Pores with Undulating Opening Diameter and Their Importance for Resistive-Pulse Experiments. *Analytical Chemistry*, 86(20):10445–10453, 2014.

[20] K. Healy, B. Schiedt, and A. P. Morrison. Solid-State Nanopore Technologies for Nanopore-Based DNA Analysis. *Nanomedicine*, 2(6):875–897, 2007.

[21] J. J. VanDersarl, A. M. Xu, and N. A. Melosh. Nanostraws for Direct Fluidic Intracellular Access. *Nano Letters*, 12(8):3881–3886, 2012.

[22] M. Sattig, S. Reutter, F. Fujara, M. Werner, G. Buntkowsky, and M. Vogel. NMR Studies on the Temperature-Dependent Dynamics of Confined Water. *Physical Chemistry Chemical Physics*, 16(36):19229–19240, 2014.

[23] T. Wehr, R. Rodríguez-Díaz, and M. Zhu, editors. *Capillary Electrophoresis of Proteins*. Marcel Dekker, New York, 1999.

[24] F. Reimann and F. M. Ashcroft. Inwardly Rectifying Potassium Channels. *Current Opinion in Cell Biology*, 11(4):503–508, 1999.

[25] C. A. Doupnik, N. Davidson, and H. A. Lester. The Inward Rectifier Potassium Channel Family. *Current Opinion in Neurobiology*, 5(3):268–277, 1995.

[26] D. N. Kelly, R. H. Wakabayashi, and A. M. Stacy. A Modified Sol-Gel Technique for Pore Size Control in Porous Aluminum Oxide Nanowire Templates. *ACS Applied Materials & Interfaces*, 6(22):20122–20129, 2014.

[27] P. Chen, T. Mitsui, D. B. Farmer, J. Golovchenko, R. G. Gordon, and D. Branton. Atomic Layer Deposition to Fine-Tune the Surface Properties and Diameters of Fabricated Nanopores. *Nano Letters*, 4(7):1333–1337, 2004.

[28] A. J. Storm, J. H. Chen, X. S. Ling, H. W. Zandbergen, and C. Dekker. Fabrication of Solid-State Nanopores with Single-Nanometre Precision. *Nature Materials*, 2(8):537–540, 2003.

[29] J. C. T. Eijkel and A. van den Berg. Nanofluidics: What is it and what can we expect from it? *Microfluidics and Nanofluidics*, 1(3):249–267, 2005.

[30] P. Abgrall and N.-T. Nguyen. *Nanofluidics*. Artech House, Boston, 2009.

[31] R. J. Hunter and H. J. L. Wright. The Dependence of Electrokinetic Potential on Concentration of Electrolyte. *Journal of Colloid and Interface Science*, 37(3):564–580, 1971.

[32] J. A. Davis, R. O. James, and J. O. Leckie. Surface Ionization and Complexation at the Oxide/Water Interface. *Journal of Colloid and Interface Science*, 63(3):480–499, 1978.

[33] Z. Siwy, E. Heins, C. C. Harrell, P. Kohli, and C. R. Martin. Conical-Nanotube Ion-Current Rectifiers: The Role of Surface Charge. *Journal of the American Chemical Society*, 126(35):10850–10851, 2004.

[34] A. J. Wei, C.and Bard and S. W. Feldberg. Current Rectification at Quartz Nanopipet Electrodes. *Analytical Chemistry*, 69(22):4627–4633, 1997.

[35] Z. Wei, M. Kondratenko, L. H. Dao, and D. F. Perepichka. Rectifying Diodes from Asymmetrically Functionalized Single-Wall Carbon Nanotubes. *Journal of the American Chemical Society*, 128(10):3134–3135, 2006.

[36] S. Umehara, N. Pourmand, C. D. Webb, R. W. Davis, K. Yasuda, and M. Karhanek. Current Rectification with Poly-L-Lysine-Coated Quartz Nanopipettes. *Nano Letters*, 6(11):2486–2492, 2006.

[37] P. Y. Apel, Y. E. Korchev, Z. Siwy, R. Spohr, and M. Yoshida. Diode-Like Single-Ion Track Membrane Prepared by Electro-Stopping. *Nuclear Instruments and Methods in Physics Research Section B: Beam Interactions with Materials and Atoms*, 184(3):337–346, 2001.

[38] Z. Siwy, P. Apel, D. Dobrev, R. Neumann, R. Spohr, C. Trautmann, and K.-O. Voss. Ion Transport Through Asymmetric Nanopores Prepared by Ion Track Etching. *Nuclear Instruments and Methods in Physics Research Section B: Beam Interactions with Materials and Atoms*, 208:143–148, 2003.

[39] Z. Siwy and A. Fuliński. A Nanodevice for Rectification and Pumping Ions. *American Journal of Physics*, 72(5):567, 2004.

[40] P. Y. Apel, I. V. Blonskaya, S. N. Dmitriev, O. L. Orelovitch, A. Presz, and B. A. Sartowska. Fabrication of Nanopores in Polymer Foils with Surfactant-Controlled Longitudinal Profiles. *Nanotechnology*, 18(30):305302, 2007.

[41] A. Wolf-Reber. *Aufbau eines Rasterionenleitwertmikroskops: Stromfluktuationen von Nanoporen*. PhD Thesis, Goethe Universität Frankfurt, Frankfurt, 2002.

[42] S. Müller, C. Schötz, O. Picht, W. Sigle, P. Kopold, M. Rauber, I. Alber, R. Neumann, and M. E. Toimil Molares. Electrochemical Synthesis of Bi_{1-x} Sb_x Nanowires with Simultaneous Control on Size, Composition, and Surface Roughness. *Crystal Growth & Design*, 12(2):615–621, 2012.

[43] C. Wang, Q. Fu, X. Wang, D. Kong, Q. Sheng, Y. Wang, Q. Chen, and J. Xue. Atomic Layer Deposition Modified Track-Etched Conical Nanochannels for Protein Sensing. *Analytical Chemistry*, pages 8227–8233, 2015.

[44] R. Karnik, R. Fan, D. Yue, M.and Li, P. Yang, and A. Majumdar. Electrostatic Control of Ions and Molecules in Nanofluidic Transistors. *Nano Letters*, 5(5):943–948, 2005.

[45] R. Fan, M. Yue, R. Karnik, A. Majumdar, and P. Yang. Polarity Switching and Transient Responses in Single Nanotube Nanofluidic Transistors. *Physical Review Letters*, 95(8), 2005.

[46] E. B. Kalman, O. Sudre, I. Vlassiouk, and Z. S. Siwy. Control of Ionic Transport through Gated Single Conical Nanopores. *Analytical and Bioanalytical Chemistry*, 394(2):413–419, 2009.

[47] R. C. Furneaux, W. R. Rigby, and A. P. Davidson. The Formation of Controlled-Porosity Membranes from Anodically Oxidized Aluminium. *Nature*, 337(6203):147–149, 1989.

[48] H. Masuda and K. Fukuda. Ordered Metal Nanohole Arrays Made by a Two-Step Replication of Honeycomb Structures of Anodic Alumina. *Science*, 227:1466–1468, 1995.

[49] K. Nielsch, J. Choi, K. P. Schwirn, R. B. Wehrspohn, and U. Gösele. Self-Ordering Regimes of Porous Alumina: The 10% Porosity Rule. *Nano Letters*, 2(7):677–680, 2002.

[50] G. E. J. Poinern, N. Ali, and D. Fawcett. Progress in Nano-Engineered Anodic Aluminum Oxide Membrane Development. *Materials*, 4(3):487–526, 2011.

[51] J. Martín, M. Martín-González, J. Francisco Fernández, and O. Caballero-Calero. Ordered three-dimensional interconnected nanoarchitectures in anodic porous alumina. *Nature Communications*, 5:5130, 2014.

[52] R. L. Fleischer. *Nuclear Tracks in Solids: Principles and Applications*. University of California Press, Berkeley, 1975.

[53] Reimar Spohr. In Klaus Bethge, editor, *Ion Tracks and Microtechnology*. Vieweg+Teubner Verlag, Wiesbaden, 1990.

[54] P. Y. Apel and S. N. Dmitriev. Micro- and Nanoporous Materials Produced Using Accelerated Heavy Ion Beams. *Advances in Natural Sciences: Nanoscience and Nanotechnology*, 2(1):013002, 2011.

[55] T. Steckenreiter, E. Balanzat, H. Fuess, and C. Trautmann. Pyrolytic Effects Induced by Energetic Ions in Polymers. *Nuclear Instruments and Methods in Physics Research B*, 151:161–168, 1999.

[56] T. W. Cornelius, P. Y. Apel, B. Schiedt, C. Trautmann, M. E. Toimil Molares, S. Karim, and R. Neumann. Investigation of Nanopore Evolution in Ion Track-Etched Polycarbonate Membranes. *Nuclear Instruments and Methods in Physics Research Section B: Beam Interactions with Materials and Atoms*, 265(2):553–557, 2007.

[57] M. Toulemonde, C. Trautmann, E. Balanzat, K. Hjort, and A. Weidinger. Track Formation and Fabrication of Nanostructures with MeV-Ion Beams. *Nuclear Instruments and Methods in Physics Research Section B: Beam Interactions with Materials and Atoms*, 216:1–8, 2004.

[58] R. Spohr. Status of Ion Track Technology-Prospects of Single Tracks. *Radiation Measurements*, 40(2-6):191–202, 2005.

[59] C. Trautmann. Micro- and Nanoengineering with Ion Tracks. In R. Hellborg, H. J. Whitlow, and Y. Zhang, editors, *Ion Beams in Nanoscience and Technology*, pages 369–387. Springer, Berlin, Heidelberg, 2009.

[60] M. E. Toimil Molares. Characterization and Properties of Micro- and Nanowires of Controlled Size, Composition, and Geometry Fabricated by Electrodeposition and Ion-Track Technology. *Beilstein Journal of Nanotechnology*, 3:860–883, 2012.

[61] L. Burr, I. Schubert, W. Sigle, C. Trautmann, and M. E. Toimil Molares. Surface Enrichment in Au-Ag Alloy Nanowires and Investigation of the Dealloying Process. *The Journal of Physical Chemistry C*, 119(36):20949–20956, 2015.

[62] L. Movsesyan, I. Schubert, L. Yeranyan, C. Trautmann, and M. E. Toimil Molares. Influence of electrodeposition parameters on the structure and morphology of ZnO nanowire arrays and networks synthesized in etched ion-track membranes. *Semiconductor Science and Technology*, 31(1):014006, 2016.

[63] M.E. Toimil Molares, J. Brötz, V. Buschmann, D. Dobrev, R. Neumann, R. Scholz, I.U. Schuchert, C. Trautmann, and J. Vetter. Etched heavy ion tracks in polycarbonate as template for copper nanowires. *Nuclear Instruments and Methods in Physics Research Section B: Beam Interactions with Materials and Atoms*, 185(1-4):192–197, 2001.

[64] O. Picht, S. Müller, I. Alber, M. Rauber, J. Lensch-Falk, D. L. Medlin, R. Neumann, and M. E. Toimil Molares. Tuning the Geometrical and Crystallographic Characteristics of Bi_2Te_3 Nanowires by Electrodeposition in Ion-Track Membranes. *The Journal of Physical Chemistry C*, 116(9):5367–5375, 2012.

[65] K. B. Jirage, J. C. Hulteen, and C. R. Martin. Nanotubule-Based Molecular-Filtration Membranes. *Science*, 278(5338):655–658, 1997.

[66] F. Muench, M. Oezaslan, T. Seidl, S. Lauterbach, P. Strasser, H.-J. Kleebe, and W. Ensinger. Multiple Activation of Ion Track Etched Polycarbonate for the Electroless Synthesis of Metal Nanotubes. *Applied Physics A*, 105(4):847–854, 2011.

[67] M. Rauber, I. Alber, S. Müller, R. Neumann, O. Picht, C. Roth, A. Schökel, M. E. Toimil Molares, and W. Ensinger. Highly-Ordered Supportless Three-Dimensional Nanowire Networks with Tunable Complexity and Interwire Connectivity for Device Integration. *Nano Letters*, 11(6):2304–2310, 2011.

[68] D. G. Coronell, E. W. Egan, G. Hamilton, A. Jain, R. Venkatraman, and B. Weitzman. Monte Carlo Simulations of Sputter Deposition and Step Coverage of Thin Films. *Thin Solid Films*, 333(1-2):77–81, 1998.

[69] W. F. A. Besling, M.-L. Ignacimouttou, A. Humbert, M. Mellier, and J. Torres. Continuity and Morphology of TaN Barriers Deposited by Atomic Layer Deposition and Comparison with Physical Vapor Deposition. *Microelectronic Engineering*, 76(1-4):60–69, 2004.

[70] T. Karabacak and T.-M. Lu. Enhanced Step Coverage by Oblique Angle Physical Vapor Deposition. *Journal of Applied Physics*, 97(12):124504, 2005.

[71] G. B. Raupp and T. S. Cale. Step Coverage Prediction in Low-Pressure Chemical Vapor Deposition. *Chemistry of Materials*, 1(2):207–214, 1989.

[72] T. S. Cale, David F. Richards, and D. Yang. Opportunities for Materials Modeling in Microelectronics: Programmed Rate Chemical Vapor Deposition. *Journal of Computer-Aided Materials Design*, 6:283–309, 1999.

[73] G. Ozaydin-Ince and K. K. Gleason. Tunable Conformality of Polymer Coatings on High Aspect Ratio Features. *Chemical Vapor Deposition*, 16(1-3):100–105, 2010.

[74] L. Djomeni, T. Mourier, S. Minoret, S. Fadloun, F. Piallat, S. Burgess, A. Price, Y. Zhou, C. Jones, D. Mathiot, and S. Maitrejean. Study of low temperature MOCVD deposition of TiN barrier layer for copper diffusion in high sspect ratio through silicon vias. *Microelectronic Engineering*, 120:127–132, 2014.

[75] P. Shukla, E. M. Minogue, T. M. McCleskey, Q. X. Jia, Y. Lin, P. Lu, and A. K. Burrell. Conformal Coating of Nanoscale Features of Microporous Anodisc^{tm} Membranes with Zirconium and Titanium Oxides. *Chemical Communications*, 18:847, 2006.

[76] E. Bauer, A H. Mueller, I. Usov, N. Suvorova, M. T. Janicke, G. I. N. Waterhouse, M. R. Waterland, Q. X. Jia, A. K. Burrell, and T. M. McCleskey. Chemical Solution Route to Conformal Phosphor Coatings on Nanostructures. *Advanced Materials*, 20(24):4704–4707, 2008.

[77] Z. Miao, D. Xu, J. Ouyang, G. Guo, X. Zhao, and Y. Tang. Electrochemically Induced Sol-Gel Preparation of Single-Crystalline TiO_2 Nanowires. *Nano Letters*, 2(7):717–720, 2002.

[78] Y. Xu, X. Zhu, Y. Dan, J. H. Moon, V. W. Chen, A. T. Johnson, J. W. Perry, and S. Yang. Electrodeposition of Three-Dimensional Titania Photonic Crystals from Holographically Patterned Microporous Polymer Templates. *Chemistry of Materials*, 20(5):1816–1823, 2008.

[79] M. Ali, B. Schiedt, K. Healy, R. Neumann, and W. Ensinger. Modifying the Surface Charge of Single Track-Etched Conical Nanopores in Polyimide. *Nanotechnology*, 19(8):085713, 2008.

[80] M. Ali, B. Yameen, J. Cervera, P. Ramírez, R. Neumann, W. Ensinger, W. Knoll, and O. Azzaroni. Layer-by-Layer Assembly of Polyelectrolytes into Ionic Current Rectifying Solid-State Nanopores: Insights from Theory and Experiment. *Journal of the American Chemical Society*, 132(24):8338–8348, 2010.

[81] N. Pinna and M. Knez. *Atomic Layer Deposition of Nanostructured Materials*. John Wiley & Sons, 2011.

[82] S. O. Kucheyev, J. Biener, Y. M. Wang, T. F. Baumann, K. J. Wu, T. van Buuren, A. V. Hamza, J. H. Satcher, J. W. Elam, and M. J. Pellin. Atomic Layer Deposition of ZnO on Ultralow-Density Nanoporous Silica Aerogel Monoliths. *Applied Physics Letters*, 86(8):083108, 2005.

[83] J. W. Elam, G. Xiong, C. Y. Han, H. H. Wang, J. P. Birrell, U. Welp, J. N. Hryn, M. J. Pellin, T. F. Baumann, J. F. Poco, and J. H. Satcher. Atomic Layer Deposition for the Conformal Coating of Nanoporous Materials. *Journal of Nanomaterials*, 2006:1–5, 2006.

[84] J. Biener, T. F. Baumann, Y. Wang, E. J. Nelson, S. O. Kucheyev, A. V. Hamza, M. Kemell, M. Ritala, and M. Leskelä. Ruthenium/Aerogel Nanocomposites via Atomic Layer Deposition. *Nanotechnology*, 18(5):055303, 2007.

[85] T. W. Hamann, A. B. F. Martinson, J. W. Elam, M. J. Pellin, and J. T. Hupp. Aerogel Templated ZnO Dye-Sensitized Solar Cells. *Advanced Materials*, 20(8):1560–1564, 2008.

[86] H. C. M. Knoops, E. Langereis, M. C. M. van de Sanden, and W. M. M. Kessels. Conformality of Plasma-Assisted ALD: Physical Processes and Modeling. *Journal of The Electrochemical Society*, 157(12):G241, 2010.

[87] J. Muñoz Rojas, D.and MacManus-Driscoll. Spatial Atmospheric Atomic Layer Deposition: a New Laboratory and Industrial Tool for Low-Cost Photovoltaics. *Materials Horizons*, 1(3):314, 2014.

[88] P. Poodt, R. Knaapen, A. Illiberi, F. Roozeboom, and A. van Asten. Low Temperature and Roll-to-Roll Spatial Atomic Layer Deposition for Flexible Electronics. *Journal of Vacuum Science & Technology A: Vacuum, Surfaces, and Films*, 30(1):01A142, 2012.

[89] K. Sharma, R. A. Hall, and S. M. George. Spatial Atomic Layer Deposition on Flexible Substrates Using a Modular Rotating Cylinder Reactor. *Journal of Vacuum Science & Technology A: Vacuum, Surfaces, and Films*, 33(1):01A132, 2015.

[90] M. S. Sander, M. J. Côté, W. Gu, B. M. Kile, and C. P. Tripp. Template-Assisted Fabrication of Dense, Aligned Arrays of Titania Nanotubes with Well-Controlled Dimensions on Substrates. *Advanced Materials*, 16(22):2052–2057, 2004.

[91] J. W. Elam, D. Routkevitch, P. P. Mardilovich, and S. M. George. Conformal Coating on Ultrahigh-Aspect-Ratio Nanopores of Anodic Alumina by Atomic Layer Deposition. *Chemistry of Materials*, 15(18):3507–3517, 2003.

[92] V. Romero, V. Vega, J. García, R. Zierold, K. Nielsch, V. M. Prida, B. Hernando, and J. Benavente. Changes in Morphology and Ionic Transport Induced by ALD SiO_2 Coating of Nanoporous Alumina Membranes. *ACS Applied Materials & Interfaces*, 5(9):3556–3564, 2013.

[93] S. M. George. Atomic Layer Deposition: An Overview. *Chemical Reviews*, 110(1):111–131, 2010.

[94] Y.-H. Chang, C.-M. Liu, H.-E. Cheng, and C. Chen. Effect of Geometric Nanostructures on the Absorption Edges of 1-D and 2-D TiO_2 Fabricated by Atomic Layer Deposition. *ACS Applied Materials & Interfaces*, 5(9):3549–3555, 2013.

[95] H. Shin, D.-K. Jeong, J. Lee, M. M. Sung, and J. Kim. Formation of TiO_2 and ZrO_2 Nanotubes Using Atomic Layer Deposition with Ultraprecise Control of the Wall Thickness. *Advanced Materials*, 16(14):1197–1200, 2004.

[96] D. Jeong, J. Lee, H. Shin, J. Lee, J. Kim, and M. Sung. Synthesis of Metal-Oxide Nanotubular Structures by Using Atomic Layer Deposition on Nanotemplates. *Journal of the Korean Physical Society*, 45(5):1249–1252, 2004.

[97] C. Bae, S. Kim, B. Ahn, J. Kim, M. M. Sung, and H. Shin. Template-Directed Gas-Phase Fabrication of Oxide Nanotubes. *Journal of Materials Chemistry*, 18(12):1362, 2008.

[98] A. Abou Chaaya, M. Le Poitevin, S. Cabello-Aguilar, S. Balme, M. Bechelany, S. Kraszewski, F. Picaud, J. Cambedouzou, E. Balanzat, J.-M. Janot, T. Thami, P. Miele, and P. Dejardin. Enhanced Ionic Transport Mechanism by Gramicidin A Confined Inside Nanopores Tuned by Atomic Layer Deposition. *The Journal of Physical Chemistry C*, 117(29):15306–15315, 2013.

[99] N. Sobel, C. Hess, M. Lukas, A. Spende, B. Stühn, M. E. Toimil Molares, and C. Trautmann. Conformal SiO_2 Coating of Sub-100 nm Diameter Channels of Polycarbonate Etched Ion-Track Channels by Atomic Layer Deposition. *Beilstein Journal of Nanotechnology*, 6:472–479, 2015.

[100] Bayer. Makrofol - Elekroisolierfolien aus Polycarbonat, 1971.

[101] T. Cornelius. *Fabrication and Characterisation of Bismuth Nanowires*. PhD thesis, Universität Heidelberg, 2006.

[102] P. Sigmund. *Stopping of Heavy Ions - A Theoretical Approach*. Springer Berlin Heidelberg New York, 2004.

[103] J. D. Jackson. *Klassische Elektrodynamik*. Walter de Gruyter Berlin, New York, 1983.

[104] M. Toulemonde, C. Dufour, A. Meftah, and E. Paumier. Transient Thermal Processes in Heavy Ion Irradiation of Crystalline Inorganic Insulators. *Nuclear Instruments and Methods in Physics Research Section B: Beam Interactions with Materials and Atoms*, 166-167:903–912, 2000.

[105] F. Petersen and W. Enge. Energy Loss Dependent Transversal Etching Rates of Heavy Ion Tracks in Plastic. *Radiation Measurements*, 25(1-4):43–46, 1995.

[106] J. F. Ziegler. SRIM, 2008.

[107] N. Chtanko, M. E. Toimil Molares, T. Cornelius, D. Dobrev, and R. Neumann. Etched Single-Ion-Track Templates for Single Nanowire Synthesis. *The Journal of Physical Chemistry B*, 108(28):9950–9954, 2004.

[108] F. Dehaye, E. Balanzat, E. Ferain, and R. Legras. Chemical Modifications Induced in Bisphenol A Polycarbonate by Swift Heavy Ions. *Nuclear Instruments and Methods in Physics Research Section B: Beam Interactions with Materials and Atoms*, 209:103–112, 2003.

[109] Y. Sun, Z. Zhu, Z. Wang, Yu. Jin, J. Liu, M. Hou, and Q. Zhang. Swift Heavy Ion Induced Amorphisation and Chemical Modification in Polycarbonate. *Nuclear Instruments and Methods in Physics Research Section B: Beam Interactions with Materials and Atoms*, 209:188–193, 2003.

[110] D. Fink. *Fundamentals of Ion-Irradiated Polymers*. Springer Berlin Heidelberg New York, 2004.

[111] V. Picq, E. Balanzat, E. Ferain, and R. Legras. Swift Heavy Ions on Polymers: Hydrocarbon Gas Release. *Nuclear Instruments and Methods in Physics Research Section B: Beam Interactions with Materials and Atoms*, 209:103, 1998.

[112] D. Albrecht, P. Armbruster, R. Spohr, M. Koth, K. Schaupert, and H. Stuhmann. Small Angle Scattering from Oriented Latent Nuclear Tracks. *Nuclear Instruments and Methods in Physics Research Section B: Beam Interactions with Materials and Atoms*, 2:702, 1984.

[113] V. A. Ditlov, A. U. Gatchegov, W. Enge, F. Petersen, M. Danziger, A. Schulz, and V. Trofimov. The Radial Etching Velocity for Tracks in Polymer Film. *Radiation Measurements*, 28(1-6):137–144, 1997.

[114] W. De Sorbo. Ultraviolett Effects and Aging Effects on Etching Characteristics Of Fission Tracks in Polycarbonate Film. *Nucl. Tracks*, 3:13–32, 1979.

[115] G. Pépy, P. Boesecke, A. Kuklin, E. Manceau, B. Schiedt, Z. Siwy, M. Toulemonde, and C. Trautmann. Cylindrical Nanochannels in Ion-Track Polycarbonate Membranes Studied by Small-Angle X-ray Scattering. *Journal of Applied Crystallography*, 40(s1):388–392, 2007.

[116] B. Schiedt. *Characterization and Application of Ion Track-Etched Nanopores*. PhD thesis, Ruperto-Carola Universität Heidelberg, 2007.

[117] H.B. Lück. Mechanism of Particle Track Etching in Polymeric Nuclear Track Detectors. *Nuclear Instruments and Methods in Physics Research*, 202(3):497–501, 1982.

[118] G. Guillot and F. Rondelez. Characteristics of Submicron Pores Obtained by Chemical Etching of Nuclear Tracks in Polycarbonate Films. *Journal of Applied Physics*, 52(12):7155, 1981.

[119] D. Dobrev, J. Vetter, R. Neumann, and N. Angert. Conical Etching and Electrochemical Metal Replication of Heavy-Ion Tracks in Polymer Foils. *Journal of Vacuum Science & Technology B: Microelectronics and Nanometer Structures*, 19(4):1385, 2001.

[120] M.-C. Clochard, T.L. Wade, J.-E. Wegrowe, and E. Balanzat. Influence of Asymmetric Etching on Ion Track Shapes in Polycarbonate. *Nuclear Instruments and Methods in Physics Research Section B: Beam Interactions with Materials and Atoms*, 265(1):325–329, 2007.

[121] H. Mukaibo, L. P. Horne, D. Park, and C. R. Martin. Controlling the Length of Conical Pores Etched in Ion-Tracked Poly(ethylene terephthalate) Membranes. *Small*, 5(21):2474–2479, 2009.

[122] L. Burr. *Ion-Track Technology Based Synthesis and Characterization of Gold and Gold Alloys Nanowires and Nanocones*. PhD thesis, Technische Universität Darmstadt, Darmstadt, 2016.

[123] M. Putkonen and L. Niinistö. Organometallic Precursors for Atomic Layer Deposition. In R. A. Fischer, editor, *Precursor Chemistry of Advanced Materials*, volume 9, pages 125–145. Springer-Verlag, Berlin/Heidelberg, 2005.

[124] J. Winkler. Titandioxid. In U. Zorll, editor, *Die Technologie des Beschichtens*. Vincentz, Hannover, Germany, 2003.

[125] A. Rahtu and M. Ritala. Reaction Mechanism Studies on Titanium Isopropoxide-Water Atomic Layer Deposition Process. *Chemical Vapor Deposition*, 8(1):21, 2002.

[126] R. Kubrin, H. S. Lee, R. Zierold, A. Y. Petrov, R. Janssen, K. Nielsch, M. Eich, and G. A. Schneider. Stacking of Ceramic Inverse Opals with Different Lattice Constants. *Journal of the American Ceramic Society*, 95(7):2226–2235, 2012.

[127] H. Si. Lee, R. Kubrin, R. Zierold, A. Y. Petrov, K. Nielsch, G. A. Schneider, and M. Eich. Photonic Properties of Titania Inverse Opal Heterostructures. *Optical Materials Express*, 3(8):1007, 2013.

[128] SAFC Hitech. Titanium isopropoxide - Vapor pressure curve, 2013.

[129] J. Aarik, Al. Aidla, M. Uustare, T.and Ritala, and M. Leskelä. Titanium Isopropoxide as a Precursor for Atomic Layer Deposition: Characterization of Titanium Dioxide Growth Process. *Applied Surface Science*, 161(3-4):385–395, 2000.

[130] O. W. Flörke, H. A. Graetsch, F. Brunk, L. Benda, S. Paschen, H. E. Bergna, W. O. Roberts, W. A. Welsh, C. Libanati, M. Ettlinger, D. Kerner, M. Maier, W. Meon, R. Schmoll, H. Gies, and D. Schiffmann. Silica. In *Ullmann's Encyclopedia of Industrial Chemistry*. Wiley-VCH, Weinheim, 2008.

[131] J. W. Klaus, S. Ofer, and S. M. George. Growth of SiO_2 at Room Temperature with the Use of Catalyzed Sequential Half-Reactions. *Science*, 278(5345):1934–1936, 1997.

[132] Y. Du, X. Du, and S.M. George. SiO_2 Film Growth at Low Temperatures by Catalyzed Atomic Layer Deposition in a Viscous Flow Reactor. *Thin Solid Films*, 491(1-2):43–53, 2005.

[133] W. Kollenberg, editor. *Technische Keramik: Grundlagen, Werkstoffe, Verfahrenstechnik*. Vulkan-Verlag, Essen, 2004.

[134] Ulrich Hilleringmann. *Silizium-Halbleitertechnologie*. Springer Fachmedien Wiesbaden, Wiesbaden, 2014.

[135] SAFC Hitech. Trimethylaluminium - Product Information, 2012.

[136] M. Di Ventra, S. Evoy, and J. R. Heflin. *Introduction to Nanoscale Science and Technology*. Kluwer Academic Publishers, Boston, 2004.

[137] J. W. Perram, R. J. Hunter, and H. J. L. Wright. Charge and Potential at the Oxide/Solution Interface. *Chemical Physics Letters*, 23(2):265–269, 1973.

[138] S. H. Behrens and D. G. Grier. The Charge of Glass and Silica Surfaces. *The Journal of Chemical Physics*, 115(14):6716, 2001.

[139] A. W. Adamson and A. P. Gast. *Physical Chemistry of Surfaces*. Wiley, New York, 6th edition, 1997.

[140] K. Kim. Chemical and Electrical Characterization of Virgin and Protein-Fouled Polycarbonate Track-Etched Membranes by FTIR and Streaming-Potential Measurements. *Journal of Membrane Science*, 134(2):199–208, 1997.

[141] M. Kosmulski. Compilation of PZC and IEP of Sparingly Soluble Metal Oxides and Hydroxides from Literature. *Advances in Colloid and Interface Science*, 152(1-2):14–25, 2009.

[142] M. Kosmulski. The pH-Dependent Surface Charging and the Points of Zero Charge. *Journal of Colloid and Interface Science*, 253(1):77–87, 2002.

[143] H. R. Kruyt, G. H. Jonker, and J. Th. G. Overbeek. *Colloid Science*, volume 1. Elsevier, Amsterdam, 1952.

[144] G. L. Hornyak, H. F. Tibbals, J. Dutta, and J. J. Moore, editors. *Introduction to Nanoscience & Nanotechnology*. CRC Press, Taylor and Francis Group, New York, 2009.

[145] G. Cao and Y. Wang, editors. *Nanostructures and Nanomaterials: Synthesis, Properties, and Applications*. World Scientific Publishing Co. Pte. Ltd., Singapore, 2nd edition, 2011.

[146] R. B. Schoch, J. Han, and P. Renaud. Transport Phenomena in Nanofluidics. *Reviews of Modern Physics*, 80(3):839–883, 2008.

[147] G. Ehrenstein. Surface Charge, www.biophysics.org/Portals/1/PDFs/Education/ ehrenstein.pdf, 2001.

[148] R. B. Schoch, H. van Lintel, and P. Renaud. Effect of the Surface Charge on Ion Transport through Nanoslits. *Physics of Fluids*, 17(10):100604, 2005.

[149] K. H. Bhatt, S. Grego, and O. D. Velev. An AC Electrokinetic Technique for Collection and Concentration of Particles and Cells on Patterned Electrodes. *Langmuir*, 21(14):6603–6612, 2005.

[150] J. Lyklema and J. Th. G Overbeek. On the interpretation of electrokinetic potentials. *Journal of Colloid Science*, 16(5):501–512, 1961.

[151] R. J. Hunter. *Zeta Potential in Colloid Science: Principles and Applications*. Number 2 in Colloid Science. Academic Press, London ; New York, 1981.

[152] Y. Gu and D. Li. The ζ-Potential of Glass Surface in Contact with Aqueous Solutions. *Journal of Colloid and Interface Science*, 226(2):328–339, 2000.

[153] R. B. Schoch. *Transport Phenomena in Nanofluidics: From Ionic Studies to Proteomic Applications*. PhD thesis, EPFL, Lausanne, 2006.

[154] W. Sparreboom and J. C. T. van den Berg, A .and Eijkel. Transport in Nanofluidic Systems: A Review of Theory and Applications. *New Journal of Physics*, 12(1):015004, 2010.

[155] B. Yameen, M. Ali, R. Neumann, W. Ensinger, W. Knoll, and O. Azzaroni. Synthetic Proton-Gated Ion Channels via Single Solid-State Nanochannels Modified with Responsive Polymer Brushes. *Nano Letters*, 9(7):2788–2793, 2009.

[156] N. R. Tas, P. Mela, T. Kramer, J. W. Berenschot, and A. van den Berg. Capillarity Induced Negative Pressure of Water Plugs in Nanochannels. *Nano Letters*, 3(11):1537–1540, 2003.

[157] F. Urban, H. L. White, and E. A. Strassner. Contribution to the Theory of Surface Conductivity at Solid-Liquid Interfaces. *The Journal of Physical Chemistry*, 39(3):311–330, 1934.

[158] S. Kittaka and T. Morimoto. Surface Conductance of Silica in Electrolyte Solutions. *Journal of Colloid and Interface Science*, 55(2):431–439, 1976.

[159] J. Löbbus, M.and Sonnfeld, H. P. van Leeuwen, W. Vogelsberger, and J. Lyklema. An Improved Method for Calculating Zeta-Potentials from Measurements of the Electrokinetic Sonic Amplitude. *Journal of Colloid and Interface Science*, 229(1):174–183, 2000.

[160] G. Schmid. Electrochemistry of capillary systems with narrow pores. *Journal of Membrane Science*, 150(2):151–157, 1998.

[161] B. Hille. *Ion Channels of Excitable Membranes*. Sinauer, Sunderland, Mass, 3rd ed edition, 2001.

[162] M. Ali, W. Ensinger, R. Neumann, and B. Schiedt. Chemical Modification of Track-Etched Single Conical Nanopores Inducing Inversed Inner Wall Polarity. *GSI Scientific Report*, 2006.

[163] J. Cervera, B. Schiedt, R. Neumann, S. Mafé, and P. Ramírez. Ionic Conduction, Rectification, and Selectivity in Single Conical Nanopores. *The Journal of Chemical Physics*, 124(10):104706, 2006.

[164] D. Woermann. Analysis of Non-Ohmic Electrical Current-Voltage Characteristic of Membranes Carrying a Single Track-Etched Conical Pore. *Nuclear Instruments and Methods in Physics Research Section B: Beam Interactions with Materials and Atoms*, 194(4):458–462, 2002.

[165] D. Woermann. Electrochemical Transport Properties of a Cone-Shaped Nanopore: High and Low Electrical Conductivity States Depending on the Sign of an Applied Electrical Potential Difference. *Physical Chemistry Chemical Physics*, 5(9):1853–1858, 2003.

[166] D. Woermann. Electrochemical Transport Properties of a Cone-Shaped Nanopore: Revisited. *Physical Chemistry Chemical Physics*, 6(12):3130, 2004.

[167] R. Karnik, C. Duan, K. Castelino, H. Daiguji, and A. Majumdar. Rectification of Ionic Current in a Nanofluidic Diode. *Nano Letters*, 7(3):547–551, 2007.

[168] I. Vlassiouk and Z. S. Siwy. Nanofluidic Diode. *Nano Letters*, 7(3):552–556, 2007.

[169] J. C. Maxwell. *A Treatise on Electricity and Magnetism*, volume 1. Oxford: Clarendon, 3rd edition, 1892.

[170] P. Y. Apel, I. V. Blonskaya, O. L. Orelovitch, B. A. Sartowska, and R. Spohr. Asymmetric Ion Track Nanopores for Sensor Technology. Reconstruction of Pore Profile from Conductometric Measurements. *Nanotechnology*, 23(22):225503, 2012.

[171] C. C. Harrell, Y. Choi, L. P. Horne, L. A. Baker, Z. S. Siwy, and C. R. Martin. Resistive-Pulse DNA Detection with a Conical Nanopore Sensor. *Langmuir*, 22(25):10837–10843, 2006.

[172] J. E. Wharton, P. Jin, L. T. Sexton, L. P. Horne, S. A. Sherrill, W. K. Mino, and C. R. Martin. A Method for Reproducibly Preparing Synthetic Nanopores for Resistive-Pulse Biosensors. *Small*, 3(8):1424–1430, 2007.

[173] P. Scopece, L. A. Baker, P. Ugo, and C. R. Martin. Conical Nanopore Membranes: Solvent Shaping of Nanopores. *Nanotechnology*, 17(15):3951–3956, 2006.

[174] M. E. Toimil Molares, V. Buschmann, D. D. Dobrev, R. Neumann, I. U. Scholz, R.and Schuchert, and J. Vetter. Single-Crystalline Copper Nanowires Produced by Electrochemical Deposition in Polymeric Ion Track Membranes. *Advanced Materials*, 1(13):62–65, 2001.

[175] S. Goßner. *Grundlagen der Elektronik*. Shaker, Aachen, 7 edition, 2008.

[176] M. Engel, B. Stühn, J. J. Schneider, T. Cornelius, and M. Naumann. Small-Angle X-ray Scattering (SAXS) off Parallel, Cylindrical, Well-Defined Nanopores: From Random Pore Distribution to Highly Ordered Samples. *Applied Physics A*, 97(1):99–108, 2009.

[177] B. Kuttich, M. Engel, C. Trautmann, and B. Stühn. Tailored Nanochannels of Nearly Cylindrical Geometry Analysed by Small Angle X-ray Scattering. *Applied Physics A*, 114(2):387–392, 2014.

[178] T. Bierschenk. *Swift Heavy Ion Irradiation of Amorphous Ge, Amorphous Si and Amorphous Si 1-x Ge x Alloys*. PhD thesis, Australian National University Canberra, Canberra ACT 0200, Australia, 2014.

[179] P. Kluth, C. S. Schnohr, O. H. Pakarinen, F. Djurabekova, D. J. Sprouster, R. Giulian, M. C. Ridgway, A. P. Byrne, C. Trautmann, D. J. Cookson, K. Nordlund, and M. Toulemonde. Fine Structure in Swift Heavy Ion Tracks in Amorphous SiO_2. *Physical Review Letters*, 101(17), October 2008.

[180] D. R. Lide. *CRC Handbook of Chemistry and Physics*. CRC Press, Boca Raton, FL, 2005.

[181] T. W. Cornelius, B. Schiedt, D. Severin, G. Pépy, M. Toulemonde, P. Y. Apel, P. Boesecke, and C. Trautmann. Nanopores in Track-Etched Polymer Membranes Characterized by Small-Angle X-ray Scattering. *Nanotechnology*, 21(15):155702, 2010.

[182] N. Sobel. *Entwicklung einer Anlage zur thermischen Atomlagenabscheidung von nanoskaligen Metalloxiden auf poröse Substrate*. PhD thesis, Technische Universität Darmstadt, Darmstadt, 2015.

[183] J. T. Mayer, U. Diebold, T. E. Madey, and E. Garfunkel. Titanium and Reduced Titania Overlayers on Titanium Dioxide(110). *Journal of Electron Spectroscopy and Related Phenomena*, 73:1–11, 1995.

[184] C.-Y. Wu, Y.-S. Lee, Y.-L.and Lo, C.-J. Lin, and C.-H. Wu. Thickness-Dependent Photocatalytic Performance of Nanocrystalline TiO_2 Thin Films Prepared by Sol-Gel Spin Coating. *Applied Surface Science*, 280:737–744, 2013.

[185] F. Himpsel, F. McFeely, A. Taleb-Ibrahimi, J. Yarmoff, and G. Hollinger. Microscopic Structure of the SiO_2/Si Interface. *Physical Review B*, 38(9):6084–6096, 1988.

[186] C. A. Wilson, R. K. Grubbs, and S. M. George. Nucleation and Growth during Al_2O_3 Atomic Layer Deposition on Polymers. *Chemistry of Materials*, 17(23):5625–5634, 2005.

[187] J. Kim, K. Chakrabarti, J. Lee, K.-Y. Oh, and C. Lee. Effects of Ozone as an Oxygen Source on the Properties of the Al_2O_3 Thin Films Prepared by Atomic Layer Deposition. *Materials Chemistry and Physics*, 78:733–738, 2003.

[188] J. P. Lucas, N. R. Moody, S. L. Robinson, J. Hanrock, and R. Q. Hwang. Determining Fracture Toughness of Vitreous Silica Glass. *Scripta Metallurgica et Materialia*, 32(5):743–748, 1995.

[189] V. Hatty, H. Kahn, and A. H. Heuer. Fracture Toughness, Fracture Strength, and Stress Corrosion Cracking of Silicon Dioxide Thin Films. *Journal of Microelectromechanical Systems*, 17(4):943–947, 2008.

[190] www.azom.com. TiO_2, www.azom.com/article.aspx?articleid=1179.

[191] N. Claussen. Fracture Toughness of Al_2O_3 with an Unstabilized ZrO_2 Dispersed Phase. *Journal of the American Ceramic Society*, 59(1-2):49–51, 1976.

[192] L. Movsesyan. *Synthesis and Characterisation of ZnO Nanowires and 3D Nanowire Networks*. PhD thesis, Technische Universität Darmstadt, Darmstadt, 2016.

[193] C. Kormann, D. W. Bahnemann, and M. R. Hoffmann. Photolysis of Chloroform and Other Organic Molecules in Aqueous Titanium Dioxide Suspensions. *Environmental Science & Technology*, 25(3):494–500, 1991.

[194] W. Stumm, L. Sigg, and B. Sulzberger. *Chemistry of the Solid-Water Interface: Processes at the Mineral-Water and Particle-Water Interface in Natural Systems*. Wiley, New York, 1992.

[195] G. Tarì, S.M. Olhero, and J.M.F. Ferreira. Influence of Temperature on Stability of Electrostatically Stabilized Alumina Suspensions. *Journal of Colloid and Interface Science*, 231(2):221–227, 2000.

[196] R. K. Iler. *The Chemistry of Silica: Solubility, Polymerization, Colloid and Surface Properties, and Biochemistry*. Wiley, New York, 1979.

[197] P. V. Brady and J. V. Walther. Controls on Silicate Dissolution Rates in Neutral and Basic pH Solutions at 25 °C. *Geochimica et Cosmochimica Acta*, 53(11):2823–2830, 1989.

[198] B. J. Kirby and E. F. Hasselbrink. Zeta Potential of Microfluidic Substrates: 2. Data for Polymers. *Electrophoresis*, 25(2):203–213, 2004.

[199] Z. S. Siwy. Ion-Current Rectification in Nanopores and Nanotubes with Broken Symmetry. *Advanced Functional Materials*, 16(6):735–746, 2006.

[200] L.-H. Yeh, M. Zhang, and S. Qian. Ion Transport in a pH-Regulated Nanopore. *Analytical Chemistry*, 85(15):7527–7534, 2013.

List of Abbreviations

ALD Atomic Layer Deposition

Al_2O_3 Alumina

Au Gold

Cu Copper

D_i Inner Diameter (after ALD)

D_o Initial Diameter (after Etching)

EDL Electrical Double Layer

EDX Energy Dispersive X-ray Spectroscopy

FET Field Effect Transistor

I_D Source-Drain Current

$I-V$ Current-Voltage

IEP Isoelectric Point

JFET Junction Field Effect Transistor

KCl Potassium Chloride

NaOH Sodium Hydroxide

PC Polycarbonate

PET Polyethylene Terephthalate

PZC Point of Zero Charge

r Rectification Ratio

SAXS Small Angle X-ray Scattering

SEM Scanning Electron Microscopy

SiO_2 Silicon dioxide

TiO_2 Titania

T Layer Thickness (Deposited by ALD)

UV Ultraviolet

v_B Bulk Etching Velocity

V_{DS} Source-Drain Voltage

V_{GS} Gate Voltage

V_p Pinch-Off Voltage

v_T Track Etching Velocity

XPS X-ray Photoelectron Spectroscopy

List of Figures

List of Tables

About the Author

Education

04/2013 – 07/2016	**PhD Student** in Materials and Earth Sciences *Technische Universität Darmstadt* Title: Surface Modification of Etched Ion-Track Polymer Membranes by Atomic Layer Deposition
10/2010 – 12/2012	**Master of Science** in Physics *Philipps-Universität Marburg* Specialization: General Physics
10/2011 – 12/2012	Master Thesis in Molecular Solids Title: Friction Force Microscopy on Molecular Thin Films
10/2007 – 07/2010	**Bachelor of Science** in Physics *Philipps-Universität Marburg* Specialization: General Physics
04/2010 – 07/2010	Bachelor Thesis in Surface Science Title: Test of a Time of Flight Detector for Time-Resolved Photoelectron Spectroscopy

Awards

05/2015	**Best Poster Award**, Swift Heavy Ions in Mater (SHIM) 2015

Acknowledgements

Here, I would like express my gratitude to all people who contributed to the success of this work over the last three years. Especially, I thank

- Prof. Dr. Christina Trautmann for the opportunity to perform this work in her research group and to get deep insight into the operation of an ion accelerator facility. I am deeply thankful for her constant support of my research, particularly the introduction to fruitful collaborations as well as the possibility to attend several international workshops and conferences. Her support during the organization of the Power Week was remarkable.

- Dr. Maria Eugenia Toimil Molares for the supervision of my work including the introduction to ion-track technology, guiding my work, scientific discussions, and proofreading this thesis. I am grateful for her support regarding the ALD as well as the preparation of abstracts and conference contributions. Additionally, I thank her for the pleasant atmosphere during the conferences in the US.

- Prof. Dr. Wolfgang Ensinger for being co-referee of this work. Prof. Dr. Robert Stark and Prof. Dr. Christian Hess (Eduard-Zintl-Institut für Anorganische und Physikalische Chemie, TU Darmstadt) for being examiners. I am very grateful to Prof. Dr. Hess for his engagement as member of my HGS-HIRe for FAIR graduate school committee and the interesting discussions.

- Deutsche Forschungsgemeinschaft (DFG) for financial support via FOR-1583.

- Helmholtz Graduate School for Hadron and Ion Research (HGS-HIRe for FAIR) for financial support, soft skill courses, networking events, and enabling of the Power Week at Materials Research, GSI.

- all the collaborators of this PhD project:
  - From the Eduard-Zintl-Institut für Anorganische und Physikalische Chemie (TU Darmstadt) I am deeply thankful to Prof. Dr. Christian Hess, Dr. Nicolas Sobel, and Philip Ruff for all the SiO_2-coatings, the insight into their ALD machine as well as technical and scientific discussions. I am grateful to Dr. Nicolas Sobel and Karl Kopp for the XPS investigations. I thank Christian Schilling for the investigation of the free-standing nanocones with UV-Vis spectroscopy.
  - From the Institut für Nanostruktur- und Festkörperphysik (Universität Hamburg) I am deeply thankful to Prof. Dr. Kornelius Nielsch, Dr. Robert Zierold, Dr. J. M. Montero Moreno for the first series of TiO_2 and Al_2O_3 depositions. During my stay, all members of the group provided very helpful information about the installation and running of an ALD machine.

  - From the Institut für Festkörperphysik (TU Darmstadt) I thank Prof. Dr. Bernd Stühn, Manuela Lukas, and Ann-Kathrin Grefe for the SAXS analysis of numerous samples with their laboratory instrument.
  - From the Australian National University Canberra (Australia) I thank Prof. Dr. Patrick Kluth, Dr. Daniel Schauries, and Andrea Hadley for the SAXS measurements and analyses at the synchrotron facility in Melbourne, Australia. I am grateful for their fast and efficient responses in limited time enabling me to describe the results in this work.
  - From the Eduard-Zintl-Institut für Anorganische und Physikalische Chemie (TU Darmstadt) I thank Prof. Dr. Gerd Buntkowsky and Dr. Torsten Gutmann for the investigation of network samples with DNP-NMR.
  - From the Fakultät für Chemie und Chemische Biologie (TU Dortmund) I thank Prof. Dr. Roland Winter and Melanie Bergmann for the SAXS analysis of part of the samples and the ongoing work about lipids in ALD-coated etched ion-tracks.

- Jesse Riedl, Leonard Gura, Nils Ulrich, and Paul Hofmann, who supported me as research assistant, intern, or Bachelor student. I acknowledge their constant enthusiasm for this topic, their creative new ideas and their outstanding independent working style. Working with them was a great pleasure.

- all members of the MF group for the great working atmosphere, the discussions about science and life, and the team-spirit during endless beam times. In particular, I acknowledge the dedicated technical support for the ALD and SEM by Arne Siegmund, the detailed instruction and sharing the responsibility for the SEM with Dr. Ina Schubert, the introduction to and discussions about *I-V* measurements with Dr. Mubarak Ali and Gonzalo Perez-Mitta as well as the technical and soft ware support of the *I-V* set ups by Dr. Kay-Obbe Voss.
  Last but definitely not least thanks to all the other PhD candidates having their office on the second floor of C27 for discussions, support, motivation, proof reading, balancing activities such as PhD Dinners, and fun. Namely, I thank Liana Movsesyan and Michael Wagner for sharing their experience on networks, Loïc Burr and Liana Movsesyan for introducing me to nanocones, and Janina Krieg for the shared organization of the Power Week.

- my parents, my brother, and Simon for permanent encouragement and support in various ways as well as being appreciative during all states of my studies.

T H A N K S!